Investigations on Low Latitude Ionosphere under Varying Space Weather Conditions

A thesis submitted in partial fulfilment of

the requirements for the degree of

Doctor of Philosophy

by

Ankit Kumar

(Roll No. 17330006)

Under the guidance of

Prof. Dibyendu Chakrabarty

Space & Atmospheric Sciences Division

Physical Research Laboratory, Ahmedabad, India

Discipline of Physics

Indian Institute of Technology Gandhinagar

2022

Dedicated to

my parents

Declaration

I declare that this written submission represents my ideas in my own words and where others' ideas or words have been included, I have adequately cited and referenced the original sources. I also declare that I have adhered to all principles of academic honesty and integrity and have not misrepresented or fabricated or falsified any idea/data/fact/source in my submission. I understand that any violation of the above can cause disciplinary action by the Institute and can also evoke penal action from the sources which have thus not been properly cited or from whom proper permission has not been taken when needed.

Ankit Kumar

(Roll No: 17330006)

Certificate

I feel great pleasure in certifying that the thesis entitled "**Investigations on Low Latitude Ionosphere under Varying Space Weather Conditions**" by **Mr. Ankit Kumar** has been carried out under my supervision and this work has not been submitted anywhere else for any degree or diploma.

Prof. Dibyendu Chakrabarty
(Thesis supervisor)
Physical Research Laboratory
Ahmedabad-380009, Gujarat, India

Acknowledgements

First and foremost, I would like to express my sincere gratitude to my advisor Prof. Dibyendu Chakrabarty for his continuous support of my Ph.D. research and for his patience, motivation, enthusiasm, and immense knowledge. He supported me academically in all kinds of peaks and valleys during my Ph.D. tenure. His guidance helped me to perform research work and write this thesis. I could not have imagined having a better advisor and mentor for my Ph.D. study. His vision, sincerity, and motivation have deeply inspired me. He taught me the methodology to carry out scientific research work, and he taught me to present the research works as clearly as possible. I will be indebted to him for my entire life.

After joining my supervisor, I got a chance to interact with Prof. R. Sekar. I want to thank him for his excellent scientific discussion. Although I had little interaction with him, I learned some of the ionospheric physics nuances. I would like to thank Late Prof. S.P. Gupta for sharing his scientific/non-scientific experience with us.

I share the credit of my work with my international and national collaborators. I thank Prof. Bela Fejer, Utah State University, Logan; Dr. G. D. Reeves, Los Alamos National Laboratory, Los Alamos, New Mexico, USA; Dr. G. K. Seemala, Indian Institute of Geomagnetism, Navi, Mumbai, India; Dr. S. Sripathi, Indian Institute of Geomagnetism, Navi, Mumbai, India; Dr. Surendra Sunda, Airport Authority of India, Ahmedabad, India; Dr. Kuldeep Pandey, University of Saskatchewan, Saskatoon, SK, Canada; Dr. Diptirnajna Rout, GFZ German Research Centre for Geosciences, Potsdam, Germany, and Mr. Anil K. Yadav, Physical Research Laboratory, Ahmedabad, India. I feel privileged to have scientific interaction with Prof. Bela Fejer and Dr. G. D. Reeves, and I thank you for your feedback and suggestions. I would like to take the liberty to say to Dr. Pandey and Dr. Rout that I enjoyed the scientific and non-scientific discussions with you. I hope It will be continued forever.

My sincere thanks go to Prof. Kazuo Shiokawa and Dr. Yuichi Otsuka, Institute for Space-Earth Environmental Research (ISEE), Nagoya University, Nagoya, Japan, for providing me an opportunity to work in their group under the program of the JSPS core-to-core program (B: Asia-Africa Science Platforms) entitled "International collaboration of southeast Asia and Africa for study of geospace valiability". I regret that I couldn't work with them due to COVID-19. In addition, I would like to thank Dr. Astrid Maute, National Center for Atmospheric Research, High Altitude Observatory, Boulder, USA, for agreeing to be my host for the Newkirk Fellowship. My discussion with you while writing a *proposal extended my knowledge of the field of space weather.*

I would like to express my deepest gratitude to my DSC committee members, Prof. D. Pallamraju, Dr. Amitava Guharay, and Dr. Aveek Sarkar, for encouraging me to be a better researcher. Their constructive and valuable comments/suggestions helped me to improve my scientific approach immensely.

I would like to acknowledge Prof. Anil Bhardwaj, the director PRL. He allowed me to join Prof. Dibyendu Chakrabarty in carrying out my doctoral thesis work. I would like to extend my gratitude to Dean, Registrar, and Academic Committee for their support and help. My sincere thanks go to all the PRL faculties for providing an overall research view. I thank the staff members of PRLs Computer center, Library, Canteen, CMG for continuously providing the necessary facilities to carry out the research work smoothly. I thank the medical facility of PRL and Dr. Samir Dani, and Dr. Sheetal Patel for always being available. I am thankful to staff members of PRL's Mount Abu guest house (Hill View) for very their hospitality during airglow campaigns. I would like to thank the Director, Dean, Associate Dean, and the academic section of IIT Gandhinagar for their support and help.

I am indebted to my present/past fellow, labmates/colleagues, Kuldeep, Dipti, Sandeep, Sivakandan, Avik, Suman, Aaditya, Anil, Yogesh, Bijoy, Rahul, Jacob, Abhishek, Mitesh, Surajit, Sumanjit. You made the lab environment very lively. I always enjoyed your company and all the parties we had together. Our scientific and non-scientific discussions taught me a lot. My sincere thanks to Mr. Atul Manke. He resolved all kinds of issues related to computers and Matlab programming. I would like to special acknowledge Anil and Mitesh for their fantastic association during the experimental campaign at Mount Abu.

My deepest appreciation goes to my batchmates (JRF batch 2017). I thank Satyajit, Milan, Hirdesh, Himanshu, Abhay, Neeraj, Sushant, Sovan, Vipin, Aravind, Shanwalee, Biswajit, Abhijit, Ritu, Sarika, Subith, Ramanuj, Madhu, Partha, Amit, Atif, Shivani, Alka, Sana, Anshika, Sudipta, Deepak, Hrushi, Pravin, Tanmay, Suraj, Kamlesh. Despite our busy schedules, I enjoyed your company whenever we had time to talk.

I would like to extend my gratitude to a few seniors: Diptiranajan, Kuldeep, Deepak Karan, Navpreet, Prahlad, Rukmani, Satish, Subir, Archita, Aarthy, Kaustav, Rahul, Nidhi, Shefali, Surendra, Sandeep, Priyank, Harish, Abdur, Deepika, Nisha who encourage me so much. I also thank my wonderful juniors: Yogesh, Sunil, Naval, Yash, Vikas, Dayanand, Anju, Monika, Aakansha, Deepak Rai, Deepak Gaur, Meghna, Namita, Bijoy, Kshitiz, Gourav, Soumya, Vineet, Birendra, Dharmendra, Kamran, Mansi, Aakansha, Mallika, Debashis, Wafikul, Arup, Aaditya.

My deepest gratitude goes to my teacher Mr. Mahendra Kumar (Associate Professor, Hindu College, Moradabad), who encourage me to do research. I want to thank my teachers, Drs. Mohit Agrawal, K.K. Agrawal (Maharaja Agrasen Mahavidyalay, Bareilly), Mr. Pramod Gangwar, Mr. Anil Gangwar, Late Mr. Govind Ram, Mr. Mahendra Gangwar, and several who encourage and support me at a different stage of the educational journey.

This journey cannot be completed without acknowledging my school and college friends. I thank Lokesh, Gaurav, Saurabh, Vinay, Vimal, Prempal, Parvindar (PMS, Milak), Aniket, Amit, Arun, Mukesh, Upendra, Madhav, Pradeep, Premprakash, Raj, Priyanshu, Saurabh, Omhari, Vikas, Shalendra, Omendra, Dharmendra, Satendra, Mahaveer (SJIC, Milak), Sumit, Prashant, Pradeep, Bhagat, Ratnesh, Rajesh, Rajat, Aman, Akhil (MAM, Bareilly), Ajay, Shivpraksh, Pranav, Pravesh, Jaydeep, Akhilesh, Ganesh, Kaushal, Rahul, Ajit, Vijay (RGSC, BHU), Utkarsh, Amit, Anshik, Shradhha, Siddhant, Iktesh, Ravikant (HC, Moradabad) and Sachin, Pankaj, Ritik, Ikram, Kanchan (Moradabad).

Last but not least, I would like to express my sincere gratitude to my Parents (Mr. Madan Lal and Mrs. Rajbala Devi) for their unconditional love and sacrifices. I thank my brother (Punit), sister-in-law (Soni), sisters (Neetu and Reena), and brothers-in-law (Devendra and Rampal) for their love and support in any situation. I would like to express my love to my nephews/ nieces, Daksh, Pragya, Taksham, and Shivika. I am grateful to all my paternal/maternal uncles/aunties and my cousin, brothers/sisters for your blessings.

Finally, my thanks go to all the people who have supported me in completing the research work directly or indirectly.

Ankit Kumar

Abstract

The central theme of the present thesis work is to understand the role of ionospheric electrodynamics over the equatorial ionosphere in the plasma distribution over the low latitude sector, in general, and the EIA crest region, in particular, during different seasons, solar fluxes, and solar activity conditions. The dip equatorial electric field perturbations related to space weather events are also investigated during post-sunset as well as post-midnight hours and their effects over low latitude plasma distribution are investigated.

Based on 10 years' of observations (2010-2019) of the vertical total electron content (VTEC) over Ahmedabad (23.0°N, 72.6°E, dip angle 35.2°) and campaign based observations of OI 630.0 nm airglow intensity over Mt. Abu (24.6°N, 72.7°E, dip angle 38.0°), enhancements in VTEC/airglow intensity are brought out during post-sunset hours. Morphologically, these enhancements are found to start any time after 1900 LT and peak around 2000 LT. It is found that these enhancements are primarily caused by the pre-reversal enhancement (PRE) of the zonal electric field over the dip equator through re-invigorated plasma fountain process assisted by the latitudinal plasma density gradients. Interestingly, the post-sunset enhancements in VTEC over the EIA crest region are conspicuous during the December solstice and Equinox in the high solar activity period only. This is consistent with the seasonal and solar activity dependence of the amplitudes of PRE-associated vertical drifts over the dip equator. This suggests that the post-sunset enhancements are related to PRE. The thesis propounds that as the daytime equatorial plasma fountain (EPF) process decides the plasma distribution over the low latitudes, the PRE-driven re-invigorated EPF determines the degree of post-sunset enhancements over the low latitudes. Interestingly, the response time of the EIA crest region corresponding to the PRE-driven plasma fountain is found to be $\sim$ 1.7 hr in contrast to the 3-4 hrs of response time corresponding to the daytime plasma fountain. The TEC measurements by the Indian Satellite-based Augmentation System (SBAS) GAGAN (GPS Aided Geo Augmented Navigation) suggest that PRE drives plasma from 5°-10° magnetic latitude to the EIA crest region, leading to a shorter response time during post-

sunset hours. Further analysis of Ahmedabad VTEC reveals that the post-sunset enhancements depend on the solar flux levels and are conspicuous if the solar flux level exceeds ∼110 sfu during December solstice and Equinox. As PRE is also solar flux dependent, this provides further credence to the direct role of PRE in driving the post-sunset enhancements over the EIA crest region. However, it is suggested that PRE is a necessary condition but not a sufficient condition for the post-sunset VTEC enhancements over the EIA crest region. This is because plasma densities and vertical drifts obtained from the Thermosphere Ionosphere Electrodynamics- General Circulation Model (TIE-GCM) suggest that latitudinal plasma gradients work in tandem with the PRE to determine the degree of post-sunset enhancements in plasma density over the EIA crest region.

In addition to the quiet conditions, the present thesis also brings out a few cases of space weather-induced electric field perturbations during post-sunset and post-midnight hours. These investigations are carried out to understand the changes in the post-sunset ionosphere over low latitudes during disturbed space weather conditions. Several kinds of space weather-induced electric field perturbations are investigated that often worked in tandem or in opposition. These investigations suggest that many anomalous electric field perturbation events cannot be explained based on the conventional penetration electric field paradigm that solely depends on the solar wind electric field related to IMF Bz and solar wind velocity. In fact, these investigations show that unconventional drivers like IMF By, substorm induced electric field etc., can play important roles in modulating the amplitude and polarity of penetration electric field perturbations during both post-sunset and post-midnight hours. These have ramifications for evaluating the state of the low latitude ionosphere at night during disturbed space weather conditions.

Keywords: F region ionosphere, equatorial ionosphere, equatorial ionization anomaly (EIA), equatorial plasma fountain (EPF), space weather, zonal electric field, vertical drift, Pre-Reversal Enhancement (PRE), post-sunset enhancements, geomagnetic storm, prompt penetration (PP) electric field, overshielding (OS) electric field, disturbance dynamo (DD) electric field, magnetospheric substorm,

IMF By, 630.0 nm airglow intensity, total electron content (TEC).

Contents

List of Figures

List of Tables

Chapter 1

Introduction

1.1 Background

The Earth's upper atmosphere and its' magnetic field save us from the harmful radiations and high energetic particles of the Sun. The incoming radiation of the Sun is absorbed by the neutral species of the Earth's atmosphere, and the atmosphere becomes partially ionized. If we neglect the transport of plasma, it is the competition between the production and recombination of plasma that determine the degree of ionization available at a given altitude in the atmosphere. The high energetic X-ray and EUV radiations make the Earth's upper atmosphere ionized. This ionized region is known as the ionosphere, where the plasma is available in sufficient amount to affect the radio wave propagation [e.g., *Schunk and Nagy*, 2009]. Although plasma density is significant in the ionosphere, the neutral density is sufficiently higher (~ 3 orders) than the plasma concentrations and hence, plasma-neutral coupling affects the properties of this atmospheric region in a significant manner. It is, therefore, not surprising that this region is often referred as ionosphere-thermosphere system (ITS). Low latitude ionosphere is known for several large scale plasma processes e.g., equatorial electrojet (EEJ), equatorial plasma fountain (EPF) and equatorial spread-F (ESF). These phenomena are primarily explained based on the electrodynamics of the equatorial and low latitude ionosphere. EEJ is the strong jet of current flowing in the E region of the ionosphere in a narrow latitudinal belt around the dip equator. EPF distributes the equatorial F region ionospheric plasma over the low latitudes generating two crests of enhanced plasma density over low latitudes and a trough over the dip equatorial region. ESF, on the other hand, generates plasma irregularities over the dip equatorial ionosphere during post-sunset hours. All these processes are primarily driven by the solar quiet (Sq) ionospheric electric field. This Sq electric field gets perturbed during disturbed space weather conditions. The electric field perturbations during disturbed space weather conditions affect the large-scale ionospheric plasma processes like EPF and ESF. Hence the low latitude ionosphere shows a lot of variabilities during quiet and disturbed space weather conditions. As the ionosphere plays an important role in the communication and navigational applications, it is important to understand the quiet and disturbed time electric field perturbations and their associated effects over low and equatorial ionosphere not only for the purpose of understanding the ionospheric physics in a critical manner but also from an application perspective.

1.2 The Earth's atmosphere and Ionosphere

This chapter will provide a brief description of the ionosphere-thermosphere system. The generation of Sq electric field over low latitude ionosphere is discussed. The low latitude ionospheric phenomena like EEJ, EPF, and equatorial ionization anomaly are introduced in this chapter. The present thesis provides a number of investigations over the post-sunset F region ionosphere during quiet and disturbed space weather conditions. The pre-reversal enhancement (PRE) of zonal electric field/vertical plasma drifts occupies the central stage in the present thesis and hence the PRE mechanism is introduced in detail. A short description of space weather electric field perturbations and the associated polarities are provided in this chapter. This provides the context to the results related to the disturbed space weather conditions presented in this thesis. In addition, the delayed electric field perturbations by the disturbance dynamo (DD) mechanism is also discussed for completeness.

The Earth's atmosphere is an envelope of neutral gases. The density of the

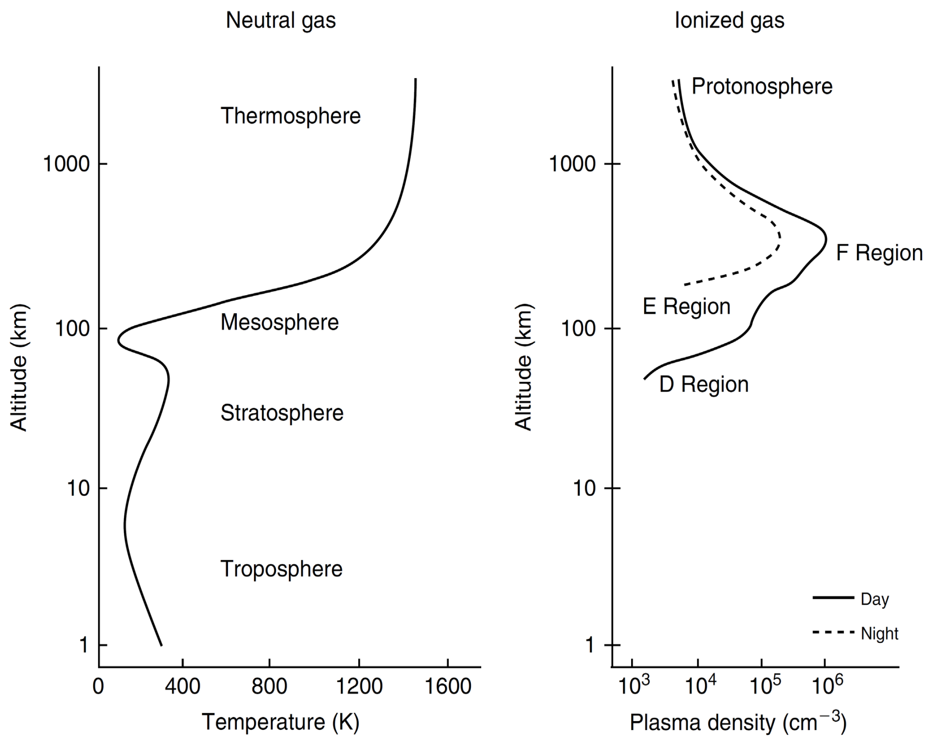

Figure 1.1: The neutral temperature profile of the Earth's atmosphere and the ionospheric plasma density profile. [From ***Kelley*, 2009**]

neutral species of the atmosphere decreases exponentially with increase in altitude. The atmosphere decays so rapidly that 99% of Earth's atmosphere is confined below 50 km. Based on the compositions of neutral species, the neutral atmosphere is divided into two parts- homosphere and heterosphere. Below 100 km altitude (in the homosphere), the neutral atmosphere is well-mixed due to turbulence, whereas in the heterosphere, the neutral species are found in diffusive equilibrium.

The Earth's atmosphere is divided into four major layers based on the altitude profile of neutral temperature (Figure 1.1). The lowest layer of the atmosphere is the troposphere, and the temperature decreases in this layer with a lapse rate of 6.5 K/km up to a height ~8 km at the pole and ~16 km at the equator. The Earth's surface absorbs the Sun's radiations in the visible domain and re-emits in the form of infrared radiation. The effect of this infrared radiation decreases with altitude, and thus, one can notice the decreasing pattern of temperature in the troposphere (Figure 1.1). The very next layer of the Earth's atmosphere is stratosphere. This region is stratified from ∼20 to 50 km altitudes, and the increase in temperature in this region is due to the absorption of the ultraviolet (UV) radiations by the stratospheric ozone. The third layer of the atmosphere is the mesosphere, which is extended from ∼ 60 km to 90 km. The temperature falls in this region rapidly due to the radiative cooling by the CO_2 molecules and OH radicals. The fourth layer of the atmosphere is the thermosphere which extends from ∼ 90 to 1000 km altitude. In this region, the temperatures rise to around 1000 K or higher in accordance with solar activity. The temperature within the thermosphere increases rapidly, mainly due to the absorption of extreme ultraviolet (EUV) radiation. The neutral and ionized species of the thermosphere are shown in Figure 1.2. It can be noticed that the neutral species exist in a diffusive equilibrium.

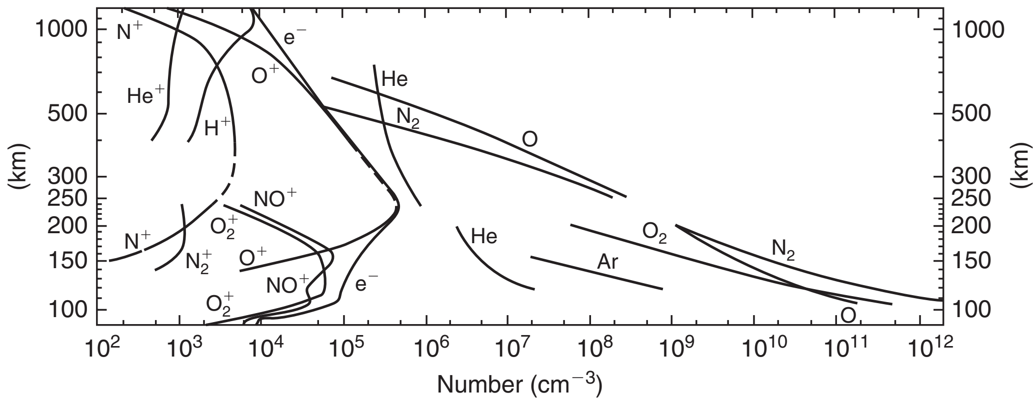

Figure 1.2: Altitude profiles of neutral and ionized species of the thermopshere [From *Kelley*, 2009]

Almost 99 % part of the ionosphere is embedded in the thermosphere. A typical variation of ionospheric electron densities during the day (solid line) and night (dashed line) is shown in Figure 1.1. Based on electron density variations, the ionosphere is divided into three layers- D-layer (70-90 km), E- layer (90-150 km), and F-layer (160-1000 km). Typical electron densities of D, E and F- layers are $10^3 - 10^4$ cm^{-3}, $10^5 - 10^6$ cm^{-3} and 10^6 cm^{-3}, respectively. In all three layers, the production and loss processes of ionized species are different. In the D region, X-rays (0.1-0.8 nm) and Hydrogen Lyman α line (121.6 nm) are the main sources of ionization [e.g., *Nicolet and Aikin*, 1960; *Francey*, 1970]. The species are ${O_2}^+$,

${N_2}^+$, H_3O^+ and $H^+(H_2O)_2$ are in abundance in this region. In the E- region, the required energies for photo-ionizations are UV radiations (91.1-102.7 nm) and soft X-ray (0.8-14.0 nm). In this region, the most dominant species are the NO^+ and ${O_2}^+$. NO^+ is formed by the reaction of molecular nitrogen with atomic oxygen ions. The primary ionization source of the F region is primarily the solar EUV radiation (17-91.1 nm). He-I (58.4 nm) and He-II (30.4 nm) radiations are also important for the lower F region. The lower F region is dominated by NO^+ and ${O_2}^+$ ions, whereas the upper F region is populated by O^+ ions. At higher altitudes ($\sim$ 1000 km), in general, H^+ ions are the dominant ionized species. The recombination processes are different in the E and F regions. The square loss rate dominates in E and lower F regions, whereas the topside F region is characterized by the linear loss rate. At a particular altitude in the F layer, both loss rates are found to be equal and this altitude is known as the transition height. During the daytime, the F region is split up into the F1 and F2 layers due to the competition between production and two different loss processes prevalent at lower and above the transition height. Linear loss is a slow process in which the atomic species take part. On the other hand, the square loss rate is a faster process because the recombination rate of ionized molecular species is faster. This is why the upper E region and F region of the ionosphere sustain during night [e.g., *Rishbeth and Garriott*, 1969] when solar radiation is not present.

The D, E, and F regions can be distinguished based on the relative dominance of gyro-frequencies (Ω) and collision (with neutral) frequencies (ν) of ions and electrons. In the presence of a magnetic field, electrons (e) and ions (i) experience Lorentz force. These particles gyrate around the magnetic field line with a particular frequency which is called gyro-frequencies ($\Omega_{i,e}$). While gyrating, the electrons and ions collide with the neutral species with a particular frequency which is called collision frequency (ν). Gyro frequency depends on the mass, charge of the species and geomagnetic field strength. On the other hand, collision frequency depends on the concentrations and temperatures of the species. In the next section, we will briefly discuss the Earth's magnetic field and its components. The motions of the ions and electrons in the D region are controlled by the neutral wind. The collision frequencies of both ions and electrons are higher than their gyro-frequencies in the D region ($\nu_{i,e} >> \Omega_{i,e}$). In the F-region, the motions of charged species are mainly controlled by the geomagnetic field ($\nu_{i,e} << \Omega_{i,e}$). Interestingly, the ions and electrons show differential behaviors in the E-region. In this region, the motion of ions is collisionally dominated ($\nu_i >> \Omega_i$), whereas the motion of electrons is controlled by the magnetic field ($\nu_e << \Omega_e$). The differential behavior of ions and electrons in the E region is primarily responsible for the generation of the primary electric field. This aspect will be discussed in the E region dynamo section.

1.3 The Earth's magnetic field

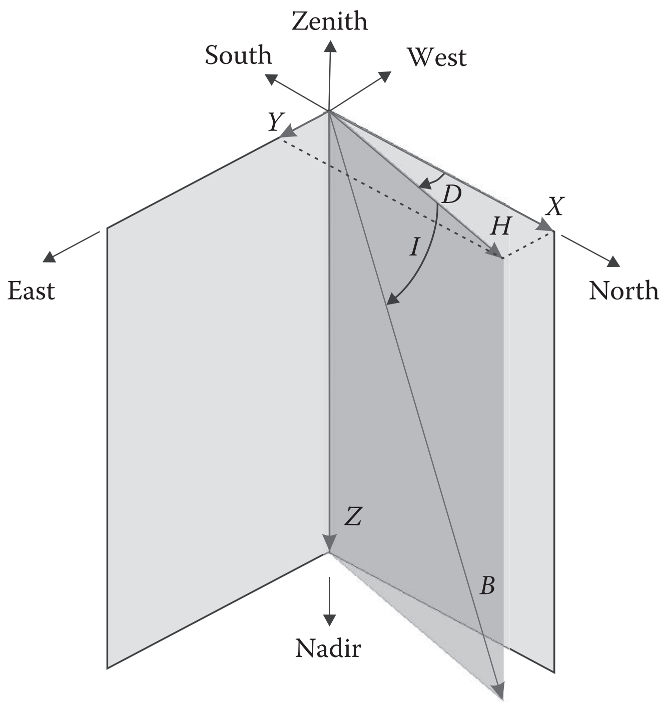

Figure 1.3: The magnetic field components in the local geodetic coordinate system [From *Khazanov*, 2016].

The Earth's magnetic field plays a crucial role in the ionospheric plasma dynamics. The Earth's magnetic field changes on a geological time scale. The movement of the molten lava in the Earth's outer core is considered the main cause of the Earth's magnetic field [e.g., *Inglis*, 1981]. The strength of the magnetic field is higher at the poles and minimum at the equator. Over the Indian dip equator near the surface, the magnetic field is around 38000 nT, and at the pole, its strength is about 65000 nT [e.g., *Alken et al.*, 2021]. The Earth's magnetic field can be described in a geodetic system where $+X$, $+Y$, and $+Z$ are in the geographic North, geographic East, and vertically downward directions (Figure 1.3). Another system is HDZ coordinate system. H is the horizontal component of the Earth's magnetic field in the X-Y plane. D is the declination angle that is defined by the angle between the geographic and magnetic meridian (Figure 1.3). The total magnetic field at any place is defined as B that is directed towards the North, and the angle between the H and B is known as the dip angle (I).

From Figure 1.3,

$$H = B\cos I \qquad \text{and} \qquad Z = B\sin I$$

$$\begin{aligned} X &= H\cos D = B\cos I\cos D \\ Y &= H\sin D = B\cos I\sin D \\ Z &= B\sin I \end{aligned}$$

From the above equations, we get

$$\begin{aligned} H &= \sqrt{X^2+Y^2} \\ B &= \sqrt{H^2+Z^2} = \sqrt{X^2+Y^2+Z^2} \\ D &= \tan^{-1}\left(\frac{Y}{Z}\right) \qquad \text{and} \qquad I = \tan^{-1}\left(\frac{Z}{B}\right) \end{aligned}$$

1.4 Role of the neutral wind

In the E region, the tidal winds are prevalent, and their sources are the upward propagating tides from the lower atmosphere. The Sun and Moon produce tidal forces in the atmosphere. These tidal winds are primarily responsible for E region dynamo [e.g., *Rishbeth*, 1977].

The thermospheric neutral winds are important to understand the electrodynamics and plasma distributions in the F-region [e.g., *Rishbeth*, 1972, 1977;

Richmond et al., 2015]. Thermospheric winds flow in the zonal (East-West), meridional (North-South), and vertical (up-down) directions. The meridional wind can affect the F region plasma dynamics in a number of ways. First, it can push the plasma along the magnetic field lines by ion-neutral drag and can contribute to the vertical movement of the plasma at those places where the dip angle has a finite value [e.g., *Krishna Murthy*, 1990; *Rishbeth*, 1977]. Second, it can change the plasma diffusion along the magnetic field line [*Anderson*, 1971; *Rishbeth*, 1972; *Titheridge*, 1995]. Third, trans-equatorial meridional wind can cause an asymmetry in the equatorial ionization anomaly crests on either side of the dip equator [e.g., *Rishbeth*, 1972; *Anderson and Roble*, 1981]. The zonal winds are westward during the daytime and eastward during the nighttime at the F region altitudes. In the F region, the zonal winds drive the F region dynamo that is more effective at the dusk terminator [e.g., *Richmond et al.*, 2015].

In addition to the zonal and meridional wind, the vertical wind has an important role in ionospheric electrodynamics. At high latitudes, the magnitude of vertical wind is higher [e.g., *Larsen and Meriwether*, 2012; *Smith*, 1998; *Raghavarao et al.*, 1993]. Nevertheless, it's role over low latitudes has also been indicated [e.g., *Raghavarao et al.*, 1987, 1993].

1.5 E region dynamo

The E region dynamo is generated by the global tidal winds. These winds in the E region are produced by the solar and lunar tides, which are generated by the differential heating by the Sun and gravitational pulls by the Moon on the Earth's atmosphere. The time periods of the solar and lunar tides are the fractions of the time period of one solar and lunar day. The largest atmospheric tides are the diurnal and semi-diurnal tides driven by solar heating. It is known that the ions in the E region respond to the winds. The tidal winds carry ions along with them and when ions cut across the geomagnetic field lines, the dynamo action is mimicked. As a consequence, an induced electric field gets generated. This induced electric field drives the current in the E region, which is called the Solar quiet (Sq)

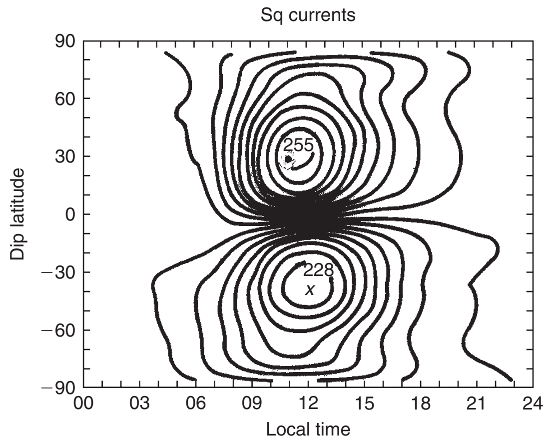

Figure 1.4: Contours of the vertical magnetic fields induced from the horizontal Sq currents [From *Kelley*, 2009]

current. It flows in an anti-clockwise direction in the northern hemisphere and a clockwise direction in the southern hemisphere [e.g., *Matsushita*, 1969; *Yamazaki and Maute*, 2017]. The horizontal Sq current variations are shown in Figure 1.4. Due to the anisotropic nature of the ionospheric conductivities, Sq current can not flow freely and an electric field is set up to make this current divergence-less. This is how the E-region dynamo works [*Rishbeth and Garriott*, 1969]. The electric field, thus generated, is mapped from the low latitude E region to the equatorial F region and drives the large-scale ionospheric plasma process like EPF in the daytime. The eastward and westward electric fields provide the upward and downward vertical drifts [e.g., *Fejer et al.*, 2008a]. Vertical drift variations at different solar flux levels have been shown in Figure 1.5. The zonal component of the electric field over the low latitudes maps in the zonal direction, whereas the poleward component of the electric field maps in the vertically upward directions [*Farley*, 1959] over the dip equator.

1.6 F region dynamo

The E region dynamo works effectively during the day and night. However, during post-sunset hours, the F region dynamo becomes effective as the integrated F region conductance is higher than the E region conductance [e.g., *Rishbeth*, 1971a,

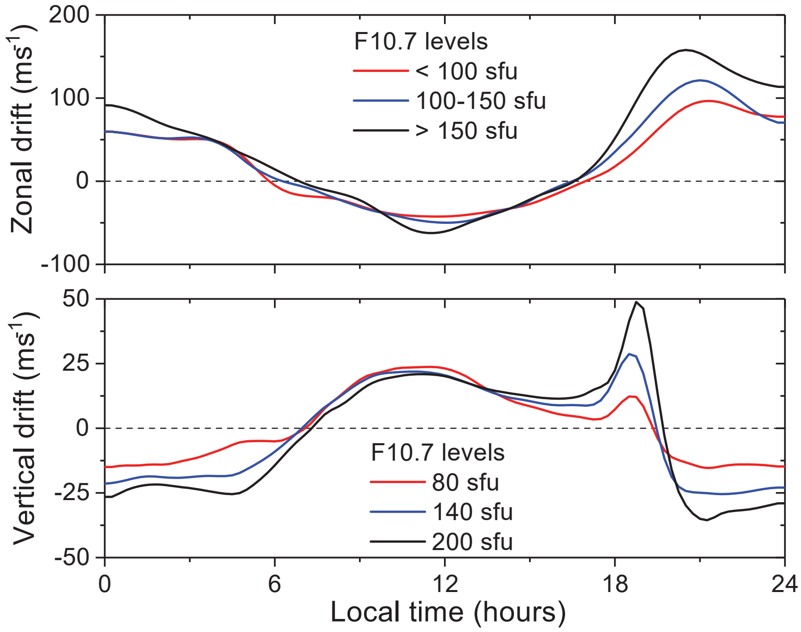

Figure 1.5: Local time variations of the F region plasma zonal drift in the top panel [From *Fejer et al.*, 1991] and vertical drifts in the bottom panel [From *Scherliess and Fejer*, 1999] over the Jicamarca sector during the equinoctial month at different solar flux levels. This figure is reproduced from *Pandey* [2018]

1981]. Due to the sharp fall in electron density in the E region during the post-sunset hours, the conductance of the E region falls sharply [e.g., *Heelis et al.*, 1974]. The F region dynamo operates during the daytime also. However, any current generated during daytime by the F region dynamo gets shorted out [e.g., *Richmond et al.*, 2015; *Rishbeth*, 1977] through the highly conductive magnetic fied lines that are connected to the E region (due to the higher integrated E region field line Pedersen conductivities). In the F region, zonal winds are, in general, westward during the day and eastward during the night [e.g., *Drob et al.*, 2015]. During evening hours, the zonal winds start turning towards the east in the F region. The ion Pedersen conductivity is higher at the F region altitude, which is proportional to the plasma density and ion-neutral collision frequency. Over the dip equatorial region, when the eastward wind cuts across the geomagnetic field lines, an upward ion Pedersen current flows. To make this current divergence-less, a downward electric field is generated that drives the large eastward drift over the dip equator [e.g., *Fejer et al.*, 1985]. This is called the F region dynamo [e.g., *Richmond et al.*, 2015; *Heelis*, 2004; *Rishbeth*, 1977]. The main role of the F region dynamo is to drive the large F region zonal plasma drift that is almost of the same amplitude as that of the thermospheric zonal wind. The zonal drifts during the post-sunset hours depend on the solar flux levels [e.g., *Fejer et al.*, 1991]. The F region zonal plasma drifts are shown at different solar flux levels in Figure 1.5. In addition, the F region dynamo plays a crucial role in enhancing the pre-reversal enhancement (PRE) of vertical plasma drift. *Fejer et al.* [1999] have shown that the F region irregularities are related to the magnitude of the PRE. One important outcome of this thesis is the result that PRE plays a very important role in deciding the post-sunset plasma distribution over low latitude F regions (Chapters-3 and 4).

1.7 Low latitude ionospheric processes

As discussed earlier, the low latitude ionosphere is known for phenomena like EEJ, EPF, and EIA etc. In this section, these phenomena will be discussed in detail.

1.7.1 Equatorial electrojet

The equatorial electrojet is an intense jet of current that flows during the daytime over the dip equator within a narrow latitudinal band [*Chapman*, 1951]. The generation mechanism of EEJ can be understood by the thin slab geometry that is shown in Figure 1.6. In this slab, axes X, Y, and Z represent the eastward, northward, and upward directions, respectively. In the E region, the ions are collisionally bound. On the other hand, electrons experience Hall drift. The eastward zonal electric field (E_X) and horizontal northward magnetic field (B) push electrons vertically upward. However, the electrons can not go far in altitude due to the sharp fall in conductivity, and an upward vertical polarization electric field (E_Z) gets developed. As a result, a net current flow in the vertical direction,

$$J_Z = \sigma_P E_Z - \sigma_H E_X \tag{1.1}$$

Where σ_P and σ_H are the Pedersen and Hall conductivities.
This current cannot flow out of the slab. This implies $J_Z = 0$, Equation 1.1 turns into,

$$E_Z = \frac{\sigma_H}{\sigma_P} E_X \tag{1.2}$$

This vertical polarisation electric field is almost 30 times greater than the zonal electric field. This large vertical electric field in the presence of the northward geomagnetic field causes the Hall drift to the electrons in the westward directions, and an intense current flows in the eastward direction, which is called the EEJ current.

$$J_X = \sigma_P E_X + \sigma_H E_Z \tag{1.3}$$

From equation 1.2 and 1.3

$$J_X = \frac{[\sigma_P{}^2 + \sigma_H{}^2]}{\sigma_P} E_X = \sigma_C E_X \tag{1.4}$$

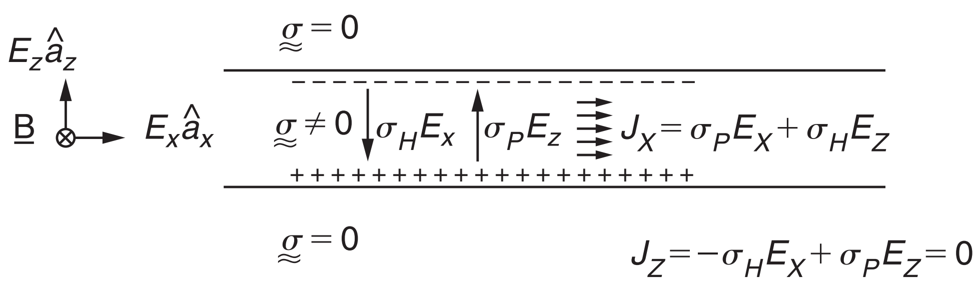

Figure 1.6: A slab geometry to explain the mechanism of EEJ [From *Kelley*, 2009].

Where σ_C is cowling conductivity. σ_C maximizes at around 105 km altitude. Due to this, the strength of this current is maximum near 105 km altitude. Although this current flows in a narrow latitudinal band (±3°), the strength of this current is maximum over the dip equator. This is because the vertical electric field decreases with an increase in the dip angle (I). It is verified from the in-situ measurements of E region current density by magnetometer experiments onboard rockets flight that the magnitude of EEJ is maximum at $\sim$ 105 km altitude [e.g., *Davis et al.*, 1967; *Sampath and Sastry*, 1979]. The continuous measurements of EEJ along the globe can be obtained from ground-based magnetometer observations. One typical variation over the Indian longitude is shown in Figure 1.7. In Figure 1.7, the local time variation of the induced magnetic field due to EEJ is depicted.

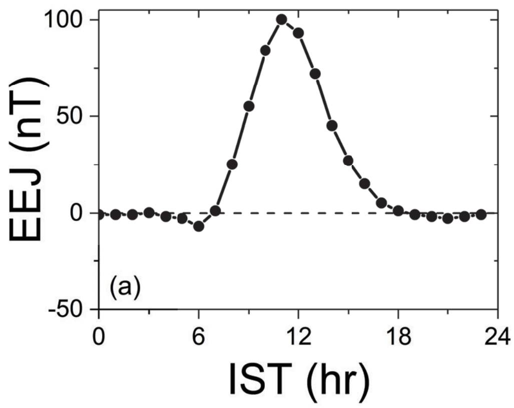

Figure 1.7: Diurnal variation of the induced magnetic field due to the EEJ current [From *Pandey*, 2018]

1.7.2 Equatorial Plasma Fountain and Equatorial Ionization Anomaly

The equatorial plasma fountain (EPF) results from the E×B drift (Hall drift) over the dip equator followed by ambipolar diffusion. A schematic of this process is shown in Figure 1.8. Over the magnetic dip equator, the eastward electric field and horizontal magnetic field configuration cause vertical E×B drift of the F region plasma. As plasma moves vertically upward, it also diffuses (ambipolar diffusion) along the magnetic field lines due to the gravity and pressure gradient forces. This process is called the equatorial plasma fountain [e.g., *Balan et al.*, 2018; *Rajaram*, 1977; *Anderson*, 1971; *Hanson and Moffett*, 1966]. Due to this process, the ionization becomes higher over the $\sim \pm 15°$ magnetic latitudes. As more ionization is expected over the dip equatorial region due to enhanced production, this effect is called the equatorial ionization anomaly (EIA) [*Mitra*, 1946;

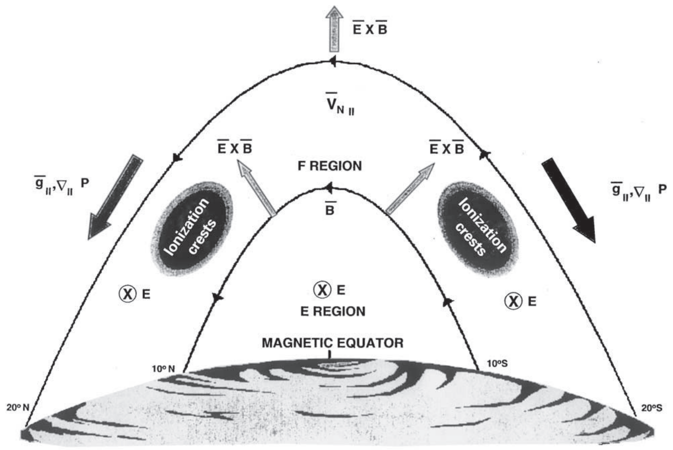

Figure 1.8: A schematic of equatorial plasma fountain (EPF) over the dip equator in the F region [From *Basu et al.*, 2002]

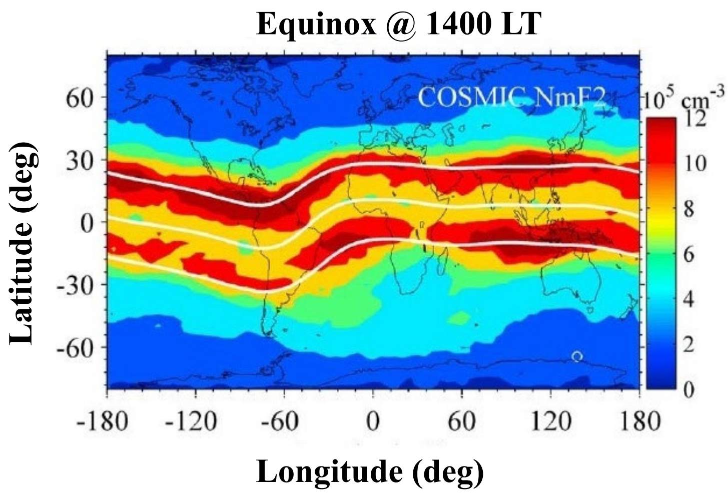

Figure 1.9: A global map of the NmF2 obtained from the COSMIC satellite observation during the equinoctial months of low solar activity at 1400 LT along the globe [From *Liu et al.*, 2010]

Appleton, 1946]. The higher plasma density regions over the low latitudes on both the northern and southern hemispheres are called the EIA crests, and the depleted plasma density region over the dip equator is called the EIA trough. A typical global variation of the peak electron density (NmF2) during the equinoctial period of low solar activity period at ∼1400 LT is shown in Figure 1.9 [*Liu et al.*, 2010] which is constructed by the IRO (Ionospheric radio occultation) observations of COSMIC (Constellation Observing System for Meteorology, Ionosphere and Climate) satellite.

1.8 The Pre-reversal enhancement (PRE) of zonal electric field

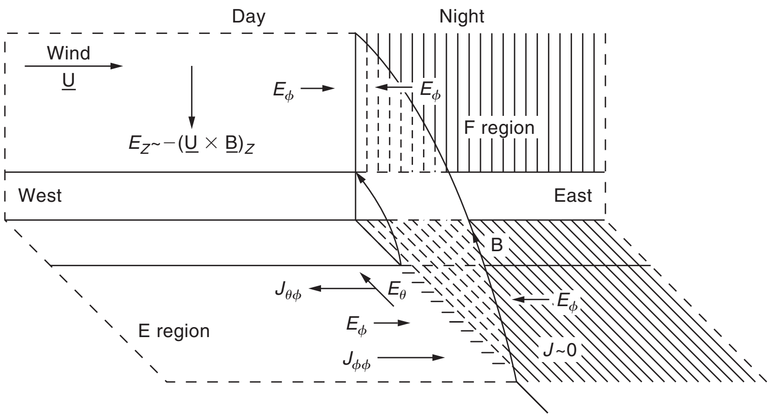

Figure 1.10: A schematic of simplified model [*Farley et al.*, 1986] for pre-reversal enhancement (PRE) is shown. The vertical and horizontal planes are used as equatorial F region and low latitude E region respectively. Both planes are connected by the geomagnetic field lines [From *Kelley*, 2009].

F region vertical drifts are positive (upward) and negative (downward) during day and night, respectively (Figure 1.5). During evening hours, before reversal of the vertical drifts to the downward direction, vertical drifts become upward. This feature is known as the pre-reversal enhancement (PRE) of the vertical plasma drift [e.g., *Scherliess and Fejer*, 1999; *Fejer*, 2011; *Fejer et al.*, 1991; *Fejer*, 1981; *Fejer et al.*, 1979a; *Woodman*, 1970]. These F region vertical drifts show the seasonal and solar flux dependencies [*Fejer et al.*, 2008a; *Madhav Haridas et al.*, 2015]. There are several mechanisms proposed to explain PRE. *Eccles et al.* [2015] reviewed three main mechanisms that had been proposed in the past to explain PRE. *Eccles et al.* [2015] argued that all three mechanisms may be important in isolation or in tandem under different conditions. One of these mechanisms is the response of the ionosphere electric field to maintain the curl-free condition when rapid change in the vertical electric field occurs near the sunset terminator

[*Rishbeth*, 1971b; *Eccles*, 1998]. The second mechanism proposes PRE as the consequence of the divergence of Hall current in the low latitude E region near the sunset terminator [e.g., *Farley et al.*, 1986]. The third mechanism deals with the feedback effect of EEJ conductances on PRE amplitudes around the sunset terminator [e.g., *Haerendel and Eccles*, 1992]. Each mechanism has its limitations, and any single theory can not explain PRE fully. We will briefly explain the mechanism related to the Hall current divergence away from the dip equator in the ensuing paragraph.

A schematic diagram in this regard is provided in Figure 1.10 [*Farley et al.*, 1986]. In Figure 1.10, the vertical plane represents the equatorial F region, and the horizontal plane represents the low latitude E region. Both regions are connected by highly conductive geomagnetic field lines. In the previous section, it has been discussed that the upward ion Pedersen current does not get shorted out in the E region during evening hours. As a result, a downward electric field (E_z) drives the zonal drift. This downward electric field also maps to the low latitude E region in the equatorward direction and drives a westward current ($J_{\theta\phi}$) by providing the Hall drifts mainly to the electrons (note, electrons are magnetized in the E region) towards the dusk terminator. Due to the huge difference in conductivity at the dusk terminator, electrons are piled up there. To make $J_{\theta\phi}$ divergence-less, a current $J_{\phi\phi}$ flows in the eastward directions. This generates an eastward electric field (E_ϕ). This eastward (zonal) electric field gets mapped from the low latitude E region to the equatorial F region and generates the larger F region vertical plasma drifts. The F region vertical drifts are shown in Figure 1.5.

Rishbeth [1977] suggested that the E region dynamo is analogous to a voltage generator, whereas the F region dynamo is akin to a current generator. During day and night, the F region electric field comes from the E region dynamo, while during the PRE hours, the E and F region dynamos compete with each other. *Fejer et al.* [1979b] showed, using the data from Jicamarca radar that the ionospheric electric field over the dip equator satisfies the curl-free condition.

1.8.1 PRE, Post-sunset F region plasma irregularities and L-band scintillation:

The dip equatorial F region ionosphere hosts, on many occasions, plasma instability structures with scale sizes ranging from a few centimeters to a few hundred of kilometers. These structures are primarily created by the Raylor-Taylor instability (RTI) process in which the heavier fluid sits on a lighter fluid and the perturbations on the base of the lighter fluid, under suitable conditions, grow. It is to be noted that the photoionization process ceases after sunset. As the E region is dominated by molecular ions, it depletes faster after sunset due to recombination. On the contrary, the F region, dominated by atomic ions, survive for a much longer duration. This is analogous to a situation where the heavier F region is located on top of the lighter E region. Due to this, a vertical steep plasma density gradient is formed at the lower F region altitude. Under suitable conditions when the steep plasma density gradient becomes anti-parallel to gravity, it gives rise to Rayleigh-Taylor (RT) instability. In addition, the zonal electric field increases during PRE hours, which takes the F region to a higher height. At a higher height, the ion-neutral collision frequency reduces. Therefore, PRE generates favorable conditions to make the bottom side of the F layer susceptible for the generation of plasma irregularities. The seed perturbation can come through gravity waves or other factors. These instabilities generate ionospheric plasma irregularities, which have a scale sizes of hundreds of kilometers to a few centimeters and can be noticed up to ∼1000 km altitude. In the presence of plasma irregularities, the ionosonde echoes get diffused in the frequency/range or in both, which is traditionally known as spread-F. Over the equatorial region, these spreads of echoes are known as Equatorial Spread-F (ESF). Several theoretical and experimental studies are done in the past to understand the generation and evolution of these irregularities [e.g., *Woodman and La Hoz*, 1976; *Subbarao and Krishna Murthy*, 1994; *Muralikrishna et al.*, 2003; *Sekar et al.*, 2004, 2012; *Rodrigues et al.*, 2015; *Huba et al.*, 1987; *Sekar and Raghavarao*, 1987; *Sekar and Kelley*, 1998; *Sekar and Chakrabarty*, 2008; *Huba and Joyce*, 2007; *Huba et al.*, 2008].

The F region plasma irregularities cause scintillations of radio waves depending on the scale size of irregularities. These irregularities may cause phase and amplitude scintillations of radio waves. The GPS constellation traditionally uses L band frequencies that get affected by centimeters size irregularities. In the past, several studies were carried out to understand and characterize the L-band scintillations [e.g., *Basu et al.*, 1988; *Huba and Joyce*, 2010; *Yokoyama*, 2017; *Bhattacharyya et al.*, 2019; *Aol et al.*, 2020].

1.9 Magnetosphere-Ionosphere system

In the previous sections, a general overview of the ionosphere-thermosphere (IT) system is provided. The generation mechanism of the Sq ionospheric electric field is discussed. During a space weather event, the Sq electric field can be modulated and this may impact the ionospheric processes. The solar wind interacts with the Earth's magnetosphere and transfers energy to the magnetosphere through solar wind-magnetosphere coupling [e.g., *Pulkkinen et al.*, 2007; *Gonzalez et al.*, 1989; *Baker*, 1985]. The changes in the magnetosphere affect the high and low latitude ionosphere directly. The solar wind electric field is imposed on the polar ionosphere and eventually, global ionosphere gets affected. In the next sections, we will discuss the magnetosphere-ionosphere coupling during the geomagnetic storm and magnetospheric substorm and associated electric field perturbations over low latitude ionosphere.

1.10 Geomagnetic storm

Geomagnetic storms disturb the terrestrial magnetic field that is measured over ground-based magnetometer observatories. The primary driver of a geomagnetic storm is the solar wind. The solar wind is a continuous outward flow of plasma from the Sun. The density of the solar wind plasma is very low (~ 5 cm^{-3}), and the electric conductivity is very high. Owing to these, the magnetic field is "frozen in" the solar wind plasma. An analogy of the "frozen in" concept is described in *Hargreaves* [1992]. However, an observer sitting on the Earth's frame

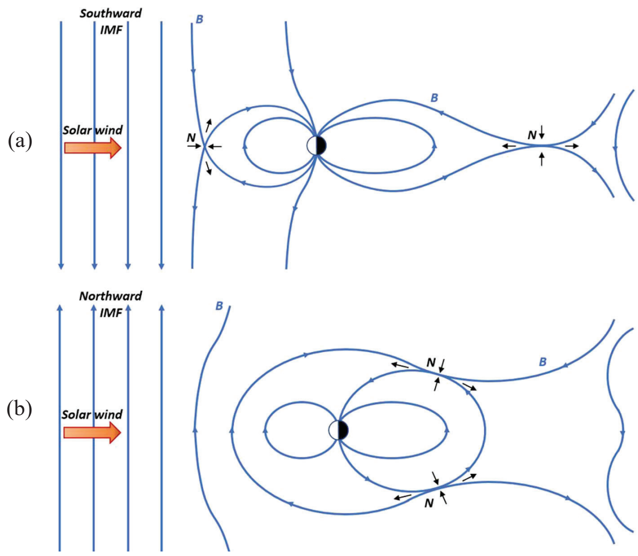

Figure 1.11: Magnetic reconnection in the presence of southward IMF Bz (a) and northward IMF Bz (b) [From *Trattner et al.*, 2021]

of reference can experience the solar wind interplanetary electric field (IEF).

$$IEF = -V_{SW} \times B_{SW} \tag{1.5}$$

In equation 1.5, V_{SW} and B_{SW} are the velocity and magnetic field (interplanetary magnetic field or IMF) of the solar wind. For magnetic reconnection to occur, the southward component of the solar wind magnetic field is important [*Dungey*, 1961]. To understand the solar wind-magnetosphere interaction, two coordinate systems are used. These coordinate systems are Geocentric Solar Ecliptic (GSE) and Geocentric Solar Magnetospheric (GSM). In the GSE frame, the X-axis is positive towards the Sun, Z-axis is positive towards the ecliptic north, and Y-axis is perpendicular to the X and Z-axis. In GSM coordinate system, X-axis is positive towards the Sun, Z-axis is positive parallel to the magnetic meridian, and Y-axis is perpendicular to both axis. The GSM coordinate system is used widely in the magnetospheric system. The solar wind flows in the negative X-direction (away from the Sun). From equation 1.5, it can be seen that the IEFy is in positive Y-direction (dawn-to-dusk direction) for southward IMF Bz.

The Z-component of the interplanetary magnetic field (IMF) is the main driver of geomagnetic storms. When the Z-component of the solar wind magnetic field turns southward, the merging happens at the dayside. This process allows the solar wind plasma and energy to enter into the earth's magnetosphere. This energy is eventually supplied to the IT system. Magnetic reconnection is important to understand the geomagnetic storms that are first proposed by *Dungey* [1961]. He suggested that the solar wind plasma and IMF decide the input energy to the magnetosphere from the solar wind. A schematic of the reconnection under southward and northward IMF Bz is shown in Figure 1.11. The magnetic reconnection at low latitudes happens in the presence of southward IMF Bz (Figure 1.11a), whereas in the presence of northward IMF Bz, reconnection may occur at high latitudes (Figure 1.11b).

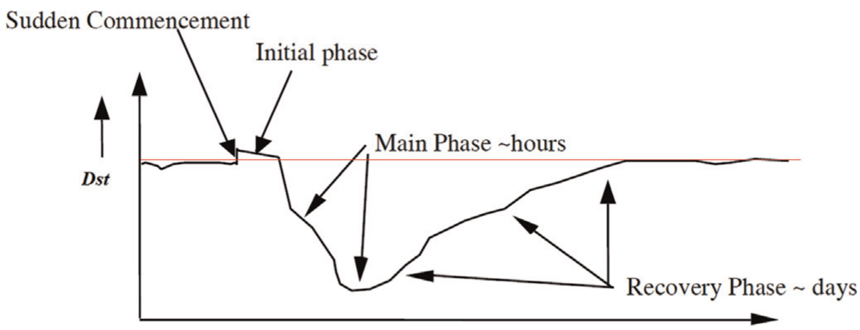

Figure 1.12: Based on Dst index, different phases of geomagnetic storms are depicted. Solid red line represents the zero value of Dst [e.g. ***Andriyas and Andriyas*, 2015**]

When the solar wind strikes the Earth's magnetosphere at dayside, the southward IMF Bz of solar wind reconnects with the northward magnetic field of the Earth, and the magnetic field lines open up. These magnetic field lines are dragged by the solar wind plasma over the magnetosphere. These open magnetic field lines reconnect at the nightside. The energy released during the magnetic reconnection accelerates the plasma towards the sunward direction in the equatorial plane. This convective plasma reaches 5-6 R_E (R_E, earth radius 6371 km) and experiences gradient and curvature drifts due to the closed geomagnetic field lines. As a result, ions move toward the dusk side, and electrons move to the dawn side. A westward current flows at $\sim 5-6\ R_E$ known as the magnetospheric ring current. This current gives a depression in the horizontal component of the geomagnetic field measured by a ground-based magnetometer and is represented by the Dst (Disturbance Strom Time) index (discussed in Chapter-2). The interaction of IMF with the geomagnetic field leads to the strengthening of the ring current. This is typically known as a geomagnetic storm. The Dst index is an hourly index measured in nano Tesla (nT), and is used as a proxy for ring current strength. Sym-H index is similar to Dst index with high temporal cadence (1 min)(discussed in Chapter-2). Different phases of a geomagnetic storm are defined based on the variation in the Dst index. A schematic diagram of different phases of the storm is shown in Figure 1.12. When the solar wind strikes the Earth's magnetosphere, a sudden positive enhancement is noticed in the Dst index, that is known as storm sudden commencement (SSC). This feature is not observed all the time. The elevated Dst index may continue for some time, which is called the initial phase of the storm. This, in general, happens during the northward IMF Bz conditions. Subsequently, the Dst index turns to negative, and the main phase of a geomagnetic storm starts. The strength of the ring current increases until the IMF Bz turns northward. Once the main phase is over with the northward turning of IMF Bz, the recovery phase starts. During this time, the ring current decreases due to the pitch angle scattering of charged particles and charge exchange processes with the neutrals [e.g., *Gonzalez et al.*, 1994]. It is noted that strong geomagnetic storms occur during the passage of interplanetary coronal mass ejections (ICME), whereas corotating interaction regions (CIR) can drive the moderate geomagnetic storm [e.g., *Tsurutani et al.*, 2020]. The more negative the Dst is, the stronger the ring current and the storm. Based on the magnitude of the Dst index, the geomagnetic storms are classified as weak (-30 nT>Dst>-50 nT), moderate(-50 nT>Dst>-100 nT), strong (-100 nT>Dst>-200 nT), severe (-200 nT>Dst>-300 nT) and super (-350 nT> Dst) [e.g., *Loewe and Prölss*, 1997].

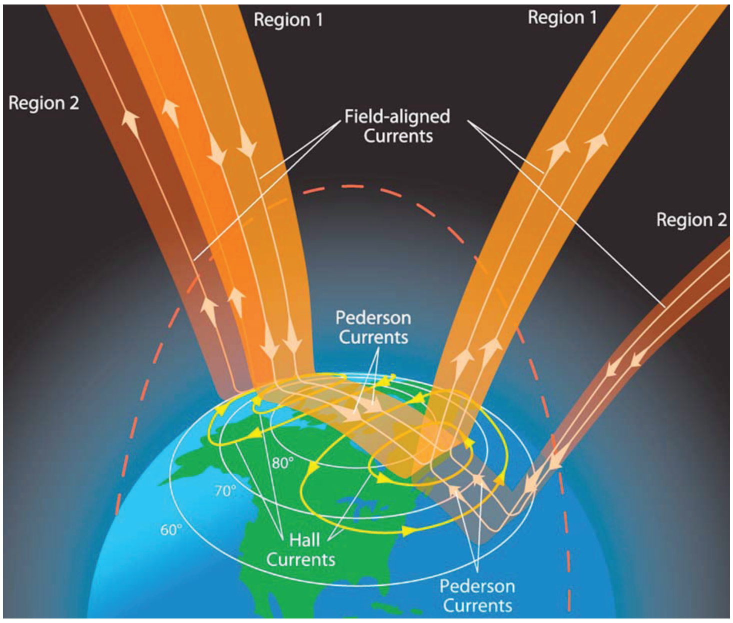

Figure 1.13: A schematic of the R1 and R2 FAC over the polar region. Downward and upward arrows represent the inward and outward currents to and from the ionosphere[From *Le et al.*, 2010].

1.10.1 Prompt penetration (Undershielding) and overshielding electric field

The interplanetary electric field is discussed in the previous section. For southward IMF Bz, the IEFy is dawn-dusk directed. The reconnection at the dayside only happens when the IMF Bz is southward. After the magnetic reconnection, geomagnetic field lines are opened up and the dawn-dusk component of the solar wind electric field (IEFy) is mapped to the polar ionosphere through the highly conducting magnetic field lines. The mapped electric field drives a two-cell plasma convection pattern that is known as the DP2 (Disturbance polar current type-2). The mapped electric field moves the plasma in antisunward directions near the poles and sunward at lower latitudes (see in Figure 1.13). Therefore, the effect of IEF is direct over the polar ionosphere. Since the magnetic field lines are equipotential, the nearly same amount of voltage is dropped at the nightside of magnetosphere which is referred to as the convection electric field. This convection electric field enhances the convection of the plasma in the sunward direction. Under certain conditions, this convection electric field penetrates promptly to low latitudes, which is called the Prompt Penetration (PP) Electric Field. The PP electric field and its effects over low and equatorial ionosphere have been investigated in the past by *Nishida* [1968]; *Wolf* [1970]; *Vasyliunas* [1970]; *Senior and Blanc* [1984]; *Sastri et al.* [2000]; *Kelley et al.* [2003]; *Huba et al.* [2005]; *Tsurutani et al.* [2008]; *Wang et al.* [2008]; *Chakrabarty et al.* [2005, 2015, 2017]; *Rout et al.* [2019]; *Huang et al.* [2007]; *Lu et al.* [2012]. The penetration of convection electric field over low latitude can be understood based on two equivalent scenarios. First, the shielding and overshielding mechanisms that are grossly related to the competition between convection and shielding electric field (discussed in the next paragraph) and second, in terms of the adjustment of the Region-1 and Region-2 field-aligned currents.

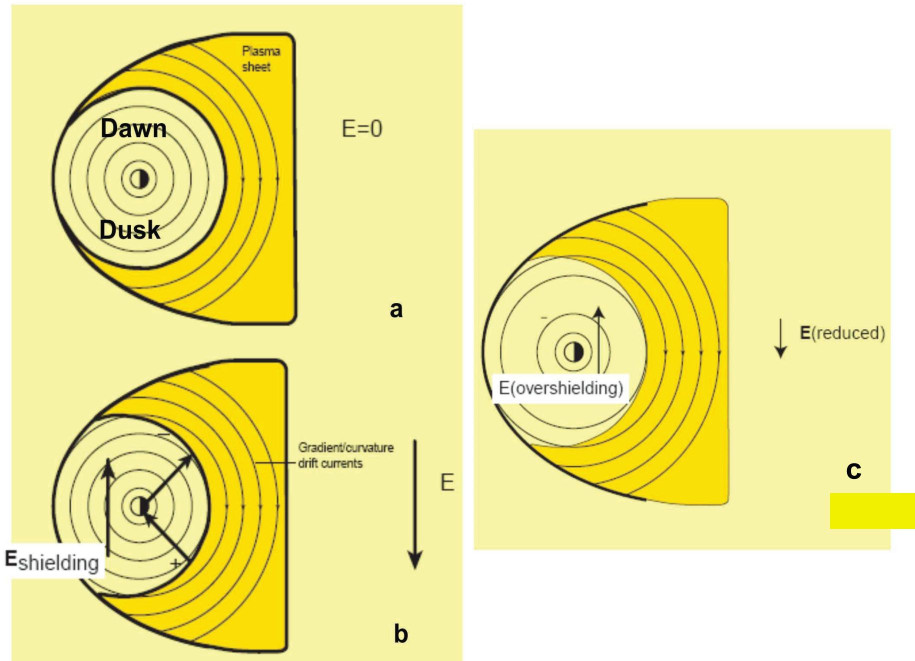

Figure 1.14: (a) represent the quiet time wherein convection electric field is not present (E=0) in the outer magnetosphere. (b) An increase in the convection electric field (E) is imposed and associated development of a shielding electric field $E_{Shielding}$. (c) Convection electric field weakens/disappears quickly leaving the shielding electric field to decay relatively slowly (residual overshielding field) in the inner magnetosphere [From *Wolf et al.*, 2007].

After occurring the magnetic reconnection at the nightside, the plasma convects in the earthward direction from the site of reconnection. When it reaches near the inner magnetosphere, the plasma experiences gradient and curvature drifts. Owing to this, the ions move towards the dusk, and electrons go to the dawnside. As a consequence, the positive and negative charges pile up at the dusk and dawn terminators, and a dusk-to-dawn electric field gets developed at the inner edge of the ring current which is opposite to the convection electric field. This electric field is known as the shielding electric field (E_S) that shields the inner magnetosphere from the convection electric field from further penetration. When this shielding electric field (E_S) is less than the convection electric field (E_C), it is called undershielding condition. Under certain conditions, when E_S becomes equal to the E_C, it is referred to as good shielding. A schematic of the convection and shielding electric field is shown in Figure 1.14. Figure 1.14a represents the situation when convection electric field is absent. As the convection electric field (E_C) increases, the E_S increases to counter E_C (Figure 1.14b). However, when E_C suddenly reduces (when IMF Bz turns to the northward direction) after remaining steady for some time (corresponding to southward IMF Bz condition), E_S (residual shielding electric field) survives in the inner magnetosphere for some time (Figure 1.14c). This happens as the convection electric field can change at a much faster time scale than the shielding electric field. This residual electric field known as the overshielding (OS) electric field.

During the convection, current densities in the inner and outer magnetosphere are imbalanced. To make this current divergence-less, the Region 1 (R1) and Region 2 (R2) Field Aligned Currents (FACs) start getting intensified [*Iijima and Potemra*, 1978; *Potemra*, 1985]. A schematic of the R1 and R2 FACs is shown in Figure 1.13 and it can be seen that these currents are connected to the Pedersen currents in the polar ionosphere. R1 FAC flows into the ionosphere at the dawn side and comes out from the dusk side at higher latitudes ($\sim 67° - 75°$). On the contrary, the R2 FACs flow opposite to the R1 FACs at relatively lower latitudes ($\sim 63° - 68°$). The R1 FAC connects with the magnetopause current (Chapman-Ferraro current) in the dayside and the tail current in the nightside. This is why R1 FAC gets changed at a shorter time scale. On the other hand, the R2 FAC ties the polar ionosphere with the partial ring current (PRC) [e.g., *Ganushkina* *et al.*, 2018]. PRC forms due to the differential ion and electron pressures in the ring current region. Since the R2 FAC is connected through the PRC, the time constant of the R2 FAC is higher than the R1 FAC. In this description, prompt penetration occurs when R1 FAC exceeds R2 FAC and overshielding happens when the reverse happens.

The time constant of the shielding electric field is higher as it is related to the R2 FAC. R2 FAC takes time to develop and also takes time in decay. As a consequence, the convection electric field penetrates to low latitude ionosphere promptly under the southward IMF Bz condition. The time constant of shielding electric field is expected, in general, to be around 20-30 minutes [e.g., *Senior and Blanc*, 1984; *Spiro et al.*, 1988; *Peymirat et al.*, 2000]. *Huang et al.* [2008] showed prompt penetration to the low latitudes sustaining for a long duration that suggest that shielding can remain open for a longer duration under favorable conditions. In general, PP electric field has eastward and westward polarities over the equatorial ionosphere during day and night [e.g., *Fejer et al.*, 2008b], and OS electric field shows the opposite polarity to the PP electric field. The modeling studies [*Nopper Jr. and Carovillano*, 1978] also suggested that the eastward perturbations of the PP electric field are expected until 2200 LT. Further, it was also shown that 6-9% of IEFy penetrates to the low latitude ionosphere [*Kelley et al.*, 2003; *Huang et al.*, 2007].

1.10.2 Transient electric field due to sudden change in solar wind dynamic pressure

A sudden increase of the solar wind pressure affects primarily the Earth's magnetosphere in the dayside. Due to sudden changes in the solar wind dynamic pressure, magnetic fluxes get reconfigured in a short time, and as a consequence, an electromotive force (emf) gets induced as per Faraday's law. This emf enhances the magnetopause current [*Ganushkina et al.*, 2018]. This current adjusts globally, and a transient electric field gets generated. This sudden change in electric field and current can be observed globally in the magnetosphere-ionosphere system [e.g., *Kikuchi and Araki*, 1979; *Araki et al.*, 1985; *Sastri et al.*, 1993; *Huang* *et al.*, 2008; *Rout et al.*, 2016]. Transient change in the ionospheric current due to the sudden impulse (SI) and sudden commencement (SC) is studied by *Le et al.* [1993]; *Russell and Ginskey* [1993, 1995]; *Araki et al.* [1985]; *Kikuchi et al.* [1985, 2001].

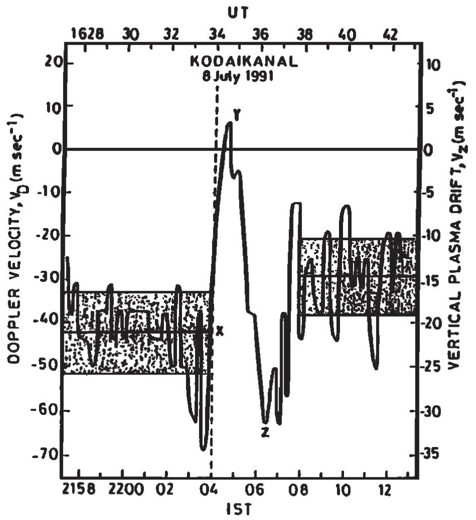

Figure 1.15: A sudden enhancement of vertical drift over Kodaiknal, India (a station near to dip equator) in response to storm sudden commencement (SSC) is observed at 1634 UT (2204 IST)[From *Sastri et al.*, 1993]

The first signature of the changes in the dip equatorial vertical drift due to changes in the solar wind dynamic pressure during a storm sudden commencement (SSC) was shown by *Sastri et al.* [1993]. A sudden change in the F-region vertical drift over Kodaikanal, India, during an SSC was reported on 6 July 1991 during the post-sunset hours (Figure 1.15). Usually, the vertical drifts are negative at this time (Figure 1.5), while during this event, the vertical drifts became positive. It shows direct evidence of MI coupling due to sudden change in solar wind dynamic pressure.

In addition, *Huang et al.* [2008] also observed the transient changes in the vertical drift over Jicamarca due to the sudden increases in the solar wind dynamic pressure. A few observations of *Huang et al.* [2008] have been shown in Figure 1.16. They found an enhancement in the vertical drift during daytime. On the other hand, *Sastri et al.* [1993] noticed an enhancement in vertical drift over the Indian sector due to SSC during the post-sunset hours. Although the

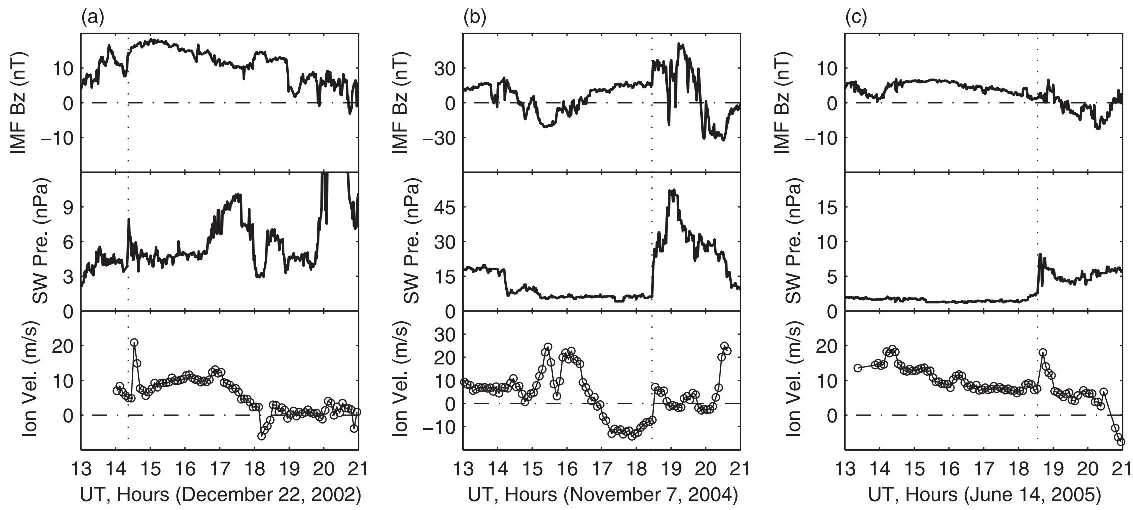

Figure 1.16: Cases of sudden increases of ion vertical drifts over the dip equatorial station Jicamarca, Peru, in response to a shock due to enhancement in the solar wind dynamic pressure. In each column, variations in IMF Bz (top panel), solar wind dynamic pressure (middle panel) and vertical ionospheric plasma drift (bottom panel) are shown [From *Huang et al.*, 2008].

transient electric field perturbations have been shown in the past in a few cases, the expected polarity of the transient electric field perturbations during changes in the solar wind dynamic pressure have not been addressed comprehensively so far. In Chapter-6, the sudden change in the solar wind pressure is studied during post-midnight hours, and their effects have been discussed over the Indian sector.

1.10.3 Effects of IMF By

In the previous section, it is observed that the two-cell convection pattern (DP2) is developed during magnetic reconnection at the dayside. These two convection cells are known as the dawn and dusk cells. These plasma convection cells are affected by the dawn-dusk component of the interplanetary magnetic field (IMF By), significantly [e.g., *Haaland et al.*, 2007; *Heelis*, 1985; *de la Beaujardière et al.*, 1985; *Clauer et al.*, 1984] and this may generate an asymmetry between both the cells. The plasma convection over high latitude affects not only the ionosphere but it also affects the thermosphere [*Liu et al.*, 2020]. *Gosling et al.* [1990] shows the impact of the IMF By over the reconnected magnetic field line.

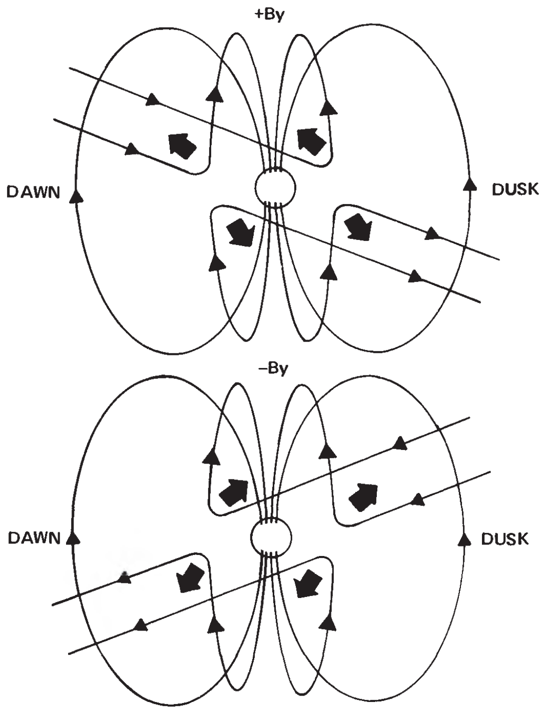

Figure 1.17: The role of positive IMF By (+By) and negative IMF By (-By) is depcited under the southward IMF Bz condition. In the top schematic, the +By and -By pull the reconnected magnetic field line towards the dawn and dusk sectors respectively over the northern hemisphere and vice-versa over southern hemisphere [From *Gosling et al.*, 1990].

In Figure 1.17, the effect of positive and negative IMF By is shown. In the top schematic, it can be seen that reconnected magnetic field lines are pulled towards the dawn and dusk sectors due to the positive IMF By (+By) and negative IMF By (-By) over the northern polar region. The effect of +By and -By is opposite over the southern hemisphere (1.17). Over the high latitudes, the impact of IMF By is studied by several researchers [e.g., *Lukianova and Kozlovsky*, 2011; *Haaland et al.*, 2007; *Clauer et al.*, 1984; *Heelis*, 1985; *de la Beaujardière et al.*, 1985]. However, very few studies are carried out to understand the effect of IMF By over low latitude ionosphere [*Kelley and Makela*, 2002; *Chakrabarty et al.*, 2017]. In this thesis, the effects of IMF By are discussed during the pre-and post-midnight hours (Chapters- 5 and 6).

1.11 Magnetospheric substorm and induced electric field perturbations

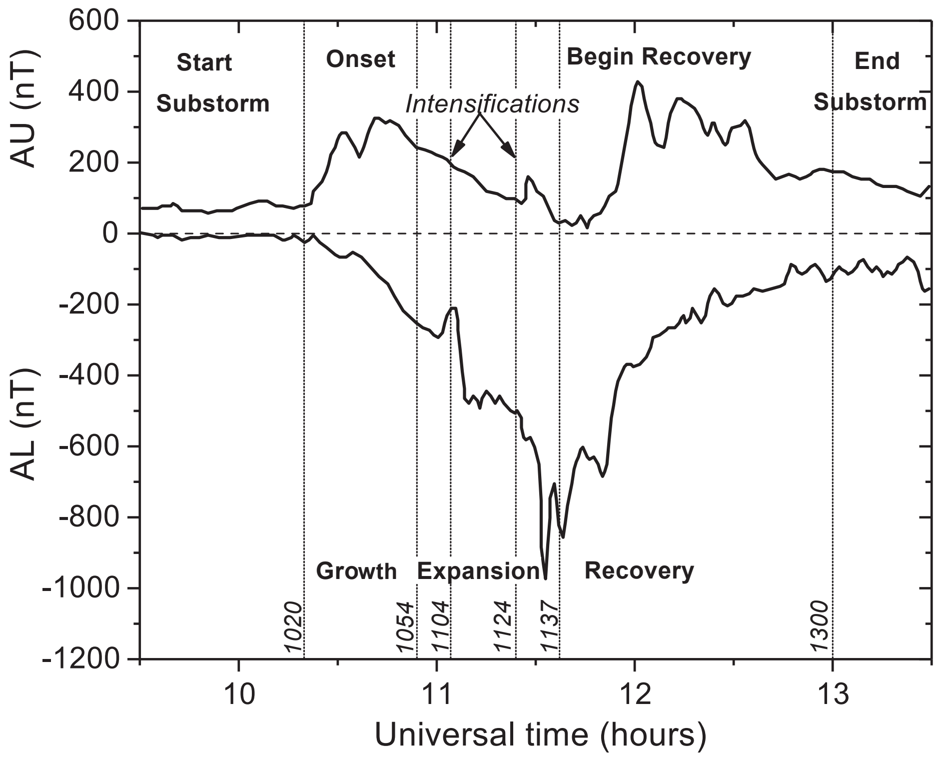

Figure 1.18: Based on AU and AL indices, the different phases of the magnetospheric substorm is shown [From *Kivelson and Russell*, 1995].

Akasofu and Chapman [1961] introduced the concept of substorm for the first time to explain the magnetic field perturbations over the polar regions. The Earth's magnetosphere interacts with the solar wind continuously, and the energy is stored in the nightside of Earth's magnetosphere. Owing to some triggers (e.g. changes in IMF Bz, solar wind ram pressure or magnetospheric plasma instability etc.), the stored energy is released from the nightside of the magnetotail to antisunward direction and very structured aurora is observed over the polar regions of both the hemispheres. Due to the substorm, maximum ionospheric perturbations occur over the polar regions. The initial notion about the substorms was that these are the building blocks of a storm [e.g., *Liu et al.*, 2011b]. However, on many occasions, it has been noticed that substorm occurs in the absence of a geomagnetic storm [e.g., *Henderson et al.*, 1996]. The exact mechanism of the substorm occurrence has not been settled until date although a number of theories, like Substorm Current Wedge model [*Kepko et al.*, 2015], Near-Earth Neutral Line model [*Baker et al.*, 1996] etc., are proposed. Like a geomagnetic storm, a magnetospheric substorm has three phases. These phases are growth, expansion, and recovery (Figure 1.18). During the growth phase, the energy is stored in the magnetotail region. In the expansion phase, dipolarization occurs and the stored energy is released. In the recovery phase, the magnetic field lines return back to the pre-substorm level. During a substorm, particularly the westward auroral electrojet currents get intensified due to a large amount of particle precipitation over the polar region (Figure 1.18). Auroral electrojet is a strong current that flows near the polar region at the E region altitude. In Figure 1.18, the induced magnetic field perturbation due to the eastward (AU) and westward (AL) current is shown. AU and AL indices are discussed in Chapter-2. In general, a substorm ends within 2-3 hours. Substorm can be identified based on the enhancement in the fluxes of multiple energy channels at the same time at the geosynchronous orbit, which is called the dispersionless particle injection [*Reeves et al.*, 1990, 2003]. A simplistic picture is shown in Figure 1.19 to understand dispersion-less particle injections. Extensive research has been carried out to understand various aspects of magnetospheric substorms in the past [e.g., *Akasofu and Chapman*, 1961; *McPherron et al.*, 1973; *McPherron*, 1979; *Rostoker et al.*, 1980; *Kikuchi et al.*, 2003; *Akasofu*, 2021] and even today the effect of substorm-related perturbations on equatorial ionosphere is not understood comprehensively[*Hui et al.*, 2017; *Rout et al.*, 2019; *Fejer et al.*, 2021].

During dipolarization, owing to the fast reconfiguration of the geomagnetic field (B), an induction electric field (E) is generated ($\nabla \times E = -\partial B/\partial t$) [*Reeves*, 1998]. This substorm-induced electric field can affect ionospheric processes over low latitudes and such effects have been reported in the past [e.g., *Chakrabarty et al.*, 2008, 2010; *Huang*, 2009; *Simi et al.*, 2012; *Hui et al.*, 2017; *Rout et al.*, 2019; *Fejer et al.*, 2021; *Sori et al.*, 2022]. On several occasions, it has been noticed that the amplitude of substorm-induced electric field over low latitudes is higher

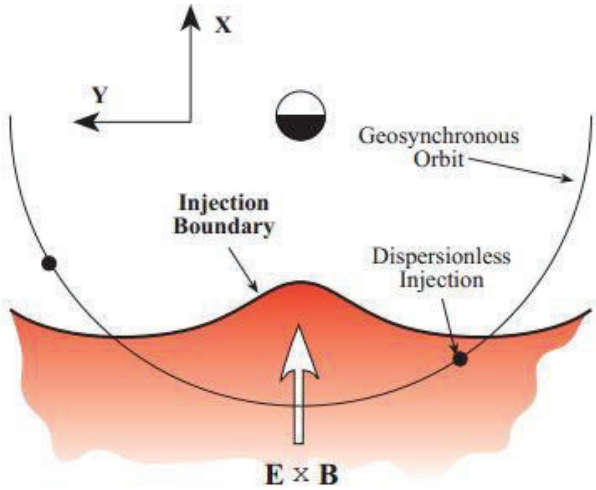

Figure 1.19: A schematic of the dispersion-less particle injection during a substorm [From *Reeves*, 1998]

than the PP electric field [e.g., *Hui et al.*, 2017; *Rout et al.*, 2019]. Further, it was shown [*Hui et al.*, 2017] that substorms can induce both eastward and westward electric field perturbations over low latitudes under steady southward IMF Bz conditions and can be as significant as the effects of PP electric field during a storm. In Chapters- 5 and 6, the role of storm-time substorm-induced electric field perturbations are discussed during pre-and post-midnight hours.

1.12 Disturbance dynamo electric field perturbations

During the main phase of the geomagnetic storms and substorms, the auroral electrojets currents are intensified. The intensification of these currents enhances the joule heating over the polar regions, and heat is transferred to the thermosphere. This alters the global wind circulation pattern. The altered meridional wind pattern from high- to low-latitude regions eventually affects the Sq current system over mid- and low-latitude regions which is called the disturbance dynamo [*Blanc and Richmond*, 1980; *Abdu et al.*, 2006; *Yamazaki and Maute*, 2017].

Blanc and Richmond [1980] proposed the mechanism of disturbance dynamo (DD) for the first time. Several researchers reviewed this mechanism [e.g., *Abdu*

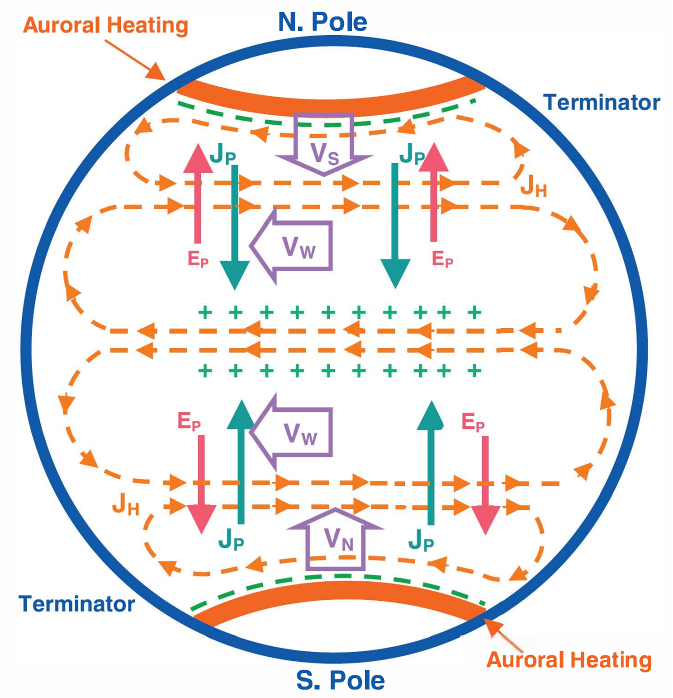

Figure 1.20: A schematic diagram of the Disturbance dynamo mechanism [From *Abdu et al.*, 2006].

et al., 2006; *Yamazaki and Maute*, 2017; *Amory-Mazaudier and Venkateswaran*, 1988]. A schematic diagram (Figure 1.20) is used here to capture the salient features of DD. Over mid-latitude, the equatorward wind (V_s) moves to the westward direction (represented by V_w) due to the Coriolis force. In the presence of a downward magnetic field configuration over the mid-latitude, the westward wind V_w drives the equatorward Pedersen current (J_P). As a result, the positive charges start to accumulate near the equator and the negative charges accumulate near the pole. When sufficient charge is accumulated, the net flow is inhibited, and a poleward electric field (E_p) gets developed. In other words, it can be understood by the divergence-less of the equatorward Pedersen current. This large poleward electric field (E_P) drives a large Hall current in the eastward and Pedersen current in the poleward directions. This eastward Hall current gets interrupted at the terminators where the zonal conductivity gradients are very high. As a result, the dusk sector gets positively charged and the dawn sector gets negatively charged. This generates a dusk-to-dawn electric field, which is westward on the dayside and eastward on the nigtside. Hence the polarity of the disturbance dynamo electric field is opposite to the quiet time ionospheric electric field polarity which is eastward on the dayside and westward on the nightside. The ionospheric current, thus, generated, flows in the anti-Sq direction. (Figure 1.4). This process is called the ionospheric disturbance dynamo.

The DD-related electric field perturbations are dominant during nighttime [e.g., *Fejer et al.*, 2008b] as ion drag forces are less during the nighttime [*Huang and Chen*]. The seasonal and solar flux dependence of DD has been reported by *Huang* [2013]. However, it has also been shown [*Pandey et al.*, 2018] that the daytime perturbations due to DD can be as high as at nighttime during Equinox in high solar activity. The DD electric field (DDEF) opposes the quiet time Sq electric field polarities, and hence the polarity of DDEF is westward and eastward during day and night, respectively [e.g., *Fejer et al.*, 2008b; *Scherliess and Fejer*, 1997].

1.13 Aim and overview of thesis

The central theme of the present thesis work is to understand post-sunset plasma distribution over low latitude, in general, and over the EIA crest region, in particular during quiet and disturbed space weather conditions. Detailed investigations are carried out to understand the variabilities (with the season, solar flux, and solar activity) and causes of the post-sunset plasma density enhancements near the EIA crest region. The roles of the dip equatorial electric field, plasma density gradient over low latitude, and thermospheric meridional wind have been evaluated to understand these enhancements. In addition, space weather electric field perturbations are studied during the post-sunset and post-midnight hours over the dip equator, and their associated effects over the low latitude ionosphere are addressed. During space weather events, several types of penetration electric fields like prompt penetration electric field, overshielding electric field, substorm induced electric field, and delayed electric field by disturbance dynamo are investigated to understand the nature of the disturbance electric field perturbations and their effects over low latitude ionosphere.

Techniques, data, and models used in the present thesis work are discussed in Chapter-2. In this chapter, salient features of the narrow spectral band, narrow field of view airglow photometric technique, measurements of VTEC by dual-frequency GPS-receiver, magnetometer data, TEC data from Indian SBAS (Satellite Based Augmented System) GAGAN (GPS Aided GEO Augmented Navigation), ionosonde technique, incoherent and coherent radar techniques, etc. are introduced. In addition, physics-based model like TIE-GCM (Thermosphere Ionosphere Electrodynamics- General Circulation Model) and global empirical models like quiet and disturbed time vertical drift model, horizontal wind model are described in brief.

After sunset, the plasma density over the EIA crest region gets enhanced, the cause of which was not comprehensively understood until date. Using systematic GPS-VTEC measurements over Ahmedabad and campaign-based OI 630.0 nm airglow intensity measurements from Mt. Abu, it is found that these enhancements are observed after 1930 LT. These enhancements are known as post-sunset enhancements. In Chapter-3, the results and analysis show that PRE drives these enhancements through the equatorial plasma fountain (EPF) process similar to daytime EPF.

Chapter-4 reveals that the PRE is a primary driver for the post-sunset enhancements over the EIA crest region. However, it is not a sufficient condition. Detailed investigation shows that the latitudinal plasma gradient works in tandem with PRE to enhance the plasma density over the EIA crest region. In this chapter, it is found that the post-sunset enhancements are solar flux dependent. The minimum value of the solar flux level that is needed for these enhancements is also established in this chapter.

The results of Chapters- 3 and 4 discuss PRE-related electric field variation and their effects over low latitudes during quiet periods. In Chapter-5, the anomalous electric field perturbations over the dip equator during post-sunset hours are discussed when the effects of PRE are expected to be observed in the low latitude ionosphere. Therefore, these anomalous electric field perturbations can throw light on the adjustment of the post-sunset plasma density enhancements over the EIA crest region. It is noticed that the penetrated electric field into the low latitude, on multiple occasions, apparently violated the conventional penetration efficiency reported in the literature. The role of IMF By and substorm induced electric field are brought out to address these apparent violations.

In order to investigate the effects of space weather-induced electric field perturbations over the low latitude ionosphere during post-midnight hours, Chapter-6 is introduced. The rationale of introducing this chapter is to compare the effects of penetration electric field during post-midnight hours with the effects during post-sunset hours reported in Chapter-5. In this chapter, the large upward vertical plasma drifts over the Indian dip equator are analyzed during the post-midnight hours. Moreover, the electric field perturbations during the post-midnight hours are also found to be anomalous. Based on two cases, it is shown that a small change in IEFy produced large vertical plasma drifts over the dip equator, whereas a relatively larger change in IEFy generated smaller upward vertical drift. Similar to Chapter-5, the important roles of other drivers like IMF By, substorm, disturbance dynamo etc. are found to be important in these cases. This chapter shows the combined effect of several kinds of space weather electric field perturbations over the dip equator during the post-midnight hours. It is difficult to evaluate the impact of each space weather electric field in isolation if they occur simultaneously.

The future scope based on this thesis work is briefly discussed in Chapter-7.

Chapter 2

Techniques, Datasets and Models

2.1 Introduction

There are several techniques to probe the F region plasma. In this thesis work, a number of ground and satellite measurements are used to understand the F region ionosphere during quiet and disturbed space weather conditions. We focus mainly on the equatorial and low latitude ionosphere over Indian longitudes. For this, the campaign-based OI 630.0 nm airglow intensity measurements from Mt. Abu and 10 years' of continuous measurements of vertical total electron content (VTEC) over Ahmedabad, SBAS-TEC data, magnetometer data, and measurements of bottom-side F-layer height are used widely. We have used mainly ground-based measurements, that have high temporal resolution and low spatial coverage. On the other hand, satellite-based measurements have the opposite limitations compared to ground-based techniques- large spatial coverage but low temporal resolution for a given place. A few model outputs have been used to overcome these limitations. In this chapter, we will briefly discuss the observational techniques, used datasets, and models.

2.2 Airglow Photometry

This is one of the techniques that is deployed to investigate the ionosphere. The atoms and molecules of the Earth's thermosphere generate feeble emissions in the wavelengths from infrared to ultra-violet are collectively known as the terrestrial/thermospheric airglow emissions. Although these emissions are produced by the de-excitation of the excited states of the atoms and molecules of the thermosphere, they carry the information about the ionospheric plasma as the excitation process involves ionospheric plasma. The airglow emissions are generated from different altitudes and carry information on the dynamics and chemistry prevalent at those altitudes. For example, the OI 630.0 nm, 777.4 nm, and 555.7 nm emissions primarily get generated in the F region near 250 km altitude, peak F region altitude, and lower thermosphere regions. All three emissions emanate from the different excited states of atomic oxygen. Thermospheric species can be excited by the chemical, photochemical and dynamical interactions between the neutrals and ions. In the process of de-excitation of a species, either allowed and forbidden transitions occur. The lifetime of forbidden (for electric dipole) transitions is more than the allowed transitions because they violate the selection rules of the electric dipole transition. In this thesis, measurements of the OI 630.0 nm emission during nighttime are used that will be discussed in the next section.

2.2.1 OI 630.0 nm airglow emission

630.0 nm airglow emission is generated by the de-excitation of ^1D state of neutral oxygen to ^3P ground states of the oxygen atom. ^1D state is a metastable state with a lifetime of 110 sec, much higher than the characteristic lifetime of a normal atomic state. During the nighttime, the ^1D state is produced by the dissociative recombination of molecular oxygen ions with the thermal electrons.

$$O_2{}^+ + e^- \longrightarrow O^*(^1D) + O \tag{2.1}$$

$$O^*(^1D) \longrightarrow O(^3P) + h\nu \tag{2.2}$$

The formation of $O_2{}^+$ ions depends upon the O_2 molecules that decrease exponentially with altitude, and 630.0 nm emission relies on the columnar concentration of O_2 and O^+. This columnar concentration decides the peak altitude ($\sim$ 250) of the airglow intensity with a thickness of $\pm$50 km. It can be said that ground-based measurements of airglow are the columnar integrated intensity. The nighttime zenith intensity of 630.0 nm airglow intensity is ∼50 R (1 R = 10^6 photons cm^{-2} s^{-1} str^{-1}) over low latitudes. *Barbier* [1961] established an empirical formula for the instantaneous intensity ($Q_{630.0nm}$) of OI 630.0 nm nightglow intensity. He used ionospheric parameters like the peak height of the F2 layer ($h_P F_2$) and the peak frequency corresponding to the F2 layer ($f_o F_2$) (a proxy for the peak electron density, $N_m F_2$). The empirical formula is as follows,

$$Q_{630.0nm} = A + B(f_o F_2)^2 exp[-\frac{h_p F_2 - 200}{40}] \tag{2.3}$$

In Equation 2.3, A and B are the constants. Equation 2.3 reveals that OI 630.0 nm airglow intensity depends on the peak F layer height and peak F region electron density. Over low latitudes, the peak height and density of the F layer can be changed by wind, electric field, and waves.

2.2.2 Narrow Band and Narrow Field of view airglow Photometer (NBNFAP)

A unique **N**arrow band (0.3 nm), **N**arrow **F**ield-of-view (3°) **A**irglow **P**hotometer (**NBNFAP**) was designed and developed at Physical Research Laboratory to measure thermospheric airglow emission intensity variation. While narrow spectral band photometry enhances the signal-to-noise ratio (SNR), narrow field-of-view (FoV) helps to detect intensity fluctuations with relatively smaller amplitudes. These aspects are discussed in *Chakrabarty et al.* [2008] and *Sekar et al.* [2012]. In the absence of systematic measurements of the ionospheric electric field, the 630.0 nm airglow photometry by this instrument is very effective in capturing the space weather perturbations [e.g., *Chakrabarty et al.*, 2005, 2015; *Kelley*, 2009]. The photometer can measure airglow intensity with 1 sec cadence, and in the present thesis, 10-sec integrated data of airglow intensity is used. The photometer has f/2 optics. This narrow band photometer is divided into three following sections Front-end optics, Filter section, and Detector section. A schematic of the airglow photometer and experimental set-up is shown in Figure 2.1.

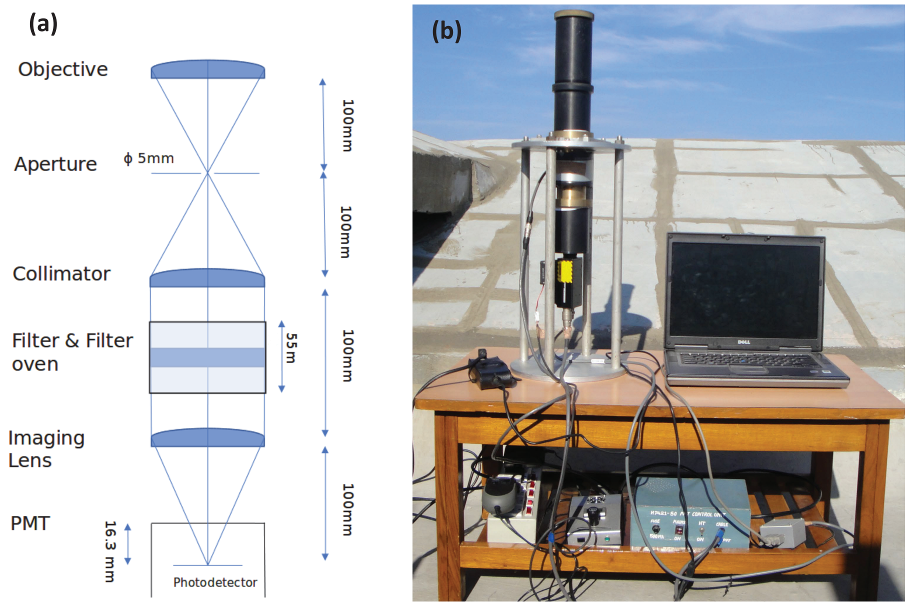

Figure 2.1: (a) A schematic diagram of the airglow photometer, (b) A set-up of narrow band and narrow field of view 630.0 nm airglow photometer at an experiment site, Mt. Abu.

Front-end optics

The front-end optics segment incorporates an objective lens, a collimating lens, and a field stop. The field of view is very narrow(3°) with a small aperture. The objective and the aperture minimize the entry of undesired light into the system from a lower elevation angle. The beam is collimated after passing this section. Front-end optics are kept on top of the filter section.

Filter section

Narrow band (bandwidth 0.3 nm) and temperature-tuned interference filters are used in the filter section. Interference filters are multi-layer thin-film devices. The principle of operation of an interference filter is analogous to a lower-order Fabry-Perot etalon. The filter works on the principle of interference. Destructive interference is used for wavelength rejection, and constructive interference provides the desired wavelength.

The central passband wavelength of an interference filter depends upon the incident angle of light. If the desired wavelength λ is incident normally on the filter, the transmitted wavelength does not change. On the other hand, if it falls on the interference filter with some angle with the normal, ϕ, then the transmitted wavelength(λ') is changed (where $\lambda > \lambda'$). The relation between λ and λ' is given by

$$\lambda' = \lambda\sqrt{1 - \left(\frac{\mu_0}{\mu_{eff}}\right)^2 sin^2\phi} \tag{2.4}$$

Where μ_0 and μ_{eff} are the refractive index of the external medium (in general, air) and the effective refractive index of the filter layers, respectively.

In addition, the transmittance of an interference filter also depends on the temperature of the filter. As the temperature increases, the layer thickness changes, and the filter refractive indices also change. Owing to this, the central wavelength shifts to longer wavelengths. To avoid this, a temperature controller is used that provides temperature stability of the order of $0.2 - 0.5°$ C.

Detector section

PMTs (photomultiplier tubes) are detectors used for the low-light level applications. PMTs consist of a photo-cathode and a series of dynodes in an evacuated glass enclosure. Photons incident over the photocathode generate electrons. These primary electrons are accelerated by the dynodes and secondary electrons are also generated by dynodes. This cascading effect creates $10^5 - 10^7$ electrons for each photon hitting the first cathode, depending on the number of dynodes and the accelerating voltage. This amplified signal is finally collected at the anode, where it can be measured. During the experiments, two PMTs named H7421-40 and H7421-50 are used. Their quantum efficiencies are 40% and 12%, respectively. The PMT is operated as a counting mode by attaching a counting unit because of the low intensity of airglow emission. This counting unit is connected to a PC to record the number of counts per second. In the process of low light detection, the counts obey the Poisson distribution.

2.3 Measurements of total electron content (TEC) by dual-frequency GPS-receiver

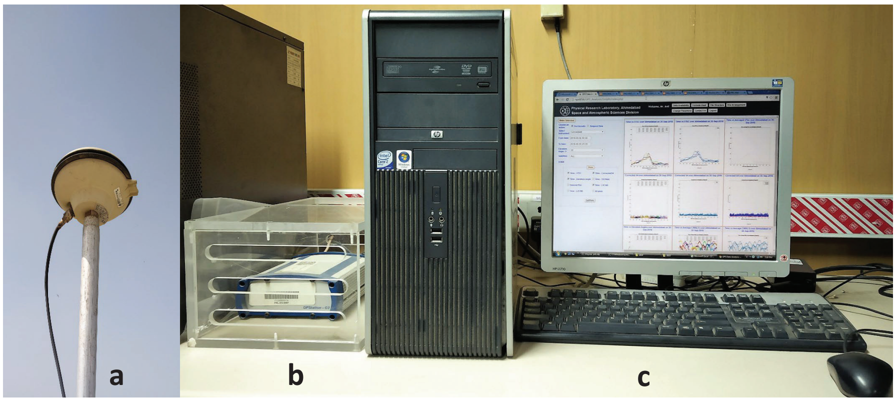

Figure 2.2: (a) Dipole antenna for the GPS receiver at PRL, (b) Dual-frequency GPS-receiver, (c) Display of VETC and Scintillation parameters at the laboratory set-up

GPS satellites were launched by the U.S. Army in 1970. Presently, there are 32+ satellites functional at a height of 20200 km. GPS is the acronym for the Global positioning system. GPS is generally used for location and time information in all weather conditions, anywhere on or near the Earth. Each GPS satellite transmits two frequency signals, L1 (1575.42 MHz) and L2 (1227.60 MHz). Both frequencies are derived from the fundamental frequency of 10.23 MHz that is generated by the precise atomic clock in the satellite. A PRN (pseudo-range number) is assigned to each satellite. This PRN is the identity of the satellite. When a transmitted signal passes through the ionosphere, the signal gets delayed due to the ionospheric plasma and irregularities. This signal is received by the GPS receiver and provides information of plasma content and irregularities of the ionosphere in the form of total electron content (TEC) and scintillation. The antenna, dual-frequency GPS-receiver and lab-view of TEC and scintillation are represented in Figure 2.2. Scintillation can be calculated using a single frequency. However, two frequencies are required to calculate the TEC between the satellite and the receiver. TEC is calculated by the pseudo-range of both the transmitted frequencies. Pseudo-range is the range/distance that is traveled by a signal from a satellite to a receiver.

Calculation of TEC

A GPS receiver receives the signals at two frequencies. As the ionosphere is a dispersive medium, the delays suffered by different frequencies are different. GPS is operated at two L-Band frequencies, namely, f_1 at 1575.42 MHz and f_2 at 1227.60 MHz. The ionosphere allows frequencies more than 50 MHz to pass through easily. These transmitted signals at f_1 and f_2 pass through the ionosphere with minimal reflection. The reflection is so small that it can be ignored. For STEC derivation, we follow the methodology and notations described by *Arikan et al.* [2008]. The Pseudo-ranges for f_1 and f_2 recorded by the receiver are P_1 and P_2, respectively.

$$P^m{}_{1,u} = p^m{}_u + c(\delta t_u - \delta t^m) + d^m{}_{trop,u} + d^m{}_{ion1,u} + c(\epsilon_1{}^m + \epsilon_{1,u}) \tag{2.5}$$

$$P^m{}_{2,u} = p^m{}_u + c(\delta t_u - \delta t^m) + d^m{}_{trop,u} + d^m{}_{ion2,u} + c(\epsilon_2{}^m + \epsilon_{2,u}) \tag{2.6}$$

where the subscript u and superscript m denote the parameters of the receiver station and satellite, respectively. p is the actual range of the satellite between satellite and the receiver. δt_u and δt_m are the clock errors for the receiver and satellite, respectively, which are the same for both signals. d_{trop} and d_{ion} are the tropospheric and ionospheric delays. The tropospheric delay is the same for both frequencies. ϵ^m and ϵ_u are the frequency-dependent satellite and receiver biases. On subtracting Equation 2.5 from equation 2.6, we get differential pseudo-range $P^m{}_{4,u}$ that is defined as follows,

$$P^m{}_{4,u} = P^m{}_{2,u} - P^m{}_{1,u} = d^m{}_{ion2,u} - d^m{}_{ion1,u} + c(\epsilon_2{}^m - \epsilon_1{}^m) + c(\epsilon_{2,u} - \epsilon_{1,u}) \tag{2.7}$$

$$\Rightarrow P^m{}_{4,u} = d^m{}_{ion2,u} - d^m{}_{ion1,u} + c(\epsilon_2{}^m - \epsilon_1{}^m) + c(\epsilon_{2,u} - \epsilon_{1,u}) \tag{2.8}$$

Differential code biases(DCB) defined for the satellite and receiver are given below [e.g., *Themens et al.*, 2013].

$$DCB^m = {\epsilon_1}^m - {\epsilon_2}^m \tag{2.9}$$

$$DCB_u = \epsilon_{1,u} - \epsilon_{2,u} \tag{2.10}$$

An approximation formula for ionospheric groups delay is given by *Liao* [2001], which is given as-

$$d^m{}_{ion,u} = -\phi^m{}_{ion,u}\,\frac{c}{f} \approx A\frac{STEC^m{}_u}{f^2} \tag{2.11}$$

Where $A = 40.3\ m^3/s^2$ and $STEC^m{}_u$ denotes the total electron content on the slant ray path between the receiver and the satellite. Now, from Equations 2.8, 2.9, 2.10 and 2.11, we get

$$P^m{}_{4,u} = A\Big(\frac{1}{{f_2}^2} - \frac{1}{{f_1}^2}\Big)STEC_u{}^m - c(DCB^m + DCB_u) \tag{2.12}$$

$$STEC_u{}^m = \frac{1}{A}\Big(P^m{}_{4,u} + c(DCB^m + DCB_u)\Big)\Big(\frac{1}{{f_2}^2} - \frac{1}{{f_1}^2}\Big)^{-1} \tag{2.13}$$

$$STEC_u{}^m = \frac{P^m{}_{4,u}}{A}\left(\frac{{f_1}^2{f_2}^2}{{f_1}^2 - {f_2}^2}\right) + \frac{c}{A}\left(\frac{{f_1}^2{f_2}^2}{{f_1}^2 - {f_2}^2}\right)DCB^m + \frac{c}{A}\left(\frac{{f_1}^2{f_2}^2}{{f_1}^2 - {f_2}^2}\right)DCB_u \tag{2.14}$$

$\frac{1}{A}\left(\frac{{f_1}^2{f_2}^2}{{f_1}^2-{f_2}^2}\right) = 9.483 \times 10^{16}/m^3$. where $A = 40.3\ m^3/s^2$ and $f_1 = 1575.42$ MHz and $f2 = 1227.60$ MHz.

Equation 2.14 can now be simplified as follows.

$$STEC_u{}^m = [9.483 \times (P^m{}_{4,u} + c\,DCB^m + c\,DCB_u)] \times 10^{16}/m^2 \tag{2.15}$$

1 TECU $= 10^{16}/m^2$

$$STEC_u{}^m = [9.483 \times (P^m{}_{4,u} + c\,DCB^m) + TEC_{RX}] \ \text{ in TECU} \tag{2.16}$$

Where,

$9.483 \times c\,DCB_u = TEC_{RX}$ = STEC contribution due to frequency dependent receiver delay.

$c\,DCB^m$ = frequency dependent differential (for C/A-and P-code here) satellite delay (in meters).

Equation 2.16 does not take into account the offset STEC value (TEC_{off}) of a particular receiver which is calibrated against the SBAS system. This offset value needs to be separately added on the right hand side of Equation 2.16. Therefore, Equation 2.16 takes the following form.

$$STEC_u{}^m = [9.483 \times (P^m{}_{4,u} + c\,DCB^m) + TEC_{RX} + TEC_{off}] \quad \text{in TECU} \tag{2.17}$$

Equation 2.17 provides the slant TEC using the pseudo-range difference ($P^m{}_{4,u}$) at frequencies f_1 and f_2. It is to be noted that TEC_{RX} is the frequency dependent delay of the receiver which is hard-coded as a data base parameter. TEC_{off} is a user-defined input parameter. This value is provided by the GPS manufacturer. The STEC is corrected for satellite inter-frequency biases too. The satellite C/A-to-P code biases are available on the website of the University of Bern (https://www.aiub.unibe.ch/research/code___analysis_center/differential_code_biases_dcb/) which is incorporated in the derivation of the STEC. The derivation of VTEC from STEC is discussed in the next section.

Derivation of VTEC from STEC

To estimate the VTEC from STEC, a single thin layer model is applied. Figure 2.3a shows the pictorial view of this model. This model assumes that all the free electrons are concentrated in a layer of infinitesimal thickness located at the altitude H (Figure 2.3a). The line of sight of the signal makes an angle (z) with the horizon on the Earth. z' is the angle of the line of sight between the ionospheric pierce point (IPP) and satellite to the perpendicular (Figure 2.3a). The VTEC is estimated at each Ionospheric Pierce Point (IPP) from the ionospheric mapping function ($MF_1(z)$), which is given by

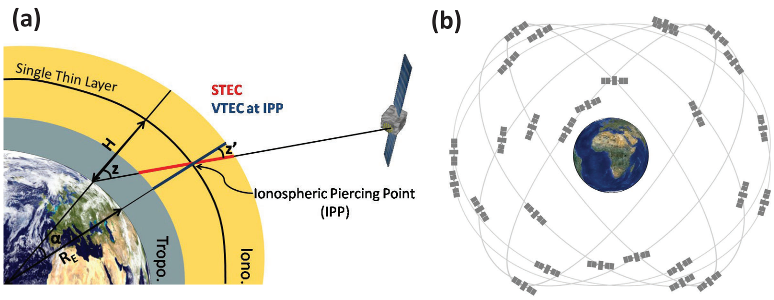

Figure 2.3: (a) Thin shell model (From- http://gnss.be/ionosphere_tutorial.php), (b) A view of the GPS satellites in geosynchronous orbit at altitude 20200 km from the Earth's surface [From- https://www.gps.gov/systems/gps/space/].

$$MF_1(z) = \frac{STEC}{VTEC} = \frac{1}{cosz'} \tag{2.18}$$

From Figure 2.3a,

$$sinz' = \frac{R_E}{R_E + H} sin(z) \tag{2.19}$$

On combining Equations 2.18 and 2.19,

$$VTEC = STEC \times cos\left(sin^{-1}\left(\frac{R_E}{R_E + H} sin(z)\right)\right) \tag{2.20}$$

R_E and H are the radius of the Earth and the height from the Earth's surface. z can be calculated from the elevation angle that is obtained from the GPS-receiver.

2.4 TEC from the Indian Regional Navigation Satellite System (IRNSS)- NaVIC (Navigation with Indian Constellation)

NavIC (Navigation with Indian Constellation) is an Indian Regional Navigation Satellite System (IRNSS). NavIC has seven satellites. Three satellites are situated in the geostationary orbit (GEO), and four satellites are located in the geosynchronous orbit (GSO). The three satellites in GEO are situated at 32.5°E, 83.0°E, and 131.5°E, and four satellites in GSO have inclination angles 29° with respect to the equatorial plane, which covers the longitudes from 55°E to 111.75°E (Figure 2.5). NavIC provides two kinds of services: Standard Positioning Service (SPS) and Restricted Service (RS). Position and time accuracy of the NavIC system are 20 m or better (up to 5 m) and ±25 ns or better. NavIC is operated at two frequencies, 1176.45 MHz and 2492.028 which belong to L-5 and S-band respectively. An IRNSS receiver is provided by the Space Application Centre, ISRO to the Physical Research Laboratory, Ahmedabad, which is operational since July 2017. We used the term NavIC-TEC in the present thesis. NavIC-TEC is derived in the same way as TEC is derived from GPS. More detail of NavIC is available on https://www.isro.gov.in/irnss-programme. An IRNSS antenna, IRNSS-receiver and lab-view of NaVIC-TEC data are shown in Figure 2.4.

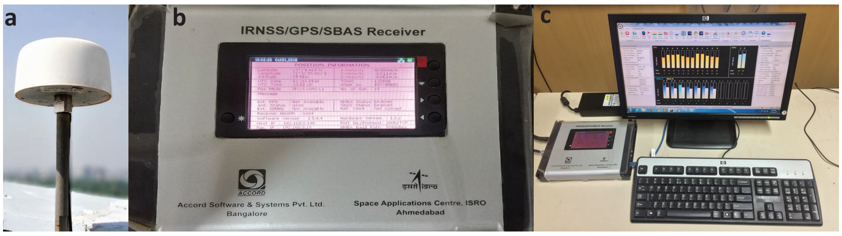

Figure 2.4: (a) Antenna for the IRNSS receiver at PRL, (b) IRNSS-receiver, (c) Laboratory set up of IRNSS receiver

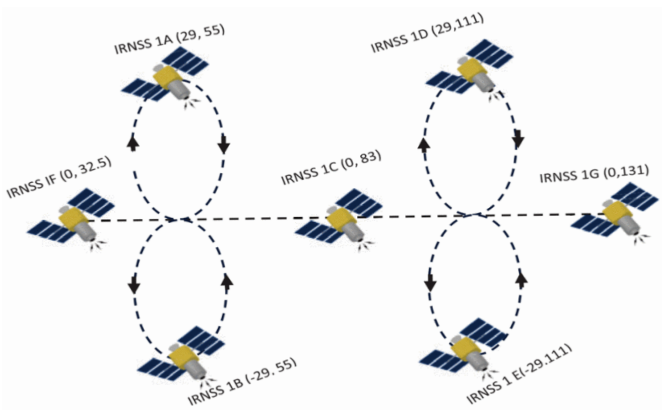

Figure 2.5: Constellations of IRNSS satellites. IRNSS 1A (29, 55), IRNSS 1B (-29, 55), IRNSS 1D (29, 111) and IRNSS 1E (-29, 111) are in GSO. IRNSS 1F (0, 32.5), IRNSS 1C (0, 83) and IRNSS 1G (0, 131) are in GEO.

2.5 GAGAN-SBAS Network

GPS Aided Geo Augmented Navigation (GAGAN) is an Indian satellite-based Augmented System (SBAS) that was commissioned in 2013–2014. This is a joint project of the Indian Space Research Organization (ISRO) and the Airport Authority of India (AAI). This joint venture was planned to provide better navigation services with accuracy, integrity, and continuity for civilian and aviation applications over Indian longitudes. More details of the GAGAN-SBAS network can be obtained from the Interface Control Document (ICD Ver. 1.1) on ISRO's official website (`https://www.isro.gov.in`). The ground segments of SBAS are fifteen Indian Reference Stations (INRES), two Indian Master Control Centers (INMCC), and three Indian Land Uplink Stations (INLUS). Fifteen INRES are located at Ahmedabad, Bengaluru, Jammu, Guwahati, Kolkata, New Delhi, Port Blair, Trivandrum, Jaisalmer, Goa, Porbandar, Gaya, Dibrugarh, Nagpur and Bhubaneshwar. Two INLUS and one INMCC are situated in Bengaluru. On the other hand, one INLUS and one INMCC are in Delhi. The relevant details on GAGAN are available in *Sunda et al.* [2015]. GAGAN satellites in GEO and GPS satellites are part of the space segments. The GPS dual-frequency measurements are recorded by the INRES and the recorded data are transferred from INRES to INMCC via a communication network in real-time. Necessary corrections are incorporated by the INMCC as per data obtained from INRES. The error corrections are generated in specified message-type numbers and transmitted to the GEO satellite through INLUS. The users receive the corrected message from the GAGAN satellite at L1 frequency, and that provides the correct location to the GPS receiver. The ionospheric conditions are broadcast with the interval of $\sim$300 s in the form of vertical delay at the pre-defined 102 ionospheric grid points (IGPs) that are applicable for a signal at L1 frequency. The estimated ionospheric delay at an IGP is known as the Grid Ionospheric Vertical Delay (GIVE). The ionospheric delay of a signal is a frequency dependent term because of the dispersive nature of the ionosphere. One m delay at the L1 frequency is corresponding to ~ 6.25 TECU (1 TECU $= 10^{16}$ electrons/m^2). *Sunda et al.* [2015] have discussed in detail the derivation of TEC from the GAGAN-SBAS network.

2.6 Ionosonde

The ionospheric sounding or Ionosonde technique is one of the oldest and very useful techniques to study the ionosphere. This technique can be used to investigate the E and F regions of the ionosphere. In this technique, radio waves (1 MHz to 30 MHz) are transmitted in the vertical direction. At a particular height of the ionosphere, the probing frequency gets reflected when it matches with the plasma frequency at that ionospheric height. Based on the elapsed time between the transmission and reception of the radio frequency, the virtual height and plasma density at that virtual height is calculated, and a graph of virtual height vs. reflected frequency is called the ionogram. The E and F region's virtual heights are denoted as $h'E$ and $h'F$. The peak height and density of the F2 region are represented by the h_mF_2 and N_mF_2. It is to be noted that the ionosphere is considered birefringent in the presence of the geomagnetic field. This can be understood by the magneto-ionic theory [*Hargreaves*, 1992]. The behavior of the radio wave in the ionosphere can be understood by the *Appleton-Hartree equation*. The refractive index (n) of an ionized medium in which a radio frequency ω propagates is given by the Appleton-Hartree equation as follows

$$n^2 = 1 - \frac{X}{1 - jZ - \left[\frac{{Y_T}^2}{2(1-X-jZ)}\right] \pm \left[\frac{{Y_T}^4}{4(1-X-jZ)^2} + {Y_L}^2\right]^{\frac{1}{2}}} \tag{2.21}$$

In Equation 2.21, X, Y and Z are the dimensionless quantity. Where $X = \frac{{\omega_N}^2}{\omega^2}$, $Y = \frac{\omega_B}{\omega}$, $Y_L = \frac{\omega_L}{\omega}$, $Y_T = \frac{\omega_T}{\omega}$ and $Z = \frac{\nu}{\omega}$. And

$\omega_N = (\frac{Ne^2}{\epsilon_0 m})^{\frac{1}{2}}$ = angular plasma frequency, N is the electron density of the medium;
$\omega_B = \frac{eB}{m}$= angular gyro frequency of electron;
ω_L = longitudinal component of ω_B with respect to the direction of propagation;
ω_T = transverse component of ω_B with respect to the direction of propagation;
ν= electron collision frequency; ω= angular frequency of the radio signal. If θ is the angle between the propagation direction and magnetic field direction, then $\omega_L = \omega_B cos\theta$ and $\omega_T = \omega_B cos\theta$.

If the collision and magnetic field are neglected, the following terms will be equal to zero.

$Z = Y_T = Y_L = 0$, Therefore, Equation 2.21 gets simplified as follows,

$$n^2 = 1 - X = 1 - \frac{{\omega_N}^2}{\omega^2} \tag{2.22}$$

Where ω_N and ω are the angular frequency of plasma and radio wave.

$$\omega_N = \left(\frac{Ne^2}{\epsilon_0 m}\right)^{\frac{1}{2}} \tag{2.23}$$

Putting the values of ϵ_0 (permittivity of free space, 8.85×10^{-12} m^{-3}kg^{-1}S^{4}A^2), e (electronic charge, 1.6×10^{-19} C) and m (mass of electron, 9.1×10^{-31} kg) $\omega_N = 2\pi f_n$, Equation 2.23 changes into the following expression

$$f_N = \sqrt{80.5N} \tag{2.24}$$

Plasma frequency (f_N in Hz) in the ionosphere can be calculated by the electron density (N in m^{-3}). Equation 2.19 tells whether the wave propagates in the medium or not. If $\omega_N > \omega$, the wave does not propagate in the medium as the refractive index becomes imaginary. The wave gets reflected back when $\omega_N = \omega$. In the case of $\omega_N < \omega$, the wave passes through the medium and does not reflect.

In the absence of incoherent scatter radar and systematic measurements of the electric field over Indian longitude, the apparent vertical drift over the dip equator based on ionospheric height variations can be used during the nighttime as a proxy for the zonal electric field. The drift measurements are relatively more accurate in the nighttime than in the daytime because of the absence of the photoionization that affects the lower part of the F layer significantly. However, vertical drift during nighttime must be corrected for chemical recombination effect (particularly below 300 km) which requires accurate information on thermospheric and ionospheric parameters (e.g., altitude profiles of O_2, N_2, temperature dependent rate constant and scale height etc.). This is one of the limitations of derivation of vertical drift based on ionosonde measurements. One more important limitation at nighttime is the uncertainty in the drift measurement introduced by plasma bubbles and irregularities. In this work, the vertical drift is calculated from the time derivative of the h'F. Further, when h'F is lower than 300 km, the recombination effect (chemical loss) contributes significantly to the upward vertical drift [*Bittencourt and Abdu*, 1981]. Therefore, true vertical drift is derived after correcting for the upward drift brought in by the chemical loss. Following the methodology of *Subbarao and Krishna Murthy* [1994], the upward drift due to chemical recombination can be calculated. After subtracting this drift from the apparent drift, the vertical plasma drift that is electrodynamic in nature can be obtained. In the present thesis work, these measurements are obtained from the Advanced Digital Ionosonde (CADI) over Tirunelveli (8.7°, 77.7°, dip angle 1.7°). The details of this CADI system can be obtained from *Sripathi et al.* [2016]. It is to be mentioned here that CADI is a digital ionosonde that is developed by the Scientific Instrumentation Lab, Canada [e.g., *MacDougall et al.*, 1995]. The operating frequency range of CADI is 1-20 MHz. In general, CADI takes an ionogram every 10 minutes, and this interval can be configured as per user requirements. The CADI system can probe altitudes ranging from 90 to 512 km (or 1020 km) with either 3 or 6 km altitude resolution.

2.7 Incoherent and coherent Scatter Radars

Ionosonde technique has limitations as it cannot measure electron density beyond the peak F region altitude, and plasma drifts are more reliable during the night. On the other hand, the Incoherent Scatter Radar (ISR) can measure electron density, ion velocity, ion and electron temperatures, ion composition etc., from $\sim$100 to $\sim$1000 km altitude. In the previous chapter, it is discussed that vertical plasma drifts are caused by the ionospheric electric field that gets generated by the E- and F- region dynamos. The ISR provides very accurate plasma drift (both zonal and vertical), and the electric field can be estimated from the plasma drifts over the dip equator. The ISR works on the principle of Thomson Scattering. The available incoherent scatter radars worldwide are being operated from 46.5 MHz to 1290 MHz. Each ISR is operated using a specific frequency. Thermal electrons in the ionosphere oscillate with the electric field component of a transmitted electromagnetic signal. These oscillating electrons re-radiate a very weak signal of nearly the same frequency as the transmitted frequency (but much narrower bandwidth than the transmitted signal) from the ground. In order to capture this weak signal, a large antenna and a sensitive receiver are used. Received spectra from the scattered signal provide the densities, temperatures, and vertical and zonal drifts of plasma. For example, the electron density is calculated from the total received power, and the doppler shifts of the spectrum in all three directions provide the plasma drifts. In the present thesis, the vertical drifts measurements are used over Jicamarca (JIC, 12°S, 75°W, dip angle 0.8°). The JIC-ISR is operated at 50 MHz that can transmit 5 MW peak power. To capture the incoherent backscatter echo, the JIC-ISR has 18,342 half-wave dipoles that cover around 85000 m^2 of area. Only a tiny fraction of the transmitted power is captured with this giant array. The description of Jicamarca Incoherent Scatter Radar is available in *Woodman et al.* [2019].

In addition to JIC-ISR measurements, the F-region plasma convection maps over the northern hemisphere are used. These convection maps are developed by the Super Dual Auroral Radar Network (SuperDARN). Currently, the SuperDARN network has 23 and 12 radars in the northern and southern hemispheres, respectively [e.g., *Gjerloev et al.*, 2018]. All SuperDARN radars are operated in the frequency range from 8 to 20 MHz. These radar work on the principle of Bragg scattering. The signal is scattered back from the irregularities with scale sizes half of the signal wavelength. Irregularities drifts can be calculated from the doppler shift. *Cahill Jr. et al.* [1978] have shown that the irregularities drift could be related to ionospheric drift. *Greenwald et al.* [1978] shows that using a dual radar network, the convection maps are constructed. The convection velocity (V) and convection potential (ϕ) are related to each other by the following formula.

$$E = -\bigtriangledown \phi_{conv} \quad \text{and} \quad V = \frac{E \times B}{B^2} \tag{2.25}$$

The convection patterns are constructed from the measurements of the plasma drifts. Since the radars do not cover the full range of the high latitudes, spherical harmonic functions are fitted for an electrostatic potential to construct the convection map [e.g., *Ruohoniemi and Greenwald*, 1996; *Ruohoniemi and Baker*, 1998].

2.8 Particle flux measurements by LANL and GOES satellites

It is believed that the most confirmative signatures of magnetospheric substorms are dispersion-less particle injection at the geosynchronous orbit [e.g., *Reeves et al.*, 1990]. During a substorm, the fluxes at all energy channels increase simultaneously, it is referred to as dispersionless particle injection [e.g., *Reeves et al.*, 1991]. A satellite can observe the dispersion-less particle injection only if it is situated within the injection front region. In the present work, the energetic particle flux data is obtained from the Los Alamos National Laboratory (LANL) satellites and Geostationary Operational Environmental Satellites (GOES). All energy channels of electron and proton flux data of LANL-01A, 02A, 04A, 97A, 080, and 084 are used, whereas four energy channels of electron fluxes of GOES-13 satellite are used in the present thesis work. LANL satellites are situated at 6.6 R_E (R_E, Earth's radius). The electron and proton fluxes are measured by the Synchronous Orbit Particle Analyzer (SOPA) on board LANL satellites. On the other hand, electron fluxes at four energy channels are obtained from the Energetic Particle Sensor (EPS) on-board geostationary GOES-13.

2.9 Ground-based magnetometer measurements

In the present thesis work, the ground-based magnetometer measurements are used. Equatorial electrojet (EEJ) strength can be derived from the ground-based magnetometer data. In addition, various geomagnetic indices like Kp, Ap, AE, AL, AU, Sym-H, Asym-H, Sym-D, Asym-D, and PC indices are derived based on the ground-based magnetometer data. The data corresponding to these indices with 1 min cadence are provided by the World Data Center (WDC) for Geomagnetism Kyoto (`https://wdc.kugi.kyoto-u.ac.jp/`) as well as Coordinated

Data Analysis Web (CDAWeb, https://cdaweb.gsfc.nasa.gov/) of Goddard Space Flight Center- Space Physics Data Facility (GSFC-SPDF). The ground-based magnetometer data from different sectors of the Globe can be obtained from the SuperMAG (https://supermag.jhuapl.edu/) as well as INTERMAGNET (https://www.intermagnet.org/). In a worldwide collaboration, magnetometer measurements over more than 300 observatories are available on SupeMAG. 1 min and 1 sec cadence data are available in the SuperMAG. These magnetometer data are recorded by the fluxgate magnetometers [e.g. *Miles*, 2017].

Derivation of Equatorial Electro-Jet (EEJ) strength

A large number of magnetometer observatories provides an opportunity to study the Sq- current system and EEJ strength over different longitudes on a day-to-day basis. The EEJ strength is used over the Indian and Jicamarca longitudes in the present thesis work. The magnetic flux density induced due to the EEJ current is derived by the magnetometer measurements over an equatorial and off-equatorial stations along the longitudes that are not very different [e.g., *Rastogi and Patel*, 1975; *Rastogi and Klobuchar*, 1990]. The EEJ-induced magnetic field can be derived using the horizontal magnetic field (H) variations over the equator (eq) and off-equator (off-eq) stations. Over the dip-equator, magnetospheric currents like the ring current, tail current, Chapmann-Ferraro current (H_{ring}), the earth's crustal magnetic field (H_{cru}), and EEJ current (H_{EEJ}) contribute to the ground-based magnetic field measurements. Over an off-equatorial station that is outside the influence of EEJ current, all currents except the EEJ current are measured by the magnetometer. The horizontal component of the magnetic field over the dip equator during day (${H^{day}}_{eq}$) and night (${H_{eq}}^{night}$) can be written as follows.

$$ {H_{eq}}^{day} = H_{EEJ} + {H_{ring}}^{day} + {H_{cru}}^{day} \tag{2.26} $$

$$ {H_{eq}}^{night} = 0 + {H_{ring}}^{night} + {H_{cru}}^{night} \tag{2.27} $$

On subtracting Equation 2.27 from Equation 2.26, we get

$$ (\Delta H)_{eq} = H_{EEJ} + (H^{day} - H^{night})_{ring} + (H^{day} - H^{night})_{cru} \tag{2.28} $$

For the off-equatorial (offeq) station, the variation of H during day and night is given as-

$$H_{off-eq}{}^{day} = H_{ring}{}^{day} + H_{cru}{}^{day} \tag{2.29}$$

$$H_{off-eq}{}^{night} = H_{ring}{}^{night} + H_{cru}{}^{night} \tag{2.30}$$

On subtracting the Equation 2.30 from 2.29, we get-

$$(\Delta H)_{off-eq} = (H^{day} - H^{night})_{ring} + (H^{day} - H^{night})_{cru} \tag{2.31}$$

It is to be noted here that $(H^{day} - H^{night})_{ring}$ and $(H^{day} - H^{night})_{cru}$ are nearly the same for equatorial and off-equatorial stations.

Therefore horizontal magnetic field due to EEJ can be obtained by subtracting Equation 2.31 from 2.28.

$$H_{EEJ} = (\Delta H)_{eq} - (\Delta H)_{off-eq} \tag{2.32}$$

Geomagnetic indices

K, Kp and Ap indices

Bartels et al. [1939] introduced the K index for the first time. In recent times, *Matzka et al.* [2021] reviewed the derivation methodologies of the K, Kp, and Ap indices. There are 13 observatories between $\sim$ 45° and 60° latitudes around the world in the northern and southern hemispheres that routinely measure the K index at quasi-logarithmic scale over three-hour intervals by measuring the Eastward and Northward magnetic field components [e.g., *Matzka et al.*, 2021]. The K index of a particular day and observatory is derived from the tables provided by the *Bartels et al.* [1939] and *Bartels* [1949]. Further, Kp is derived from the K index that is measured from 13 geomagnetic observatories (10 in the northern and 2 in the southern hemisphere) situated $\sim$ 44°-60°. The Ap index is the linear version of the Kp index and derived from the Kp index [*Bartels*, 1957]. The K, Kp, and Ap indices are the three hourly indices. The Kp and Ap indices provide information about the geomagnetic activity of a day.

Dst and Sym-H indices

The Dst (Disturbed storm time index) and Sym-H are the indices to measure the strength of ring current based on the ground-based magnetometer measurements. The different phases of the geomagnetic storm are identified based on the variations in the Dst or Sym-H indices. While Dst is an hourly index, Sym-H is essentially a high-resolution version of Dst and provides data with 1 min cadence. The Dst index is measured from the five observatories situated at the low to mid-latitudes (18° -36° GeoLat). However, the Sym-H index is estimated based on measurements at any six observatories out of 10 magnetometer observatories situated near ∼ 30°-50° magnetic latitudes. The derivation techniques of Dst and Sym-H are reviewed by *Wanliss and Showalter* [2006].

The AE, AO, AL, and AU indices

These indices were first introduced by *Davis and Sugiura* [1966] to measure global auroral activity quantitatively. There are 13 observatories spread from ∼ 60° to ∼ 70° magnetic latitude at different longitudes over the northern hemisphere. After subtracting the base value from each observatory, AU and AL indices are derived from the upper and lower envelopes of all the observatories at each UT. It means AU and AL values are the maximum and minimum values of the envelope. The AU and AL values represent the eastward and westward auroral electrojet strengths. The AE index is derived by subtracting AL from AU (AU-AL) index and the mean value of the AU and AL indices, i.e., (AU+AL)/2 represents the AO index. The AE index is used to understand the overall activity of the electrojets, and the AO index represents the measurements of the equivalent zonal current.

PC index

Troshichev et al. [1988] introduced the polar cap (PC) index to monitor the geomagnetic activity over the Northern and Southern hemispheres. PC index Over the Northern and Southern hemispheres is derived from the magnetic observatories at Thule and Vostok stations. *Troshichev et al.* [2000] showed that PC-index could be used as an ionospheric electric field proxy in the near pole region. This proxy can be used for high latitude to low latitude coupling studies.

2.10 F10.7 cm Solar radio flux

The F10.7 cm (2800 MHz) solar radio flux data is one of the most useful data for ionospheric studies. The F10.7 cm emission gets originated in the chromosphere and lower corona of the Sun's atmosphere. The measurements at 10.7 cm are carried out in a 100 MHz wide band centered at 2800 MHz and are averaged on an hourly basis. This F10.7 cm solar flux is measured in the unit of sfu (1 sfu = 10^{-22} W m^{-2} Hz^{-1}) and it can vary from ∼50 sfu to 300 sfu over a solar cycle. The F10.7 cm solar radio flux data show good correlations with sunspots, EUV, and visible radiations. This flux is used widely to see the solar cycle variations as this data is available for the largest period. In many ionospheric models, it is used as an input parameter.

In the present thesis, the TIE-GCM and *Fejer et al.* [2008a] quiet time vertical drift model have been used. The F10.7 cm solar radio flux data is provided as one of the inputs in both models.

2.11 Solar wind data

In the present thesis work, the solar wind parameters are obtained from the CDAWeb (`https://cdaweb.gsfc.nasa.gov/`) of NASA's GSFC-SPDF. The solar wind parameters are time-shifted until the nose of the terrestrial bow shock. This data is obtained from the measurements of different payloads on board satellites ACE, WIND, IMP 8, and Geotail. These satellites measure the magnetic field, plasma density, velocity, and temperature of the solar wind with one minute cadence. The parameters like solar wind electric field, dynamic pressure, plasma beta, and Alfven Mach number are derived from these measurements.

2.12 Model used

A few model outputs have been used in the present thesis work. A brief description of these models is provided below.

2.12.1 Thermosphere Ionosphere Electrodynamics- General Circulation Model (TIE-GCM)

Thermosphere-Ionosphere-Electrodynamics General Circulation Model (TIE-GCM) is a self-consistent, first principles (linear momentum and continuity equations applied for each species), three-dimensional and physics-based model that is developed at the High Altitude Observatory, National Center for Atmospheric Research. The earlier version of TIE-GCM was the Thermospheric General Circulation Model (TGCM) [*Dickinson et al.*, 1984] that calculated upper atmospheric parameters like temperature, neutral density, etc. *Roble et al.* [1988] and *Richmond et al.* [1992] included the self-consistent ionosphere and the electrodynamics part, respectively, in the TGCM to make it TIE-GCM. In order to generate the outputs, this model solves the momentum, energy, and continuity equation in three dimensions for each neutral and ion species at each altitude (pressure surface) and time step. TIE-GCM is capable of simulating the thermospheric neutral wind and ionospheric electric field, conductivity, and current self-consistently. TIE-GCM generates the outputs along the globe with $2.5° \times 2.5°$ in latitudes and longitude bins from 100km to 500-700 km altitudes (according to solar flux). The required input parameters to run this model are the magnetic field, velocity, and plasma density of the solar wind, year and day of the year. This model can be run on request to the Community Coordinated Modelling Center (CCMC).

2.12.2 Climatological global vertical drift Model

In the absence of any incoherent scatter radar, accurate and systematic measurements of vertical drift/electric field are not available from the Indian dip equatorial sector. In this scenario, the quiet time vertical drift outputs are generated using the quiet time global climatological model of *Fejer et al.* [2008a].

Fejer et al. [2008a] developed a global empirical model for equatorial F region vertical plasma drifts for quiet time (Kp$\leq$3) using 5 years of measurements of drifts from Ionospheric Plasma and Electrodynamics Probe Instrument (IPEI) on board Republic of China Satellite-1 (ROCSAT-1) during 1999-2004. In order to develop this global model, the measurements of drifts are averaged over the $\pm$7.5° dip latitude and $\pm$15° longitude bin. This model provides vertical drifts at different local times and solar flux values at different seasons. It has been shown earlier [e.g., *Pandey et al.*, 2017] that the vertical drifts from this model show a better correlation with the measurements over the Indian sector. In the present thesis, the vertical drifts are generated along 75° E longitude.

2.12.3 Horizontal Wind Model (HWM)-14

The direct or Indirect measurements of thermospheric neutral wind over the Indian longitudes are not available during the solar cycle 24. To understand the variations in the meridional wind over low latitudes, the Horizontal wind model (HWM-2014) [*Drob et al.*, 2015] is used. This empirical wind model provides the vector wind fields from the surface of the Earth to exobase ($\sim$ 450 km) as a function of latitude, longitude, altitude, day of the year, time of the day, and Ap values (average geomagnetic condition of the day). The HWM-14 includes $\sim 73 \times 10^6$ measurements from 44 different instruments (ground-based measurements from Incoherent Scatter Radar and Fabry-Perot Interferometers and satellite-based measurements) spanning over 60 years around the globe. This model produces better outputs for the post-sunset hours than the previous versions of the model. This is an improved version of HWM-07 [*Drob et al.*, 2015] for the quiet time thermospheric wind measurements. For disturbed periods, DWM-07 [*Drob et al.*, 2015] is used, which was previously used in HWM-07 [*Drob et al.*, 2008].

Chapter 3

Post-sunset plasma density enhancements near the EIA crest region

Excerpts

This chapter is focused on F region plasma distribution over low latitudes and the response time of the EIA crest region during post-sunset hours. A large dataset of vertical total electron content (VTEC) over Ahmedabad (23.0° N, 72.6° E, dip angle: 35.2°), spanning around 10 years and campaign-based OI 630.0 nm airglow intensity measurements from Mt. Abu (24.6° N, 72.7° E, dip angle: 38.0°) are analysed and it is found that post-sunset plasma density enhancements near the EIA crest region vary with season and solar flux level during magnetically quiet periods. Morphologically, these enhancements start anytime after 1900 LT and peak around 2000 LT. These post-sunset enhancements are more conspicuous during the December solstice and Equinox at higher solar flux levels. Based on these datasets, it is noticed that the post-sunset peak, in general, is observed first in VTEC over Ahmedabad and later in airglow intensity over Mt. Abu. Comparison of the post-sunset enhancement in VTEC with the vertical drifts measurements over Tirunelveli (8.7° N, 77.7° E, dip angle: 1.7°) reveals that the pre-reversal enhancement of the zonal electric field is primarily responsible for these enhancements over the crest region. By comparing the average VTEC values with the global empirical vertical drifts value, it is found that the post-sunset enhancements in VTEC occurs $\sim$ 1.7 hrs after the occurrence of the peak value of PRE during the December solstice and Equinox in high solar flux conditions. This time delay is half the response time (~3-4 hrs) associated with the daytime plasma fountain. This shorter response time during post-sunset hours is explained by SBAS-TEC data. Based on the latitudinal plasma density gradient obtained from the SABS-TEC data, it is suggested that the PRE drives plasma from $5°-10°$ magnetic latitudes to the EIA crest region leading to a shorter response time.

3.1 Introduction

The Equatorial F region plasma fountain process controls the low latitudes plasma distribution. Under a geomagnetically quiet condition, the equatorial zonal electric field is eastward during daytime and westward during nighttime [e.g., *Fejer et al.*, 2008a]. Equatorial plasma fountain (EPF) process is initiated over the dip equatorial F region due to the eastward electric field and horizontal geomagnetic field configuration. This process generates the equatorial ionization anomaly (EIA) crest over low latitudes and trough over the equator (see Figure 1.9). This process is discussed in detail in section 1.7.2. Meridional winds generate interhemispheric-asymmetry in the intensity and location of the EIA crest regions [e.g., *Anderson*, 1973a]. The plasma distribution over the EIA crest regions shows day to day variability [e.g., *Huang et al.*, 1989] as well as seasonal and solar flux varaiability [e.g., *Chakrabarty et al.*, 2012; *Huang and Cheng*, 1995; *Mo et al.*, 2018]. Investigation of the EIA crest region is important as it is one of the most L-band scintillation regions in the globe [e.g., *Basu et al.*, 1988]. This radio band scintillations are sometimes so severe that it can affect the positional, navigational and communication applications significantly.

During geomagnetically quiet periods, the EIA crest region gets formed in the afternoon hours [e.g., *Balan et al.*, 2018; *Chen et al.*, 2016; *Mo et al.*, 2018; *Sastri*, 1990]. The occurrence time of a well-developed EIA crest region during quiet period can, in general, be explained by adding a typical diffusion time of 3-4 hours with the occurrence time of peak eastward electric field over the dip equator around noon. There are a number of ways to decide the response time of the EIA crest region. In the present study, the response time of the EIA crest regions is determined based on the time of occurrence of peak VTEC over the EIA crest region and the time of occurrence of peak vertical drift value. Previously, this response time is calculated based on the time difference in the occurrence of the peak VTEC over the EIA crest and the occurrence of peak EEJ strength [derived from Figure 4 of *Rama Rao et al.*, 2006] or hmF2 [e.g., *Aswathy et al.*, 2018]. During the local evening hours, the equatorial F-region zonal electric field is greatly enhanced that is known as the pre-reversal enhancement (PRE) of the zonal electric field [e.g., *Eccles et al.*, 2015; *Fejer*, 2011]. On those occasions, when the amplitudes of the PRE [e.g., *Fejer et al.*, 2008a] are comparable to the daytime maximum, one can expect that the PRE should affect the EIA crest region by re-invigorating the plasma fountain process during evening hours [e.g., *Abdu et al.*, 2008]. However, the equatorial zonal electric field changes to the westward direction after PRE and eventually, reverse plasma fountain [e.g., *Balan et al.*, 1995, 1997; *Chen et al.*, 2017; *Sridharan et al.*, 1993; *Yadav et al.*, 2020] sets in. This stops further supply of plasma to the poleward direction. Therefore, it is important to understand how much time EIA crest region takes to respond to PRE and how does it compare to the response time during day. In addition, the role of the meriodional wind in the plasma distribution over low latitudes is also an important factor that may affect the response time. Although several studies in the past reported [e.g., *Bittencourt et al.*, 2007; *Farelo et al.*, 2002; *Rao and Kulkarni*, 1973; *Su et al.*, 1994; *Xiong et al.*, 2016] conspicuous variations in the plasma density over the EIA crest region during post-sunset hours, the exact role of the PRE remains unclear. This important and unresolved scientific issue is addressed in the present chapter.

3.2 Details of the dataset/Models

The scientific problem mentioned in the previous section is addressed with a few relevant datasets and global empirical model outputs that are discussed in the following sections. The datasets belong to ground stations shown in Figure 3.1. The GAGAN stations are detailed in section 2.5. It must be noted here that Ahmedabad and Mt. Abu are not exactly below the EIA crest region all the time, but these stations may be near the EIA crest region on a statistically significant number of occasions if the equatorial electric field is eastward. It is also to be mentioned that EIA crest location can vary during disturbed space weather conditions.

3.2.1 Datasets

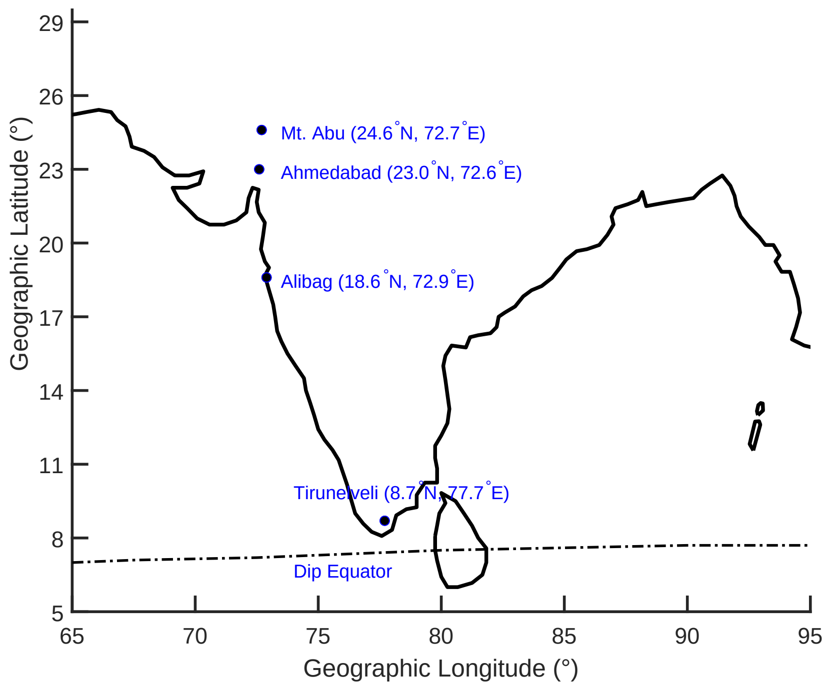

Figure 3.1: Location of ground stations over the Indian sector, the data from which are used in the present thesis work. The stations are Tirunelvelui (8.7°N, 77.7°E), Alibag (18.6°N, 72.9°E), Ahmedabad (23.0°N, 72.6°E) and Mt. Abu (24.6°N, 72.7°E). The dip equator is shown with a dotted-dashed line. Note that the dip equator is plotted in geographic coordinates.

In the present investigations, OI 630.0 nm airglow intensity data over Mt.

Abu (24.6° N, 72.7° E, dip angle 38.0°) is captured by a narrow band and narrow field-of-view (bandwidth: 0.3 nm and field of view: 3°) airglow photometer in campaign mode during moonless and cloudless nights in the winter months. This airglow photometer is discussed in detail in Chapter-2. In the present work, airglow intensity data with 10 s cadence are used.

10 years' vertical total electron content (VTEC) data during 2010-2019 is taken from the GPS receiver GISTM GSV4004B) at Physical Research Laboratory (PRL), Ahmedabad (23.0° N, 72.6° E, dip angle 35.2°). The details of the receiver and the VTEC technique are discussed in Chapter-2. Raypath elevation angles less than 30° are masked in this work to minimize the multipath error and tropospheric scattering effects. The VTEC is calculated by averaging VTEC from all the visible satellites. Five minutes' average VTEC data are used for this study. Based on variations in F10.7 solar radio flux, the VTEC data is classified into two categories. The VTEC data from 2011–2015 is categorized as belonging to high solar activity years, and the rest of the data are categorized as falling under low solar activity years. Average F10.7 flux levels for high and low solar activity periods during 2010–2019 are ∼130 sfu and ∼80 sfu (sfu = solar flux unit, 1 sfu = 10^{-22} $\mathrm{Wm^{-2}Hz^{-1}}$) respectively. The VTEC data in both the solar epochs are further categorized into three seasons, namely December solstice (November, December, January, and February), Equinox (March and April, September and October), and June solstice (May, June, July, and August). It is important to mention here that this work pertains to geomagnetically quiet periods, and these quiet periods are picked up based on the Ap index (Ap $\leq$15 on the chosen day and the previous day).

The TEC maps over the Indian region are constructed by the GAGAN SBAS-TEC network. GPS Aided Geo Augmented Navigation (GAGAN) is an Indian Satellite-based Augmentation System (SBAS). A brief description of the GAGAN-SBAS network is provided in Chapter-2. GAGAN-SBAS provides 5 minute cadence of TEC data over 102 grid points which are separated by 5° × 5° over Indian sectors. GAGAN TEC maps are used to examine the latitudinal variation of F region plasma over the Indian sector.

Equatorial electrojet (EEJ) over the Indian sector [*Rastogi and Patel*, 1975] is calculated using the horizontal component of the magnetic field from a dip equatorial station Tirunelveli (TIR, 8.7° N, 77.7° E, dip angle 1.7°) and the off-equatorial station Alibag (ABG, 18.6° N, 72.9° E, dip angle 26.4°). EEJ can be calculated by the following formula. $H_{EEJ} = \Delta H_{TIR} - \Delta H_{ABG}$. Here, ΔH represents the daytime instantaneous H value corrected for the nighttime base value of H. In the present work, 1 minute cadence data of EEJ is used. The integrated EEJ strength (in nT-h) is calculated by calculating the area under the curve of the variation in the EEJ strength between 0700 and 1700 LT. This is used as a proxy of the daytime equatorial electric field.

The vertical drift over the Indian dip equator is derived from the measurements of the bottomside F layer height ($h'F$, in km) of the Canadian Advanced Digital Ionosonde (CADI). The details of the CADI system are available in the work of *MacDougall et al.* [1995] and *Sripathi et al.* [2016]. The temporal derivative of the $h'F$, ($dh'F/dt$, in ms^{-1}) is used as a vertical drift during post-sunset hours. In the present work, the chemical recombination corrections in the vertical drifts are not required as the values of $h'F$ are mostly above 300 km [e.g., *Bittencourt and Abdu*, 1981]. Before calculating the $dh'F/dt$, $h'F$ is first subjected to Savitzky-Golay (SG) algorithm [e.g., *Savitzky and Golay*, 1964] with 15% smoothing window as the data are slightly noisy. The smoothing through SG algorithm removes the fast fluctuation from the time series data without introducing distortion in data. It is verified that after smoothing of $h'F$, derived vertical drift doesn't loose its' variations.

3.2.2 Global climatological model of equatorial F-region vertical drift

The model outputs are generated for 75° E longitude corresponding to 130 and 80 sfus for December solstice, Equinox and June solstice. It is also to be noted that the local time for all the datasets with respect to 75° E longitude (LT = UT + 5 h)is used in this work.

3.2.3 Horizontal wind model (HWM)-14

Horizontal Wind Model (HWM-14) is run for the three seasons (December solstice, Equinox and June solstice) at altitudes of 250, 300 and 350 km for the year 2014 over Mt. Abu for quiet condition (Ap=5).

3.2.4 Movement of plasma along the field line: the parallel velocity $V_{\|}$

The meridional component (parallel to the geomagnetic field) of thermospheric wind plays an important role in transporting plasma [e.g., *Rishbeth*, 1977] to and from the EIA crest region and can modulate the vertical drifts in varying degrees. Zonal winds, on the other hand, are important drivers for the E- and F-region dynamo (Discussed in detail in Chapter-1). *Anderson* [1971] derived an expression for plasma velocity along the magnetic field (henceforth, parallel velocity) over low latitude ionosphere. The basic principle of the Anderson formalism is that while F region plasma is pushed vertically upward through zonal electric field over the dip equatorial region, the plasma simultaneously diffuses along the magnetic field lines due to non-electromagnetic forces. Therefore, at this juncture, it is important to discuss the non-electromagnetic forces and derive an expression for the parallel velocity. *Sivaraman et al.* [1976] studied this model to understand the development of the ionization anomaly during solar maxima and minimum conditions. For present investigations, this model is used to calculate the plasma velocity along the magnetic field lines during December solstice and Equinox in year 2014.

It is well known that the rate of change of ionospheric plasma density at a given place depends upon production (P), loss (L), and transport of ionization. All three are important for F region plasma distribution, whereas the E region is mainly controlled by photochemical processes wherein production and loss are the primary factors that determine plasma density at a given place. In the F-region, the rate of change in ionization density at a given place is governed by the continuity equation as follows.

$$\frac{\partial N}{\partial t} = P - L + \vec{\boldsymbol{\nabla}} \cdot (N\vec{V}) \tag{3.1}$$

Where N and $\vec{V}$ are the plasma density and transport velocity. $\vec{V}$ comprises of two components $\vec{V_\parallel}$ and $\vec{V_\perp}$. $\vec{V_\parallel}$ and $\vec{V_\perp}$ are the components of V parallel and perpendicular to the magnetic field. Equation 3.1 can then be rewritten as

$$\frac{\partial N}{\partial t} = P - L + \vec{\boldsymbol{\nabla}} \cdot (N\vec{V_\parallel} + N\vec{V_\perp}) \tag{3.2}$$

In the ionosphere, charge species mainly experiences the forces due to the gravity, electric field, magnetic field and collisions. The equations of forces for electrons and ions are as follows-

$$m_e \frac{d\vec{V_e}}{dt} = m_e \vec{g} - \frac{1}{N_e}\vec{\boldsymbol{\nabla}}(N_e k T_e) - e(\vec{E} + \vec{V_e} \times \vec{B}) - m_e \nu_{en}(\vec{V_e} - \vec{U}) - m_e \nu_{ei}(\vec{V_e} - \vec{V_i}) \tag{3.3}$$

$$m_i \frac{d\vec{V_i}}{dt} = m_i \vec{g} - \frac{1}{N_i}\vec{\boldsymbol{\nabla}}(N_i k T_i) + e(\vec{E} + \vec{V_i} \times \vec{B}) - m_i \nu_{in}(\vec{V_i} - \vec{U}) - m_e \nu_{ei}(\vec{V_i} - \vec{V_e}) \tag{3.4}$$

Where m, $\vec{V}$, N and T represent mass, velocity, density and temperature respectively. Subscripts i and e are used for ions and electrons. $\vec{U}$, $\vec{g}$, $\vec{E}$, and e are the neutral wind velocity, acceleration due to gravity, ionospheric electric field, and electronic charge respectively. $\vec{B}$, ν_{en}, ν_{in} and ν_{ei} are the magnetic field vector (magnetic flux density), electron-neutral, ion-neutral and electron-ion collisional frequencies.

In both equations 3.3 and 3.4, the force terms on the left side are small compared to the collisional terms on the right. In both equations 3.3 and 3.4, the variations in $\vec{V_i}$ and $\vec{V_e}$ occur in the time scale of hour whereas the collisional forces vary in seconds. So, the derivative terms on the left side can be set to zero. For F region, it can be assumed that $V_i = V_e = V$. Here, a few assumptions are also made. To hold the quasi-neutrality of the plasma, it can also be assumed that $N_e = N_i = N$ (density of ionospheric plasma). Further, ν_{in} is ≈ 40 times smaller than the ν_{en}. However, m_i is ≈ 1000 times greater than m_e [e.g., *Rishbeth* *and Garriott*, 1969]. Therefore, the term $m_e \nu_{en}(\vec{V_e} - \vec{U})$ can be ignored. Applying all these assumptions and adding equations 3.3 and 3.4, we get

$$0 = (m_e + m_i)\vec{g} - \frac{1}{N}\vec{\nabla}(NkT_i + NkT_e) - m_i\,\nu_{in}(\vec{V} - \vec{U}) \tag{3.5}$$

As $m_e << m_i$

$$m_i\,\nu_{in}(\vec{V} - \vec{U}) = m_i\,\vec{g} - \frac{1}{N}\vec{\nabla}(NkT_i + NkT_e) \tag{3.6}$$

Upon considering only the parallel velocity, Equation 3.6 can be modified for parallel transport of plasma.

$$m_i \nu_{in}(\vec{V_\parallel} - \vec{U_\parallel}) = m_i\,\vec{g_\parallel} - \frac{1}{N}\vec{\nabla}_\parallel(NkT_i + NkT_e) \tag{3.7}$$

$$\vec{V_\parallel} - \vec{U_\parallel} = \frac{1}{m_i \nu_{in}}\left[m_i\,\vec{g_\parallel} - \frac{1}{N}\vec{\nabla}_\parallel(NkT_i + NkT_e)\right] \tag{3.8}$$

It can be noticed in Equation 3.8 that ionospheric plasma can be transported parallel to the magnetic field by non-electromagnetic forces.

The diffusion coefficient (D_a) of charge particles in the ionosphere with respect to neutral wind is defined as follows

$$D_a = \frac{k(T_i + T_e)}{m_i \nu_{in}} \tag{3.9}$$

where, $\epsilon = \frac{T_i + T_e}{T_i} \iff T_i + T_e = \epsilon T_i$. Equation 3.9 can be written as

$$\frac{D_a}{k\epsilon T_i} = \frac{1}{m_i \nu_{in}} \tag{3.10}$$

from equation 3.8 and 3.10,

$$\vec{V_\parallel} - \vec{U_\parallel} = \frac{D_a}{k\epsilon T_i}\left[m_i\,\vec{g_\parallel} - \frac{1}{N}\vec{\nabla}_\parallel(Nk\epsilon T_i)\right] \tag{3.11}$$

$$\implies \vec{V_\parallel} - \vec{U_\parallel} = D_a\left[\frac{m_i\,\vec{g_\parallel}}{\epsilon k T_i} - \frac{1}{N\epsilon T_i}\vec{\nabla}_\parallel(N\epsilon T_i)\right] \tag{3.12}$$

Let us assume a unit vector tangential to the direction of $\vec{B}$. Further, $\vec{B}$ is assumed to be purely dipolar with radial (r) and meridional (θ) components. Therefore,

$$\hat{i_t} = sinI\ \hat{i_r} + cosI\ \hat{i_\theta}$$

$\vec{g_\parallel}$, $\vec{\boldsymbol{\nabla}}_\parallel$ and $\vec{U_\parallel}$ can be defined in the direction of $\hat{i_t}$ as-

$$\vec{g_\parallel} = (\hat{i_t} \cdot \vec{g})\ \hat{i_t}$$

$$\vec{\boldsymbol{\nabla}}_\parallel = (\hat{i_t} \cdot \vec{\boldsymbol{\nabla}})\hat{i_t}$$

$$\vec{U_\parallel} = (\hat{i_t} \cdot \vec{U_\parallel})\ \hat{i_t}$$

if $\vec{U_\parallel} = U_r\ \hat{i_r} + U_\theta\ \hat{i_\theta}$, we can write,

$$\vec{U_\parallel} = (U_r\ sinI + U_\theta cosI)\ \hat{i_t}$$

In a dipolar coordinate system, $\vec{\boldsymbol{\nabla}}$ is being considered only for radial and meridional components,

$$\vec{\boldsymbol{\nabla}} = \hat{i_r}\ \frac{\partial}{\partial r} + \hat{i_\theta}\ \frac{1}{r}\frac{\partial}{\partial \theta}$$

After combining these equations, we get

$$\vec{g_\parallel} = -g\ sinI\ \hat{i_t}$$

Substituting the values of $\vec{g_\parallel}$, $\vec{\boldsymbol{\nabla}}_\parallel$ and $\vec{U_\parallel}$ in Equation 3.12,

$$\vec{V_\parallel} - (U_r sinI + U_\theta cosI)\hat{i_t} = -D_a \left[\frac{m_i\ gsinI}{\epsilon k T_i} + \frac{1}{N\epsilon T_i}(sinI\ \frac{\partial(\epsilon N T_i)}{\partial r} + \frac{cosI}{r}\ \frac{\partial(\epsilon N T_i)}{\partial \theta})\right]\hat{i_t} \tag{3.13}$$

The scale height of ions can be defined as

$$H = \frac{kT_i}{m_i g}$$

Therefore, Equation 3.13 turns into

$$\vec{V_\parallel} - (U_r sinI + U_\theta cosI)\hat{i_t} = -\frac{D_a}{N}\left[\frac{N\ sinI}{\epsilon H} + \frac{1}{\epsilon T_i}(sinI\ \frac{\partial(\epsilon N T_i)}{\partial r} + \frac{cosI}{r}\ \frac{\partial(\epsilon N T_i)}{\partial \theta})\right]\hat{i_t} \tag{3.14}$$

The right-hand side of Equation 3.14 represents the diffusion velocity (V_{diff}), where,

$$V_{\text{diff}} = -\frac{D_a}{N}\left[\frac{N\,sinI}{\epsilon H} + \frac{1}{\epsilon T_i}(sinI\,\frac{\partial(\epsilon N T_i)}{\partial r} + \frac{cosI}{r}\,\frac{\partial(\epsilon N T_i)}{\partial \theta})\right] \tag{3.15}$$

$$\vec{V}_{\|} - (U_r\ \sin I + U_\theta\ \cos I)\ \hat{i}_t = V_{\text{diff}}\ \hat{i}_t \tag{3.16}$$

Over low latitudes regions, the meridional component of velocity is more variable and I is also small over low latitudes. Therefore, the term $U_\theta\ cosI$ is significant, and the term $U_r sinI$ can be neglected.

With the above considerations, the parallel velocity can be expressed as

$$V_{\|} = -\frac{D_a}{N}\left[\frac{N\,sinI}{\epsilon\,H} + \frac{1}{\epsilon\,T_i}(sinI\,\frac{\partial\,(\epsilon\,N\,T_i)}{\partial r} + \frac{cosI}{r}\,\frac{\partial\,(\epsilon\,N\,T_i)}{\partial \theta})\right] + U_\theta\,cosI \tag{3.17}$$

In Equation 3.17, D_a is the ambipolar diffusion which is calculated by using the following expression [Anderson, 1971].

$$D_a = \left(\frac{T_i + T_e}{T_i}\right)\left(\frac{1}{n_O + 10^5}\right)\left[6.9\times 10^{18}\left(\frac{T_n}{1000}^{1/2}\right)\right]. \tag{3.18}$$

Here, H is the scale height of ions given by $H = \frac{kT_i}{m_i g}$. ϵ is defined as $\epsilon = \frac{T_i+T_e}{T_i}$. Ion and electron temperatures (T_i and T_e), and electron density (N), are obtained from the IRI-16 model. Neutral temperature (T_n) and density of atomic oxygen (n_O) are taken from the MSISE-00 model. Magnetic field parameters, e.g., dip angle (I), etc., are generated from the IGRF-13 model. The meridional component of neutral wind (U_θ) is obtained from the HWM-14. k and m_i are the Boltzmann's constant ($= k = 1.38\times 10^{-23}$ J/K) and mass of ionized oxygen atom (16 a.m.u. or 2.65×10^{-26} kg).

3.3 Results

Figures 3.2a and 3.2b depict the variations in 630.0 nm nightglow intensity (solid red line), VTEC (solid blue line), and EEJ strength (gray area) from 0600 LT to midnight on 29–30 November, 2013. Figures 3.2c–3.2f depict the same except for

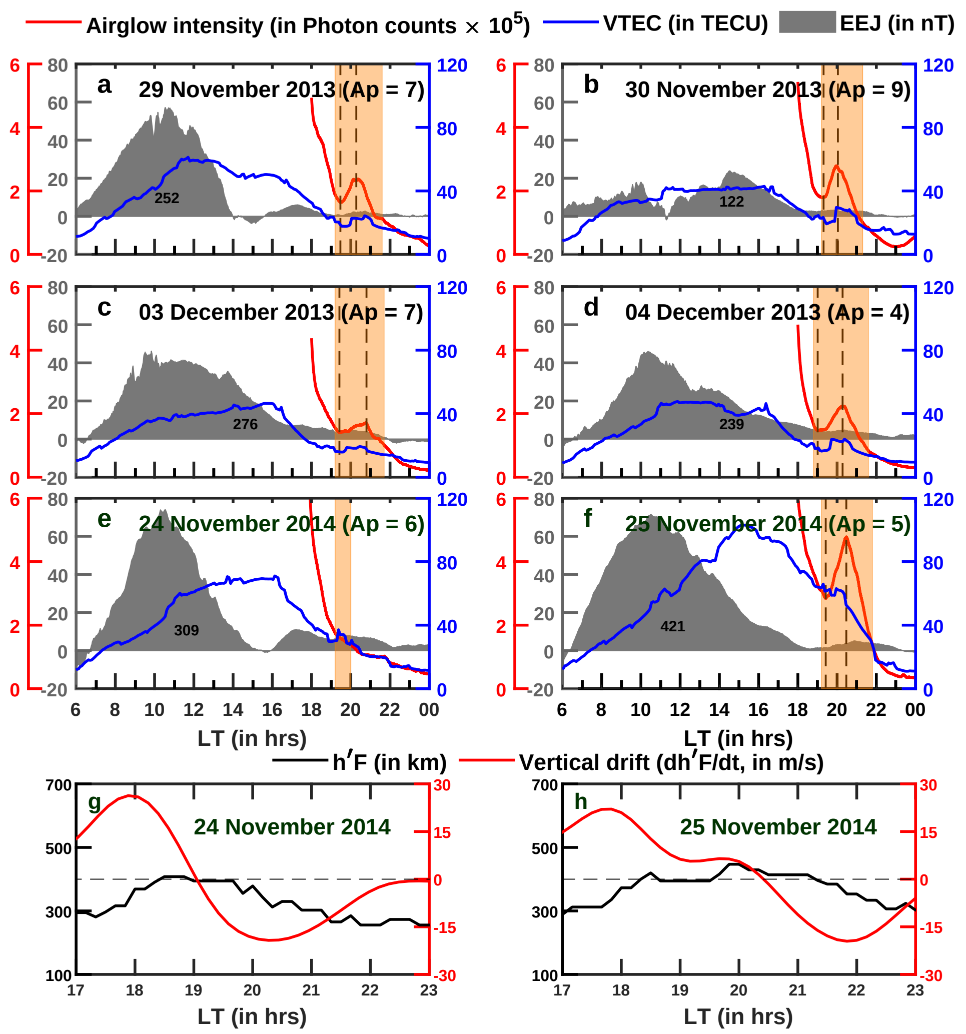

Figure 3.2: Variation of thermospheric OI 630.0 nm airglow intensity over Mt. Abu (red), VTEC over Ahmedabad (blue), and Equatorial electrojet (gray area) with local time on (a) 29 November 2013, (b) 30 November 2013, (c) 03 December 2013, (d) 04 December 2013, (e) 24 November 2014, and (f) 25 November 2014. Calculated integrated EEJ strength (numeric value) is written with black color over gray area. The local time variations in bottomside F-layer height (black) from CADI measurement over Tirunelveli and its derivative dh'F/dt (red) on (g) 24 November 2014, and (h) 25 November 2014.

03–04 December 2013 and 24–25 November 2014. The post-sunset enhancements in airglow intensity and VTEC are conspicuously noticed during 1945–2045 LT in Figures 3.2a–3.2d. It seems that daytime peak VTEC values vary in accordance with the integrated EEJ strength. However, the integrated EEJ strength can be seen to be uncorrelated to the post-sunset enhancements in the airglow intensity and VTEC (particularly, see Figures 3.2b and 3.2e). For example, the integrated EEJ strength is 309 nT-hr in Figure 3.2e and 122 nT-hr in Figure 3.2b. However, the post-sunset enhancement in airglow intensity and VTEC are conspicuous and higher in Figure 3.2b than in Figure 3.2e. This shows that higher integrated EEJ strength does not automatically guarantee the presence of post-sunset enhancements in airglow intensity and VTEC. It is clearly noticed in Figures 3.2a–3.2d and 3.2f that the enhancements in airglow intensity over Mt. Abu start slightly earlier than the onset of increases in the VTEC over Ahmedabad during post-sunset hours (marked by orange vertical boxes). However, it is interesting to note that the airglow intensity peak occurs slightly later than VTEC peak. It is to be mentioned here that, unlike the sharp airglow intensity peaks, VTEC variations are, in general, characterized by a step-like increase followed by a gradual decrease. The time corresponding to the peak VTEC is taken as the time corresponding to the endpoint of the steplike increase. In order to aid visual inspection, two vertical dashed lines are superimposed that mark the times corresponding to the onset of increase and peak of the airglow intensity. Further, it can be noticed in Figure 3.2e that although there is a peak in VTEC at $\sim$ 1920 LT, there is no corresponding enhancement in airglow intensity. In contrast to Figure 3.2e, a strong intensity peak is observed in Figure 3.2f. It can also be noticed that the enhancement in VTEC occurs slightly earlier in Figure 3.2e ($\sim$ 1920 LT) compared to Figure 3.2f ($\sim$ 2000 LT). This difference in timing makes the peak in VTEC to coincide with the sharp fall in the airglow intensity associated with the F-region sunset in Figure 3.2e. This is in contrast to Figure 3.2f, when the peak in VTEC coincides with the inflection point when airglow intensity starts increasing again after the sharp fall associated with the F region sunset.

Although airglow observations for a number of nights are available, two representative cases (24 and 25 November, 2014) of contrasting post-sunset variations in airglow intensity are chosen for further investigations. These are depicted in Figures 3.2g and 3.2h, respectively. It is interesting to note that while post-sunset VTEC peaks are observed on both the days, the airglow intensity peak is significant on 25 November and almost absent on 24 November. In order to understand the location of the bottomside F-layer height over the dip equator and its vertical movement on 24 and 25 November 2014, the variations in $h'F$ (in black)and smoothed vertical drift ($dh'F/dt$ in red) during 1700–2300 LT are depicted in Figures 3.2g and 3.2h. On 25 November, the PRE-associated vertical drifts are upward for a longer duration compared to 24 November. The vertical drift associated with PRE sustains until $\sim$ 1900 LT and $\sim$ 2015 LT on 24 and 25 November, respectively. These differences in vertical drifts on 24 and 25 November 2014 affect the post-sunset enhancements in VTEC and airglow intensity shown in Figures 3.2e and 3.2f, and will be discussed later.

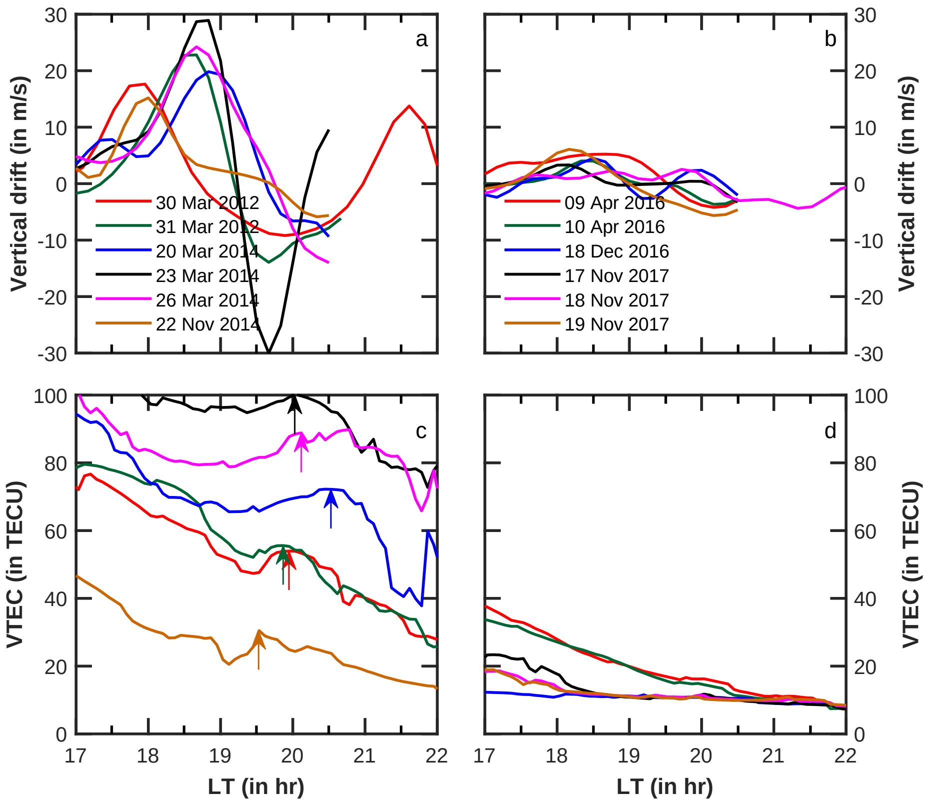

Figure 3.3: Variation of $dh'F/dt$ and VTEC is shown for the 30 March 2012 (red), 31 March 2012 (green), 20 March 2014 (blue), 23 March 2014 (black), 26 March 2014 (magenta), and 22 November 2014 (dark orange) in panels (a and c) respectively. The colored arrows indicate the time of occurrence of the peak VTEC. Similar variations on 09 April 2016 (red), 10 April 2016 (green), 18 December 2016 (blue), 17 November 2017 (black), 18 November 2017 (magenta), and 19 November 2017 (dark orange) are shown in panels (b and d).

For a detailed investigation and to find the causal connection between the PRE and the post-sunset enhancement near the EIA crest region, Figure 3.3 is presented. Figures 3.3a and 3.3b represent two contrasting vertical drift variations over Tirunelveli with strong PRE and absent/subdued PRE during 1700–2200 LT. In each category, six representative days are shown. Figures 3.3c and 3.3d represent the VTEC variations over Ahmedabad for the same local time corresponding to Figures 3.3a and 3.3b, respectively. In both the categories, the local time variations in vertical drift and VTEC are shown with same color to avoid any confusion. The time interval on the X-axis in Figures 3.3b and 3.3d are deliberately made different to bring out the post-sunset features in VTEC clearly. It is because the post-sunset enhancements are noticed after the occurrence of PRE. Interestingly, conspicuous enhancements in VTEC (peaks marked by colored arrows) can be noted in Figure 3.3c and absence of clear enhancements in Figure 3.3d. Therefore, Figure 3.3 suggests that post-sunset enhancements in VTEC near the EIA crest region occur whenever the PREs occur with stronger amplitudes. It is also important to mention that the time delay between the peak vertical drift and post-sunset VTEC peak ranges from $\sim$ 1.4 h (31 March 2012) to $\sim$ 2 h (30 March 2012).

It is to be noted in this context that a few samples of day-to-day variability in the post-sunset enhancements in VTEC and airglow intensity near the EIA crest regions have been shown in Figures 3.2 and Figure 3.3 to indicate the causal connection between the PRE amplitude and the degree of post-sunset enhancements in VTEC and airglow intensity near the EIA crest region. In Figure 3.4, the large dataset of VTEC and global empirical model drifts are brought together to understand the seasonal and solar activity dependence of the post-sunset enhancements in VTEC near the EIA crest region (Ahmedabad) and its' morphological connection with the equatorial vertical drifts over the dip equatorial region. Individual quiet days' VTEC variations in three seasons during high (left column) and low (right column) solar activity years are represented in gray lines for the three seasons in Figures 3.4a–3.4f. The average variations in VTEC (black line) are overlaid on all these subplots. The number of days of VTEC

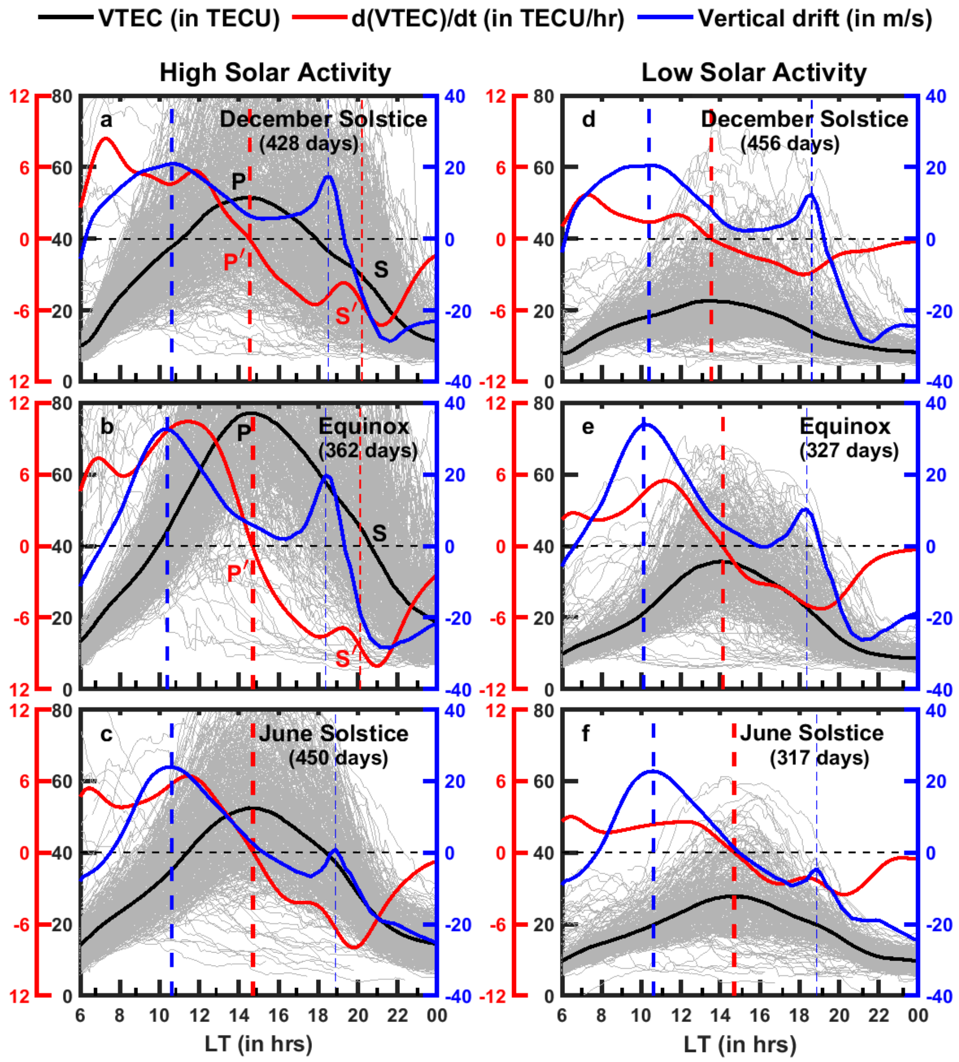

Figure 3.4: Variation of individual days' VTEC over Ahmedabad (gray), average of seasonal VTEC (black), temporal derivative of seasonal VTEC (red), and vertical drift (blue) in December solstice (top), Equinox (middle), and June solstice (bottom) under high (left panel) and low (right panel) solar activity years. The number of days used to calculate the seasonally averaged VTEC curve is also mentioned in each subplot. The points P and S represent primary (afternoon) and secondary (post-sunset) maxima of VTEC. P and S are determined based on P' and S' that are overall and local zero crossing points of dVTEC/dt. The intervals between the thick and thin vertical dashed lines (blue and red) are the response times of the EIA crest region during noon and post-sunset hours respectively.

data used to construct the average VTEC curves in Figures 3.4a–3.4f is 428, 362, 450, 456, 327 and 317. In each subplot, model vertical drifts obtained from *Fejer et al.* [2008a] (blue line) for 75°E longitude and smoothed d(VTEC)/dt (red line) are also overlaid. The smoothed d(VTEC)/dt is derived in the same way as smoothed vertical drifts derived from $h'F$ shown earlier in Figures 3.2g and 3.2h. The derivative of VTEC is used purportedly to identify the post-sunset enhancements. The noon hours' peak VTEC values (primary maximum) and post-sunset enhancements (secondary maximum) are identified by P' and S' respectively in the d(VTEC)/dt curves shown in Figures 3.4a and 3.4b. P' is the point when d(VTEC)/dt becomes zero that indicates the primary maxima of VTEC variation (daytime/overall maximum in VTEC). The trickier part is the S' point, based on which the secondary maximum (post-sunset peak) in VTEC is identified. Note that S' is midway (local zero-crossing point) between the point when d(VTEC)/dt starts increasing and the point when it returns back to the original variation. The P' and S' points help to identify the points P and S that are the maxima during noon and post-sunset hours. This method is adopted after doing a number of exercises and verifications. This method is useful to bring out the post-sunset increment in VTEC that is embedded in the large amplitude diurnal variation. Figure 3.4 reveals that peak VTEC values are larger during high solar activity period. Interestingly, it is noticed that the post-sunset enhancements in VTEC (after the occurrence of the PRE) occur only in December solstice (Figure 3.4a) and Equinox (Figure 3.4b). The times of occurrence of daytime peaks in vertical drifts and PRE-associated peak vertical drifts are marked by thick and thin vertical dashed lines in blue. On the other hand, peaks of daytime VTEC and the post-sunset enhancement in VTEC are identified by thick and thin vertical dashed lines in blue. Based on the average variation in VTEC, it is noticed that the daytime peaks in the VTEC occur during 1330–1500 LT for all seasons and solar epochs, whereas the post-sunset peaks in VTEC occur at $\sim$ 2000 LT in December solstice and Equinox during the high solar activity period only. Interestingly, PRE-associated peak vertical drifts during December solstice and Equinox occur at $\sim$ 1830 LT. At this juncture, the response time of the EIA crest region can be defined as the interval between the time of occurrences of the peak drift (the daytime peak and the PRE-associated peak) and the peak VTEC (the points P and S). According to this definition, the response time during afternoon hours can be seen to be more than three hours. However, the response time during post-sunset hours are found to be applicable only during December solstice and Equinox in high solar activity epoch as post-sunset enhancements in VTEC are conspicuously observed after the PRE only during these two seasons. The response times in these two cases are estimated to be $\sim$ 1.7 h. An evening peak in VTEC is also noted during June solstice in high solar epoch (Figure 3.4c). It can be noticed in Figures 3.4c and 3.4f that peak in average VTEC occurs slightly before the PRE and it can be safely stated that this peak is not causally connected to the PRE. Understanding the physical mechanism responsible for this VTEC peak is beyond the scope of the present work and will not be discussed further. Therefore, based on Figure 3.4, it can be inferred that the response time of the EIA crest region during post-sunset hours is almost half compared to the response time during the day.

In order to understand the plasma distribution over low latitudes consequent to the peak vertical drifts during the day and post-sunset hours, SBAS-TEC maps are constructed for the two contrasting days- 24 (insignificant post-sunset VTEC and airglow intensity enhancements) and 25 (significant enhancements in VTEC and airglow intensity) December 2014. Figure 3.5 depicts the SBAS-TEC maps around noon (first and third columns) and post-sunset hours (second and fourth columns) for 24 and 25 November, 2014 respectively. In each subplot, the locations of Ahmedabad and Mt. Abu are represented by black (filled) circles, and local times are also depicted. Different color scales are adopted for all four columns to bring out the conspicuous large-scale plasma features. It is striking to notice that as time progresses in the afternoon hours, TEC gradually decreases over Mt. Abu/Ahmedabad on 24 November (Figures 3.5a–3.5d), whereas it gradually increases (Figures 3.5i–3.5l) on 25 November. Interestingly, during post-sunset hours on 24 November, a sharp decrease in TEC is observed over the EIA crest region (Figures 3.5e–3.5h). However, on 25 November, the TEC values are comparatively larger over Ahmedabad and Mt. Abu until $\sim$ 2100 LT (Figures 3.5m–3.5o), and it decreases slowly on 25 November. In fact, a very important feature that arises after analysing SBAS-TEC maps on many days during high

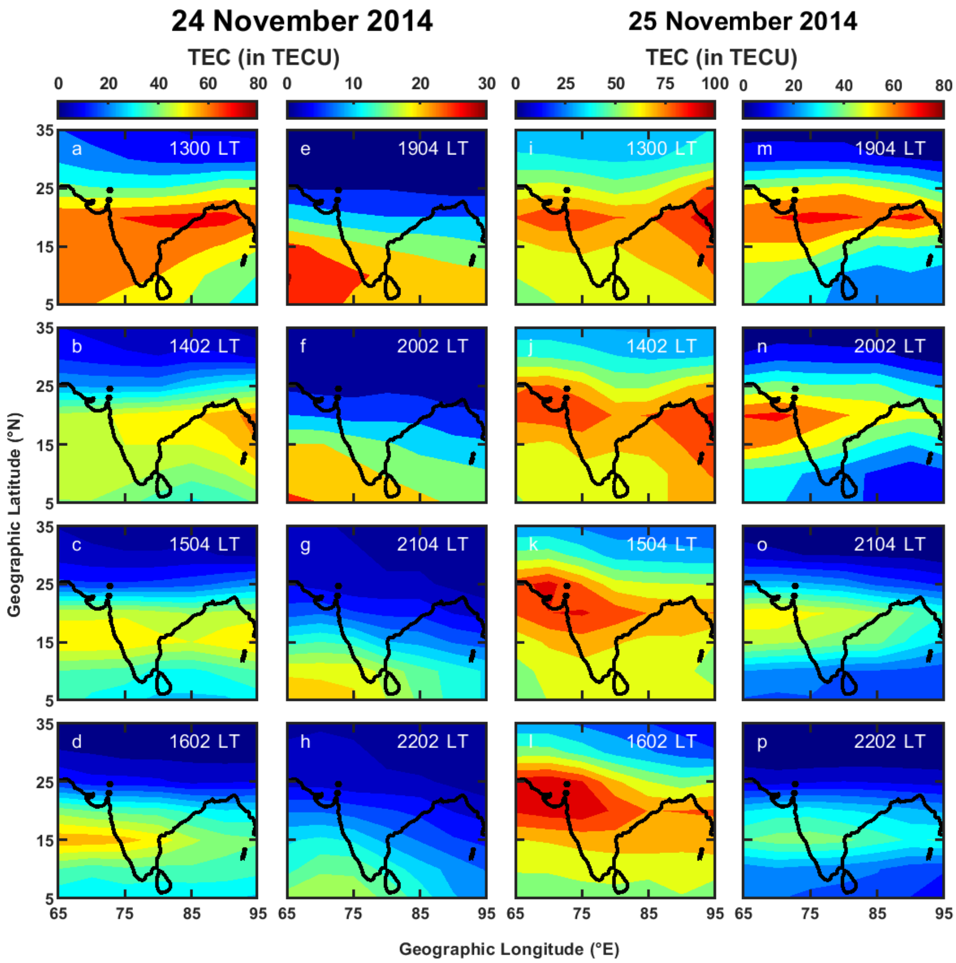

Figure 3.5: SBAS-TEC maps are shown for 24 November 2014 (a–h) and 25 November 2014 (i–p). Different color scales are adopted for all the four columns to make the large-scale plasma features conspicuous.

solar activity periods (not shown here) is that the daytime EIA crest is stronger during afternoon hours over the Mt. Abu/Ahmedabad region, and the strength of crest region weakens (less TEC) in the evening hours. Although during post-sunset hours, TEC again enhances in a smaller degree over this region, it decreases monotonically during the nighttime. It is also to be noted that the post-sunset observations of TEC around Ahmedabad/Mt. Abu are mostly consistent with the post-sunset peak observed in airglow intensity on 24–25 November (Figures 3.5e and 3.5f).

Figure 3.5 shows the SBAS-TEC maps during noon and evening hours, while the Figure 3.6 is planned to bring out the latitudinal gradient in TEC during

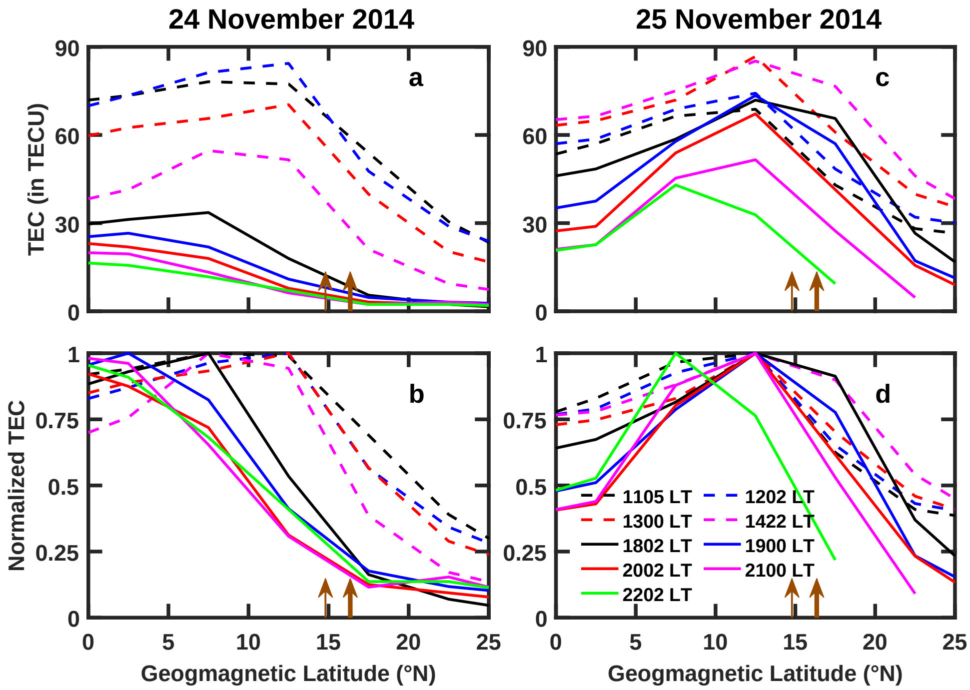

Figure 3.6: Panels (a) and (c) show the latitudinal variation of SBAS-TEC on 24 and 25 November 2014, respectively along 75° E geographic longitude (148° E geomagnetic longitude). Panels (b) and (d) represent the latitudinal variation of normalized SBAS-TEC corresponding to panels (a) and (b) respectively. Dashed and solid lines are used to show the variations during daytime (1105, 1202, 1300, and 1422 LT) and post-sunset hours (1802, 1900, 2002, 2100, and 2202 LT). Thin and thick brown arrows denote the latitudes of Ahmedabad and Mt. Abu, respectively.

the noon and evening hours. Figures 3.6a and 3.6c represent the latitudinal variations in SBAS-TEC along the 75° E longitude at multiple noon/afternoon (dashed lines) and post-sunset/pre-midnight (solid lines) local times on 24 and 25 November 2014. For better comparison, Figures 3.6b and 3.6d depict the same plots in normalized scales. Normalized TEC is obtained for each time with respect to the maximum TEC observed at that local time across all latitudes. The latitudinal variation of normalized VTEC is easy to compare at different local times. The latitudes of Ahmedabad and Mt. Abu are indicated by vertical thin and thick brown arrows, respectively, at the X-axes of each panel. TEC variations around noon (1105, 1202, 1300, and 1422 LT) and sunset hours (1802, 1900, 2002, 2100, and 2202 LT) are shown by dashed and solid lines (in different colors), respectively. From Figures 3.6b and 3.6d, the locations of the EIA crest region can be clearly identified at different local times. It is interesting to note in Figure 3.6 that the daytime latitudinal TEC gradients on the equatorial side of the EIA crests are much smaller than the post-sunset gradients on 25 November. It is also clear that the daytime location of the crest is closer to the location of Ahmedabad/Mt. Abu (between 10° and 15°) on both 24 and 25 November. However, the nighttime EIA crest is shifted earlier on 24 November and located much closer to the dip-equator during the post-sunset hours. In contrast, the crest location on 25 November in post-sunset hours is situated closer to the daytime crest location and moves toward the dip-equator around 2200 LT (green solid line in Figure 3.6d). This is a classic example of the reverse fountain, and this happens, in general, between 2100 and 2200 LT. It is important to point out that the latitudinal gradient in TEC gradually decreases and becomes maximum during 2000–2100 LT just before the reverse fountain process starts. The salient features obtained from Figure 3.6 will be discussed in detail in the ensuing section.

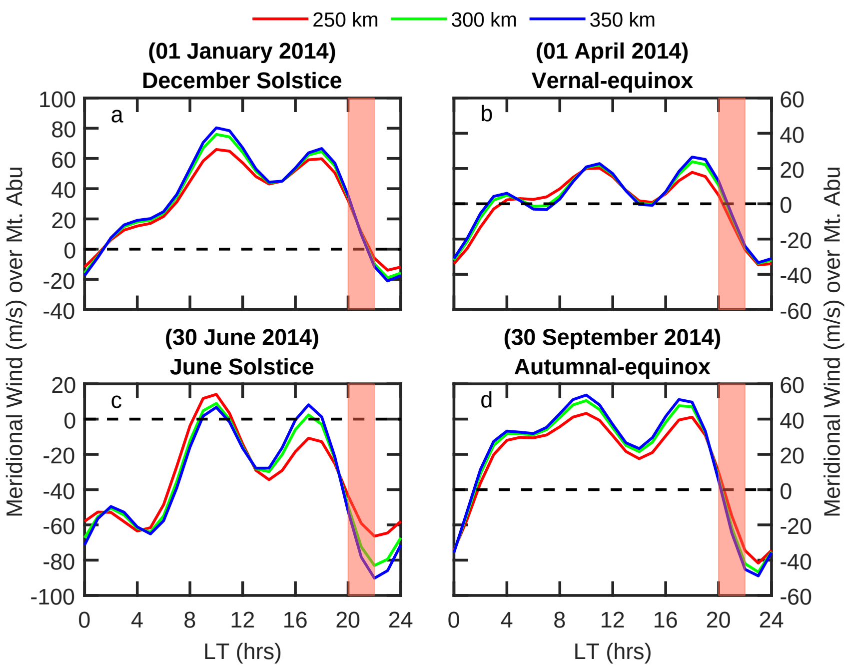

Figure 3.7: Local time variations of meridional wind over Mt. Abu (24.6° N, 72.7° E, dip angle 38°) are shown at 250, 300, and 350 km altitude for (a)December solstice, (b)Vernal-equinox, (c) June solstice, and (d) Autumnal-equinox. Wind outputs are generated by the horizontal wind model-2014 (HWM-14) for year 2014.

Although low latitudes plasma is transported by gravity and pressure gradient forces, meridional wind may also play an important role (see equation 3.17). Meridional wind outputs are generated over Mt. Abu for December solstice (01 January 2014), Vernal-equinox (01 April 2014), June solstice (30 June 2014) and Autumnal-equinox (30 September 2014), and the variations are depicted in Figures 3.7a-3.7d. The period 2000-2200 LT is marked with orange rectangular boxes in all panels where the post-sunset enhancements in airglow intensity over Mt. Abu are, in general, noticed. Positive and negative values of wind represent the poleward and equatorward wind, respectively. During December solstice (Figure 3.7a) and Autumnal-equinox (Figure 3.7d), the meridional winds are more poleward during daytime. During nighttime, the winds are more equatorward during the June solstice (Figure 3.7c). During both the equinoctial months (Figure 3.7b and 3.7d), the amplitudes of poleward and equatorward winds are similar during the day and night, although the magnitudes are different between the equinoxes. It can be noticed from the variations within the orange rectangular boxes that wind is continuously decreasing and closer to zero/equatorward during 2000-2200 LT in the equinoctial months. This means that depending on the time of occurrence of the post-sunset enhancements, meridional wind may have some role in taking the ionospheric layers upward and thereby, in enhancing VTEC by reducing the quenching effect [*Rishbeth*, 1977]. However, this proposition is contrasted by the variation of meridional wind during June solstice, where, similar to Equinox, one observes more equatorward wind but no VTEC enhancements. Unlike the Equinox and June solstice, the meridional wind is decreasingly poleward and very close to zero during 2000-2200 LT in the December solstice. Therefore, in this season, one may expect reduced VTEC owing to enhanced quenching if the post-sunset enhancements are due to the effects of meridional wind. This shows that meridional wind may have a role in the post-sunset enhancements in VTEC but it may not be the decisive factor. This aspect will again be taken up subsequently in the discussion section.

Tables 3.1 and 3.2 represent parallel velocity along the 75° E ($\sim$ 148 E magnetic meridian) in December solstice and Equinox, respectively, at 1030 LT, 1430

Table 3.1: Parallel velocity is estimated along 75° E longitude at 350 km altitude during December solstice. This velocity is calculated only for 1030, 1430, 1830, and 1930 LT at 0°, 5°, 10° and 15° magnetic latitudes.

December solstice				
Magnetic Latitude (in deg)	**1030 LT**	**1430 LT**	**1830 LT**	**1930 sfu**
	Parallel velocity in ms^{-1}			
0°	80	10	64	60
5°	88	17	65	56
10°	84	25	62	50
15°	70	32	54	42

Table 3.2: Similar to December solstice but for Equinox.

Equinox				
Magnetic Latitude (in deg)	**1030 LT**	**1430 LT**	**1830 LT**	**1930 sfu**
	Parallel velocity in ms^{-1}			
0°	10	01	10	08
5°	16	03	16	02
10°	19	06	22	12
15°	19	05	23	16

LT, 1830 LT and 1930 LT at four magnetic latitudes- 0°, 5°, 10°, and 15°. Parallel velocity ($V_{\|}$)is calculated from equation 3.17. The relevant plasma, neutral, geomagnetic field and meridional wind parameters used as inputs are taken from IRI-16 [*Bilitza et al.*, 2017], NRLMSISE-00 [*Picone et al.*, 2002], IGRF-13 [*Alken et al.*, 2021], and HWM-14 [*Drob et al.*, 2015] models respectively. It can be noticed in both Tables that the parallel velocities are higher at 1030, 1830 and 1930 LT during both December solstice and equinox. Further, the magnitudes of parallel velocities are larger in December solstice. Interestingly, it can be seen that parallel velocities during evening/post-sunset hours are, in general, less compared to those during morning hours at all magnetic latitudes.

3.4 Discussion

Post-sunset enhancements in F region plasma over low latitudes have been reported in earlier works [e.g., *Bittencourt et al.*, 2007; *Farelo et al.*, 2002; *Kulkarni*, 1969; *Rao and Kulkarni*, 1973; *Su et al.*, 1994; *Xiong et al.*, 2016]. However, the processes responsible for these enhancements are not understood comprehensively. It is seen from Figures 3.2 and 3.4 that the post-sunset enhancements in airglow intensity and VTEC are not directly connected with the daytime plasma fountain. Interestingly, the enhancements in airglow intensity over Mt. Abu start slightly earlier than the onset of the increase in VTEC over Ahmedabad. This happens probably due to the reversal of the vertical drift from upward to downward direction associated with the reversal in the zonal electric field. This takes plasma slightly at a lower height which is closer to the airglow emission altitude. On careful examination, it is noted that the onset of the increase in airglow intensity starts sometime during ∼1900–1930 LT. This approximately coincides with the time of polarity reversal in the model vertical drift over the Indian dip equatorial station (indicated by Figures 3.4a and 3.4b). A downward drift supplies more plasma to the airglow emission height resulting in an increase in airglow intensity at this time. As the upward/downward drift does not change the total columnar content of electrons instantly, VTEC is not affected significantly. In fact, VTEC around the EIA crest region during post-sunset hours may change due to the meridional transport of plasma. Therefore, the arrival of additional plasma from the meridional direction causes the onset of increase in VTEC. In the intervening period between the onset of increase and the peak intensity, the airglow intensity variations are expected to be governed by both downward vertical drift and the meridional plasma transport. In addition to these factors, recombination chemistry can mask the enhancements in airglow intensity to a certain degree by contributing to vertical drift [e.g., *Bittencourt and Abdu*, 1981; *Subbarao and Krishna Murthy*, 1994]. However, VTEC can be affected by the meridional wind only. Nevertheless, the peak in the airglow enhancement over Mt. Abu occurs at a slightly later time than the peak VTEC during post-sunset hours over Ahmedabad. It indicates the role of the meridional transport of plasma. Further, during this time (2000–2030 LT), the changes in the downward drift are not significant as suggested by the model drifts in Figures 3.4a and 3.4b. Therefore, it is believed that both VTEC and airglow intensity enhancements at this time are governed by poleward plasma transport. This also rules out the effective role of reverse plasma fountain [e.g., *Balan et al.*, 1997; *Sridharan et al.*, 1993] that transports the plasma equatorward. Further, the reverse fountain over the EIA crest region reported by the earlier works suggests its arrival at a later time compared to that of the post-sunset peak. This is supported by Figure 3.6d, wherein the reverse fountain is detected sometime between 2100 and 2200 LT. Note the peaks of the post-sunset enhancements occur mostly before the reverse fountain effect comes into play.

In order to explore the possible role of meridional wind, the outputs from the Horizontal Wind Model-14 [HWM-14, *Drob et al.*, 2015] are shown for December solstice and Equinox at 250, 300, 350 km altitudes in Figure 3.7. These outputs as well as previous results [e.g., *Balan et al.*, 1997; *Drob et al.*, 2015] reveal that the poleward wind near the EIA crest region monotonically decreases during the time of occurrence of post-sunset enhancement in airglow intensity reported in this work. From 250 to 350 km altitude, there is a very slight variation noticed in the magnitudes of meridional wind. Under this condition, the poleward wind will be less efficient in pushing the plasma to the airglow emission altitude band centered at ~ 250 km. Therefore, the airglow intensity is expected to reduce monotonically during post-sunset hours. This is in contrast to the observations reported in the present work. In case of possible equatorward wind at this local time (during equinox), one can expect an enhancement in VTEC. However, if that were the case, one would have seen similar VTEC enhancements during June solstice also. Therefore, the role of meridional wind does not appear to be straightforward and consistent with the variabilities of the post-sunset enhancements in VTEC during the three seasons. Nevertheless, the contribution of meridional wind, along with others parameters, is already included in the derivation of the parallel component of plasma diffusion velocity (Equation 3.17). It is also noteworthy that a significant reductions in the amplitudes of the post-sunset VTEC peaks are seen during equinox in low solar activity years despite similar magnitudes in the daytime peak eastward electric field (Figures 3.4b and 3.4e). Therefore, the direct role of the daytime plasma fountain in causing the post-sunset VTEC enhancement near the EIA crest region can be ruled out.

One can get a clue about the causal connection between PRE and the post-sunset enhancements in VTEC near the EIA crest region by analyzing Figure 3.3. The cases represented in Figure 3.3 reveals that the time delays between the peak vertical drift associated with the PRE and the peak VTEC range from 1.4 to 2 hrs. These time delays are consistent with the average time delay ($\sim$ 1.7 hrs) between the PRE and post-sunset enhancement in VTEC near the EIA crest region shown in Figure 3.4. Interestingly, the post-sunset peaks in VTEC appear only during December solstice and equinoctial months in high solar activity periods, and an enhanced PRE is a hallmark feature for these two seasons in high solar activity years [*Fejer et al.*, 2008a] as seen in Figure 3.4. This result is also consistent with the statistical work of *Farelo et al.* [2002]. They found in their work that the amplitudes of the pre-midnight peak in NmF2 over low latitudes are most pronounced during the winter solstice and Equinox in high solar activity years. It is to be noted that post-sunset peaks in VTEC are absent on those occasions when the PRE is subdued or absent (Figure 3.4). Therefore, it can be inferred that the higher amplitudes of PRE strengthen the plasma fountain in the evening/post-sunset hours, and this causes enhancements in VTEC and OI 630.0 nm airglow intensity near the EIA crest region with an average time delay of $\sim$ 1.7 hrs.

The above discussion poses a conundrum. The post-sunset VTEC peak near the EIA crest region is observed $\sim$ 1.7 hrs later than the occurrence time of the peak PRE. This response time is significantly shorter than the corresponding response time during day, which is of the order of 3-4 hrs. It is to be noted in this context that not only the response time (dip equator to crest) during day is consistent with the earlier work of *Rama Rao et al.* [2006] but the occurrence of minimum delay during December solstice in low solar activity years is also consistent with the observations reported by *Aswathy et al.* [2018]. Further, it may be noted here that observationally, the PRE over the Indian sector occurs about half an hour later in Equinox compared to December solstice [e.g., *Madhav Haridas et al.*, 2015; *Sripathi et al.*, 2016]. This may reduce the response time of the EIA crest region during Equinox if one uses vertical drift observations from the dip equatorial station. Considering the objective of the present work is to show the reduced response time of the EIA crest region corresponding to the PRE, the conclusion drawn in this work regarding the reduced response time remains unaffected. In order to understand the significance of the smaller response time of the EIA crest region during post-sunset hours, it is important to consider the parallel component ($V_{\parallel}$) of plasma diffusion velocity in the meridional direction is important to discuss. It is assumed that the perpendicular component ($V_{\perp}$) is negligible over low latitudes. The assumption is valid as, over low latitudes, the contribution of $V_{\perp}$ to the crest-ward movement of plasma is expected to decrease as the dip angle increases. Tables 3.1 and 3.2 shows the variations in $V_{\parallel}$ during December solstice and Equinox. It can be said from Tables that $V_{\parallel}$ is higher during December solstice. Interestingly, it can be noticed in Table 3.1 that $V_{\parallel}$ is smaller in post-sunset hours ($\sim$42-60 ms^{-1}) compared to pre-noon time ($\sim$70-88 ms^{-1}) in December solstice. On the other hand, the $V_{\parallel}$ values during post-sunset and pre-noon hours vary from $\sim$08-19 ms^{-1} in Equinox. This is primarily due to the weaker meridional wind during Equinox (Figure 3.7). Although $V_{\parallel}$ values are smaller in Equinox than in December solstice during post-sunset hours, the enhancements in VTEC over the EIA crest region occur around the same local time in these two seasons (Figures 3.4a and 3.4b). It is because PRE occurs later in Equinox than in December solstice [e.g., *Madhav Haridas et al.*, 2015; *Sripathi et al.*, 2016]. Further, it is also interesting to note that $V_{\parallel}$ during post-sunset hours (see Tables 3.1 and 3.2) is either of similar magnitude or less compared to daytime. However, the response time is significantly less during post-sunset hours. This suggests that PRE is the main driver for the post-sunset enhancement (2000-2100 LT) of VTEC or 630.0 nm airglow intensity over the EIA crest region.

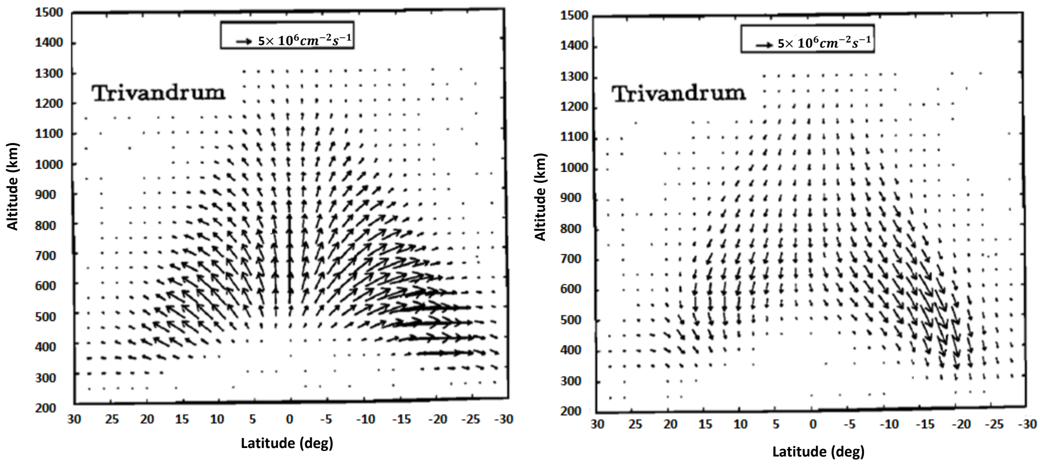

Figure 3.8: Vector plasma fluxes at 1900 LT (left) and 2100 LT (right); the fluxes are plotted on a linear scale, and the minimum vector length (zero length) correspond to plasma fluxes less than 5×10^6 cm^{-2}s^{-1}; positive magnetic latitude is northward. Note the differences in the velocity vectors at these two local times [From *Balan et al.*, 1997].

Two important points emerge from the above discussion. The post-sunset enhancement in VTEC near the EIA crest region depends on PRE (Figure 3.5). In addition, Figure 3.6 suggests that the latitudinal gradient in the F region plasma density becomes steeper during post-sunset hours. It is also verified that these results are grossly consistent with the global GPS TEC maps (one can verify on this link: `https://cdaweb.gsfc.nasa.gov/`). Such an enhancement in TEC over the EIA crest region and depletion over the EIA trough region during post-sunset hours can also be noticed in the earlier works corresponding to geomagnetically quiet [e.g., Figure 1 of *Chen et al.*, 2017] and disturbed periods [e.g., Figure 6 of *Rout et al.*, 2019]. A few earlier studies [e.g., *Liu et al.*, 2007; *Sunda and Vyas*, 2013] have reported the crest to trough ratio (CTR) to be larger during the post-sunset hours. Based on Sheffield University Plasmasphere Ionosphere Model (SUPIM), *Balan et al.* [1997] studied the equatorial plasma fountain under magnetically quiet equinoctial conditions in high solar activity

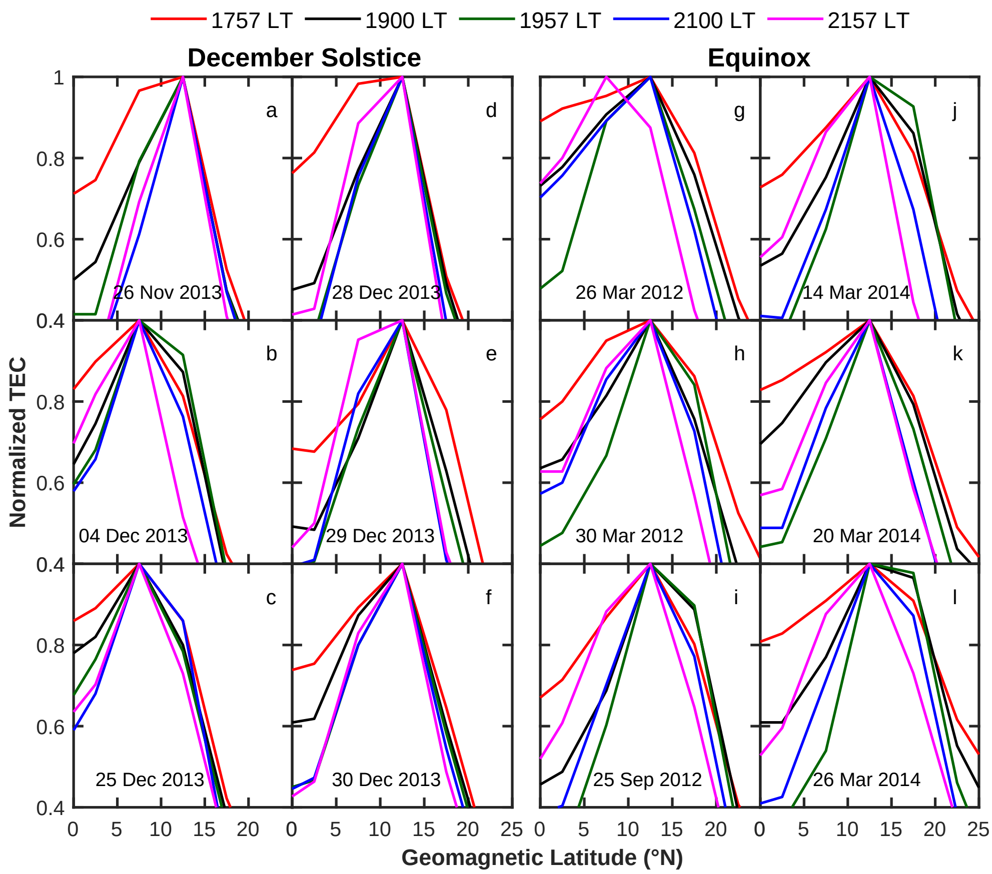

Figure 3.9: Variations of normalized SBAS-TEC with magnetic latitude (similar to Figures 3.6b and 3.6d) at 1757, 1900, 1957, 2100, and 2157 LT for six representative days during December solstice (a–f) and Equinox (g–l) are shown. It can be seen that the latitudinal gradient from 5°N to 10°N to the EIA crest region maximizes and then decays during the post-sunset hours.

period. Figure 3.8 presented here is taken from *Balan et al.* [1997], and this reveals that at the time of the PRE (1900 LT), the F region plasma gets transported to the EIA crest region from 5°N to 10°N magnetic latitude. As the plasma transport from the dip equatorial region to the EIA crest is expected to take 3–4 hrs, the post-sunset enhancement over the EIA crest region is unlikely to have plasma contribution from latitudes closer to the dip equator. Owing to the significant magnitude of $V_{\perp}$ until $\sim 7.5°$ dip latitude [*Fejer et al.*, 1995] plasma would primarily have vertical motions closer to the dip equator and would not get sufficient time to reach the EIA crest region before electric field reversal. Therefore, it is evident that the relative dominance of horizontal plasma transport from 5° to 10°N causes the enhancement of VTEC and airglow intensity at the EIA crest region during post-sunset hours. As the latitudinal coverage is almost half, the time taken for the PRE-driven plasma to reach the EIA crest region is also reduced almost by half. In order to confirm this proposition, the latitudinal TEC variations (normalized as in Figures 3.6b and 3.6d) on a large number of days have been investigated. Figure 3.9 shows the latitudinal TEC variations at five different local times (1757, 1900, 1957, 2100, and 2157 LT) separated by about an hour for six representative days during December solstice (Figures 3.9a–3.9f) and Equinox (Figures 3.9g–3.9l). It can be noted that the latitudinal gradient from 5°N to 10°N to the EIA crest region keeps increasing in the post-sunset hours, maximizes sometime during 2000–2100 LT, and decreases afterward as the plasma moves towards the equator from the crest region (Figure 3.8). This strongly suggests plasma transport from low latitude to the EIA crest region during 2000–2100 LT, resulting in steep latitudinal gradient in TEC. The fact that the latitudinal gradient decreases from 5°N to 10°N to the EIA crest region before $\sim$ 2200 LT suggests that the PRE-driven transport of plasma gets over before this time. It is intuitively obvious that had the plasma traveled from the dip equator to the EIA crest region, it would have taken similar time as it takes during day. The PRE driven plasma closer to the dip equator does not get that time as the reverse fountain starts around 2100 LT (Figure 3.8). Once the reverse fountain starts, plasma starts to move towards the equator that leads the weakening in the post-sunset enhancement in VTEC and airglow intensity.

As a concluding remark, it can be stated that if the plasma transport from 5°N to 10°N to the EIA crest region occurs during the sharp fall in airglow intensity that is associated with the F region sunset, the signature of the PRE-driven fountain may not be conspicuous in airglow. This is because the rate of reduction in airglow intensity is much higher during the F region sunset, and it will obscure the enhancements due to the PRE (Figure 3.2e).

3.5 Summary

In the present chapter, using the CADI measurements over Tirunelveli, the role of pre-reversal enhancement of zonal electric field over the dip equatorial region for the post-sunset enhancement in VTEC and OI 630.0 nm airglow intensity near the EIA crest region is discussed. It is found that PRE causes the enhancement in the plasma density near the EIA crest region during post-sunset hours before the occurrence of the reverse fountain process. These enhancements are only noticed only during December solstice and equinoctial months in high solar activity years. Using SBAS-TEC data, it is proposed that plasma gets transported from 5°N to 10°N magnetic latitude to the EIA crest region under the influence of stronger PRE in these two seasons resulting into VTEC and airglow enhancements. The response time of the EIA crest region corresponding to the PRE-driven fountain is found to be almost half compared to that associated with daytime plasma fountain. Merdional wind is higher during daytime. However, its' strength weakens during evening hours. It will contribute less in the parallel velocity. This suggests less significant role of meridional wind. In summary, the present chapter suggests that PRE is the driver for post-sunset enhancements of plasma density over the crest region of equatorial ionization anomaly.

Chapter 4

PRE is a necessary but not sufficient condition

Excerpts

In Chapter-3, it is shown that the post-sunset enhancements over the EIA crest region are primarily driven by the pre-reversal enhancement of zonal electric field. In this chapter, it is shown that although PRE is the most important factor, it is not only the factor that determines the degree of post-sunset enhancements over the EIA crest region. In Chapter-3, the response time of the EIA crest region during the afternoon and post-sunset hours is discussed with respect to peak amplitudes of the dip equatorial F-region vertical drifts during daytime and evening hours. It is also shown that the post-sunset enhancements are conspicuous during December solstice and Equinox only in high solar flux levels. In this chapter, we focus on the mechanism of the post-sunset enhancements in more detail. In this chapter, based on 10 years of VTEC data in solar cycle 24 over Ahmedabad, it is shown that post-sunset enhancements in VTEC are conspicuous during 2000-2100 LT in Equinox and December solstice when solar flux level exceeds 110 sfu. However, post-sunset enhancements are not seen in June solstice under similar solar flux levels. Further, these enhancements are not observed during the period of sudden stratospheric warming events, even when the solar flux levels are higher than 110 sfu. Notably, it is found that integrated enhancements in the crest region plasma during post-sunset hours show linear and parabolic dependence on the solar flux level in December solstice and Equinox. Detailed analysis shows that parabolic/quadratic fitting is better suited for December solstice and brings out the saturation in VTEC enhancements during post-sunset hours at high (> 160 sfu) solar flux levels. Based on these observations and Thermosphere Ionosphere Electrodynamics-General circulation model (TIE-GCM) outputs, it is advocated that the pre-reversal enhancement in the equatorial F region zonal electric field works in tandem with the latitudinal gradient in the F region plasma density to determine the degree of VTEC enhancement over the EIA crest region during post-sunset hours. In addition, the interhemispheric asymmetries in different seasons over the crest location are also partly captured by TIE-GCM outputs at different solar flux levels.

4.1 Introduction

The low latitude ionosphere is the most affected region in the whole globe as far as the L-band scintillation during post-sunset hours is concerned. *Basu et al.* [1988] showed that the scintillations over the EIA crest region are the most pronounced during high solar activity. Because of maximum L band scintillation, the EIA crest region faces significant problems as far as communication and navigational applications are concerned. These scintillations are caused by the F region irregularities [e.g., *Aol et al.*, 2020]. In addition to these plasma irregularities and associated scintillations, the low latitude ionosphere is also known for the post-sunset enhancement in the F region plasma [e.g., *Bittencourt et al.*, 2007; *Farelo et al.*, 2002; *Kulkarni*, 1969; *Rao and Kulkarni*, 1973; *Su et al.*, 1994; *Xiong et al.*, 2016] as discussed in Chapter-3. In Chapter-3, it is discussed that these enhancements occur after sunset and peak at 2000 LT morphologically. It is also noticed that these enhancements can be captured in VTEC and OI 630.0 nm airglow intensity measurements near the EIA crest region.

In Chapter-3, it is noticed that to understand the genesis of these post-sunset enhancements, one has to understand the F region equatorial plasma fountain

(EPF) process [e.g., *Anderson*, 1973a,b] as this process changes the distribution of F region plasma over low latitudes (discussed in section 1.7.2). The EPF generates two higher plasma density regions around $\pm 15°$ magnetic latitudes. Plasma near equatorial region gets depleted. The enhanced and depleted plasma region is known as the EIA crest and the EIA trough region (See section 1.7.2 and Figure 1.9). It is known that the EIA crests become asymmetric due to the effects of the meridional wind [e.g., *Anderson*, 1973a].

It is known that the F region electric field shows eastward/westward polarities during daytime/nighttime. However, this transition is not monotonic and punctuated by the enhancement of the F region electric field. This enhancement in the zonal electric field (or vertical drift) is known as pre-reversal enhancement (PRE) [e.g., *Fejer*, 2011; *Eccles et al.*, 2015]. The mechanism and variabilities of PRE are discussed in detail in Chapter-1. It is argued in Chapter-3 that as the zonal electric field gets enhanced during PRE hours, it is expected that the plasma fountain process should get reinvigorated at this time, and it would change the low latitude plasma distribution. The PRE rejuvenated fountain process enhances the plasma distribution over the low latitudes in general and the EIA crest region specifically.

It was already discussed in the previous chapter that the post-sunset F region plasma density enhancements over the EIA crest region are pronounced during two seasons- December solstice and Equinox in the period of high solar activity. These seasonal and solar activity dependences of the post-sunset enhancements seem to be connected to what had been noticed in the case of PRE [e.g., *Scherliess and Fejer*, 1999; *Fejer et al.*, 2008a]. It has been shown in Chapter-3 that the post-sunset plasma density enhancements near the EIA crest show the day to day and seasonal dependences that are consistent with the day to day and seasonal variabilities of PRE. However, at this juncture, it is not known whether the post-sunset enhancement in VTEC near the EIA crest region shows similar solar flux dependence as that of PRE. This is an important missing link, and evidence in this regard will strengthen the causal connection between PRE of the F region zonal electric field over the dip equator and the post-sunset enhancement in VTEC over the EIA crest region.

In the previous studies, a few researchers provided indications on the solar flux dependence of the low latitude plasma distribution in post-sunset hours and the role of PRE. The work of *Whalen* [2004] shows that both post-sunset EIA and PRE vary linearly with solar flux. *Abdu et al.* [2008] suggested that the PRE-driven plasma fountain in the evening hours can significantly change the TEC, foF2 and the intensity of EIA, and these changes are solar flux dependent. However, it was not mentioned whether these enhancements would occur at any solar flux level and whether PRE is a necessary as well as a sufficient condition for the post-enhancements. Further, *Chen et al.* [2017] modeled the PRE outputs by coupled ionosphere-thermosphere data assimilation and presented a stronger EPF during evening hour under the influence of a stronger PRE. Owing to stronger EPF during the evening hours, they observed a deepening of the EIA trough. These results are consistent with the observations [e.g., *Liu et al.*, 2007; *Zhang et al.*, 2009] in which it is shown that the latitudinal plasma gradient from trough to crest as well as crest to trough ratio (CTR) becomes higher during post-sunset hours. Interestingly, in their works, they noticed that CTR showed stronger solar flux dependence during post-sunset hours than noon hours. Further, the local time [e.g., *Zhang et al.*, 2009; *Oryema et al.*, 2016], seasonal [e.g., *Olwendo et al.*, 2016], solar flux [e.g., *Liu et al.*, 2007; *Zhang et al.*, 2009], longitudinal [e.g., *Sunda and Vyas*, 2013] and solar activity dependence [e.g., *Zhao et al.*, 2009] of CTR had also been brought out. *Oryema et al.* [2016] noticed the maximum value of CTR during the period 21-23 LT. *Liu et al.* [2007] compared the CTR of evening/post-sunset and noon time and found 2-3 times higher CTR during post-sunset hours with increasing solar activity. The above results as well as our results discussed in Chapter-3 motivated us to understand the solar flux dependence of the post-sunset enhancements of the plasma density over the EIA crest region in greater detail and to address its' causal connection with PRE. In the present chapter, a detailed attempt is made to explore what minimum amplitude of PRE is required for a detectable enhancement of plasma density near the EIA crest region and/or there are other additional factors that contribute to these enhancements. In other words, the present chapter deals with the question- Is PRE a necessary as well as a sufficient condition for the post-sunset enhancement over the EIA crest region? PRE is a necessary as well as a sufficient condition for the post-sunset enhancements reported in Chapter-3.

4.2 Datasets used

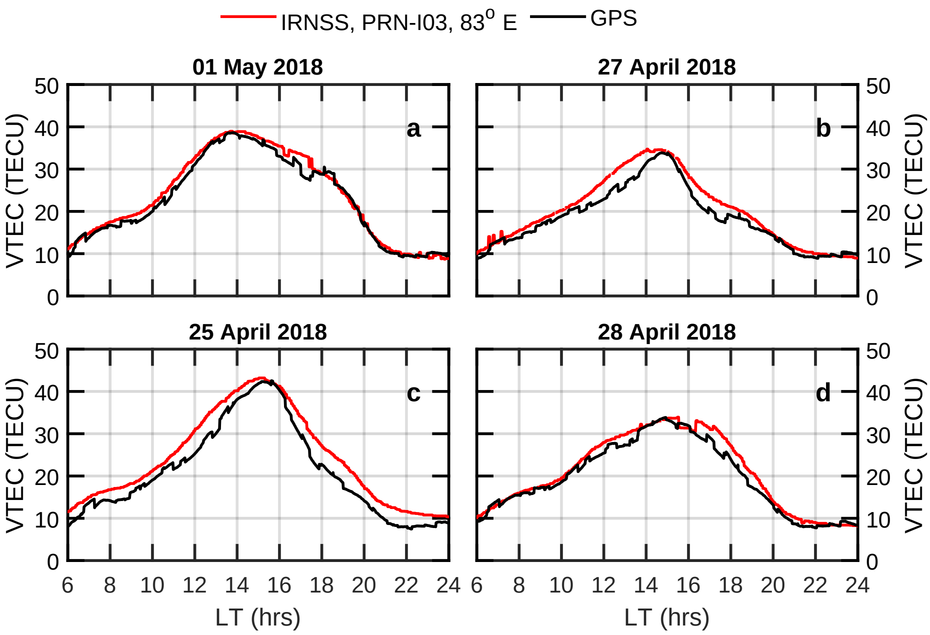

Figure 4.1: Comparison of NavIC-VTEC and GPS-VTEC for four quiet days 01 May 2018 (a), 27 April 2018 (b), 25 April 2018 (c),and 28 April 2018 (d) over Ahmedabad.

The vertical total electron content (VTEC) data over Ahmedabad (23.0° N, 72.6° E, dip angle 35.2°) is described briefly in Chapter-3, and the derivation technique is discussed in Chapter-2. VTEC data for more than a decade (November 2009-December 2019) is used in the present analysis. In this work, the quiet period data are selected based on the Ap index. Daily mean Ap $\leq$ 15 on the chosen day and the previous day qualify the chosen day as a "quiet day." Based on the GPS observations, the slant TEC (STEC) values are derived first. These STEC values are converted to vertical TEC values (VTEC) using an obliquity factor or mapping function [*Mannucci et al.*, 1993], which is a function of the elevation angle of the respective GPS satellite. In the present investigation, an elevation mask of 30° is used to minimize the multipath and troposphere scattering effects [e.g., *Chakrabarty et al.*, 2012] as these effects are more prominent at lower elevation angles. It is also to be noted here that the ionospheric pierce points (IPPs) change with the movements of the GPS satellites [e.g., *Huang et al.*, 2020]. This may result in slight changes in the averaged GPS-VTEC. However, for geostationary (GEO) satellites, the IPPs are nearly stationary. Therefore, before using GPS-VTEC data in the present work, we compared GPS-TEC variations with the GEO-VTEC variations from the same location (Ahmedabad). The GEO-VTEC data used in the present work comes from the Indian Regional Navigation Satellite System (IRNSS) known as NavIC (Navigation with Indian Constellation). IRNSS-NavIC system is described in Chapter-2 and the technique to derive VTEC from NavIC is also discussed there. It has been shown [e.g., *Ayyagari et al.*, 2020] that the NavIC-VTEC and GPS-VTEC are remarkably consistent over the Indian sub-continent in general and the northern EIA crest region in particular. Similar to this work, we have also verified this for the Ahmedabad station. Four geomagnetically quiet days, 01 May 2018, 25, 27 & 28 April 2018, are chosen to compare the VTEC values obtained from GPS and NavIC receivers located at the Physical Research Laboratory, Ahmedabad. NavIC-VTEC is obtained from one of the IRNSS-NavIC satellites named IRNSS-1C (PRN I03 at 83° E). IRNSS-1C is one of the geostationary satellites of NavIC. Figure 4.1 depict the comparison of the IRNSS-VTEC (in red) and GPS-VTEC (in black). It can be noted that the GPS-VTEC and NavIC-VTEC variations are nearly identical. However, the post-sunset VTEC enhancements seen in GPS-VTEC are not so conspicuous in NavIC-VTEC probably because of the larger ray path and smaller magnitudes of the enhancements. The GPS-VTEC values are well within 15% of the NavIC-VTEC values regardless of the local time.

The GPS-VTEC data are grouped into three seasons for 10 consecutive years (November 2009 to October 2019) and compared. To give an example, the data for the year 2009-10 comprise the VTEC data from November 2009 to October 2010, 2010-11 consists of the VTEC data from November 2010 to October 2011 and so

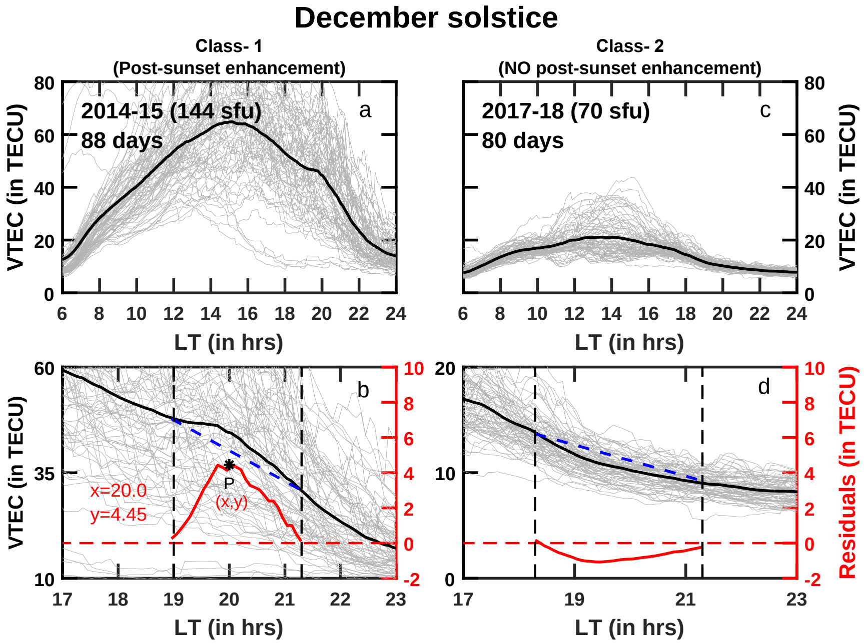

Figure 4.2: Two representative classes of diurnal VTEC variations (a) Class-1: with post-sunset enhancement (December solstice, 2014-2015) and (c) Class-2: without post-sunset enhancement (December solstice, 2017-2018) are shown. The gray curves in a-d are the variations on individual days and the bold black curves represent the average variations. The solar flux levels and the number of days' data used to construct the average curve are also provided in each Figure. VTEC variations during 17-23 LT are blown-up in Figures b and d to show the presence and absence of post-sunset enhancement in VTEC in the average variations. Linear fitting (blue dashed lines) is carried out to extract the residuals (red lines) that reveal the post-sunset enhancement in (b) and post-sunset reduction (d) in VTEC in the average variations. The coordinates of the point P (x,y) in (b) shows the peak VTEC level during the post-sunset enhancement period and the corresponding local time.

on. Further, each year is divided into three seasons - December solstice (November, December, January, and February), Equinox (March and April, September and October), and June solstice (May, June, July, and August). Daily average F10.7 cm solar radio flux is also grouped in the same manner for comparison. In addition, to quantify the relationship between the post-sunset enhancements in VTEC (ΔVTEC) and the solar flux, the ΔVTEC (ΔVTEC is defined in Figure 4.6-a,e) data are also grouped according to the solar flux values ranging from 80-180 sfu (sfu = solar flux unit, 1 sfu = $10^{-22} W m^{-2} Hz^{-1}$) in a bin size of 5 sfu.

It is to be noted here that the bins with less than 10 days' of VTEC data are not considered in the present work. 5 minutes' average VTEC data is used in the present investigation.

In order to identify the post-sunset enhancements in VTEC, two representative classes are chosen and shown in Figure 4.2. Figure 4.2 (a, c) show the local time variations of individual VTEC variations (gray lines) during 06-24 LT in December solstice in the year 2014-15 and 2017-18. In class-1 (2014-15), the post-sunset enhancement in VTEC is observed, and in class-2 (2017-18), it is not. This is diagnosed by the average curve (black, bold line) superimposed on the gray curves, and this average curve is constructed based on the mean of VTEC variations for all the individual days shown in gray lines. The average solar flux levels and the number of days used to construct the average curve are also mentioned in the figures. Even without the aid of any analysis, it can be noted that the post-sunset enhancement in VTEC in the average curve at ∼20 LT is conspicuously identifiable for class-1 and not for class-2. In order to clearly identify the enhancements, the VTEC variations during 17-23 LT are expanded and shown in Figures 4.2 (b, d). In these figures, the linear fitting technique is applied to join the points that mark the start and end of the enhancements as in Figure 4.2b (or negative enhancements/decrease as in Figure 4.2d). The start and end of the linear fits are marked by the vertical dashed lines. The linear fits are shown in dashed blue lines. The residuals obtained by subtracting the blue lines from the black lines are shown by the red curves and the corresponding Y-axis scales are also shown on the right hand side of Figures 4.2 (b, d). Positive residuals suggest the presence of enhancements in VTEC and negative residuals suggest the absence of any enhancement. Note, the first order derivative is used to identify the time of occurrence of the post-sunset enhancement (Figure Figure 3.6 of Chapter-3). However, when it comes to the quantification of the enhancements, the residuals are used as described here. There, the first order derivative is used to find the post-sunset enhancement. The details can be found in Chapter-3. It can be seen that in case of class-1 (Figure 4.2b), the residuals are positive, whereas in the case of class-2 (Figure 4.2d), the residuals are negative. The peak value of the positive residual (enhancement) is marked by a black star and denoted by P(x, y) where x, y denote the abscissa and the ordinates. For example, in case of Figure 4.2b, the peak in the post-sunset enhancement is found to occur at 2000 LT with the magnitude of enhancement of 4.45 TECU. In Figure 4.2 and subsequently, in Figures 4.3-4.5, the coordinate values (x, y) of the peak positive residual are mentioned wherever enhancements are found. It is to be noted here that in some of the earlier works [e.g., *Young et al.*, 1970; *Balan and Rao*, 1984; *Liu et al.*, 2013] related to post-sunset enhancements, exponentially fitted curves are used to extract the post-sunset enhancements in foF2 and VTEC. While the linear fitting may under/over-estimate the post-sunset enhancements to some extent on occasions, the exponential fitting is sensitive to the choice of the initial point from where the fitting starts. This too may lead to under/over-estimations of residuals. Nevertheless, it has been verified that the residuals obtained by both fitting procedures closely match with each other if done carefully. In order to minimize the fitting subjectivity from one curve to another, a linear fitting procedure is adopted in the present work to extract the residuals and to identify the post-sunset enhancements in VTEC.

TIE-GCM outputs

Thermosphere-Ionosphere-Electrodynamics General Circulation Model (TIE-GCM) is used to understand the altitudinal and latitudinal variation of the plasma density and vertical drift over low latitude ionosphere at different solar flux levels. The electron density and vertical drift outputs in the present work are generated for the height range of 100-700 km for the whole globe and simulation results are used according to a requirement in the present study. For model run, the input solar wind magnetic field, velocity and plasma density are taken as 0 nT, 400 $\mathrm{km\,s^{-1}}$ and 4 $\mathrm{cm^{-3}}$ respectively. TIE-GCM outputs are obtained for three seasons - December solstice, Equinox, and June Solstice and at three solar flux levels (100, 130, and 160 sfu) and also obtained at higher solar flux from 170 to 200 sfus in steps of 10 sfu only for December solstice and Equinox. The dates for the model runs are chosen accordingly during 2009-2019.

4.3 Results

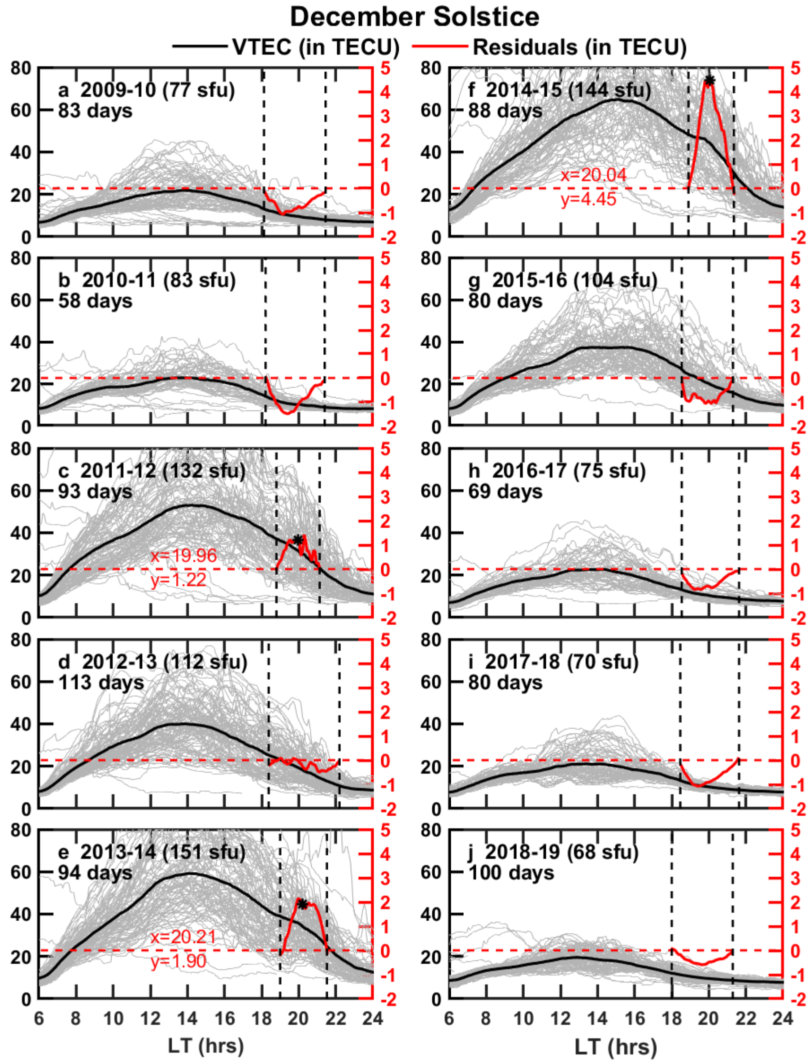

Figure 4.3: VTEC variations on individual days (gray), average variation of VTEC (black) and residuals of average VTEC (red) in December solstice during 2009-10 (a), 2010-11 (b), 2011-12 (c), 2012-13 (d), 2013-14 (e), 2014-15 (f), 2015-16 (g), 2016-17 (h), 2017-18 (i), and 2018-19 (j). The start/end times of the residuals are marked with the vertical dashed lines. The number of days that goes into the calculation of the average VTEC variations and corresponding average solar flux levels are also mentioned for each year. Unambiguous post-sunset enhancements are seen during 2011-2012, 2013-2014 and 2014-2015. In 2012-2013, the residuals start becoming positive.

Figures 4.3 (a-j) depict the daily variations in VTEC (gray lines), mean variation in VTEC (black line) and the residuals (red line), respectively, for consecutive

10 years (2009-2019) during the December solstice in solar cycle 24. Two vertical dashed lines in black color mark the intervals for which the residuals are calculated based on the linear fitting technique as described in Figure 4.2. The number of days to construct the average VTEC, as well as the average solar flux level of those days are provided in each subplot. By following the dashed black vertical lines, one can figure out the occurrence of post-sunset enhancements in VTEC in varying degrees identified by the residuals. It is interesting to note that the residuals have positive values in Figures 4.3c (2011-12, 132 sfu), 4.3e (2013-14, 151 sfu), and 4.3f (2014-15, 144 sfu) only. In these three years, the peak residuals occur at $\sim$ 2000 LT (with an amplitude of 1.22 TECU), $\sim$ 2010 LT (with an amplitude of 1.90 TECU) and $\sim$ 2000 LT (with an amplitude of 4.45 TECU), respectively. On other occasions, either residuals are close to zero/slightly positive (as in 2012-13) or unambiguously negative (the rest of the cases). It is noted that the amplitude of the post-sunset peak in VTEC starts increasing as the solar activity starts increasing in cycle 24 with the exception of 2012-13. The amplitude seems to become maximum in 2014-15 and decreases thereafter. Interestingly, it appears from Figure 4.3 that the amplitude of the post-sunset enhancement in VTEC during December solstice starts to become positive if the solar flux value exceeds at least 112 sfu (as in 2012-13). It is also important to note here that the year 2012-13 and particularly the December solstice of 2012-13 is associated with a number of sudden stratospheric warmings (SSWs) events [e.g., *Nath et al.*, 2016]. Obviously, Figure 4.3d suggests that the amplitudes of VTEC residuals are less during SSWs events. Therefore, for the sake of simplicity, this lower limit of the solar flux level at which the residuals start turning positive is taken at approximately 110 sfu. In the absence of SSW, this solar flux level may lie below 110 sfu but we will neglect this consideration here. It can be found in the ensuing paragraph that the choice of 110 sfu as a lower cut-off is consistent with Equinox also.

While Figure 4.3 shows the variations in December solstice, Figure 4.4 depicts similar variations during Equinox. During this season, the positive values of residuals or the post-sunset enhancements in VTEC are noticed in Figures 4.4b

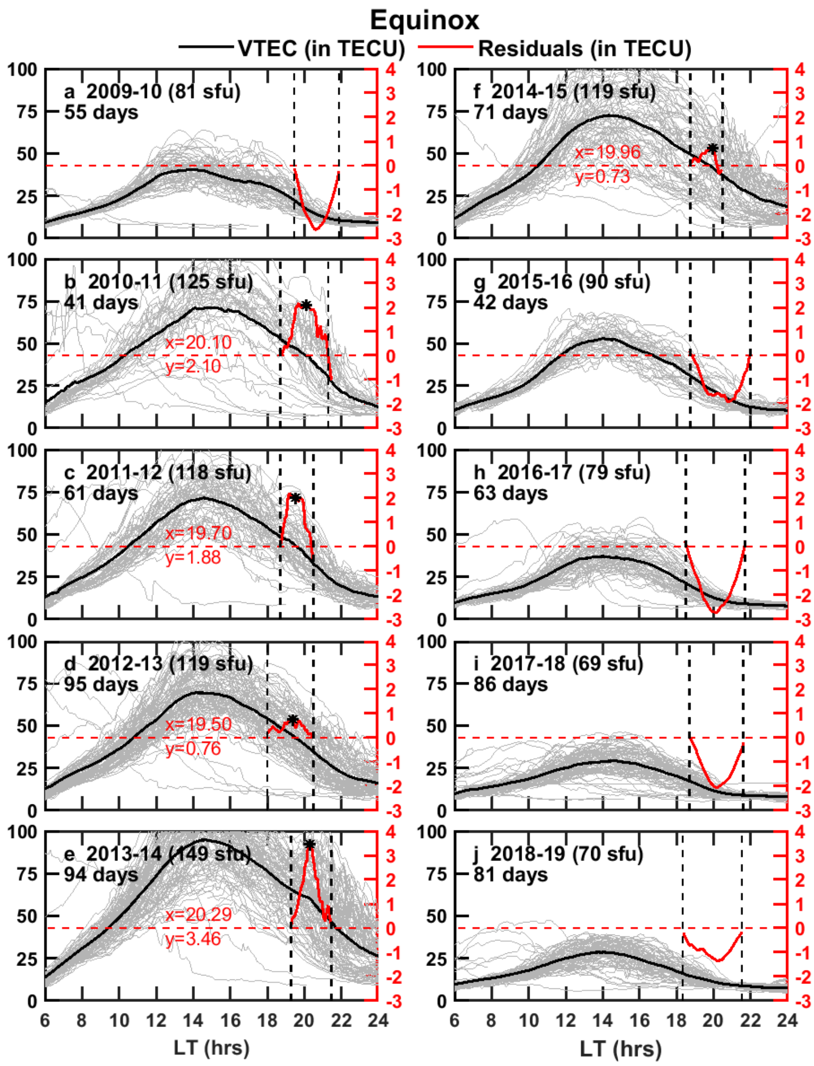

Figure 4.4: Same as Figure 4.3 but for Equinox.

(2010-11, 125 sfu), 4.4c (2011-12, 118 sfu), 4.4d (2012-13, 119 sfu), 4.4e (2013-14, 149 sfu), and 4.4f (2014-15, 119 sfu). The peak residuals occur at ∼ 2006 LT (with an amplitude of 2.10 TECU), ∼ 1940 LT (with an amplitude of 1.88 TECU), ∼ 1930 LT (with an amplitude of 0.70 TECU), ∼ 2020 LT (with an amplitude of 3.46 TECU) and ∼ 2000 LT (with an amplitude of 0.73 TECU), respectively. On other occasions, the residuals are unambiguously negative. The highest solar flux year during Equinox is noted in 2013-14 (Figure 4.4e), and the magnitude of peak residual is also found to be the highest (3.46 TECU) in this year. It is also interesting to note that corresponding to the same solar flux levels noticed in 2012-13 (Figure 4.4d) and 2014-15 (Figure 4.4f), the magnitudes of the peak residuals are also nearly equal. Unlike December solstice, the post-sunset enhancement in VTEC is present in the year 2012-13. Since the residual is unambiguously positive, corresponding to the solar flux level of 119 sfu (2014-2015), and it is negative for the solar flux level of 90 sfu (2015-2016), we assume that the residuals start becoming positive midway between 119 and 90 sfu. This mid solar flux level is $\sim$ 105 sfu. Therefore, for simplicity, it is assumed in this case also that if the solar flux level exceeds 110 sfu (lower cut-off), the residuals will be positive.

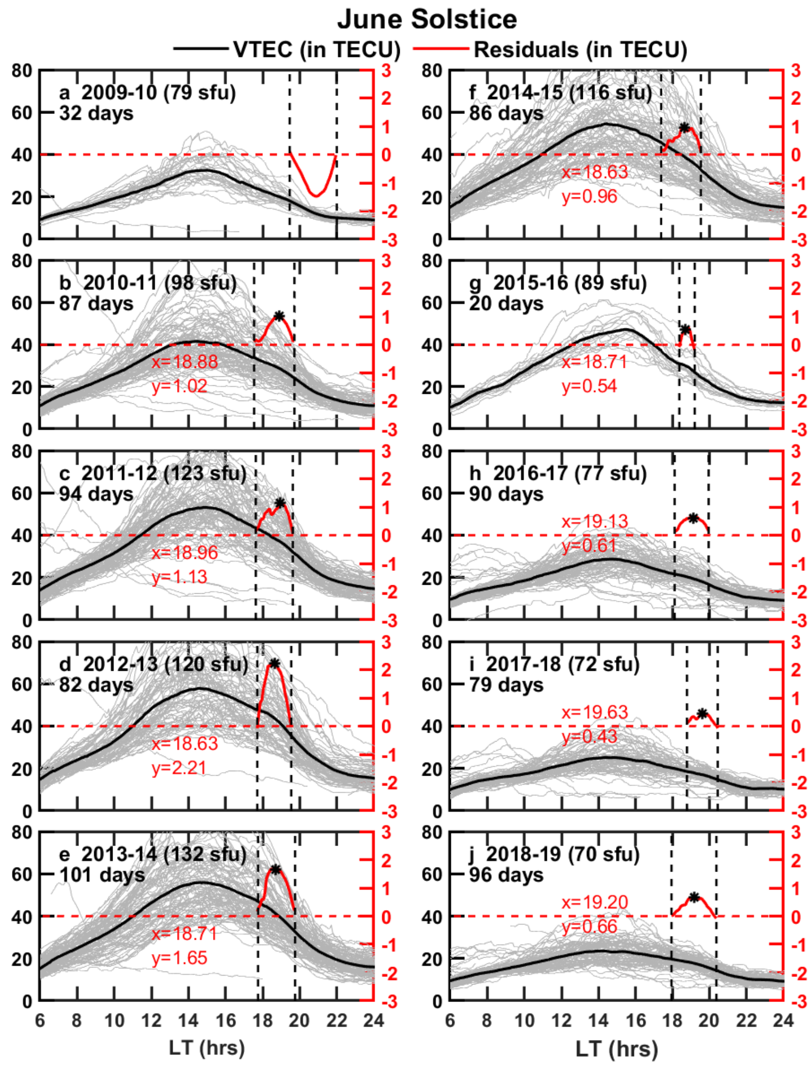

Figure 4.5: Same as Figures 4.3 and4.4 but for June Solstice.

Similar to Figures 4.3 and 4.4, Figure 4.5 also depicts the daily variations in VTEC, mean variation in VTEC and residuals but for June Solstice. In contrast to Figures 4.3 and 4.4, positive residuals are observed in all the years in June solstice except in 2009-10. However, most importantly, the peaks in positive residuals occur mostly around 1900 hrs or before except mainly during 2017-18, when it occurs considerably later than 1900 LT. This is in sharp contrast with the December solstice and Equinox, wherein the peaks in the positive residuals occur mostly $\sim$ at 2000 LT. In fact, negative residuals (not shown here) are obtained during 2000-2100 LT for almost all the years in June solstice. Another noticeable feature is the apparent disconnect of the amplitude of the positive residual with the solar flux levels. For example, in 2012-13, when the solar flux level is 120 sfu, the amplitude of the positive residual is 2.21 TECU, whereas in 2013-2014, when the solar flux level is 132 sfu, the amplitude of the positive residual is 1.65 TECU. Therefore, it appears that the VTEC residuals have little connection with the solar flux levels in June solstice. This aspect is addressed in detail again in Figure 4.6.

Figures 4.3-4.5 bring out the variations in the VTEC residuals with solar activity for three seasons in solar cycle 24 over Ahmedabad. However, since post-sunset enhancements take place for a finite interval, it is necessary to consider the integrated VTEC under the residual curves to quantitatively explore the relationship between the post-sunset enhancement in VTEC and solar flux levels. In other words, the area under the curve of the residual VTEC curve (ΔVTEC) is more important than the peak amplitude of residual VTEC. The area under the curve of VTEC is important because PRE occurs for a finite period. This is done in Figure 4.6 for December solstice, Equinox and June solstice. Figures 4.6a and 4.6b depict the representative local time variation of VTEC for individual days (in gray) as well as average VTEC (black line) with the standard deviations ($\pm 1\sigma$) during Equinox wherein the solar flux levels vary between 146-150 sfu. For the sake of clear representation, $\pm 1\sigma$ variations are shown only at a few points. The upper and lower envelopes of the $\pm 1\sigma$ variations are marked by solid and dashed blue lines. The calculation of integrated VTEC is carried out in two ways and demonstrated in Case-1 (Figure 4.6a) and Case-2 (Figure 4.6b). In Case-1, only the residual area under the curve is considered (marked by the red shaded

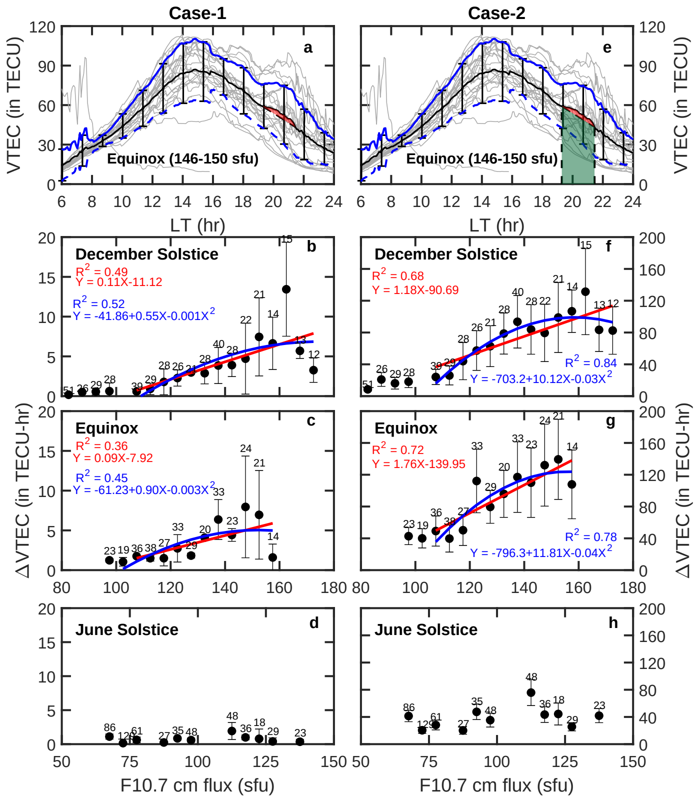

Figure 4.6: Local time variations in VTEC over Ahmedabad, two methods of calculating integrated VTEC and as well as the solar flux dependences of post -sunset enhancements in VTEC are shown. Figure (a and e): The variations during Equinox (gray lines) along with the average VTEC (black line) variation and standard deviations (a few $\pm 1\sigma$ lines are only shown to avoid cluttering) are shown. Integrated VTEC (ΔVTEC) calculated in two different ways during the post-sunset enhancement period. During this period, the solar flux levels vary between 146-150 sfu. The solid and dashed blue lines in Case-1 and Case-2 are the upper and lower envelopes of $\pm 1\sigma$ variations respectively. While in Case-1, only the area under the curve of residual enhancement (shaded by red) is calculated, the total area under the curve of residual enhancement (shaded by red + green in Figure b) is calculated for Case-2. Figure (b-d) and (f-h) show the variations of ΔVTEC (along with the $\pm 1\sigma$ calculated based on the solid and dashed blue curves in Figures a and e) with respect to the binned (in steps of 5) F10.7 cm solar flux levels for three seasons but for Case-1 and Case-2 respectively. Note the X-axis scales for December solstice and Equinox are different from that of June solstice. For both Case-1 and Case-2, the linear fits (red line), parabolic fits (blue lines) as well as the corresponding correlation coefficients (R^2) are shown along with the fitting equations for December solstice and Equinox. Fitting starts from 110 sfu. The ΔVTEC and F10.7 cm solar flux seem to be unrelated for June solstice unlike December solstice and Equinox.

area) and in Case-2, the total area under the curve (red + green shaded area) is considered. Therefore, while in Case-1, only the integrated residual enhancement in VTEC is calculated, the integrated total VTEC enhancement is calculated in Case-2. We term these as integrated residual VTEC (Case-1) and integrated total VTEC (Case-2). It is obvious that Case-2 additionally integrates the background VTEC level over Ahmedabad on which the post-sunset enhancement can be thought to be superimposed. In a similar fashion, the area under the curves is also calculated for the $\pm 1\sigma$ curves marked in red and blue lines in Figures 4.6a and 4.6e. The number of days that goes into the calculation of each point in a particular solar flux bin is mentioned and the $\pm 1\sigma$ values are shown in Figures 4.6 (b-d) and 4.6 (f-h). The unit of ΔVTEC in both cases is TECU-hr.

In Figure 4.6(b-d), ΔVTEC changes as per Case-1 are averaged over 5 sfu bin for December solstice, Equinox and June solstice, respectively, and are plotted against the binned solar flux levels. On the other hand, in Figures 4.6(f-h) the same is done for Case-2. In Figure 4.6(b, c) and 4.6(f, g), the linear and parabolic fits are shown with red and blue lines along with the fitted equations and corresponding R^2 values. Both the linear and parabolic fits start from 110 sfu as the residuals start becoming positive from this solar flux level (stated while describing Figures 4.3 and 4.4). A few important observations can be made based on Figure 4.6 (b, c, f, g) that are listed below.

1. The R^2 values are not significantly different for December solstice and Equinox for both Case-1 and Case-2 and fits (compare 4.6b-4.6c and 4.6f-4.6g).

2. Most importantly, the R^2 values in Case-2 are significantly higher than those in Case-1 during both December solstice and Equinox for both linear and parabolic fits (compare 4.6b-4.6f and 4.6c-4.6g). Therefore, it appears that the background VTEC level, on which the post-sunset enhancement is superposed, is an important factor if one wants to evaluate the correlation between solar flux and post-sunset enhancement (ΔVTEC).

3. Based on R^2 values, it can also be inferred that parabolic fits approximate

the relationship between ΔVTEC and F10.7 cm solar flux in a slightly better way than the linear fits, particularly during December solstice for Case-2 (Figure 4.6f). It is inferred here that integrated VTEC over the crest region has higher dependency on solar flux.

4. The better applicability of parabolic fit during December solstice for the total integrated VTEC (Figure 4.6f) seems to suggest a possible saturation effect at higher solar flux levels.

5. In sharp contrast to December solstice and Equinox, no systematic relationship could be established between ΔVTEC and solar flux levels during June solstice in both cases as seen in Figure 4.6(d, h).

6. The degree of scatter seems to increase as one goes to higher solar flux levels during December solstice and Equinox.

7. Finally, the slope of the linear fit is more for Equinox (slope = 1.76, see Figure 4.6g) than for December solstice (Slope = 1.18, for Figure 4.6f). The correlation coefficient is also higher in Equinox than December solstice.

In order to understand the results obtained in Figure 4.6 from a bigger perspective, TIE-GCM outputs are obtained. These results are shown in Figure 4.7. In this figure, the TIE-GCM outputs are shown for the three seasons (December solstice, Equinox and June solstice), for three different solar flux conditions (100, 130 and 160 sfu) and at five local times (1800, 1900, 2000, 2100 and 2200 hr). This figure is labelled as a matrix consisting of 5 × 3 subplots wherein the December solstice, Equinox and June solstice are represented by a, b and c, respectively. The subplots in the first ($a_{11} - a_{51}$), second ($a_{12} - a_{52}$) and third ($a_{13} - a_{53}$) columns of a particular season represent the temporal evolution of F region plasma density in the geomagnetic latitude (from −30° to +30° N) and altitude (from 100 to 700 km) plane during post-sunset hours. One can note from Figure 4.7 that not only the location of the crest region (identified by the maximum plasma density over latitudes) but also the density over the EIA crest region varies with solar flux, seasons, and local time. In order to calculate the

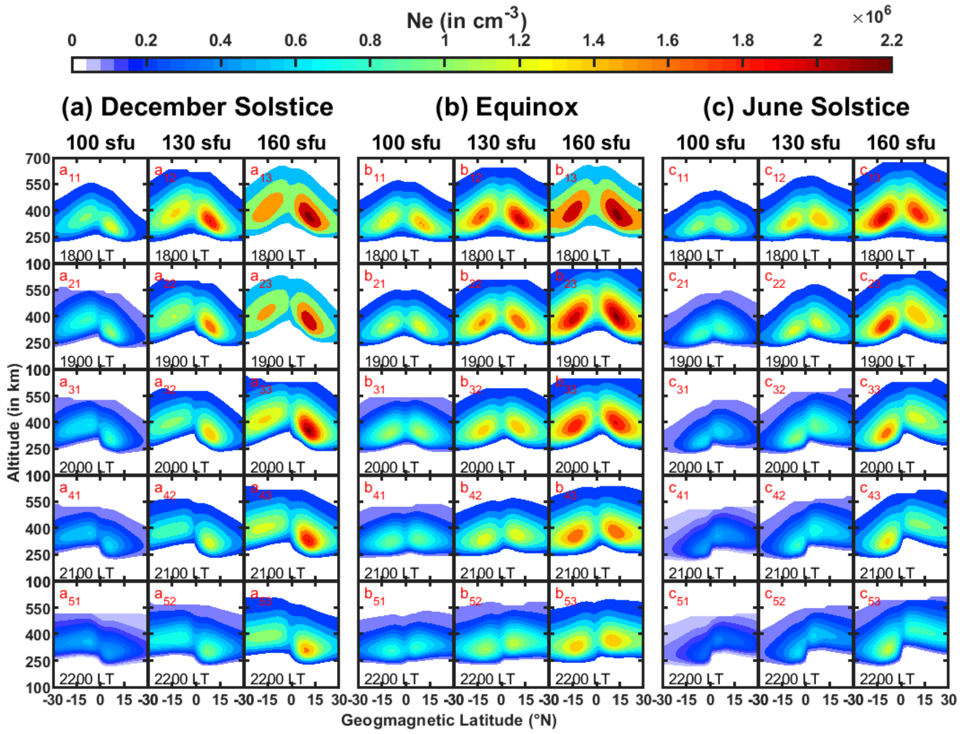

Figure 4.7: (a) Left to right: Electron density variations in the magnetic latitude (from -30° to $+30^{\circ}$) vs altitude (from 100 to 700 km) plane along 75° E longitude in December solstice corresponding to solar flux levels of 100, 130, and 160 sfu. Panels b and c are same as a but for Equinox and June solstice respectively. From top to bottom, the local time increases from 1800 to 2200 LT. A common color scale is used throughout the figure. This figure is generated based on TIE-GCM model outputs.

latitudinal plasma density gradient, the altitude corresponding to the maximum F region plasma density (N^{max}_{crest}) over the EIA crest region is identified. The F region plasma density over the EIA trough region corresponding to the same altitude is taken as N^{min}_{trough}. For the present work, the latitudinal plasma density gradient in the northern hemisphere is considered as the Ahmedabad-TEC measurements are from the northern hemisphere. The latitudinal plasma density gradient is defined here as $(N^{max}_{crest} - N^{min}_{trough})/(Lat_{crest} - Lat_{trough})$ in the unit of $\text{cm}^{-3}\,\text{deg}^{-1}$. Table 4.1 lists the values of the maximum (peak) plasma density over the EIA crest, latitudinal plasma density gradients and the equatorial vertical drift derived from the TIE-GCM outputs for five local times, three solar flux levels and three seasons. Figure 4.7 reveals that the plasma density over the EIA crest region is lower at 100 sfu and as the solar flux level increases, the plasma density over the crest region increases conspicuously (Table 4.1). The density at the trough does not seem to change so significantly with solar flux levels. This leads to a higher crest to trough ratio (CTR) and latitudinal plasma density gradient at higher solar flux levels as confirmed by the values shown in Table 4.1. The latitudinal density gradient is, therefore, highest at 160 sfu. Interestingly, the latitudinal density gradient during December solstice (Figures $a_{13} - a_{53}$) and Equinox (Figures $b_{13} - b_{53}$) are larger than that during June solstice (Figures $c_{13} - c_{53}$). It can also be noted that the plasma densities over the EIA crest region during December solstice and Equinox are either comparable or slightly higher during December solstice. This is why the latitudinal density gradients are found to be higher during the December solstice, as can be noted from Table 4.1.

Based on TIE-GCM outputs, variations in vertical drift is shown within magnetic latitude $-30°$-$+30°$ at five local times 1800, 1900, 2000, 2100 and 2200 local time (from top to bottom in each column) during three seasons December solstice, Equinox and June solstice from left to right columns at 100 sfu in Figure 4.8. Similarly, Figures 4.9 and 4.10 show vertical drift variations at 130 and 160 sfu, respectively. The dip equatorial vertical drift values depicted in Figures 4.8, 4.9 and 4.10 are listed in Table 4.1 at five local times and three solar flux levels for the three seasons as well. It is noted from Figures 4.8, 4.9, and 4.10 that the maximum (more positive) vertical drift associated with PRE occurs at 1900 LT for all three seasons (see panels b, g and f in Figures 4.8, 4.9 and 4.10). This is slightly delayed as one compares this with the observations over the Indian sector [e.g., *Madhav Haridas et al.*, 2015; *Pandey et al.*, 2017] and also with the global empirical model outputs [*Fejer et al.*, 2008a]. It is to be noted that during June solstice, PRE associated vertical drift becomes significantly positive at 160 sfu only. Further, for a given solar flux level, the equatorial vertical drift at 1900 LT during Equinox is more than the corresponding drift during December solstice (see panels b & g in Figures 4.8, 4.9 & 4.10). This is in contrast with the outputs obtained for latitudinal plasma density gradients for these two seasons. Interest-

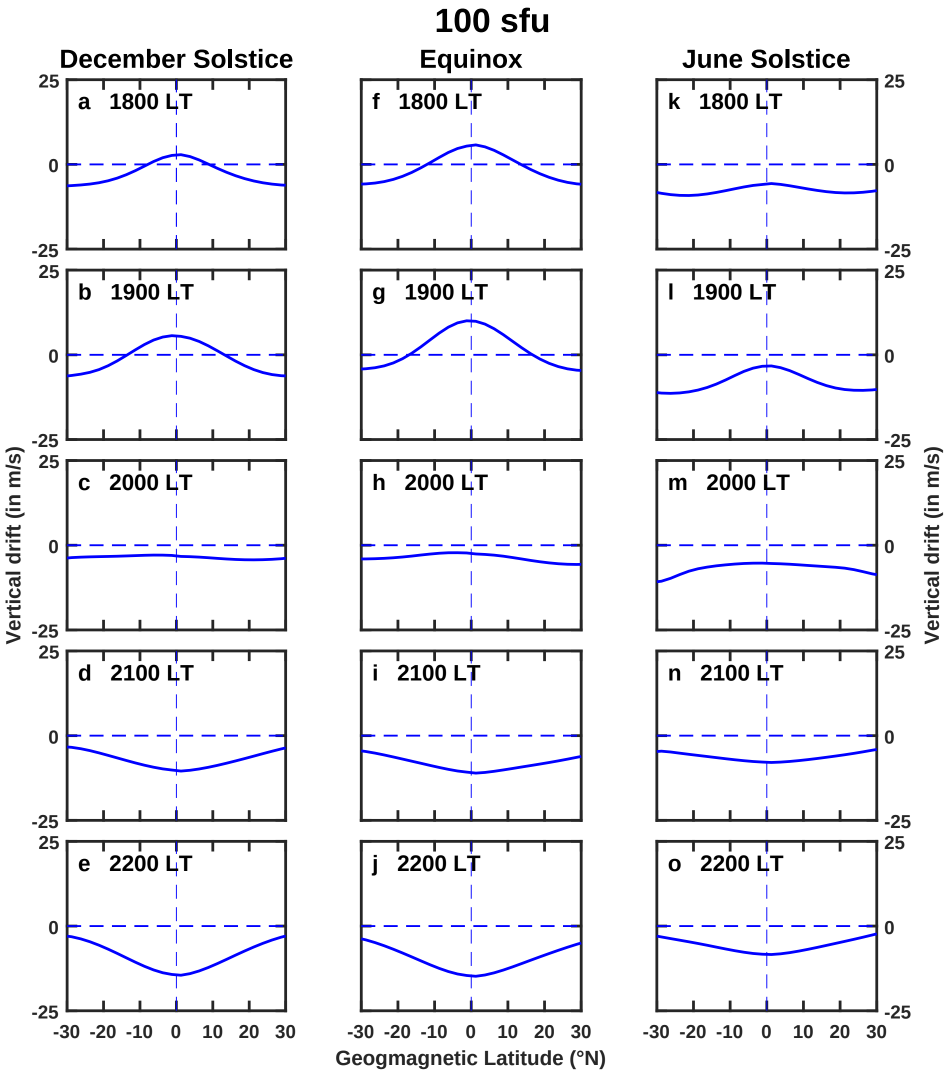

Figure 4.8: Variation in vertical drift with magnetic latitude in December solstice (left panel), Equinox (middle panel) and June solstice (right panel) along 75° E longitude. From top to bottom, the local time increases from 1800 to 2200 LT. This figure is generated based on TIE-GCM model outputs corresponding to 100 sfu.

ingly, both the latitudinal plasma density gradient and equatorial vertical drift are minimum during June solstice. One more point is noted in Figures 4.8-4.10 the dip equatorial vertical drifts become more negative during December solstice and Equinox. This feature can probably help to understand the reverse plasma fountain. However, lest we lose focus, this aspect is not addressed in detail in the present thesis and will be taken up in future work. The implications of these results are discussed in the ensuing section.

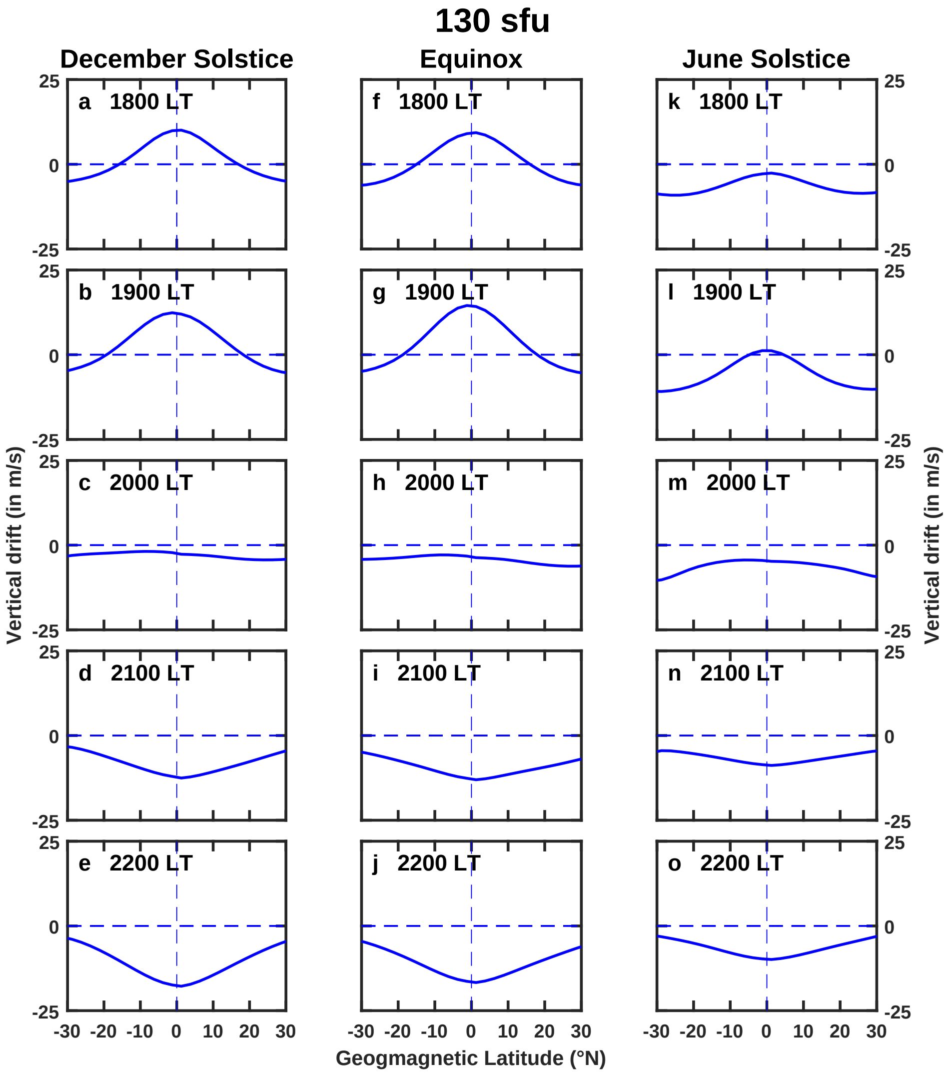

Figure 4.9: Similar to Figure 4.8 but at 130 sfu.

4.4 Discussion

Several researchers [e.g., *Bittencourt et al.*, 2007; *Farelo et al.*, 2002; *Kulkarni*, 1969; *Su et al.*, 1994; *Xiong et al.*, 2016] have previously reported the post-sunset enhancements in the F region plasma density over low latitudes but its causative mechanism is not comprehensively investigated. *Su et al.* [1994] showed the post-sunset enhancement in TEC and suggested the role of PRE. They concluded their results based on TEC observations, only. Further, the work of *Kumar et al.* [2021] confirmed that these enhancements during December solstice and Equinox are driven by the reinvigorated plasma fountain driven by PRE in the post-sunset

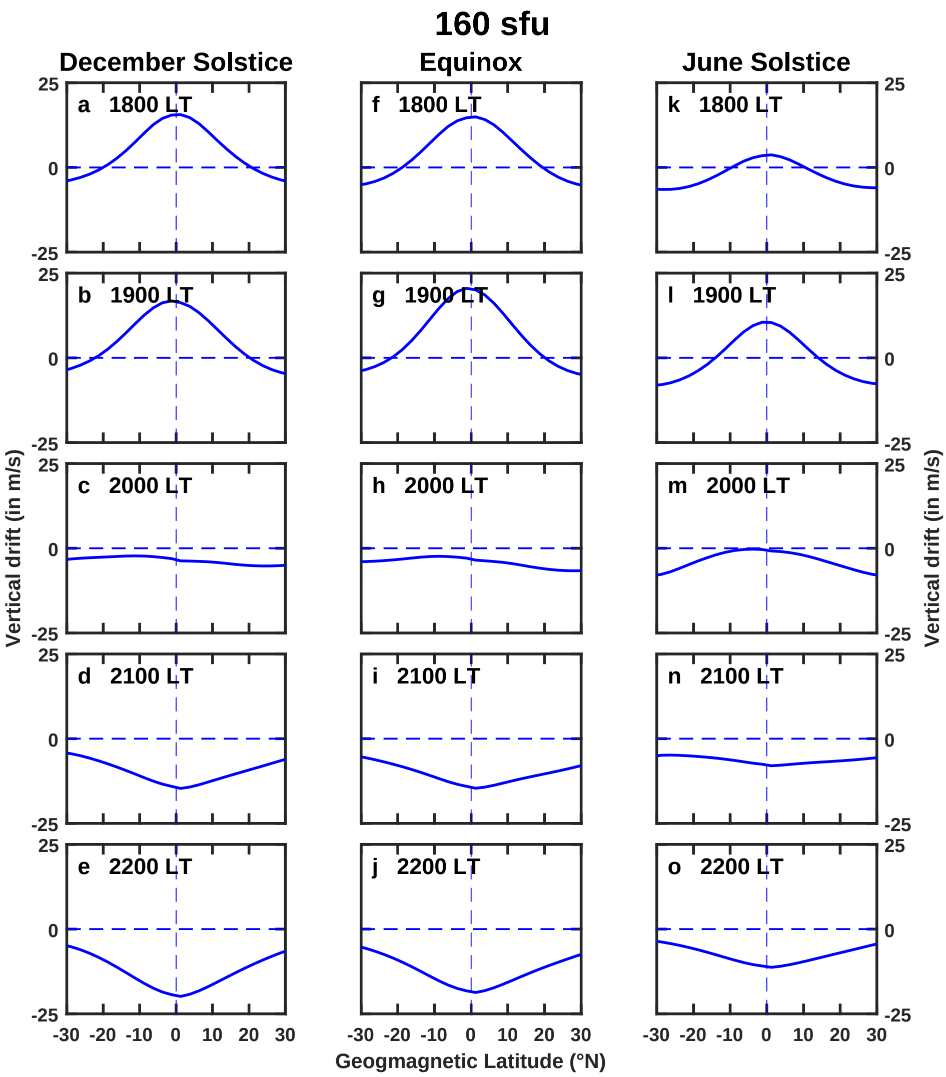

Figure 4.10: Similar to Figures 4.8 and 4.9 but at 160 sfu.

hours using the GPS-TEC, dip equatorial drifts data over near Indian longitudes. The present investigation takes it a step forward by analyzing the year-wise progression of the post-sunset enhancements in solar cycle 24 (2009-2019) and elicits that these enhancements are significant only if the solar flux level exceeds 110 sfu during December solstice and Equinox. Since the post-sunset enhancements are primarily driven by PRE and the amplitude of the PRE depends on solar flux level [e.g., *Fejer et al.*, 1989, 1991, 2008a; *Ramesh and Sastri*, 1995], it can be expected that for a detectable post-sunset enhancement near the EIA crest region, one requires a minimum PRE amplitude or vertical drift over the dip equator. In fact, the work of *Scherliess and Fejer* [1999] suggests that the amplitude of

Table 4.1: Latitudinal plasma gradients in black (in 10^5 cm^{-3} deg^{-1}) and vertical drifts (in m s^{-1}) over the dip equator in blue at 1800, 1900, 2000, 2100 and 2200 LT (top to bottom) in December solstice corresponding to 100, 130 and 160 sfu levels (left to right), as derived from the TIEGCM outputs, are tabulated in the left block. Similar data derived for Equinox and June solstice are provided in middle and right blocks respectively.

	December solstice			Equinox			June solstice		
Local time	**100 sfu**	**130 sfu**	**160 sfu**	**100 sfu**	**130 sfu**	**160 sfu**	**100 sfu**	**130 sfu**	**160 sfu**
	Peak plasma density over the EIA crest in units of 10^6 cm^{-3} Latitudinal density gradients are in units of 10^5 cm^{-3} deg^{-1} and equatorial vertical drifts are in units of m s^{-1}								
1800	1.35 1.0 2.9	2.04 1.3 10.0	2.66 1.6 15.6	1.61 0.8 5.8	2.14 1.1 9.3	2.65 1.4 15.0	1.20 0.4 -5.7	1.59 0.7 -2.6	1.91 0.8 3.7
1900	1.08 0.8 5.7	1.79 1.5 12.4	2.43 1.8 16.8	1.33 0.8 10.0	1.78 1.0 14.5	2.27 1.2 20.5	0.92 0.4 -3.3	1.29 0.6 1.2	1.57 0.7 10.5
2000	0.85 0.8 -3.3	1.6 1.4 -2.7	2.29 1.7 -3.7	1.14 0.6 -2.5	1.55 0.7 -3.7	2.02 1.2 -3.5	0.66 0.2 -5.4	1.01 0.4 -4.8	1.28 0.5 -0.8
2100	0.64 0.4 -10.5	1.33 1.0 -12.5	2.02 1.5 -14.7	0.96 0.6 -11.0	1.35 0.7 -13.0	1.80 1.0 -14.6	0.51 0.3 -8.0	0.80 0.3 -8.8	1.04 0.3 -8.0
2200	0.47 0.3 -14.5	1.01 0.9 -17.8	1.66 1.3 -19.9	0.82 0.4 -14.8	1.17 0.7 -16.7	1.58 0.7 -18.7	0.39 0.3 -8.4	0.62 0.5 -10.0	0.84 0.5 -11.3

PRE is close to zero during June solstice as well as in December solstice and significantly less than the daytime maximum of the zonal electric field at 90 sfu. Therefore, it is understandable that the solar flux needs to exceed a threshold level to make the PRE amplitude large enough to cause post-sunset enhancement near the EIA crest region. Figure 4.11 [taken from *Ramesh and Sastri*, 1995] explored the association of solar flux level and equatorial vertical drift over the Indian sector, and it is noticed manually by scaling that the magnitude of vertical drift is $\sim 16\ ms^{-1}$ during December solstice and Equinox at 110 sfu whereas it is $\sim 10\ ms^{-1}$ for the same solar flux level at the June solstice. Therefore, it implies that the equatorial vertical drift associated with PRE should be at least $\sim 16\ ms^{-1}$ over the Indian sector for detectable post-sunset enhancement of VTEC near the EIA crest region. This explains why even during high solar flux conditions, the post-sunset enhancement in VTEC is not observed over the EIA crest region during June solstice. This is because PRE amplitude during June solstice does not exceed this threshold level on most of the occasions over the Indian sector, even during high solar flux conditions.

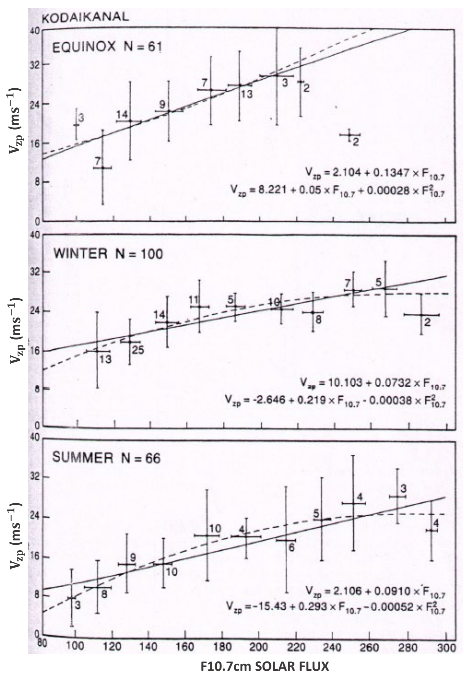

Figure 4.11: Variations in average peak PRE amplitude (in $\mathrm{ms^{-1}}$) over Kodaikanal with average solar flux values during Equinox (top), Winter (middle) and Summer (bottom) [From *Ramesh and Sastri*, 1995]

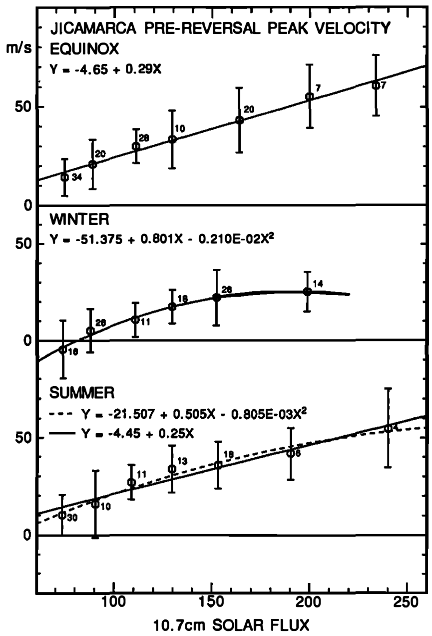

Figure 4.12: variation in average pre-reversal vertical drift with solar flux during Equinox (top), Winter (middle) and Summer (bottom) [From *Fejer et al.*, 1991].

At this stage, one more point needs to be discussed. This is the better applicability of the parabolic fit while constructing the empirical relationship between the F10.7 cm flux and post-sunset enhancement of VTEC near the EIA crest region during the December solstice. As the VTEC enhancements are caused by the PRE, as shown by *Kumar et al.* [2021], it is important to evaluate the variation of PRE with the solar flux levels at different seasons for different levels of solar flux. Using Jicamarca observations, *Fejer et al.* [1989] first indicated that average vertical drifts during winter (May-August for the Southern hemisphere) remain nearly constant beyond a solar flux level. This solar flux level can change with magnetic activity. The indication obtained in this work was consolidated and quantified further in a follow-up work [*Fejer et al.*, 1991] wherein the evening PRE of vertical drifts was shown to increase linearly with the solar flux during Equinox but saturate beyond a high solar flux level during winter. This inference was drawn based on the applicability of linear and parabolic fits [see Figure 4.12, taken from *Fejer et al.*, 1991]. Over the Indian sector, similar results were obtained by *Ramesh and Sastri* [1995] (Figure 4.11). Interestingly, and for the first time, we do see such effects over the EIA crest region when the VTEC enhancements reveal similar seasonal and solar flux behavior (Figure 4.6) like PRE. This puts the cause of these enhancements on a very firm footing, and based on the work of *Kumar et al.* [2021] and this work, it becomes obvious that PRE of the equatorial zonal electric field is responsible for the post-sunset enhancements in VTEC over the EIA crest region. Therefore, as PRE vertical drift tends to saturate during December solstice at higher solar flux levels, VTEC enhancements also tend to saturate, and parabolic fit works better than the linear fit. In this work, we do see saturation effect is kicking in beyond 150-160 sfu over the Indian sector. This solar flux level can change at different magnetic activity levels, as suggested by *Fejer et al.* [1989, 1991]. However, since only the quiet time cases are considered here, we do expect that estimation of the higher cut-off of this solar flux level is relatively robust. Another interesting point is, similar to *Fejer et al.* [1991], we also observe a relatively large degree of scatter at higher solar flux levels (particularly Figures 4.6- b, c) during December solstice and Equinox. As suggested by *Fejer et al.* [1991], this may be due to the large variability of

PRE amplitudes at higher solar flux levels during these two seasons. In addition, the slope of the linear fit (1.76) in Equinox (Figure 4.6g) is significantly higher than that (1.18) during December solstice in Figure 4.6f which is also consistent with the results of *Ramesh and Sastri* [1995], wherein they obtained (see Figure 4.11) higher slope (0.13) in Equinox than December solstice (0.07) for the linear relationships between average peak PRE vertical drift and F10.7 flux for these seasons. These observations strengthen the arguments that PRE plays the primary role in the post-sunset enhancement of VTEC over the EIA crest region. However, the possible saturation effect of PRE of vertical drift during winter remains an unresolved problem until date and further modeling works (beyond the scope of the present work) are needed to understand this enigmatic aspect of PRE in future. It is at this context, the work of *Liu and Chen* [2009] is important who investigated the dependence of TEC with F10.7 cm solar flux and EUV flux. The study revealed that the saturation effects of TEC are seen over low latitudes (over the northern hemisphere) with respect to F10.7 but not with respect to EUV flux, suggesting that F10.7 cm solar flux is not linearly proportional to EUV intensity. The lack of sufficient VTEC data at higher solar flux levels (beyond 160 sfu) prevents us from observationally addressing this feature in detail. It is interesting to note that TIE-GCM outputs capture this saturation effect, particularly during December solstice (Figure 4.13). It is possible that changes in thermospheric neutral composition, neutral wind, background ionospheric electric field, and conductivity during higher solar activity interact with one another in such a way that VTEC gets saturated. Since PRE that drives post-sunset enhancements in VTEC gets saturated [e.g., *Fejer et al.*, 1991] with increasing solar flux level, it is expected that VTEC also gets saturated with the increasing solar flux levels. However, the exact processes that lead to PRE/VTEC saturation need to be understood comprehensively based on further investigation and importantly, through modelling studies. This problem can be addressed with a physics based model like TIE-GCM by generating outputs until 200 sfu solar flux level.

The above discussion suggests that the amplitude of PRE is an important and a necessary factor that determines the post-sunset enhancement in VTEC over the EIA crest region. In this regard, the current work extends arguments of Chapter-3. More importantly, this work takes this argument one step further, and shows that PRE is not a sufficient condition for the degree of post-sunset enhancements over the EIA crest region. One needs to also take in account the background F region plasma distribution over the low latitudes upon which the PRE-driven plasma fountain operates during post-sunset hours and enhance the VTEC during post-sunset hours. This aspect can be guessed from Figure 4.6 wherein the correlation coefficients (for both linear or parabolic fits) are found to increase significantly when background VTEC levels are taken into account while calculating enhancement in VTEC (Figure 4.6f, 4.6g vis-à-vis Figure 4.6b, 4.6c). The background VTEC levels over the EIA crest region during post-sunset hours are decided by the daytime plasma fountain process. The PRE-driven post-sunset plasma fountain acts on the low latitude plasma distribution that has been left behind by the daytime plasma fountain. Figure 4.6 reveals that the correlation coefficients between the post-sunset enhancement (ΔVTEC) and solar flux for Case-2 (total integrated VTEC) are higher during both December solstice and Equinox when compared with the post-sunset enhancements (ΔVTEC) for Case-1 (residual integrated VTEC). It comes out that the higher background ionospheric plasma content around the EIA crest is more likely to give rise to higher post-sunset enhancements in VTEC, except probably during intervals when integrated VTEC gets saturated at higher solar flux levels. But it might not be true on every occasion, for example, at higher solar flux where the saturation is noticed in integrated VTEC (Figure 4.6). *Fejer et al.* [2008a] shows that the vertical drift remains upward throughout the daytime in Equinox and December solstice over the Indian sector. However, around 1600 LT in June solstice, the polarity of vertical drift is reversed at low and moderate solar flux levels [e.g., *Pandey et al.*, 2018] and remains close to zero even at higher solar flux levels [e.g., *Fejer et al.*, 2008a]. Therefore, it is apparent that during June solstice, the plasma fountain process doesn't operate continuously, unlike December solstice and Equinox when EPF supplies plasma to low latitudes until the PRE occurs. On top of that, the amplitude of PRE is significantly more/more during Equinox/December solstice than the daytime maximum amplitude of the zonal electric field in high solar flux condition over the Indian sector. During June solstice, even during high solar flux condition, the amplitude of PRE does not exceed the maximum amplitude of the daytime zonal electric field during quiet periods. Therefore, during Equinox and December solstice, the PRE amplitudes are quite higher or at least equivalent to the daytime zonal electric field during evening hours. Owing to this higher electric field, during post-sunset hours, the plasma fountain operates on already present higher plasma density background over low latitudes generated by the daytime plasma fountain process that, in turn, is driven by the daytime zonal electric field over the dip equatorial region. Therefore, PRE, during these two seasons at higher solar flux levels, can push more plasma to the EIA crest region from the trough region, causing the post-sunset enhancement in VTEC. This explains the higher correlation coefficients between ΔVTEC and solar flux for during both Equinox and December solstice (Figure 4.6b vs. 4.6f and 4.6c vs. 4.6g). However, one aspect stil remains unclear in this discussion. Why is the slope of the linear fit more for Equinox (slope = 1.76, see Figure 4.6g) than for December solstice (Slope = 1.18, for Figure 4.6f)? This suggests that the post-sunset enhancement in VTEC over the crest region changes more rapidly with solar flux levels during Equinox than in December solstice. Interestingly, this feature is consistent with the variations in PRE over the Indian (Figure 4.11) but not over the Jicamarca (Figure 4.12) sectors. This could happen due to the enhanced sensitivity of the electric field amplitudes related to PRE to the changes in the solar flux (possibly through changes in ionospheric conductivity over northern and southern low latitudes) over the Indian sector in Equinox than in December solstice. This proposition is speculative at present and requires a detailed investigation.

In order to verify whether post-sunset enhancements in VTEC are captured by the TIE-GCM outputs, TIE-GCM is also run for the three seasons. These results are shown in Figure 4.13. In Figure 4.13, TEC variations corresponding to 23° N and 23° S along the 75° E meridian are shown for different solar flux levels during December solstice (left), Equinox (middle) and June solstice (right

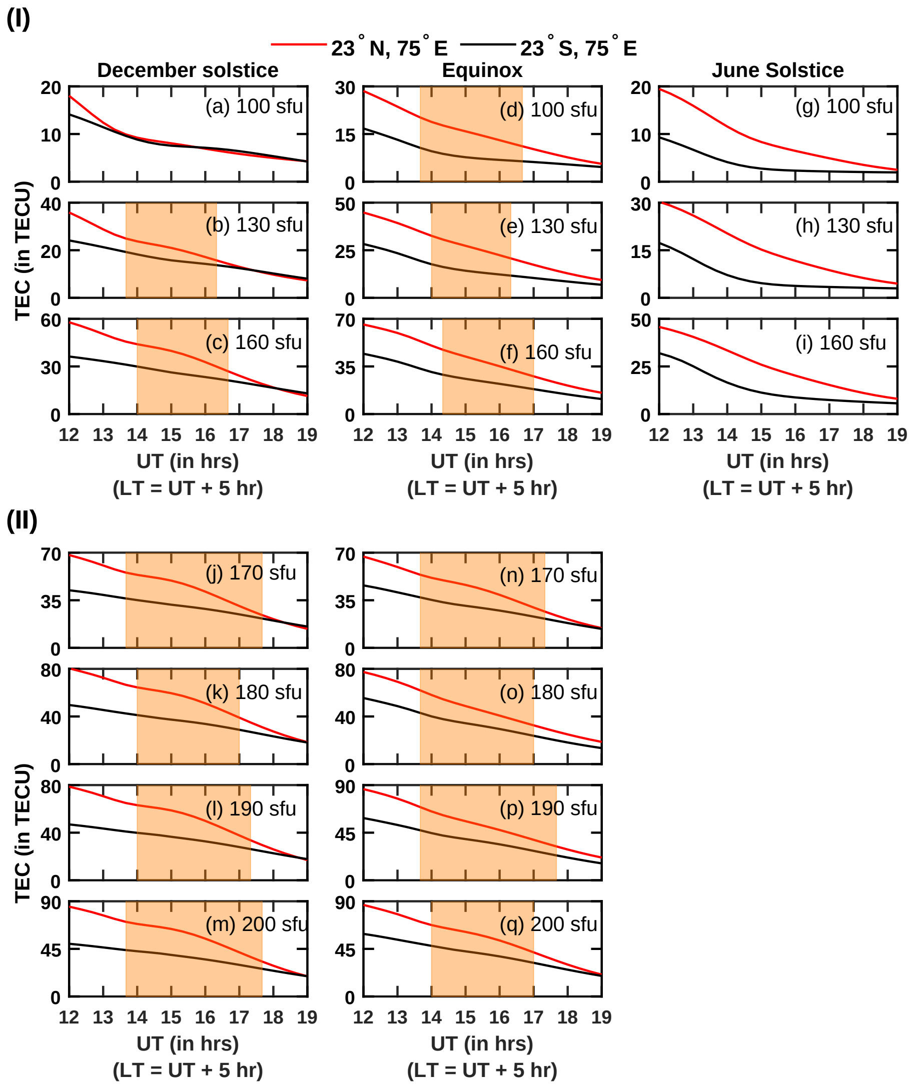

Figure 4.13: (I) TEC variations at 23° N (in red line) and 23° S (in black line) along 75° E meridian is shown at 100, 130 and 160 sfu for the three seasons. (II) Similar variations for 170- 200 sfu in steps of 10 sfu are shown only for December solstice and Equinox. The duration of post-sunset enhancements are marked by orange vertical boxes.

columns). While the outputs corresponding to three seasons are generated for 100, 130 and 160 sfu, shown in section-I, additional runs are made for December solstice and Equinox for 170-200 sfu in steps of 10 sfu, depicted in section-II. These additional runs are made to check the saturation effect during December solstice and Equinox, as noticed in integrated VTEC (Figures 4.6) and PRE amplitudes (Figures 4.11 and 4.12) at high solar flux values. A few interesting features are noted from these outputs.

1. The post-sunset enhancements in TEC are conspicuous in December solstice. This is consistent with the observations reported here.

2. Although the post-sunset enhancements are observationally captured during Equinox, it is not captured by TIEGCM, conspicuously. This is where the observations differ from the model outputs.

3. The post-sunset enhancements are absent in June solstice in accordance with observations.

4. The saturation effect seems to be present in the TIE-GCM outputs and particularly visible during December solstice.

5. Interhemispheric asymmetry is observed during post-sunset hours in VTEC as seen in TIE-GCM output. Observationally, this could not be verified as unavailability of VTEC data from a conjugate station in the southern hemisphere at 75° E meridian (part of Indian ocean). In this situation, the work is carried out by *Wan et al.* [2022] is relevant. They argued that role of wind in generating interhemispheric effects on the diurnal evolution of TEC along 75° E meridian using International GNSS service- total electron content (IGS-TEC) and International reference ionosphere (IRI)-2016 model outputs. Detailed investigations in the future are required to understand a number of aspects regarding the interhemispheric and longitudinal asymmetries of the post-sunset enhancements.

Figures 4.7-4.10 and Table 4.1 capture the values of latitudinal density gradient and equatorial vertical drifts obtained from TIE-GCM outputs which are related to the post-sunset plasma density enhancement over the EIA crest region at different seasons and solar flux levels. It has been shown in Chapter-3 that the plasma gets transported in the meridional direction during the post-sunset hours from $5° - 10°$ magnetic latitudes to the EIA crest region under the influence of PRE associated plasma fountain process. Table 4.1 suggests that PRE amplitudes at 1900 LT are greater in Equinox than in December solstice. In fact, the works of *Scherliess and Fejer* [1999] and *Fejer et al.* [2008a] reveal that the amplitude of PRE during Equinox is more than that in December solstice. Therefore, the TIE-GCM outputs are consistent with the earlier observations in this regard. More importantly, Figure 4.7 and Table 4.1 (TIE-GCM outputs) also reveal that the latitudinal plasma density gradient shows contrasting features. It is noticed that these density gradients are more during December solstice than Equinox over the northern hemisphere in TIE-GCM. Since the latitudinal plasma density gradient is higher at 1900 LT in December solstice in high solar flux conditions (at 160 sfu), the peak plasma density is also higher despite the equatorial vertical drift being less in December solstice compared to Equinox. Considering ionospheric plasma as an incompressible fluid and neglecting the production and loss processes, one can see from the continuity equation that the rate of change of plasma density over low latitudes depends on the $\mathbf{V}.\nabla\mathbf{N}$ term where $\mathbf{V}$ is the velocity and $\nabla\mathbf{N}$ is the plasma density gradient. It is obvious from this term that the rate of change of plasma density over low latitude depends on the amplitude of PRE (upward velocity) during post-sunset hours as well as the latitudinal plasma density gradients. Therefore, it seems that although PRE amplitude is important, it may not be a sufficient condition to determine the post-sunset enhancement in VTEC over the EIA crest region. In fact, PRE amplitude and latitudinal plasma density gradient can be expected to work in tandem to decide the degree of post-sunset enhancement in VTEC over the EIA crest region. This proposition gets support from the fact that both PRE-associated vertical drift amplitudes and F region latitudinal plasma density gradients are much smaller in June solstice compared to Equinox and December solstice, and hence it is not surprising that the post-sunset enhancement in VTEC over the EIA crest region can not be observed during this season. It is also important to keep in mind here that the latitudinal plasma density gradient during evening hours over low latitudes is primarily a resultant of daytime equatorial plasma fountain upon which PRE-driven fountain acts. Hence, the VTEC enhancement over the EIA crest region due to the PRE-driven fountain is dependent not only on PRE amplitude but also on the F region latitudinal plasma density gradient left behind by the daytime plasma fountain process. Therefore, the daytime fountain also plays an important role in determining the degree of post-sunset enhancement in VTEC over the EIA crest region.

Interestingly, in the present work, the anomalous feature in post-sunset VTEC is noticed 2012-13 that is not consistent with the rest of the observations. At higher solar flux (slightly higher than 110 sfu) in December solstice of 2012-13, the post-sunset enhancements in VTEC are found to be absent. However, it is known from the work of *de Paula et al.* [2015] and *Nath et al.* [2016] that the December solstice of the year 2012-2013 is characterized by intense and multiple sudden stratospheric warming (SSW) events. It is also known that SSW event modulates the semi-diurnal and lunar tides that, in turn, affect the E-region electric field dynamo mechanism that generates the primary electric field in the ionosphere [e.g., *Pedatella et al.*, 2014; *Chau et al.*, 2012; *Goncharenko et al.*, 2010a]. As the low latitude E region electric field gets affected, the dip equatorial F region electric field also gets affected. It is because low latitude E region electric field is communicated to the dip-equatorial F region heights through geomagnetic field lines. As a result of this, the equatorial plasma fountain in the F region is modified. During and after SSW events, large variability in F region plasma has been noted at local noon as well as in evening hours [e.g., *Chau et al.*, 2012; *Liu et al.*, 2011a; *Goncharenko et al.*, 2010a]. *Goncharenko et al.* [2010b] found an intensification and weakening in the zonal electric field during a SSW event in the morning and evening hours, respectively. The weakening of the zonal electric field during SSW events in the local evening hours is consistent with the lack of post-sunset VTEC enhancement that we report here during December solstice in 2012-2013. *de Paula et al.* [2015] studied three major SSW events in the year 2013 and noticed that PRE-associated vertical drifts were consistently magnitudes smaller than their counterparts in the pre-SSW days. *Liu et al.* [2011a] showed the occurrence of strong counter electrojet in the afternoon hours during an SSW event. *Vineeth et al.* [2009] also reported the occurrences of counter electrojet (CEJ) with a quasi 16-day periodicity over Trivandrum, an Indian dip-equatorial station, during the polar SSW events. It is obvious that once the electric field gets reversed during CEJ events, the F region plasma fountain gets weakened and the equatorial F region plasma does not reach near the vicinity of the EIA crest region like Ahmedabad. Under this circumstance, the additional plasma would not be transported by the PRE of the zonal electric field to the EIA crest region, that leads to the weakening of the post-sunset enhancement of VTEC over the crest region. Therefore, during an SSW event, both PRE as well as the latitudinal plasma density gradient can be affected. It has been discussed that both these factors determine the post-sunset enhancement in VTEC over the EIA crest region. The absence of post-sunset enhancements in VTEC during December solstice during 2012-13 is, therefore, attributed to the recurrent occurrence of SSW events.

4.5 Summary

The present chapter can be summarised in the form of the following points.

1. The post-sunset enhancement in VTEC over the EIA crest region are solar flux dependent as the amplitude of PRE of the zonal electric field also depends on solar flux level.

2. As it is noticed that post-sunset VTEC enhancements are consistent with the PRE-amplitude, significant VTEC enhancements are conspicuously, observed over the EIA crest region during December solstice and Equinox and not in June solstice. These arguments are supported by Figures 4.6, 4.8-4.10, 4.11 and 4.13.

3. Figures 4.3-4.5 suggests that the post-sunset enhancements in VTEC can be observed in Equinox and December solstice when solar flux level exceeds $\sim$ 110 sfu. It is suggested that over Indian longitude, minimum equatorial vertical drift during PRE-hours needs to reach at least 16 $\mathrm{m\,s^{-1}}$ (obtained from Figure 4.11) so as to generate conspicuous post-sunset enhancement in VTEC near the EIA crest region.

4. Integrated VTEC variations with solar flux levels (Figure 4.6) show that VTEC near the EIA crest region becomes saturated at higher solar flux levels (>160 sfu).

5. TIE-GCM simulations confirm the presence of clear enhancement in VTEC during post-sunset hours, particularly during December solstice. Similar to observations, TIE-GCM outputs also show the absence of enhancement in TEC during June solstice. However, TIE-GCM efficiently captures enhancements well during December solstice but not in Equinox. TIE-GCM outputs also bring out the clear interhemispheric asymmetry in TEC enhancements during post-sunset hours. Interestingly, TIE-GCM outputs also confirm the TEC saturation effect during December solstice.

6. It is suggested that the amplitude of PRE is a necessary but not sufficient condition for the post-sunset enhancements in VTEC. This proposition gets support from the TIE-GCM simulation outputs (Figures 4.7-4.10 and table 4.1). This shows that the latitudinal gradient in the F region plasma density over low latitude plays an additional important role to determine the amplitude of post-sunset enhancement in VTEC over the EIA crest region. While the amplitudes of PRE are larger at 1900 LT during Equinox, the latitudinal plasma density gradient is higher at 1900 LT during December solstice. It is concluded that the combined effects of vertical drift and latitudinal plasma density gradient determine the degree of post-sunset enhancement during December solstice and Equinox. Importantly, both these parameters are significantly weaker during June solstice and this is why post-sunset enhancement over the crest region doesn't occur during June solstice at 2000-2100 LT.

7. It is proposed that the daytime plasma fountain plays an important role in determining the latitudinal plasma density gradient during post-sunset hours over low latitudes. PRE-driven plasma fountain during post-sunset hours operates on this latitudinal plasma density gradient and determine the degree of VTEC enhancement over the EIA crest region.

8. It is suggested that Sudden stratospheric events suppress the post-sunset enhancements in VTEC by reducing the electric field over the dip equator.

Chapter 5

Space weather induced perturbation electric fields during post-sunset hours

Excerpts

In the previous chapters, the variations in dip equatorial vertical drifts over Indian sectors are investigated during quiet space weather conditions. It is found that the large amplitude of vertical drifts associated with PRE affects the low latitudes plasma distribution. Since the amplitude and polarity of vertical drifts can get affected by space weather induced electric field perturbations, one can investigate the impact of these perturbations on the low latitude ionospheric plasma distribution. Although the response of equatorial and low latitude ionosphere has been investigated in the past corresponding to various space weather events, complex and anomalous (that deviates from the conventional paradigm) electric field perturbations associated with space weather events make the response over low latitude complex. Therefore, understanding complex and anomalous electric field perturbations over the equatorial ionosphere is important in general and particularly so during PRE hours. This is because low latitude ionosphere during post-sunset hours is susceptible for the generation of F-region plasma irregularities that can affect communication and navigational applications. In this chapter, a weak geomagnetic storm (Ap = 15) on 24 December 2014 is studied to understand dip equatorial electric field perturbations. The investigation reveals that penetration electric field amplitudes can be more even when magnitude of IEFy is less and vice-versa. It is shown that IMF By and substorm play important roles in making the impact of penetration electric field during post-sunset hours complex and anomalous. The effects of these anomalous electric field perturbations over low latitude ionosphere are also brought out.

5.1 Introduction

The F region vertical drifts are upward/downward in daytime/nighttime during geomagnetically quiet periods [e.g. *Fejer et al.*, 2008a]. However, the equatorial F region vertical drifts can be enhanced or reduced under the influence of space weather related perturbation electric fields. It is known that the southward directed IMF Bz drives a geomagnetic storm and during a storm, the east-west component of solar wind/interplanetary motional electric field (IEFy) maps down to the polar ionosphere. This electric field drives a two-cell ionospheric plasma convection pattern or Disturbance Polar type 2 or DP2 cells [e.g., *Nishida*, 1968]. During this period, region 1 Field aligned current (R1 FAC) develops rapidly, and region 2 field-aligned current (R2 FAC) takes time to develop as it is sluggish in nature compared to R1 FAC. Owing to the different time constants of R1 and R2 FACs, the convection electric field perturbations penetrate to low latitude ionosphere through the polar ionosphere. This is known as prompt penetration (PP) electric field. In an equivalent description, this happens under undershielding condition when the shielding electric field in the inner magnetosphere is not fully developed in response to the convection electric field imposed at the outer magnetosphere. Earlier studies [e.g. *Fejer et al.*, 2008b] reveal that PP electric field generates eastward/westward electric field perturbations in the equatorial ionosphere during daytime/nighttime. On the contrary, when IMF Bz suddenly turns northward from southward condition, R1 FAC decays quickly compared to R2 FAC, and the residual shielding electric field survives in the inner magnetosphere for some time. It is this residual electric field that has the opposite polarity of the PP electric field [e.g. *Kikuchi et al.*, 2008]. This is known as the overshielding effect and the electric field perturbations experienced in the inner magnetosphere/ionosphere during this time is commonly termed as overshielding (OS) electric field. The impact of PP electric field over low and equatorial ionosphere has been reported observationally [e.g. *Chakrabarty et al.*, 2005, 2008; *Tsurutani et al.*, 2008] and studied through simulation [e.g. *Wang et al.*, 2008; *Lu et al.*, 2012]. The modeling [e.g. *Nopper Jr. and Carovillano*, 1978] and observational [e.g. *Fejer et al.*, 2008b] studies also suggest that the eastward perturbations of PP electric field is expected until 2200 LT. Further, it is also shown that 6-9% of IEFy penetrates to the equatorial/low latitude ionosphere [e.g. *Kelley et al.*, 2003; *Huang et al.*, 2007]. Significantly large PP electric field can change the plasma distribution over low latitudes during daytime and post-sunset hours [e.g. *Tsurutani et al.*, 2008; *Balan et al.*, 2009, 2018; *Abdu et al.*, 2018; *Rout et al.*, 2019] substantially and can shift the location and strength of the equatorial ionization anomaly (EIA) crest.

In addition to storms, magnetospheric susbtorms can also generate transient electric field disturbances [e.g. *Kikuchi et al.*, 2000, 2003; *Huang et al.*, 2004; *Huang*, 2009; *Chakrabarty et al.*, 2008, 2010; *Fejer et al.*, 2021] over low latitude ionosphere. During the re-organization of the magnetic flux, the energy is stored in in the magnetotail. This energy releases to the antisunward direction. Substorms can be directly triggered by the changes in the solar wind parameters like IMF Bz flipping from southward to northward suddenly, abrupt changes in the solar wind dynamic pressure etc. [e.g. *McPherron*, 1979; *Lyons*, 1995, 1996; *Lyons et al.*, 1997] or can be spontaneously triggered [e.g. *Angelopoulos et al.*, 1996; *Henderson et al.*, 1996] wherein clear solar wind triggering is not obvious. The spontaneously triggered substorms are believed to be triggered by internal magnetospheric processes or by the self organized criticality [e.g. *Baker et al.*, 1997; *Klimas et al.*, 2000; *Tsurutani et al.*, 2004] of the plasma sheet. Substorms are nightside, longitudinally confined phenomena. Although the substorm-induced electric fields are experienced over low latitude ionosphere during nighttime [e.g., *Chakrabarty et al.*, 2015], the dayside electric field perturbations in the low latitude ionosphere due to substorms are also not uncommon [e.g., *Kikuchi et al.*, 2003; *Huang*, 2009; *Hashimoto et al.*, 2017; *Wang et al.*, 2019]. Moreover, substorms can exert both eastward [e.g., *Huang*, 2009; *Chakrabarty et al.*, 2010; *Hui et al.*, 2017] and westward [e.g., *Kikuchi et al.*, 2003; *Chakrabarty et al.*, 2015; *Hashimoto et al.*, 2017; *Hui et al.*, 2017] electric field perturbations over low latitude ionosphere. Therefore, the simultaneous presence of substorms can augment or annul the prompt electric field perturbations arising out of undershielding/overshielding effects, as shown in a few earlier studies [e.g., *Hui et al.*, 2017; *Rout et al.*, 2019]. In addition to the above processes, sudden changes in the solar wind dynamic pressure can also lead to changes in the Chapman Ferraro current and cause prompt electric field disturbances [e.g., *Sastri et al.*, 1993; *Huang et al.*, 2008] over equatorial ionosphere. In recent times, it is also unambiguously brought out that the effects of IMF By can also change the expected polarity of electric field perturbation [e.g., *Chakrabarty et al.*, 2017] over equatorial ionosphere, particularly during the post-sunset hours.

Therefore, under disturbed space weather conditions, some of the prompt electric field disturbances can occur simultaneously and can reinforce/annul individual effects making the phenomenological understanding of the equatorial impact difficult [e.g., *Chakrabarty et al.*, 2015; *Hui et al.*, 2017; *Rout et al.*, 2019]. In addition, these prompt electric field perturbations can also compete with the delayed electric field perturbations owing to what is known as disturbance dynamo mechanism [e.g., *Blanc and Richmond*, 1980] associated with the altered circulations of thermospheric wind systems following storm/substorm. Therefore, understanding the origin of prompt electric field perturbations over low-equatorial ionosphere deserves a more rigorous approach. The present investigation is important as it brings out such a case and shows that understanding of the phenomenological origin of the PP electric field perturbations over the low latitude ionosphere is more complex than what is believed.

5.2 Dataset

1-minute cadence data of the solar wind parameters like interplanetary magnetic field (IMF), solar wind velocity, dynamic pressure and density are obtained from the space physics data facility (SPDF) of Goddard Space Flight Center (https://cdaweb.gsfc.nasa.gov/). It is to be noted that the solar wind data available at this site are already time-shifted to the nose of the bow shock. In order to evaluate the ionospheric impacts, the magnetosheath and Alfven transit times are calculated and added to the lag time, point by point, following the methodology reported in *Chakrabarty et al.* [2005]. In addition, the auroral electrojet (AE) index and polar cap (PC) index are also taken from SPDF.

In the absence of incoherent scatter radar over the Indian sector, the night-time F region vertical drift over the Indian dip equator is derived by taking the temporal derivative of the bottom-side F layer height ($h'F$) from the Canadian advanced digital ionosonde (CADI) over Tirunelveli (8.7°N, 77.7°E, dip angle: 1.7°) as derived in Chapter-3. In addition, the recombination corrected drift is used in this chapter whenever the $h'F$ values are below 300 km. *Bittencourt and Abdu* [1981] suggested that below 300 km altitude, the recombination process can also introduce an apparent upward drift. Therefore, in order to obtain the actual electrodynamical vertical drift, the apparent upward drift due to chemical recombination needs to be corrected. βH values are subtracted from $dh'F/dt$ to get the corrected vertical drift where β and H are the attachment coefficient and the scale height of plasma, respectively. β is calculated by the following formula, $\beta = K_1[O_2] + K_2[N_2]$. Where K_1, K_2 and $[O_2]$, $[N_2]$ are the reaction rate coefficients and molecular density of oxygen, nitrogen, respectively. H is calculated by the following formula $\frac{1}{H} = \frac{1}{n}\frac{\partial n}{\partial h}$, where n and h are the plasma density and height from the earth's surface. The parameters K_1 and K_2 are taken from *Anderson and Rusch* [1980]. The neutral parameters, e.g., molecular densities and thermospheric temperature, are taken from the NRLMSIS 2.0 [*Emmert et al.*, 2021]. For the present investigation, the typical scale height is calculated corresponding to 2100 LT on a quiet (28 November 2014) and the event day (24 December 2014) to calculate the recombination-corrected vertical drifts wherever applicable. Typical

β is also calculated at 2100 LT (from 100 to 600 km in steps of 5 km). The typical uncertainty in the drifts derived based on ionosonde measurements is of the order of 10% [e.g., *Woodman et al.*, 2006].

In order to get an idea about the daytime ionospheric electric field behaviour, the equatorial electrojet (EEJ) strength is derived over both the Indian and Peruvian sectors. The derivation of EEJ is described in Chapter-2 and the EEJ over the Indian sector is derived by using the magnetometer measurements over Tirunelveli and Alibag in Chapter-3. The EEJ strength over the Peruvian sector is, in general, derived by taking magnetometer data over the equatorial station, e.g., Jicamarca (JIC, 11.5°S, 76.5°W, dip angle: 1.0°), and off-equatorial station, Piura (PIU, 5.2°S, 80.6°W, dip angle: 12.5°) [e.g., *Rastogi and Klobuchar*, 1990]. As the magnetometer data over Piura is not available during the event under consideration here, data from another off- equatorial station, Leticia (LET, 4.2°S, 70.0°W, dip angle: 12.6°) is used in place of Piura. The local time of Leticia is also appropriately corrected to take into account the longitudinal difference between Jicamarca and Leticia, and the resultant EEJ strength corresponds to the local time of Jicamarca. 1-minute cadence data of both magnetometer stations are used to derive EEJ strength over the Peruvian sector by the following formula, $H_{EEJ} = \Delta H_{JIC} - \Delta H_{LET}$.

Magnetometer data from a set of nearly antipodal stations (nearly 12 hours difference in the local time of the given set of stations with nearly similar latitudes) along the Indian and Peruvian longitudes are also used in this work to understand the variations of DP2 currents over the two sectors. This is done following the methodology suggested in *Chakrabarty et al.* [2017]. In this work, the important role of this approach in identifying the role of IMF By is pointed out. During the event under consideration, India is in the post-sunset/pre-midnight sector, while Peru is in the morning sector. The northward component of magnetic field, ΔX (ΔX is the instantaneous value corrected for the quiet nighttime base values), for stations is obtained from the SuperMAG worldwide network (`https://supermag.jhuapl.edu/`). For the present work, magnetometer stations along Indian (145°E-177°E) and Jicamarca (3°W-20°W) longitudes are

Novosibirsk (NVS, 45.8°N, 159.9° E) and Ottawa (OTT, 54.9°N, 3.8°W); Irkutsk (IRT, 42.4°N, 177.4°E) and Fredericksburg (FRD, 47.8°N, 5.8°W); Alma Ata (AAA, 34.5°N, 153.1°E) and Bay St Louis (BSL, 39.4°N, 18.9°W); Tirunelveli (TIR, 0.18°N, 150.7°E) and Huancayo (HUA, 2.2°S, 2.6°W) as well as Alibag (ABG, 10.4°N, 146.8°E). 1-minute cadence data are used for all the stations.

Since the present investigation requires identification of the substorm-induced electric field perturbations over the low/equatorial ionosphere, it is important to identify the occurrence of dispersionless injection of energetic particles (electrons and protons) at the geosynchronous orbit [e.g., *Reeves et al.*, 2003]. The electron and proton flux data from Los Alamos National Laboratory (LANL) -01A, 02A, 04A, 97A, 080, and 084 geosynchronous satellites, and electron flux data from Geostationary Operational Environmental Satellite System (GOES)-13 are used for the present study. The data are taken from all LANL and GOES-13 satellites for the event day from 1200 to 1900 UT (universal time).

To understand the low latitude plasma distribution over the Indian sector, and the approximate location of the EIA crest and its strength, the measurements of total electron content (TEC) by the Indian Satellite-based Augmentation System (SBAS) is used. The structure of the data is described in Chapter-2.

In addition, OI 630.0 nm airglow intensity over Mt. Abu (24.6°N, 72.7°E, dip angle: 38.0°) and vertical total electron content (VTEC) data over Ahmedabad (23.0°N, 72.6°E, dip angle: 35.2°) is also used in the present investigation. The airglow intensity and VTEC data are based on the measurements by the narrow band narrow field of view airglow photometer and GPS receiver (GISTM GSV4004B) mentioned earlier. Both airglow photometer and GPS receiver are described in Chapter-2. 10 sec cadence of airglow intensity data and 5 minutes' average VTEC data are used in the present investigation.

5.3 Results

Figure 5.1 depicts the variations of a few interplanetary (Figures 5.1a-d) and ground-based parameters (Figures 5.1e-f) from 21 to 25 December 2014. The

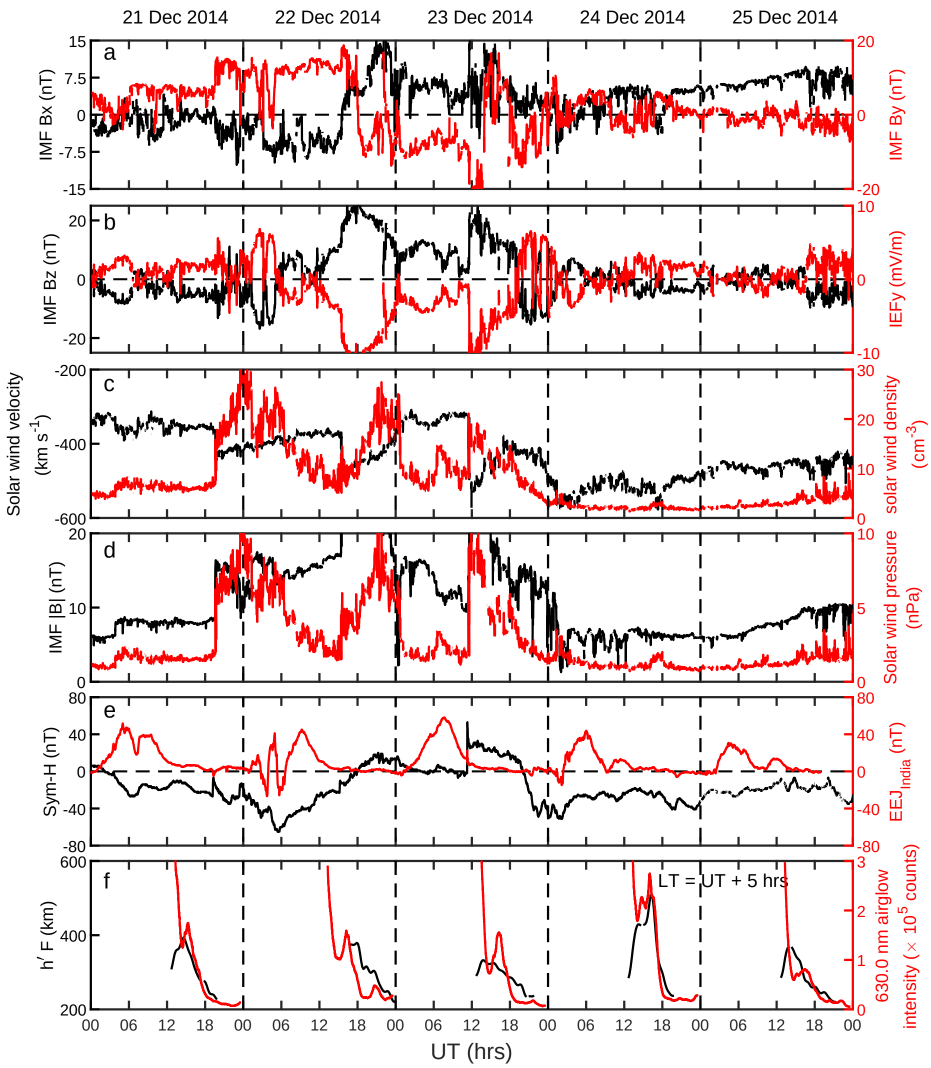

Figure 5.1: Variations in (a) IMF Bx (nT, black line) and IMF By (nT, red line), (b) IMF Bz (nT, black line) and IEFy (mV/m, red line), (c) solar wind velocity ($\mathrm{km\,s^{-1}}$, black line) and density ($\mathrm{cm^{-3}}$, red line), (d) IMF $|B|$ (nT, black) and pressure (nPa, red), (e) Sym-H index (nT, black) and equatorial electrojet strength (EEJ_{India}) over the Indian sector (nT, red), (f) $h'F$ (km, black) and OI 630.0 nm airglow intensity over Mt. Abu (in arbitrary units, red) from 21 December, 2014 to 25 December 2014.

Ap values for these days are 12, 19, 11, 15, and 11, respectively. In Figure 5.1 (from top to bottom), IMF Bx (in nT), IMF Bz (in nT), solar wind velocity (in kms^{-1}), IMF $|B|$ (in nT), Sym-H (in nT) and $h'F$ (in km) are shown in black lines while IMF By (in nT), IEFy (in mV/m), solar wind density ($\mathrm{cm^{-3}}$), solar wind pressure (nPa), EEJ_{India} (in nT) and OI 630.0 nm airglow intensity (in arbitrary units) are depicted in red lines. The Y-axes corresponding to black and red lines are marked on the left and right sides of Figure 5.1. It can be clearly noticed from Figure 5.1 that the peak $h'F$ and 630.0 nm airglow intensity are higher in the local night of 24 December, 2014 in comparison with the rest of the nights shown in Figure 5.1. This is despite IMF Bz being more southward for some time on 22 December (pre-noon hours over the Indian sector) and 23 December (pre-midnight hours over the Indian sector) compared to the interval of interest on 24 December, 2014. In fact, the characteristically different variation in OI 630.0 nm airglow intensity on this night motivated us to pursue this investigation.

Figure 5.2 puts the variations in the vertical drift (in ms^{-1}) over Tirunelveli, VTEC (in TECU) over Ahmedabad, OI 630.0 nm airglow intensity (in arbitrary unit) over Mt. Abu, GAGAN SBAS-TEC (in TECU) over the Indian sector (corresponding to 75°E) on 24 December, 2014 in perspective with a typical quiet day (28 November, 2014) behavior. Note, the daily mean Ap is 3 on 28 November, 2014 and 7 on the previous day. In all the panels, the quiet and disturbed variations are shown with blue and red colored lines, respectively. Figure 5.2a depicts the derived vertical drift variations over Tirunelveli (red) along with quiet vertical drifts (blue) which is consistent with the vertical drifts corresponding to 60°E longitude reported in *Fejer et al.* [2008a] based on ROCSAT observations. It can be seen that the pre-reversal enhancement (PRE) of the equatorial zonal electric field is enhanced on the event day (24 December, 2014). The vertical drift corresponding to PRE occurs at $\sim$ 1310 UT (1810 LT) on the event day with an amplitude of $\sim$ 42 ms^{-1}, which is higher than PRE amplitude on a quiet day ($\sim$ 25 ms^{-1}). More importantly, although the vertical drift decreases after the PRE hours, it does not turn unambiguously downward on the event night, similar to what happens on a quiet day. It can be noted that vertical drift turns downward during 1400-1430 UT (1900-1930 LT) on a quiet day. In sharp contrast to a quite day variation, the vertical drift again starts increasing from 1500 UT (2000 LT) on 24 December, 2014, and another peak in vertical drift occurs at $\sim$ 1600 UT (2100 LT) with an amplitude of $\sim$ 36 ms^{-1} on the event night. Note that the vertical drift at this local time is expected to be significantly downward,

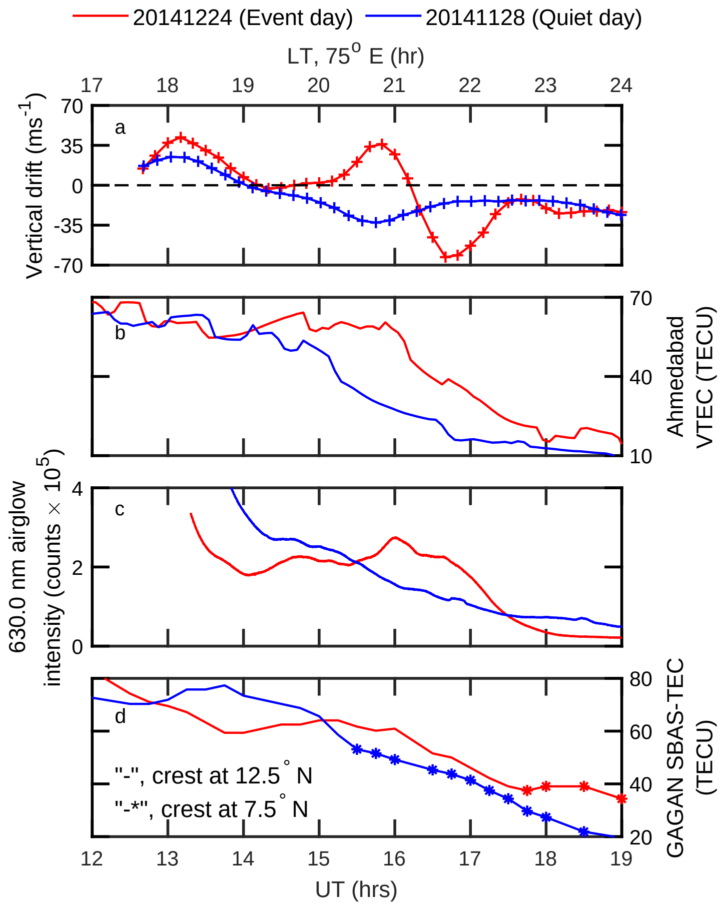

Figure 5.2: This figure illustrates the variations of a number of parameters on the event day (24 December 2014) and quiet day (28 November, 2014) with red and blue colors respectively. Subplots (a), (b), (c) and (d) represent vertical drifts (in ms^{-1}) over Tirunelveli, vertical total electron content (in TECU) over Ahmedabad, OI 630.0 nm airglow intensity (in arbitrary unit) over Mt. Abu, and SBAS-TEC (in TECU) variations over only the crest location, respectively. In subplot (d), solid and solid lines with stars are used to show the position of the crest at 12.5° and 7.5° N magnetic latitudes.

as indicated by the quiet time reference drift. Further, the vertical drift is found to be minimum (~-60 ms^{-1}) at ~ 1640 UT (2140 LT), which is significantly lower than the corresponding downward drift (~-15 ms^{-1}) during a quiet night at this local time. The vertical drift again starts decreasing just before 1700 UT (2200 LT) and becomes less downward at 1730 UT (2230 LT) to match with the corresponding quiet time drifts afterward.

Figure 5.2b shows vertical total electron content variation over Ahmedabad on 24 Decmber, 2014 (red) and 28 November, 2014 (blue), respectively. The figure reveals that the post-sunset enhancement in VTEC over Ahmedabad is higher and sustains for a longer period on the event day than on the quiet day. In Figure 5.2c, variations in OI 630.0 nm airglow intensity over Mt. Abu on the event day (red) show a different temporal pattern than what is noticed on the control day (blue). The intensity variation on the event night is characterized by three enhancements peaking at 1545, 1600, and 1640 UT (1945, 2100 and 2140 LT). In fact, the late enhancements at 1600 UT and 1640 UT are in sharp contrast with the monotonic decrease in intensity found on the control night at this local time.

Figure 5.2d is constructed with the help of SBAS-TEC data that shows the local time variations of TEC over the EIA crest location. The event and control days are marked by red and blue lines, respectively. On both days, the crest location is found either closer to 7.5°N (solid line with star) or 12.5° (solid line) magnetic latitudes during post-sunset hours. One can notice in Figure 5.2d that the EIA crest is located at 12.5°N until 1730 UT (2230 LT) on event day, whereas on the quiet day, the EIA crest is observed at 12.5°N magnetic latitudes until 1515 UT (2015 LT). After this, the location of the EIA crest is found at 7.5°N.

In order to verify whether the variations in the vertical drifts on 24 December are indeed anomalous, the drift variation on this night is compared with the vertical drifts [*Fejer et al.*, 2008a] as well as vertical perturbation drifts [*Fejer et al.*, 2008b] obtained from ROCSAT observations. Figure 5.3a (top subplot) shows the comparison of the measured vertical drifts (red) over Tirunelveli with the quiet time average vertical drifts (black) along 60°E longitude [*Fejer et al.*, 2008a]. On the other hand, the bottom subplot (Figure 5.3b) shows the associated vertical perturbation drifts (ΔVd, in red) over Tirunelveli and vertical perturbation drift (in black) obtained from ROCSAT-1 [*Fejer et al.*, 2008b] in December solstice. ΔVd is derived by subtracting the quiet day's drift from the event day. It is noticed in Figure 5.3 that the drifts on 24 December are significantly different from the ROCSAT drifts before 2230 LT. In fact, not only the magnitude of the drifts are different, but also the polarities are also opposite on certain occasions.

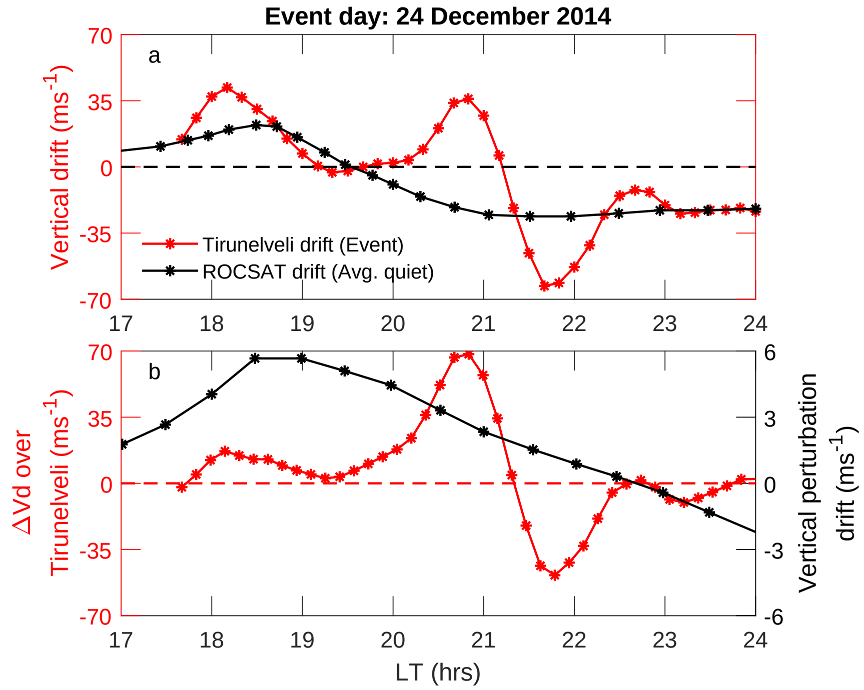

Figure 5.3: Panel (a) depicts the variations in vertical drift over Tirunelveli on the event day (similarly, shown in Figure 5.2a) in red and ROCSAT quiet time average vertical drift along 60°E longitude in black [*Fejer et al.*, 2008a]. Panel (b) shows variations in ΔVd in red and the vertical perturbation drift *Fejer et al.* [2008b] in black. All the drifts are for December solstice. Average solar flux level of event and ROCSAT vertical drift is ∼ 150 sfu.

These comparisons suggest that the variations in the vertical drift on this night are indeed anomalous before 2230 LT.

Figure 5.4 is dedicated to understand the anomalous vertical drift variations on the event night (24 December 2014). Figure 5.4a represents variations of the IMF Bz (in black) and IEFy (in red). Variations in IMF By are shown in Figure 5.4b. In Figure 5.4c, vertical drift over Tirunelveli (in red) and EEJ over Jicamarca (EEJ_{Peru} in black) are juxtaposed together to evaluate the polarity of the perturbation electric fields at the two nearly antipodal locations. Similarly, the ΔVd over Tirunelveli and ΔEEJ over Jicamarca in red and black lines, respectively, are brought in panel 5.4d to understand the change in vertical drift over Tirunelveli and EEJ_{Peru}. As already stated earlier, ΔVd is derived by subtracting the quiet day's drift from event day. ΔEEJ is calculated by subtracting

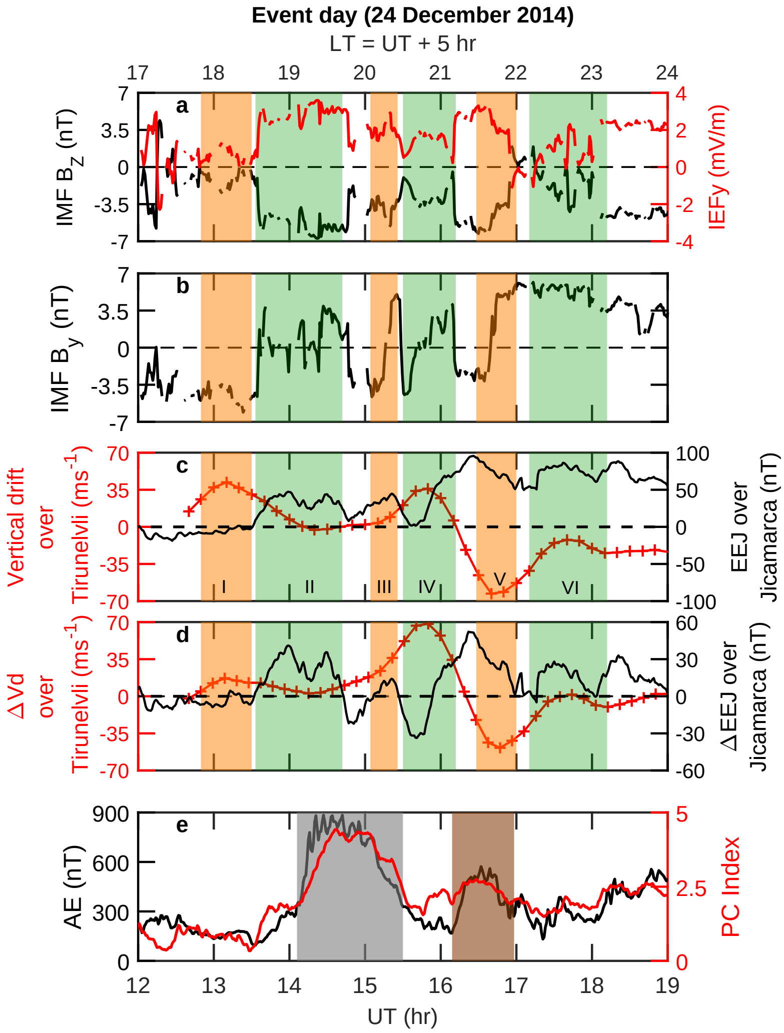

Figure 5.4: Subplots (a-e) show the variation of several parameters on the event day (24 December 2014). (a) shows the IMF Bz and IEFy variations in black and red lines. Subplot (b) depicts the variations in IMF By, (c) represents the variations in the vertical drift over Tirunelveli (in red) and EEJ over Jicamarca (in black). (d) shows the variations in the ΔVd over Tirunelveli (in red) and ΔEEJ over Jicamarca (in black) (e) depicts the variations in the AE (in black) and PC (in red) indices. Intervals (I-VI) are marked with orange and green colored rectangular boxes in the subplots a-d. In subplot (e), two conspicuous peaks in the AE and PC indices are marked with gray and brown colored rectangular boxes.

the average of four quietest days of December 2014 from the variations in EEJ strength on the event day. Auroral electrojet (AE) and polar cap (PC) indices are shown in Figure 5.4e. A few vertically shaded (in orange and green colors) intervals (marked by Roman numbers I-VI in Figure 5.4c) are also overlaid at appropriate places in Figures 5.4a-5.4d to bring out the important features that emerge from this set of observations. In Figure 5.4e, two simultaneous peaks in AE and PC indices around 1415 UT (1915 LT) and 1630 UT (2130 LT) are seen and shown in gray and brown shaded boxes.

Interval-I: During interval-I (∼1250-1330 UT, LT are shown at the top of the Figure), IMF Bz is southward, and vertical drift is upward with an amplitude of $\sim$ 42 ms^{-1}. This drift is more than the quiet time drift ($\sim$ 25 ms^{-1}) even if one considers 10% uncertainty in the vertical drift. Therefore, the enhanced PRE drift at this interval is due to the penetration of IEFy to the equatorial ionosphere and this change is noticed $\sim$ 17 ms^{-1}.

Interval-II: Interestingly, during interval II (∼1330-1440 UT), southward IMF Bz increases (∼-6 nT), leading to the enhancement in IEFy. IEFy stays around +3 mV/m during this interval. However, equatorial vertical drifts remain close to zero, and change in vertical drift is also zero or positive. Note IMF By stays predominantly positive with a few spike-like negative excursions during this interval. Interestingly, strong enhancements in AE (reaches $\sim$ 900 nT) and PC indices are observed during this interval apparently suggesting the occurrence of substorm. However, Figure 5.5 would subsequently confirm that the enhancement of AE and PC indices at this local time $\sim$ 1915 LT (1415 UT) are not due to substorm-induced electric field perturbations but possibly due to enhancement in polar cap electric field at this time due to enhanced IEFy. Another important aspect emerges from Figure 5.4c when the polarity of vertical drift (upward or nearly) over Tirunelveli and EEJ strength (positive) over Jicamarca are found to be the same during this interval. It is to be noted that the change in vertical drift and EEJ_{Peru} is almost positive in Figure 5.4d.

Interval-III: After interval-II, IMF By decreases, whereas IMF Bz becomes less southward. Interestingly, during interval-III (∼1505-1526 UT), IMF By increases sharply and turns positive. The equatorial vertical drift starts increasing at this time. It is noted that the polarities of vertical drift and EEJ (Figure 5.4c) are again found to be the same, although, before interval-III, ΔEEJ turned negative, whereas ΔVd is noted positive (Figure 5.4d). This behaviour is similar to what is seen in interval-II corresponding to positive IMF By.

Interval-IV: During interval-IV (∼1530-1615 UT), IMF By decreases first and then gradually increases. IMF Bz is less southward than interval-II. However, vertical drift unexpectedly and gradually becomes upward with a maximum amplitude of ∼ 36 ms^{-1} at 1550 UT (2050 LT). Note, the maximum vertical drift during this interval is nearly comparable to PRE-associated vertical drift during post-sunset hours on the event day. Interestingly, although IMF By turns positive (similar to interval-II and III) during this interval, ΔVd and ΔEEJ are in opposite polarities, unlike interval-II and III (Figure 5.4d). However, vertical drift is positive, and EEJ_{Peru} reaches zero.

Interval-V: Interval- V (∼1630-1700 UT) is characterized by the highest downward drift amplitude (∼-62 ms^{-1}) at ∼ 1640 UT (2140 LT) on the event day. This is significantly different than the quiet day drift (∼-15 ms^{-1}) at this local time. During this interval, IMF Bz is southward, and the amplitude is similar to interval-II. In addition, IMF By is negative. Considering 10% efficiency of the penetration electric field reaching to the dip equator, the difference in the observed and expected drifts ∼ 48 ms^{-1} (Figure 5.4d) cannot be explained even after considering a typical 10% uncertainty in the drift. Interestingly, enhancements in AE and PC indices are seen during this interval (peak ∼ 1630 UT), although these enhancements are less compared to the enhancements in these indices seen around 1415 UT. Based on Figure 5.5, it is confirmed subsequently that the enhancement of AE and PC indices at this local time (∼ 2130 LT) are due to additional effects of substorm-induced electric field perturbations. Further, similar to interval-IV, the polarity of the electric field perturbations (vertical drift over Tirunelveli and ΔEEJ over Jicamarca) over the two antipodal locations is opposite during this interval.

Interval-VI: IMF Bz turns northward in the interval-VI (∼1710-1810 UT), and vertical drift becomes less downward, indicating a eastward electric field perturbation at this time. This appears to be under the influence of the OS electric field. After the OS electric field perturbation, the vertical drift values reach the quiet time levels.

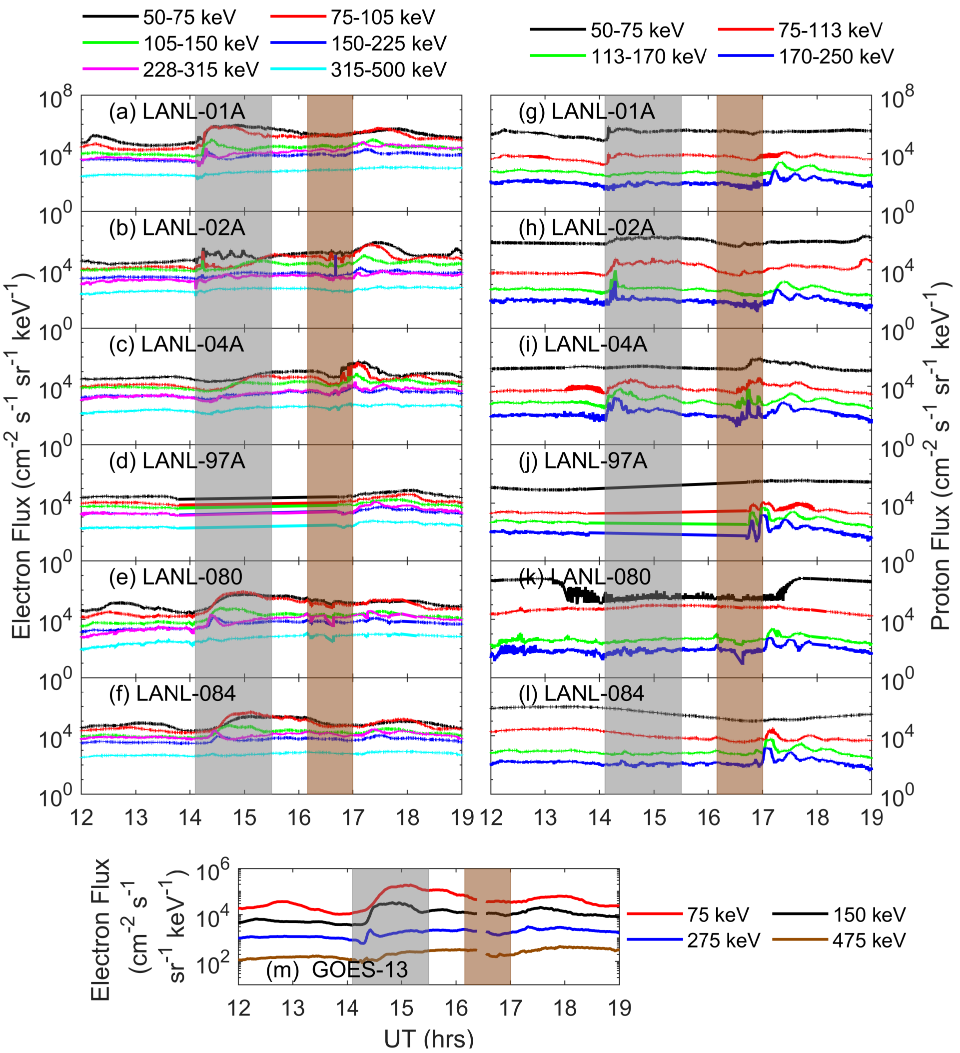

Figure 5.5: Subplots a-f and Subplots g-l represent the electron and proton flux variations measured by six LANL satellites (LANL-01A, LANL-02A, LANL-04A, LANL-97A, LANL-080, LANL-084) during 1200-1900 UT on 24 December 2014 for a number of energy channels mentioned at the top. Panel m shows the electron flux variations at four energy channels (75 kev, 150 kev, 275 kev, 475 kev) measured by GOES-13 for same interval and day depicted in panels a-l. Two intervals are marked with gray (~1405-1530 UT) and brown (~1610-1700 UT) rectangular boxes in all subplots, similarly marked in Figure 5.4e.

Figure 5.5 is used to identify the presence of substorm activity, if any, during 1400-1900 UT that encompasses the intervals (I-VI) under consideration (Figure 5.4) on 24 December 2014. In this plot, the variations in the electron and ion fluxes measured from geosynchronous orbit are presented in the left and right columns, respectively. The LANL geosynchronous satellites are LANL-01A,

LANL-02A, LANL-04A, LANL-97A, LANL-080, and LANL-084. Six energy bins for electrons and protons are used in this study. The electron energy bins are 50-75 keV, 75-105 keV, 105-150 keV, 150-225 keV, 228-315 keV and 315-500 keV whereas the ion energy bins are 0-75 keV, 75-113 keV, 113-170 keV, 170-250 keV, 250-400 keV and 400-670 keV. Differently colored lines are used to represent the different energy channels. In addition, the electron flux variations at four energy channels (75 keV, 150 keV, 275 keV and 475 keV) from GOES-13 satellites are also shown in Figure 5.5m. Here also, different colors correspond to different energy channels. Two intervals are marked with gray (∼1406-1530 UT) and brown (∼1610-1700 UT) rectangular boxes in all the subplots of Figure 5.5. These are the same intervals that are marked for AE and PC indices in Figure 5.4e. It can be seen there is no discernible substorm activity (dispersionless injection) in the electron channels of LANL during 1410-1530 UT (gray box). However, minor injection activities are seen in the electron channels of GOES and proton channels of LANL (particularly 04A) at this time. On the other hand, moderate injection activities (with dispersion) are noticed in the electron as well as ion channels starting at ∼1630 UT, which is particularly captured by LANL-04A. At this time, the injection activities captured by GOES are weak. This suggests energetic particle injection at the geosynchronous orbit closer to the location of LANL-04A. The other LANL satellites seem to be away from the proton injection front, and as a consequence, the injection signatures are quite dispersed at the other satellite locations. LANL-04A was situated near ∼ 65°E longitude (closer to the Indian longitudes) during 1400-1900 UT on the event day. The other LANL satellites are either far or not very close to Indian longitudes. Based on this figure, it appears that substorm is present during 1610-1700 UT closer to the Indian longitude. However, during 1410-1530 UT, substorm signatures are more prominent in GOES-13 measurements. The implications of these results will be discussed in the discussion section.

Figure 5.6 depicts the variations in the north-south (X) component of the magnetic field along the Indian and the Peruvian (antipodal location of Indian longitude) longitudes starting from the northern high latitudes to the equatorial

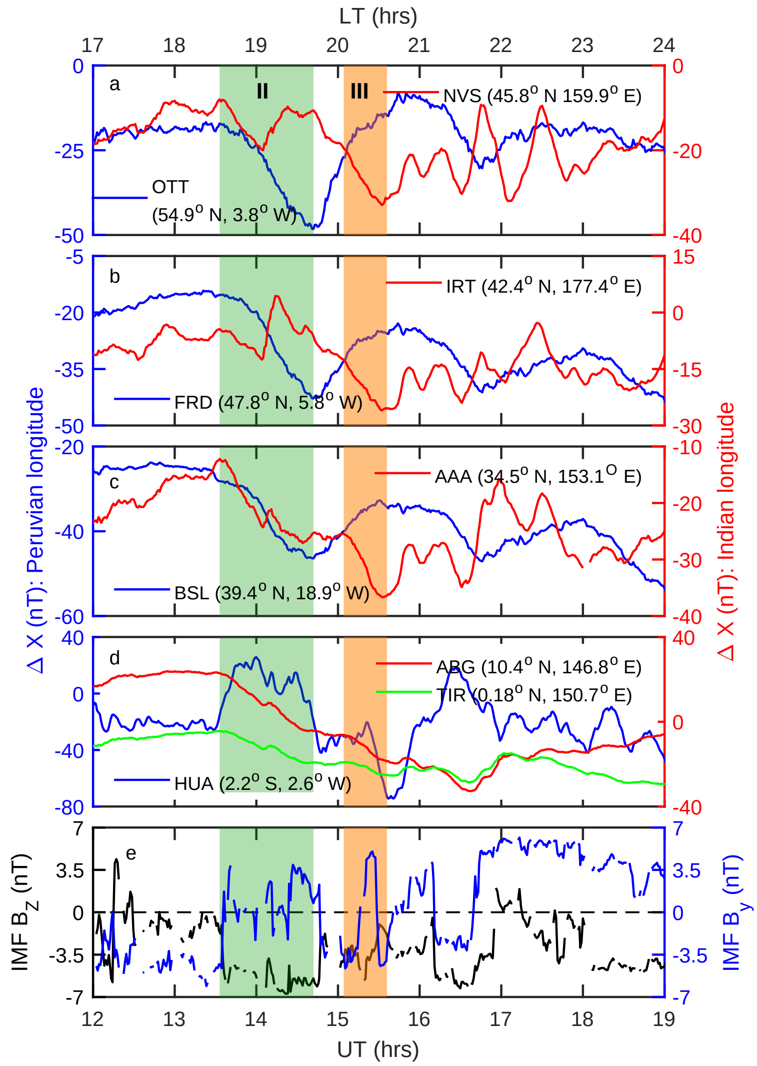

Figure 5.6: Variations of the northward component of magnetic field (ΔX) over Indian and Peruvian sectors from mid latitudes of the northern hemisphere to the equatorial region are shown in subplots (a-d) with red/green and blue colors, respectively. Subplot (e) depicts the IMF Bz and IMF By in black and blue colors respectively. Two intervals where are marked with green ($\sim$1330-1440 UT) and orange ($\sim$1510-1555 UT) colors respectively when ΔX variations are anticorrelated over mid latitudes and start becoming correlated as one comes toward the low-equatorial latitudes.

regions. ΔX variations of Indian and Peruvian magnetometer stations are shown with red/green and blue colored lines, respectively, in Figure 5.6a-d. Figure 5.6e shows the variations in IMF By and IMF Bz with blue and black colored lines, respectively (reproduced from Figure 5.1). Two intervals are marked in this figure with green (∼1330-1440 UT) and orange (∼1510-1555 UT) colored rectangular boxes. It can be noted that the ΔX variations are anti-correlated in Figure 5.6a and 5.6b (mid latitudes, see the green box in Figure 5.6) and start becoming less anti-correlated and more correlated as one comes toward the low-equatorial latitudes (Figures 5.6c and 5.6d in the green box). Note IMF By is predominantly positive (Figure 5.6d) in this interval. Similarly, in the next interval (1510-1555 UT), ΔX variations at Indian and Peruvian stations are in-phase (Figure 5.6d) over low latitudes that is in contrast with the out-of-phase variations over mid latiudes. It is also noted that IMF By sharply turns positive during this time. Interestingly, during these two intervals (marked by green and orange boxes in this Figure), the nearly identical polarity of perturbation electric fields are observed over Indian and Peruvian sectors (Figure 5.4d) that are in pre-midnight and pre-noon sectors, respectively. These aspects will be discussed in the ensuing section.

5.4 On the evaluation of quiet time vertical drift reference:

At this juncture, it is crucial to discuss the impact of the choice of a single quiet day (28 November 2014) as a reference. Figure 5.7 shows a comparison of vertical drift on 28 November 2014 (in black) with the quiet time average vertical drift (in blue) over Tirunelveli and quiet time average ROCSAT vertical drift (in red) along 60°E longitude. Four quiet days (28 November 2014, 11, 17, and 27 December 2014) in this season and solar epoch are chosen to construct the average quiet vertical drift variation over Tirunelveli. Note that the Ap values of these days are less than 6, and the Sym-H and AL values during the post-sunset hours are more than ∼-15 nT and ∼-250 nT, respectively. Based on Figure 5.7, a few points can be noted. First, the time of reversal of the polarity of the vertical drift for the chosen quiet day as well as the average quiet day is nearly identical. This means that the inference on the polarity of the electric field remains unchanged even if we use average quiet day variation as a reference. Second, it is, nevertheless, clear that the absolute magnitude of the drift beyond 1900 LT is different during intervals I-VI. Despite this, the inference on the polarity of electric field perturbations do not change. Third, it is also noted that the time of occurrence of peak PRE and reversal of vertical drift based on ROCSAT model differ from the two quiet time reference curves discussed above. Note that the longitude of Ahmedabad/Mt. Abu is ∼ 72.6°E, which is almost 12.6° apart from ROCSAT drift. In this work, we used a single day quiet time reference as OI 630.0 nm airglow intensity data from the EIA crest region (Mt. Abu) were available for comparison with the event day variation. Therefore, it can be summarized that although the magnitudes of the perturbation electric fields may vary depending on the choice of the quiet time reference, the inference on the polarity of the perturbation field remains unchanged.

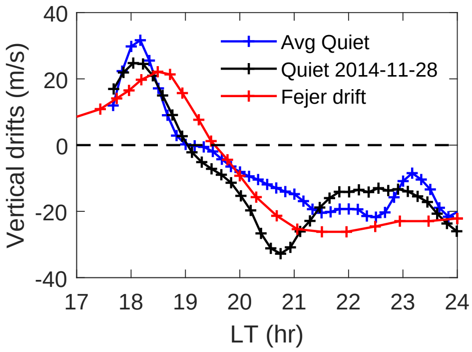

Figure 5.7: Local time variations of measured average vertical drift (in blue) and a typical quiet day (28 November 2014) vertical drift (in black) over Tirunelveli are shown. In addition, these variations also compares with the ROCSAT quiet time average vertical drift (in red) along 60°E longitude [*Fejer et al.*, 2008a]

5.5 Discussion

The important role of PP electric field in enhancing zonal electric field during local PRE hours is evident on 24 December 2014 (see Figure 5.2a). During PRE-hours, significant effects of PP electric field over the dip equatorial ionosphere have been studied by several researchers [e.g., *Rout et al.*, 2019; *Abdu et al.*, 2018; *Fejer et al.*, 2021; *Tsurutani et al.*, 2008] in the past. The role of PP electric field

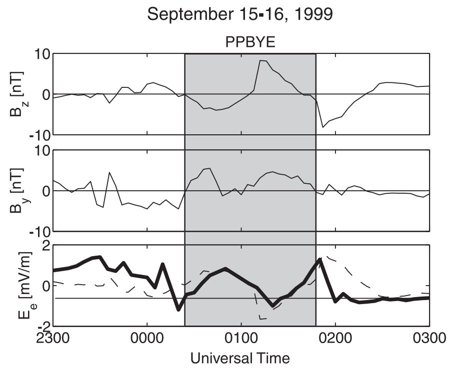

Figure 5.8: Prompt penetration effect over Jicamarca is shown on 15-16 September 1999 during 2300-0300 UT. Top panel (IMF Bz), middle panel (IMF By), and bottom panel (E_e electric field). Positive/negative values of E_e represent the westward/eastward polarity. Anomalous electric field perturbations are seen over Jicamarca during the shaded interval. [from ***Kelley and Makela*, 2002**].

in generating ionospheric super fountain [e.g., *Tsurutani et al.*, 2004; *Mannucci et al.*, 2005] over the low latitude and latitudinal expansion of EIA crest toward higher latitudes [e.g., *Rout et al.*, 2019] have also been shown. *Rout et al.* [2019] studied the largest PRE-associated vertical drift ($\sim$ 150 ms^{-1}) over Jicamarca during a space weather event in September 2017 (Shown in Figure 5.10). They also brought out latitudinal expansion of the EIA crest along the 75°W longitude. Not only the EIA crest during this event shifted around 20° with respect to the quiet day, but the TEC over the EIA crest region also got enhanced. *Kumar et al.* [2021, 2022] brought out the important role of PRE and solar flux dependence of the post-sunset enhancement of OI 630.0 nm airglow intensity and VTEC over the EIA crest region. Therefore, it is not surprising that an enhanced PRE (interval-I in Figure 5.4d) would enhance the VTEC as well as OI 630.0 nm airglow intensity over the EIA crest region, as brought out in Figures 5.2b and 5.2c. However, what is different here is the sustained (until 2100 LT or 1600 UT) enhancement of VTEC (Figure 5.2b) and airglow intensity (Figure 5.2c) over the crest region and also the longer sustenance of the EIA crest location at a higher latitude of 12.5° (Figure 5.2d) on the event day. It is also important to note that the strength of EEJ_{India} on 24 December, 2014 is, in fact, weaker compared to the other days. Despite that, we see an elevated OI 630.0 nm airglow intensity over the EIA

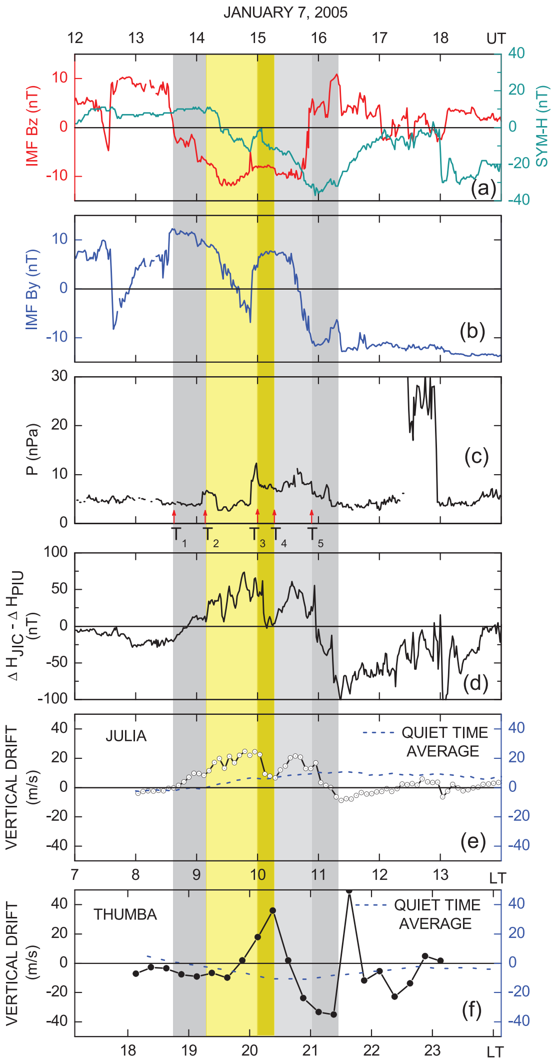

Figure 5.9: (a) IMF Bz (in red) and SYM-H (in cyan), (b) IMF By (in blue), (c) solar wind pressure P, on 7 January 2005. These variations are compared with the (d) EEJ variations over Peruvian sector ΔH_{JIC}-ΔH_{PIU}, (e) vertical plasma drift from JULIA (in black) along with its four quiet day average prior to the event (in dashed blue), and (f) vertical drift data over Thumba (in black) along with its seasonal quiet time values from *Madhav Haridas et al.* [2015] (in dashed blue). The Jicamarca and Thumba drifts have uncertainties of the order of 2 m/s and 5 m/s, respectively. Note, perturbation electric field during T_2-T_3 are eastward over both Thumba and Jicamarca simultaneously although these stations are nearly antipodal and in post-sunset and morning sectors respectively. [From *Chakrabarty et al.*, 2017]

crest region on this night. Therefore, it is apparent that the enhancements in VTEC and 630.0 nm airglow intensity on this night are not due to conditioning

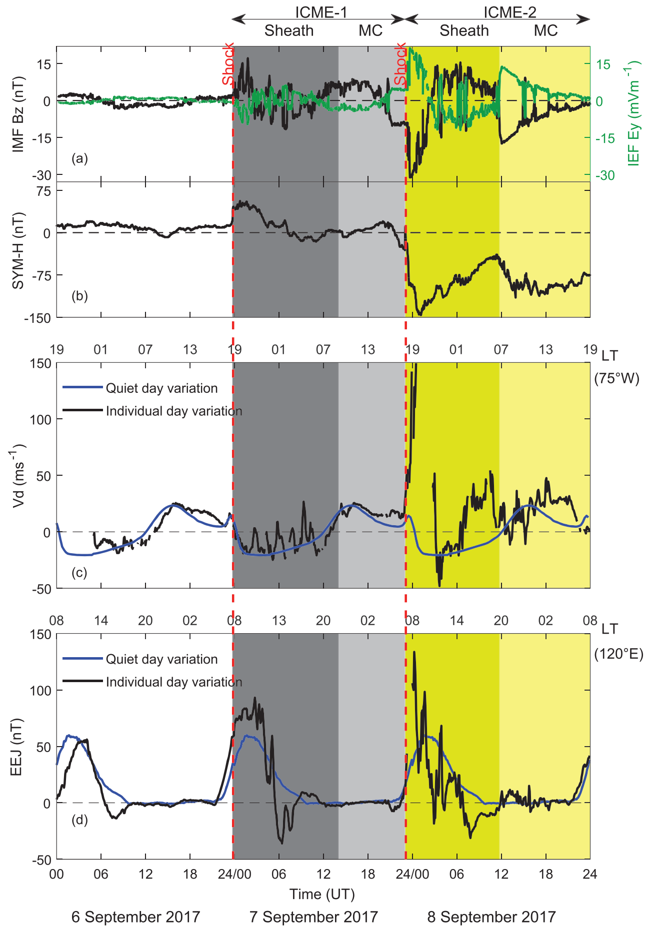

Figure 5.10: (a) IMF Bz (in black) and IEF Ey (in green), (b) Sym -H variations, (c) Vertical drift over Jicamarca and (d) EEJ over Philippines. In Panels c and d, the event and average quiet day variations are shown with black and blue colored lines. The shaded regions are marked to show the different regions of ICME-1 and ICME-2. Note the extreme changes in the Vertical drift over Jicamarca and EEJ strength over the Asian sector. [From *Rout et al.*, 2019].

of the EIA crest region by the daytime F region plasma fountain process driven by daytime zonal electric field over the equatorial ionosphere. Elevated $h'F$ over Tirunelveli in the evening hours of 24 December, 2014 provides the first clue that the impact on the EIA crest region on this night is because of what happened in the evening hours. It is noteworthy that the EIA crest is located at 12.5°N magnetic latitude until 2015 LT on the quiet day as indicated in Figure 5.2d. The fact that the vertical drift does not really become downward on the event day during the post-sunset hours (Figure 5.2a) and also gets significantly upward at

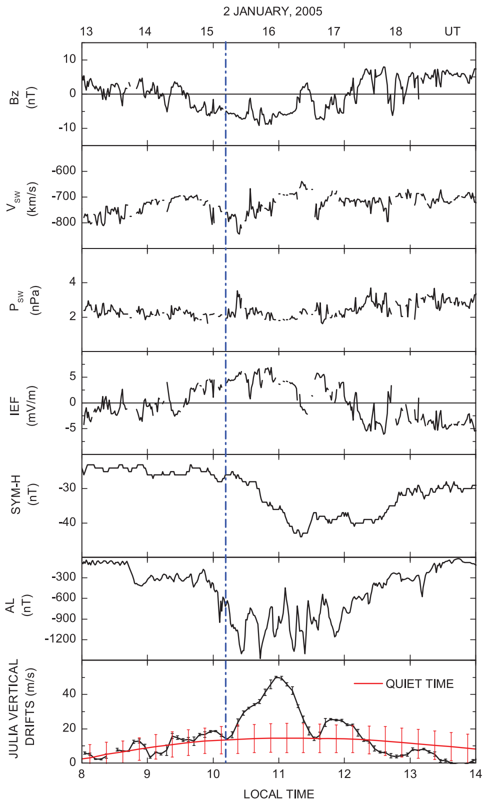

Figure 5.11: Variations of Jicamarca vertical plasma drifts as a response to changes in solar wind and geophysical parameters on 2 January 2005. From the top to bottom: (first panel) IMF Bz, (second panel) Vx, (third panel), P_{sw}, (fourth panel) IEFy, (fifth panel) SYM-H, (sixth panel) AL, and (seventh panel) JULIA vertical plasma drifts. The red line on the bottom panel shows average vertical drift with their standard deviations. The vertical dashed line indicates the commencement time of substorm. Upward perturbation in vertical (eastward electric field) drift is observed due to the substorm in daytime. [From *Hui et al.*, 2017]

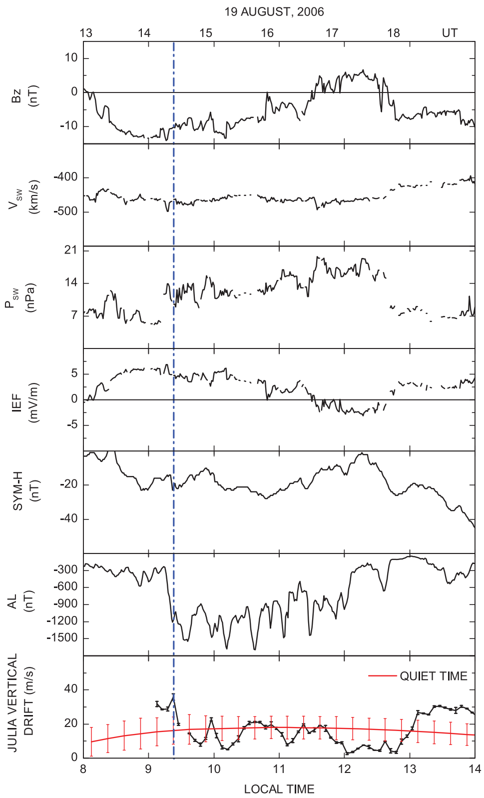

Figure 5.12: Same variations but for 19 August, 2006. Downward perturbation in vertical drift (westward electric field) is noticed due to substorm in daytime. [From *Hui et al.*, 2017]

$\sim$ 1600 UT (2100 LT) has an important connection with the behavior of the EIA crest on the event night. Therefore, the processes responsible for the unusual behavior of the vertical drift (proxy for the zonal electric field) on this night deserve critical attention.

To understand the anomalous behavior of the zonal electric field on 24 December, 2014, we now shift our attention to intervals II-V in Figure 5.4. Note IMF Bz is southward in these intervals. However, IMF Bz is more southward (IEFy is more positive) during intervals-II and -V compared to interval- III and -IV. In view of this, we expect more changes in the equatorial vertical drift during intervals II and V compared to intervals III and IV. However, what we observe is contrary to this expectation and hence counter-intuitive. The perturbations in the electric field is nominally eastward (nominally upward drift or nearly zero drift) in interval II and significantly westward (downward drift) in interval V. On the contrary, in intervals III-IV, the eastward electric field perturbations (upward drift) keeps increasing. Another interesting feature is the observation that vertical drift keeps increasing through intervals II and III, although IMF Bz becomes less southward in interval III compared to interval II. Therefore, even if eastward penetration electric field is operational during this period that resists the drifts to turn downward, one expects larger drifts when IMF Bz (or IEFy) is larger. This suggests contribution(s) from other driver(s). Therefore, not only these observations cannot be explained by the eastward penetration electric field perturbations expected until 2200 LT as per the existing understanding [e.g., *Fejer et al.*, 2008b; *Nopper Jr. and Carovillano*, 1978], but the amplitude of perturbations also needs attention here. Interestingly, LANL geosynchronous particle fluxes (Figure 5.5) confirm that there is no significant substorm occurrence closer to Indian longitude during the interval of first enhancements of AE and PC indices that occur during intervals II-III. Further, the interval of the first and strong enhancements in AE and PC indices are also marked by relatively large magnitude of IEFy. This suggests a strong influence of IEFy in the enhancements of AE and PC indices at this time. This leads us to envisage a strong IMF By role in intervals II and III. From the work of *Chakrabarty et al.* [2017], we know that predominantly positive IMF By can rotate the DP2 convection cells (generated significantly during southward IMF Bz condition) significantly so that the daytime eastward perturbation electric field encroach into the post-sunset sector and affects the polarity of the perturbation electric field during post-sunset hours. *Chakrabarty et al.* [2017] have reported that the vertical drift over Thumba and Jicamarca (two antipodal locations) are having the same polarity during post-sunset hours (Figure 5.9). This gets credence from the present observations (Figure 5.4) wherein the polarity of ΔEEJ and vertical drift over the Jicamarca and Indian sectors are identical during intervals II and III, suggesting an eastward electric field perturbations over both the sectors (Jicamarca is the day sector whereas Tirunelveli is in the night sector). Note this is the local time over the Indian sector when an westward electric field polarity (downward drift as per quiet day pattern) is expected. Considering the curl-free nature of the ionospheric electric field and the maximum impact of the penetration electric field on the ionospheric zonal component, one may expect opposite polarities of perturbation electric field at the day and night side of the dip equatorial ionosphere. Therefore, it appears that the identical polarity of penetration electric field over both Indian and Jicamrca sectors during intervals II and III are due to the effects of IMF By. The proposition of the rotation of the DP2 convection cells by the effects of IMF By [e.g., *Chakrabarty et al.*, 2017] gets further credence from Figure 5.6, wherein one can see the anti-correlation of ΔX variations over mid latitudes but correlation over low latitudes. *Kelley and Makela* [2002] found the westward penetration of the electric field over Jicamarca during the pre-midnight hours under the southward IMF Bz conditions and suspected the effect of IMF By (Figure 5.8). In the work of *Chakrabarty et al.* [2017] and this work, we see the IMF By effect during the post-sunset hours. These results are consistent with the work of *Hui and Vichare* [2021], who, using TIE-GCM simulations, showed that the effects of IMF By over low latitudes are most prominent at the terminator sector over low latitudes.

Interestingly, ΔEEJ and ΔVd (Figure 5.4d) show anti-correlations during intervals-IV and -V that is consistent with the curl-free nature of the ionospheric electric field as discussed in the previous paragraph. However, zonal electric field perturbations over the Indian sector are eastward and westward, respectively, during these intervals. Unlike intervals II and III, ΔX variations (Figure 5.6) during these intervals do not show any systematic changes in the behavior as one comes towards the low latitude (mentioned in the previous paragraph), and this is indicative of the absence of IMF By effect during intervals IV and V. Therefore, although IMF By turns positive during interval IV, we rule out IMF By effect during this interval. In the absence of any substorm during this interval, the only way an enhanced eastward electric field perturbation can arise with a reduced (compared to interval-II) amplitude of southward IMF Bz condition is through the withdrawal of IMF By effect that was present before. We suggest that the usual eastward penetration electric field perturbations are experienced over the Indian sector at this time under the influence of southward IMF Bz (dawn-to-dusk IEFy) with no modification offered by IMF By. As a consequence, the eastward electric field perturbation seems to increase at this time. On the other hand, during interval-V, we notice a westward penetration electric field that causes downward drift. We propose that the penetration electric field is already westward during this time on this night which is, in general, expected at $\sim$ 2200 LT as some of the earlier works [e.g., *Fejer et al.*, 2008b] suggested. The vertical perturbation drift is shown in Figure 5.3b. However, the magnitude of the westward electric field perturbations during interval-V cannot be explained by the IEFy magnitude during this time with even 10-15% penetration efficiency and 10% uncertainty in the drift magnitude. Interestingly, although the AE and PC indices show minor enhancements during interval V, LANL-04A observations suggest the presence of substorm-related particle injections at the geosynchronous orbit closer to the Indian longitude (Figure 5.5). GOES measurements also show minor undulations in electron flux at this time. On the other hand, IEFy starts decreasing during this interval. Therefore, we suggest that the combined effects of penetration electric fields due to IEFy and substorm cause the unusually large westward electric field perturbation during interval V. Earlier works by *Hui et al.* [2017] and *Rout et al.* [2019] show that substorm-induced electric field can enhance the conventional penetration electric fields in a significant manner. However, it is to be kept in mind that substorms have been shown earlier to cause both eastward [e.g., *Chakrabarty et al.*, 2008, 2010; *Huang*, 2009; *Hui et al.*, 2017; *Rout* *et al.*, 2019] and westward [e.g., *Kikuchi et al.*, 2000; *Chakrabarty et al.*, 2015; *Hui et al.*, 2017] electric field perturbations over the equatorial ionosphere. The observation of *Hui et al.* [2017] has been shown in Figures 5.11 and 5.12. They noticed both eastward and westward polarity of substorm-induced electric field over low latitudes under the southward IMF Bz conditions on two occasions.

During the interval VI (∼2210-2310 LT, see Figure 5.4d), the IMF Bz turns northward from southward, and an OS electric field [e.g., *Kelley et al.*, 1979; *Gonzales et al.*, 1979; *Fejer et al.*, 1979a] is imposed over the equatorial ionosphere. This provides the eastward perturbations to the ionospheric electric field. Owing to this, vertical drift becomes less downward during the interval-VI. It has been shown earlier [e.g., *Chakrabarty et al.*, 2006; *Sekar and Chakrabarty*, 2008] that on many occasions, the nighttime eastward electric field perturbations due to the overshielding effect can affect the equatorial F region plasma irregularity events.

Last but not least, two peaks are observed in VTEC (Figure 5.2b) and 630.0 nm airglow intensity (Figure 5.2c) during the post-sunset hours on 24 December 2014. The peaks are more conspicuous in the airglow intensity variation. The first peak occurs at ∼ 1445 UT (1945 LT) that is separated from the peak PRE drift (occurs at ∼ 13 UT or 18 LT) by around 1.75 hrs. This is consistent with the results of *Kumar et al.* [2021]. The second peak that occurs just before 1600 UT (or 2100 LT) is probably a consequence of less quenching as the ionosphere goes up in altitude simultaneously over the entire low latitude due to the imposition of the eastward penetration electric field.

5.6 Summary

The space weather event on 24 December 2014 reported in this investigation is unique for several reasons. First, the equatorial/low latitude impact is anomalously enhanced during the post-sunset hours of 24 December 2014 when the magnitude of IEFy is not very large but persists through local PRE/post-PRE hours. This suggests that as far as low latitude ionospheric impacts are considered, local time of the electric field disturbance is important. Penetration electric field perturbations occurring during PRE hours when the zonal electric field is already enhanced can make the equatorial impact unusually stronger. Second, during one single event, we see an occasion when a number of phenomenologically different penetration electric fields (like penetration electric fields due to IEFy, substorm etc.) acting simultaneously on the equatorial ionosphere. Therefore, the magnitude of electric field perturbations on some occasions cannot be determined based on the existing paradigm of penetration electric fields. Third and most importantly, due to the additional effects of IMF By, for some time, the response of the equatorial electric field perturbations turns out to be anomalous both in terms of magnitude and polarity. The investigation also shows that vertical drift over Tirunelveli, VTEC over Ahmedabad and OI 630.0 nm airglow intensity over Mt. Abu on this night deviate significantly from the quiet time variation due to the anomalous electric field perturbations primarily driven by substorm-induced electric field and IMF By under southward IMF Bz condition. Therefore, this event shows that phenomenological understanding of the nature of the penetration electric fields are important for future modelling efforts.

Chapter 6

Space weather induced perturbation electric fields during post-midnight hours

Excerpts

In the previous chapters, we have discussed the mechanism and modulation of post-sunset enhancements over low latitude F region during quiet and disturbed space weather conditions, respectively. In Chapter-5, the response of post-sunset F region ionosphere over equatorial and low latitudes is discussed on 24 December 2014 that is characterized by a minor geomagnetic storm. Anomalous electric field perturbations are noticed over low/equatorial ionosphere on this night. In this chapter, the responses of equatorial and low latitude ionosphere are investigated corresponding to the space weather disturbances on 21 and 23 December 2014 that are prior to the 24 December 2014 event. Unusual enhancements in the post-midnight vertical drifts are observed during both these nights. These perturbations in vertical drifts are also anomalous similar to the post-sunset perturbations in vertical drift on 24 December 2014. On 21 December, 2014, we have found the unusual variations in the dip equatorial vertical drift during post-midnight hours are caused by IMF By under the southward IMF Bz condition followed by the overshielding electric field. On the other hand, the post-midnight dip equatorial electric field perturbations on 23 December 2014 seem to be driven by the oversheilding electric field and substorm-induced electric field. Therefore, this investigation highlights the interplay of various space weather drivers in causing the electric field perturbations over the dip equator during post-midnight hours.

6.1 Introduction

The polarity of vertical drift over the dip equatorial ionosphere has been discussed during quiet and disturbed space weather conditions in section 5.1. It was discussed that F region vertical drifts are mostly upward/downward in daytime/nighttime during geomagnetically quiet days in all the seasons (See Figure 3.4). During the post-midnight hours, the vertical drifts are, in general, downward during geomagnetically quiet periods [e.g. *Scherliess and Fejer*, 1999; *Fejer et al.*, 2008a]. Many studies are carried out to understand the post-midnight vertical drift variations over the dip equatorial region during quiet periods. The unusual behavior of vertical drifts is observed during the low solar activity periods in the post-midnight hours [e.g., *Pham Thi Thu et al.*, 2022; *Zhang et al.*, 2015; *Chakrabarty et al.*, 2014; *Stoneback et al.*, 2011; *Yizengaw et al.*, 2009] during quiet periods. *Stoneback et al.* [2011] reported enhancements in equatorial vertical drifts based on C/NOFS (Communication/Navigation Outage Forecasting System) observations and they suggested the important role of large semi-diurnal tidal components during post-midnight hours in the June solstice of low solar activity periods. Interestingly, in the measurements of vertical drifts by the ROCSAT-1 satellite, the enhancement in vertical drift is observed during post-midnight [e.g., *Yizengaw et al.*, 2009] as well as dawn [e.g., *Zhang et al.*, 2015] hours. *Zhang et al.* [2015] suggested the role of magnetic declination in the enhancements of vertical drift during dawn hours, whereas *Yizengaw et al.* [2009] found that the thermospheric neutral wind drives upward drift during post-midnight hours through F region dynamo action. It is to be noted that during quiet periods, the post-midnight vertical drifts are observed upward only during low solar activity periods. Upward drift during the post-midnight hours can favor the growth of the F region plasma irregularities over the equatorial and low latitude region [e.g., *Zhan et al.*, 2018; *Otsuka*, 2018].

Using measurements of the ROCSAT-1 satellites, *Fejer et al.* [2008b] showed the perturbations in vertical drifts associated with the prompt penetration (PP) and disturbance dynamo (DD) electric fields. Zonal electric field/vertical drift perturbations over the dip equator are discussed in section 5.1. In section 5.1, it has been discussed that zonal electric field/vertical drift over the dip equator gets perturbed in a variety of ways. The polarity of the PP electric field is eastward and westward over the dip equator during the day and night hours, whereas overshielding (OS) electric field and delayed electric field by disturbance dynamo or disturbance dynamo (DD) electric field generate opposite polarity to the PP electric field over the dip equatorial ionosphere. The modelling and observational studies [e.g. *Nopper Jr. and Carovillano*, 1978; *Fejer et al.*, 2008b] suggest that the PP electric field generates eastward/upward perturbations in the zonal electric field/vertical drift till 2200 LT. It should be kept in mind that OS electric field gives eastward/upward perturbations in electric field/drift after 2200 LT or post-midnight hours. In addition, the DD electric field generates the downward [e.g., *Fejer et al.*, 2008b; *Simi et al.*, 2012] and upward [e.g., *Fejer et al.*, 2008b; *Rout et al.*, 2019; *Sori et al.*, 2022] perturbations in vertical drift during day and night respectively. It has been discussed in previous chapter and the work of *Chakrabarty et al.* [2017] that the role of the prompt electric field can not be understood easily in the presence of IMF By. Besides this, solar wind pressure-induced electric field also creates a transient change over the dip equatorial electric field [*Huang et al.*, 2008; *Rout et al.*, 2016]. On the other hand, the role of the substorm-induced electric field over low latitude regions is also important. However, the polarity of the substorm-induced electric field perturbations over the dip equatorial ionosphere [e.g., *Hui et al.*, 2017] cannot be predicted easily. The strength of a substorm also does not seem to decide the amount of electric field perturbation expected over a particular location over the dip equator and this emerges from Chapter-5. In the previous chapter, westward electric field perturbation due to substorm was reported, while *Rout et al.* [2019] observed eastward polarity during PRE/post-sunset hours. On the other hand, *Hui et al.* [2017] noticed both eastward and westward polarities of substorm-induced perturbation electric fields over the dip equator during daytime.

It is, in general, assumed that the PP electric field causes downward drift, whereas DD electric field and OS electric field cause upward drifts during post-midnight hours. In this chapter, we investigate the dip equatorial electric field perturbations during post-midnight hours for two events. Both these post-midnight space weather events are characterized by OS electric field perturbations. However, we note that the stronger overshielding event causes weaker vertical drift perturbations and vice versa. In addition, the vertical drift perturbations on these two nights cannot be explained by variations in IEFy only. These anomalous responses of the equatorial ionosphere are investigated based on the interplay of a number of space weather induced electric field drivers. This investigation, in turn, provides a context to compare these observations with similar anomalous electric field perturbations during post-sunset hours reported in the previous chapter.

6.2 Datasets

The following datasets are used in the present investigation. The data of solar wind parameters like the interplanetary magnetic field, solar wind velocity, solar wind pressure, etc. are obtained from SPDF-GSFC. The time-shifted data at the nose of the bow shock is available on this website. The magnetosheath and Alfven transit times are calculated and added to the lag time point by point to compare the space weather effects on the ionosphere. This methodology is adopted from *Chakrabarty et al.* [2005] and has already been implemented in Chapter-5. We also used the auroral electrojet (AE) index from SPDF. 1-minute cadence data of all these parameters are used in this chapter.

This study is mainly focused on the Indian sectors during post-midnight hours. Hence, the vertical drifts over Tirunelveli are used to understand the electric field perturbation and to observe the associated effects over low latitudes. This includes changes in the vertical total electron content (VTEC) over Ahmedabad and OI 630.0 nm airglow intensity over Mt. Abu. These datasets are used in Chapters-3, 4 and 5 also. Recombination corrected vertical drift over Tirunelveli (Vd_{TIR}) is used in this chapter. The recombination correction method is described in Chapter-5. In addition, the equatorial electrojet (EEJ) strength and vertical drifts over Jicamarca (antipodal location of the Indian sector) are also studied to understand the curl-free condition of the electric field. EEJ data over Jicamarca is discussed in Chapter-5. Vertical drifts over the Jicamarca sector are obtained from Incoherent scattered radar (ISR) over Jicamarca (11.9°S, 77.0°W, dip angle: 0.8°). The average vertical drifts (Vd_{JIC} averaged between 247-450 km) of 5-minute cadence is used in this work.

To identify the occurrence of substorm activity, the electron and ions flux data measured by Geostationary Operational Environmental Satellite System (GOES)-13 are used during 1200-2400 UT. These datasets have been used in Chapter-5 for similar purpose.

It is noticed in Chapter-5 that space weather perturbations are presented during 21-25 December 2014. Therefore, during this period, the effects of disturbance dynamo can be expected. Although the effects of disturbance dynamo (DD) can not be filtered during the main phase of the storm, their impacts can be evaluated during the recovery phase of the storm. In the present study, the effect of DD is characterized by using the technique discussed by *Amory-Mazaudier et al.* [2017], and *Zaka et al.* [2009].

$$D_{dyn} = \Delta H - S_R - SymH \times cos(L) \tag{6.1}$$

In Equation 6.1, ΔH and S_R are the event day and quiet time average magnetic field variations above the crustal magnetic field values. $SymH$ is the strength of the ring current. L is the magnetic latitude at that station where the magnetic disturbance is calculated. The DD shows its global impact, and its effects can be captured in horizontal magnetic field variations. The magnetometer data from both the hemispheres between the geographic longitudes 275°-300°E have been taken. Using Equation 6.1, the DD is calculated over the stations, Vernadsky (AIA, 55.4°S, 6.1°E), Trelew (TRW, 33.4°S, 6.24°E), Pilar (PIL, 21.8°S, 7.9°E), Huancayo (HUA , 2.2°S, 2.7°S), San Juan (SJG, 27.7°N, 6.8°E), Ottawa (OTT, 54.9°N, 3.7°W), Iqaluit (IQA, 73.3°N, 6.2°E), and Thule (THL, 87.1°N, 14.2°E). These data are obtained from the INTERMAGNET (https://www.intermagnet.org/index-eng.php).

6.3 Results

In Chapter-5, it has been shown that the period 21-25 December 2014 is associated with space weather disturbances. We have chosen two days-21 and 23 December- from this period for further investigation. In Figure 6.1, the variations during Event-I, Event-II, and quiet day are shown by the red, black, and blue colored lines, respectively, in two adjacent columns. Further, the vertical drift over Tirunelveli (Vd_{TIR}), vertical total electron content (VTEC) over Ahmedabad, and OI 630.0 nm airglow intensity over Mt. Abu are shown in the top, middle, and bottom panels in both the columns.

In Event-I, the peak amplitude of PRE-associated vertical drift (~ 25 ms^{-1}) is comparable to to the peak quiet time amplitude. However, the event day's PRE-associated vertical drift during the event night remains positive (upward) for a slightly longer duration than the quiet night and becomes negative (downward) after ∼1430 UT (1930 LT). It can be noticed that two peaks in vertical drift are observed at ∼1300 UT (1800 LT) and ∼ 1400 UT (19 LT) during Event-I. During this event, vertical drift is ~ -50 ms^{-1} at ∼ 1950 UT (2550 LT) that is larger than the amplitude of downward drift at the same local time on the quiet day (∼-30 ms^{-1} at 1545 UT). It is interesting to note that a larger downward vertical drift occurs later during Event-I. After the occurrence of this minimum drift (or equivalently, maximum downward drift), the vertical drift gets enhanced and reaches ∼ 50 ms^{-1} at ∼ 2200 UT (0300 LT). This post-midnight upward drift is not only anomalous (one expects downward drift at this local time), but the magnitude of this upward drift is quite large (twice the amplitude of the PRE-associated vertical drift during post-sunset hours). After half an hour,

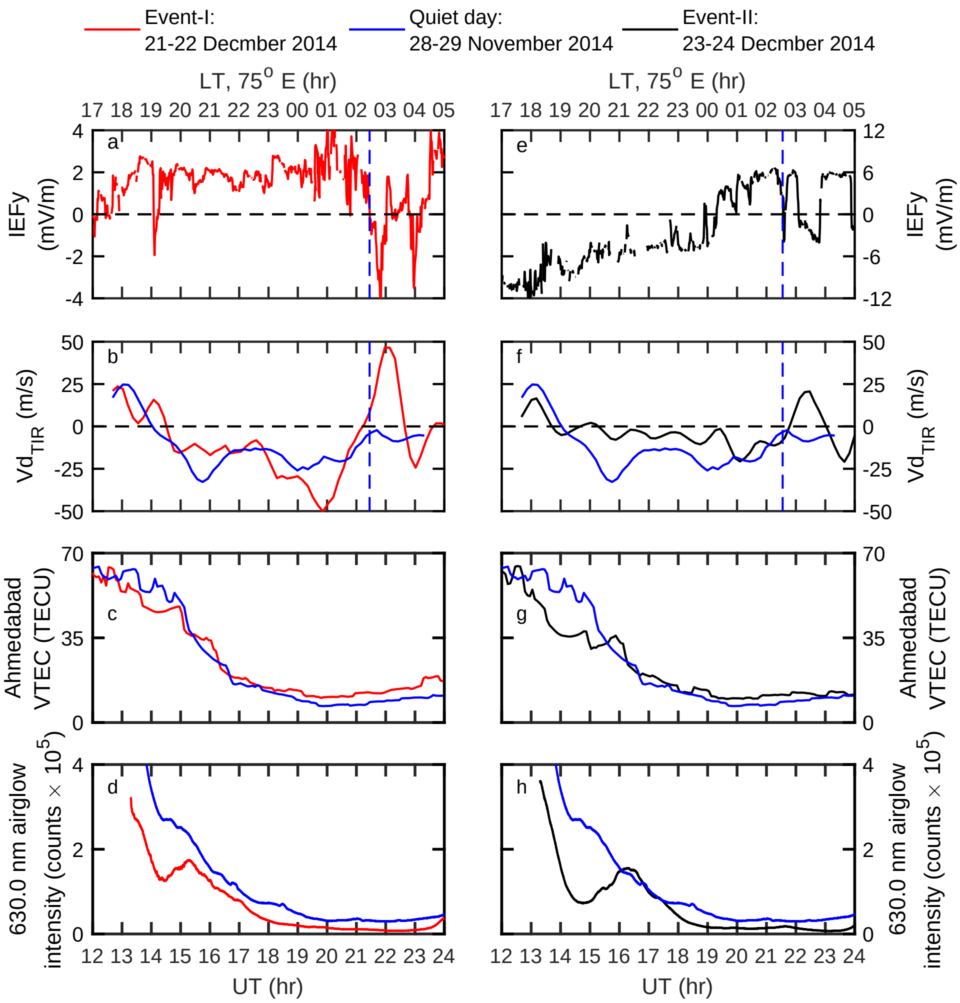

Figure 6.1: The variation in Event-I, Event-II and quiet day are depicted with red, black, and blue colored lines, respectively. Panels a & e, b & f, c & g and d & h show the variations in interplanetary electric field (IEFy), vertical drifts over Tirunelveli (Vd_{TIR}), VTEC over Ahmedabad and OI 630.0 nm airglow intensity during 12-24 UT respectively. The vertical dashed lines mark the times of onset of overshielding electric field perturbations (in panels a and e) and associated upward vertical drift perturbations (in panels b and f) over Tirunelveli during post-midnight hours during Event-1 and Event-II.

this upward drift becomes downward. In Figure 6.1c, the two VTEC peaks are noticed at $\sim$ 1453 UT (1953 LT) and $\sim$ 1553 UT (2053 LT) after the occurrence of two peaks in the vertical drift at 1300 UT (1800 LT) and 1400 UT (1900 LT). In Figure 6.1d, a clear and broad peak in airglow intensity is also observed at $\sim$ 1520 UT (2020 LT) for Event-I. Figures 6.1c and 6.1d indicate that as far as Event-I is concerned, there is no unusual impact on VTEC and airglow intensity variations over the crest region of EIA during post-sunset hours. The observations are consistent with the post-sunset impact on low latitude VTEC and airglow intensity variations discussed in Chapters- 3 and 4.

The vertical drift during Event-II at $\sim$ 1300 UT (1800 LT) is relatively smaller (peak amplitude is $\sim$ 16 ms^{-1}) than the PRE values on the quiet day and Event-I (amplitudes on both days are $\sim$ 25 ms^{-1}). The post-sunset drifts during Event-II become downward (negative) at $\sim$ 1905 LT. However, the amplitude of vertical drifts remains between -10 and 0 ms^{-1} till $\sim$ 2015 UT (0115 LT). It is interesting to note that in this case also, two peaks in VTEC are seen and these occur at $\sim$ 1453 UT (1953 LT) and $\sim$ 1553 UT (2053 LT). Further, a conspicuous and broad peak is observed in airglow intensity at $\sim$ 1600 UT (2100 LT). After 2015 UT, the vertical drift increases unusually (not expected at this local time during quiet periods) and becomes upward (the peak amplitude is $\sim$ 21 ms^{-1}) at $\sim$2225 UT (0325 LT). This post-midnight peak in vertical drift is slightly higher than the evening hours' peak amplitude in the PRE-related vertical drift. This post-midnight peak in vertical drifts is observed 25 minutes later than the post-midnight peak on Event-I. In the present investigation, we are more interested in addressing the causes of the occurrence of these post-midnight peaks in upward vertical drift, which are higher than evening/PRE-associated upward vertical drifts. Further observations related to both events will be discussed in the ensuing sections.

Figures 6.2 is presented to understand the electric field perturbation on 21-22 December 2014 over the Indian and Jicamarca sectors during 1200-2400 UT. This is done to glean clues for the unusual variations in the vertical drifts during the post-midnight hours over the Indian sector. Figure 6.2a depicts the variations in IEFy. In Figure 6.2b, the variations in IMF By (black) and IMF Bz (red) are presented. The solar wind dynamic pressure (P) is shown in Figure 6.2c. Figure 6.2d represents the AE and PC indices with black and red-colored lines. Figures 6.2 e-g depict the variations in vertical drifts over Tirunelveli (Vd_{TIR}), vertical drifts over Jicamarca (Vd_{JIC}), and EEJ over Jicamarca (EEJ_{JIC}), respectively.

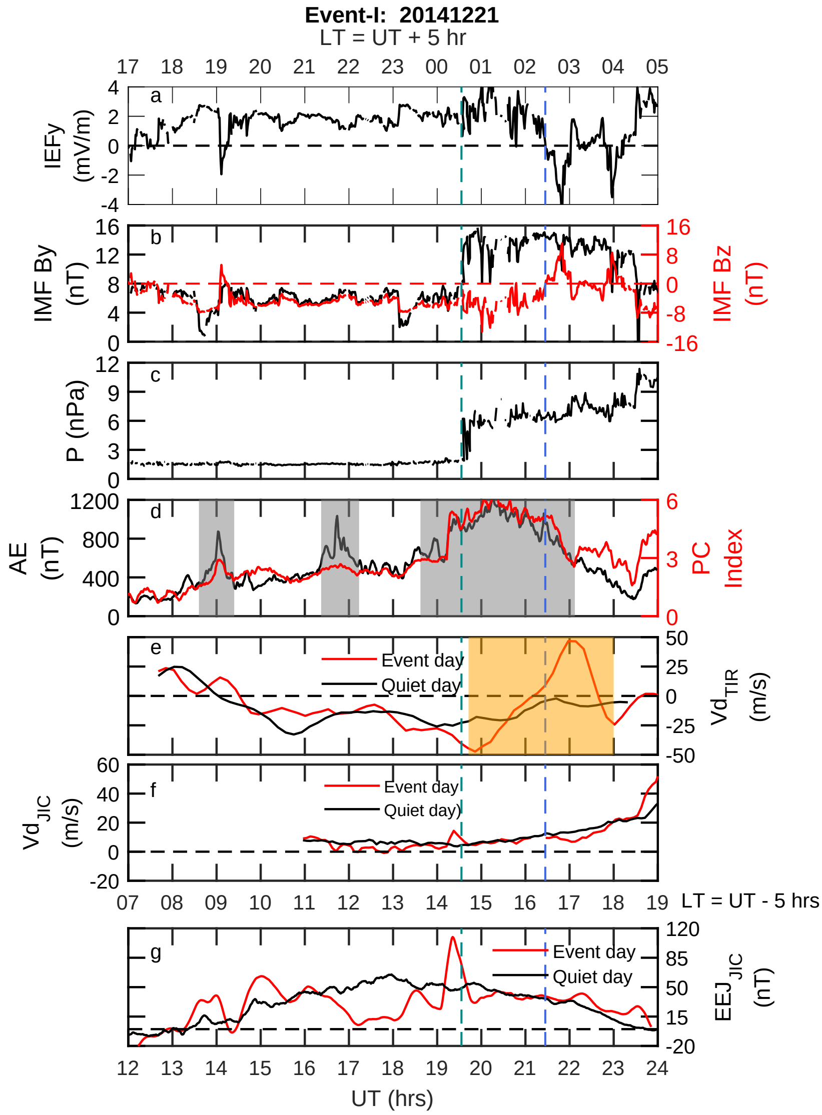

Figure 6.2: Panels a-d depict variations in (a) IEFY, (b) IMF By (in black) and IMF Bz (in red), (c) Solar wind pressure (P), and (d) AE (in black) and PC (in red) on 21-22 December, 2014 (Event-I). Panels e, f, and g represent the variations in vertical drifts over Tirunelveli (Vd_{TIR}), over Jicamarca (Vd_{JIC}), and EEJ strength over Jicamarca (EEJ_{JIC}). The variations in Event-I and quiet day are shown with red and black colored lines in panels e-g. Two dashed vertical lines are marked with cyan (at 1933 UT) and blue (at ~2130 UT) colors in all the panels. In panel d, enhancements in AE indices are marked with gray colored rectangular boxes during 1336-1424 UT, 1622-1713 UT, and 1837-2207 UT. An orange colored rectangular box (1942-2300) is also marked to show the post-midnight enhancement in vertical drift over Tirunelveli in panel f.

In Figures 6.2e-g, the red and black colored lines are used to show the variation of Event-I and quiet day, respectively. Two dashed vertical lines are shown in all panels with cyan (at 1933 UT) and blue (at ∼2130 UT) colors. An orange rectangular box is used to highlight the post-midnight peak in vertical drift in Figure 6.2d. Two spikes and one broad peak in the AE index are observed in Figure 6.2c at 1400 UT, 1645 UT, and ∼ 1900 UT, respectively, which are marked with gray color rectangular boxes. AE is, in general, used to find any substorm activity. Although AE is used here, the occurrence of substorm will be verified more reliably from Figure 6.3. The vertical drift from evening hours to midnight hours over the Indian sector is small in amplitude (both upward and downward). This is despite IEFy being continuously eastward (positive) during the whole night except on a few occasions (at 1406 UT, 2150 UT, and 2245 UT) when it is found westward (negative). Before 1933 UT or Indian midnight hours (vertical line in cyan), IEFy is positive, which is expected to generate westward PP electric field perturbations. However, there is no significant change observed in vertical drift. Now, we focus on the orange box in Figure 6.2e. At ∼1933 UT (vertical dashed line in cyan), sudden changes in IMF By (increased by 8 nT) and solar wind pressure (increased by 4.2 nPa) are noticed. At the same time, vertical drift starts to increase. In fact, both IMF By and P remain elevated after the initial step-like increase at ∼1933 LT. It is interesting to note that the AE index starts increasing just after ∼1800 UT when IEFy starts increasing from ∼2 mV/m (it was predominantly less than 2 mV/m before this time) to ∼4 mV/m. Not only that, AE peaks (∼1200 nT) at the same time (∼2030 UT) as IEFy (see the interval between cyan and blue dashed lines). Therefore, the AE index rises with an increase in IEFy and decreases with a decrease in IEFy. It appears that IEFy predominantly controls the enhancement in the auroral electrojet at this time. At ∼1933 UT, a sudden change in solar wind dynamic pressure may be expected to be more conspicuous over the dayside. Since we do not see any significant change at this time on the dayside (see Vd and EEJ over the Jicamarca sectors in Figures 6.2 f and g), we infer that the contribution due to ram pressure-induced transient electric field perturbations are minimal during post-midnight hours. Therefore, it seems that the combined effects of IMF By and IEFy enhance Vd_{TIR} from ∼-20 ms^{-1} to +20 ms^{-1} during 1930 UT - 2130 UT. We conjecture that IMF By has played an important role here as the polarity of the PP electric field is expected to be westward at this local time [e.g., *Fejer et al.*, 2008b], and this should cause downward vertical drift. Therefore, as IEFY increases at this time, we see an eastward electric field perturbation over the equatorial ionosphere. On the other side (at the antipodal location), it is surprising to note that Vd_{JIC} is not conspicuously affected. However, it is interesting to note that during 2030 - 2130 UT, the polarity of the electric field is eastward over both Indian and Jicamarca sectors. This indicates (as discussed in Chapter-5) the influence of IMF By effect. At 2130 UT (0230 LT), IEFy changes suddenly from eastward (positive) to westward (negative), which is expected to cause OS electric field perturbations. Although during this overshielding process, IEFy turns from +2 mV/m to almost -4 mV/m, Vd_{TIR} increases, and the amplitude reaches ∼ 50 ms^{-1}. Interestingly, at this time, Vd_{JIC} shows a negative deviation (w.r.t. the quiet time variation). This is, in general, expected [e.g., *Kelley and Makela*, 2002; *Chakrabarty et al.*, 2017] for antipodal locations that are located at the night and day sectors. We will argue later in the discussion section that the OS electric field at this time is not sufficient to explain the +50 ms^{-1} vertical drift over the Indian sector. It is to be noted that three peaks in AE are noticed in Figure 6.2d. These auroral electrojet intensification events might generate sufficient joule heating over the polar region, leading to disturbance dynamo (DD) activity. This aspect will again be explored in Figure 6.4. Another interesting point to be noted here is a substantially scaled-down response of these vertical drift enhancement events over the Jicamarca sector. One exception here is probably the only ephemeral and conspicuous spike in EEJ (and vertical drift) just after 1900 UT (1400 LT) concurrently with the step-like increase in AE within the broad enhancement and just before the step-like pressure increase. Therefore, during this space weather event, we note significant differences in the ionospheric response over the Indian (post-midnight) and Jicamarca (afternoon) sectors.

In order to identify the presence of substorm on Event-I (21 December 2014),

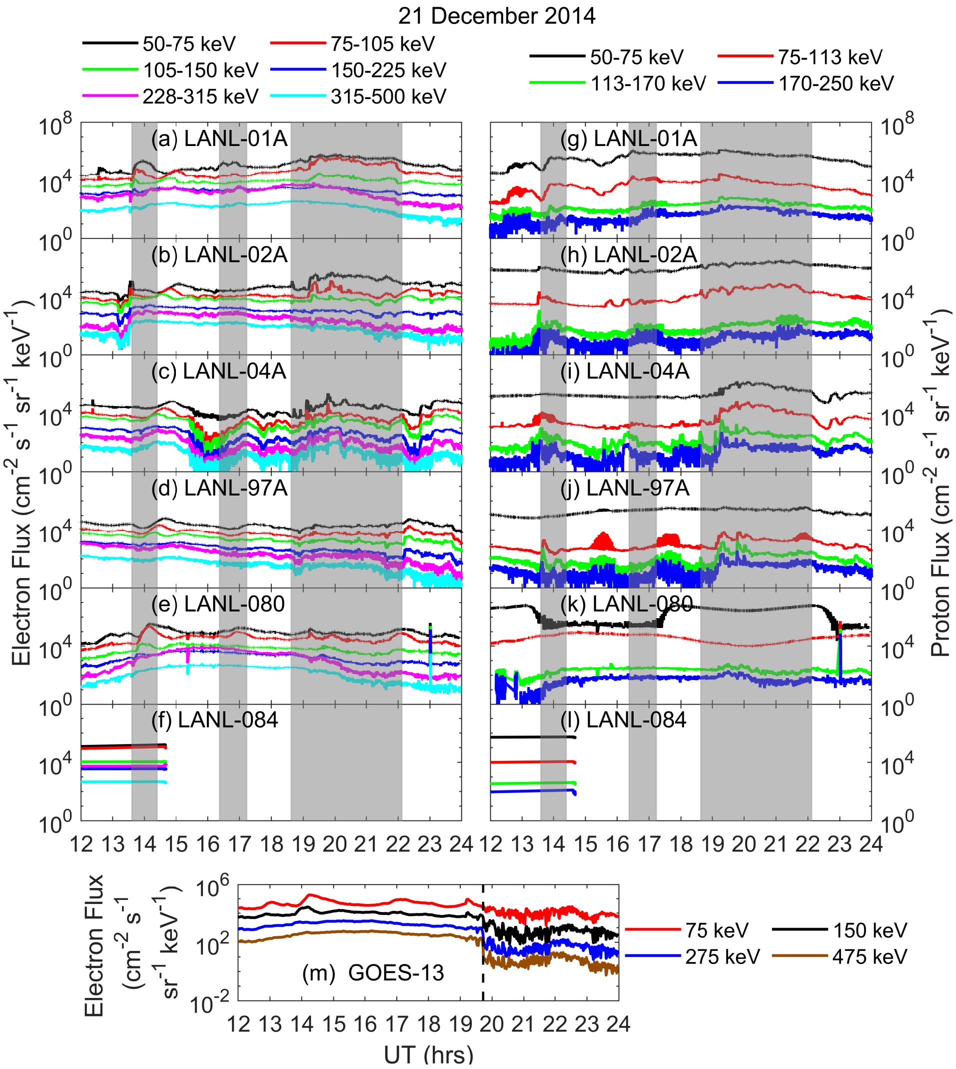

Figure 6.3: Panels a-f and g-l represent the electron and proton flux variations measured by six LANL satellites (LANL-01A, LANL-02A, LANL-04A, LANL-97A, LANL-080, LANL-084) during 1200-1900 UT on 21 December 2014 for a number of energy channels mentioned at the top of the figure. Three intervals- ∼ 1336-1424 UT, ∼1620-1715 and ∼1837-2210 UT are marked with gray color rectangular box in all panels (a-l) similarly marked in Figure 6.2d. Panel m also shows the variations of electron flux at four energy channels (depicted in the right hand side of the panel m) measured by geosynchronous satellite GOES-13. A dashed vertical line is drawn at 1943 UT where the dispersion particle injection is observed.

Figure 6.3 is used. The subplots a-f and subplots g-l show the variations in the electron and ion fluxes measured from the geosynchronous orbit, respectively. The LANL geosynchronous satellites are LANL-01A, LANL-02A, LANL-04A, LANL-

97A, LANL-080, and LANL-084. Six energy bins for electrons and protons are used in this study. The electron energy bins are 50-75 keV, 75-105 keV, 105-150 keV, 150-225 keV, 228-315 keV and 315-500 keV, respectively, whereas the ion energy bins are 0-75 keV, 75-113 keV, 113-170 keV, 170-250 keV, 250-400 keV, 400-670 keV, respectively. Three intervals- ∼1336-1424 UT, ∼1620-1715 UT, and ∼1800-2210 UT UT are marked with gray-colored rectangular boxes similar to Figure 6.2d. No conspicuous dispersionless particle injections are observed in electron fluxes and proton fluxes over the marked regions. Further, to check the occurrence of any substorm activity, electron fluxes from GOES-13 are shown in Figure 6.3m. Electron fluxes from four energy channels (75 keV, 150 keV, 275 keV, and 475 keV) are used. Owing to this significant enhancement in AE for about 4 hours in combination with sustained positive IEFy condition (southward IMF Bz) before the post-midnight vertical drift enhancement event on this night, eastward DD electric field perturbation cannot be ruled out.

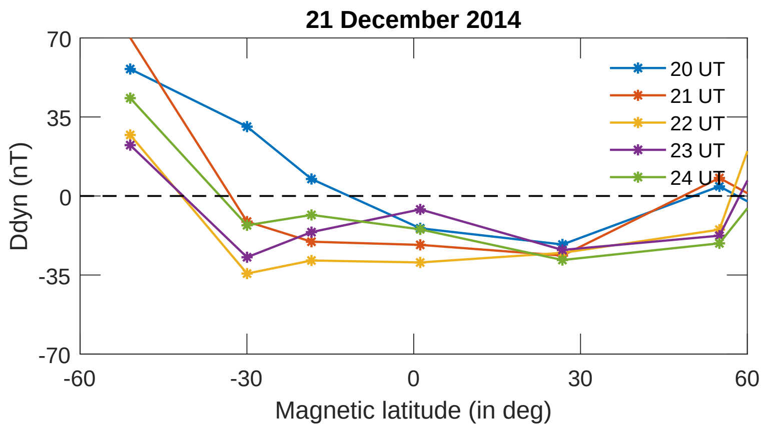

Figure 6.4: Latitudinal variations of disturbance dynamo (D_{dyn}, magnetic disturbances) on 21 December 2014 during 20-24 UT along Jicamarca longitudes.

Figure 6.4 represents the latitudinal magnetic disturbance (D_{dyn}) during Event-I (21 December 2014) on 2000 UT (in blue), 2100 UT (in red), 2200 UT (in yellow), 2300 UT (in violet) and 2400 UT (in green) along the Jicamarca longitudes. It is noticed that the maximum changes in D_{dyn} occur at 23 UT (violet line). Over the dip equatorial region, although D_{dyn} is not significantly amplified by equatorial Cowling conductivity to reach positive values. Other features [e.g., *Amory-Mazaudier et al.*, 2017], like the high value of D_{dyn} closer to the mid latitudes and decrease over low latitudes are also noticed. Therefore, the basic features of D_{dyn} are seen, although the amplitudes are not high. Therefore, weak DD electric field perturbations can be expected over Jicamarca at this time (∼2300 UT or 1800 LT). Therefore, at an antipodal location (Indian sector), a finite contribution from DD electric field cannot be ruled out during the enhanced vertical drift event in the post-midnight hours.

So far, we have discussed Event-I, and Event-II (23 December 2014) will be discussed in Figures 6.5 and 6.6. In Event-II, also one sees an overshielding event occurring at ∼2130 UT when IEFy, after being positive (southward IMF Bz) for some time, flips to have negative polarity. In fact, the changes in IEFy during this overshielding event (from +6 mV/m to -4 mV/m) are larger than the first event, where IEFy changed from +2 mV/m to -4 mV/m. Anomalous post-midnight enhancements in vertical drift are observed over Tirunelveli on this night also (similar to Event-I), and the peak vertical drift reaches ∼+20 ms^{-1} just (Figure 6.5e) after 2200 UT (or 0300 LT). Therefore, if we compare Event-I and Event-II, we see less eastward electric field perturbations corresponding to an overshielding event of a larger magnitude. Figures 6.5a-6.5e are similar to Figure 6.2a-6.2e but for 23 December 2014. In the same way, Figure 6.5f is similar to Figure 6.2g but for Event-II. This is because Vd_{JIC} measurements are not available for this event. In Figure 6.5d, broad peaks in AE and PC indices are marked with a gray rectangular box (interval 2052-2252 UT) where the substorm activity is suspected. This aspect will be verified in Figure 6.6. It is noted that vertical drift is observed slowly increases when AE becomes higher than 400 nT. In Figure 6.5e, this increase in vertical drift (with a peak amplitude of ∼21 ms^{-1} at ∼2230 UT or 0330 LT) during post-midnight hours over the Indian sector is marked with orange colored rectangular box (Interval ∼2106-2306 UT). Two vertical dashed lines with blue (∼2133 UT) and violet (∼2205 UT) colors are marked in Figures 6.5a-6.5f to show At ∼2133 UT, the IEFy is changed suddenly from positive (+6 mV/m) to negative (∼-4mV/m), which indicates the possible generation of the OS electric field. The OS electric field imposes eastward electric field perturbations over the

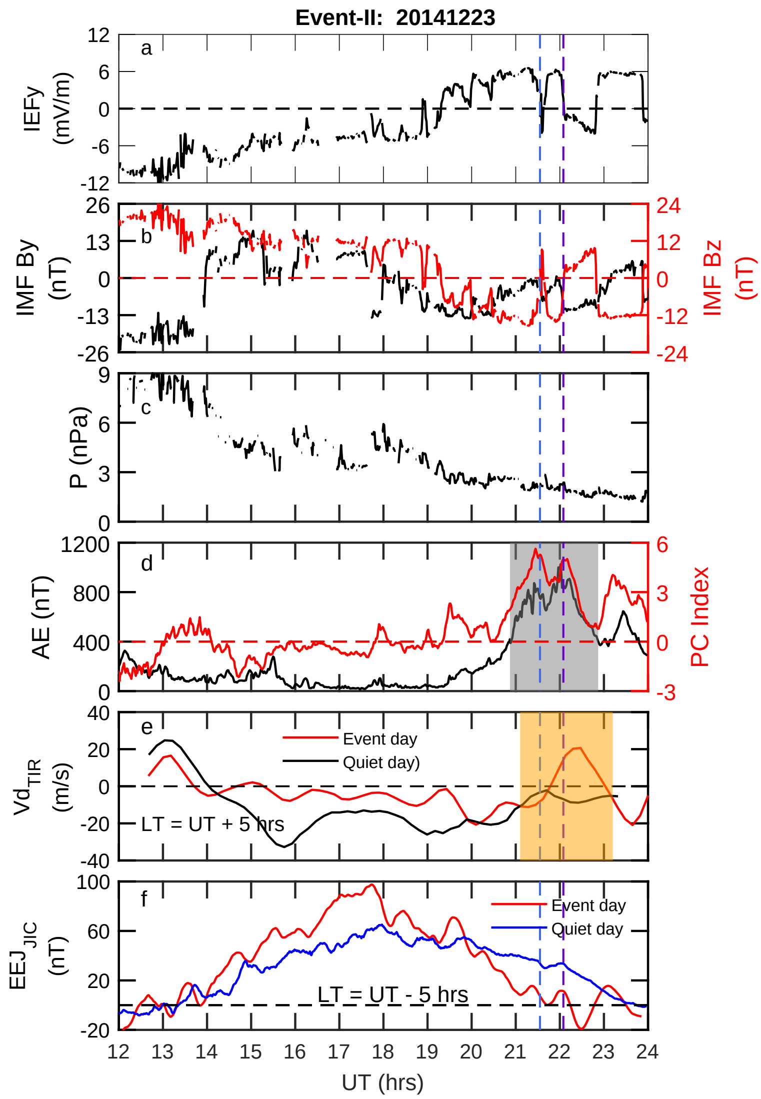

Figure 6.5: This plot is for Event-II (23 December, 2014). This is same as Event-I (Figure 6.2) but Vd_{JIC} measurements are not available for this event. A broad peak in AE and PC indices are marked by gray color rectangular box in panel d. In panel e, post-midnight peak in vertical drift is highlight by orange rectangular box. Two dashed vertical lines with blue (at 2133 UT) and purple (at 2205 UT) colors are drawn to mark the change in IEFy from positive to negative.

equatorial ionosphere that generates the upward drift. It can be seen in Figure 6.5e that vertical drift changes at a faster rate after the blue vertical dashed line. After this overshielding event, IEFy becomes positive again and remains positive for less than 30 minutes. After 30 minutes from the blue dashed vertical line, IEFy becomes negative again, although the change in amplitude is less compared to the previous overshielding event. An eastward OS electric field perturbation is again imposed that takes the vertical drift further upward. It is to be noted that the vertical drift data has 10 min cadence, and therefore, it does not capture the recovery of IEFy in between the two overshielding events. However, signatures of the two overshielding events and the intermediate recovery are clearly seen in AE and PC indices (Figure 6.5d). Interestingly, the EEJ strength shows a decrease (Figure 6.5f) after each overshielding event which is consistent with the earlier results [e.g., *Kikuchi et al.*, 2003].

Figure 6.6 depicts the same variations as shown in Figure 6.3 but for Event-II (23 December 2014). A gray color rectangular box (interval ∼2052-2252 UT) is marked in Figures 6.6a-6.6l. It is interesting to note that a clear signature of dispersion-less particle injection is noted in electron (in Figures 6.6a, 6.6b, 6.6c, and 6.6e) and proton fluxes (in Figures 6.6i and 6.6j) of several LANL satellites that confirm the occurrence of substorm at this time. However, the most prominent signature is captured by the LANL-04A satellite, which is closed to the Indian longitudes (situated at 65°E). Electron fluxes of GOES-13 (Figure 6.6m) also capture the substorm activity at 2122 UT (marked by a black dashed vertical line). At this time, the electron fluxes of all energy channels increase simultaneously. This suggests the onset of a substorm at 2122 UT. Therefore, the enhancements in AE and PC indices on this night seem to be influenced by positive IEFy (Storm contribution) and the substorm-induced particle precipitation. More importantly, the influence of substorm-induced electric field perturbations at this time over the equatorial ionosphere cannot be ruled out. Another important point to be noted here is the occurrence of the overshielding events coinciding with the two peaks in the AE and PC indices and not with the onset of the substorm event. In fact, AE and PC indices start increasing as IEFy starts turning towards positive direction. The implications of these results will be discussed in the discussion section.

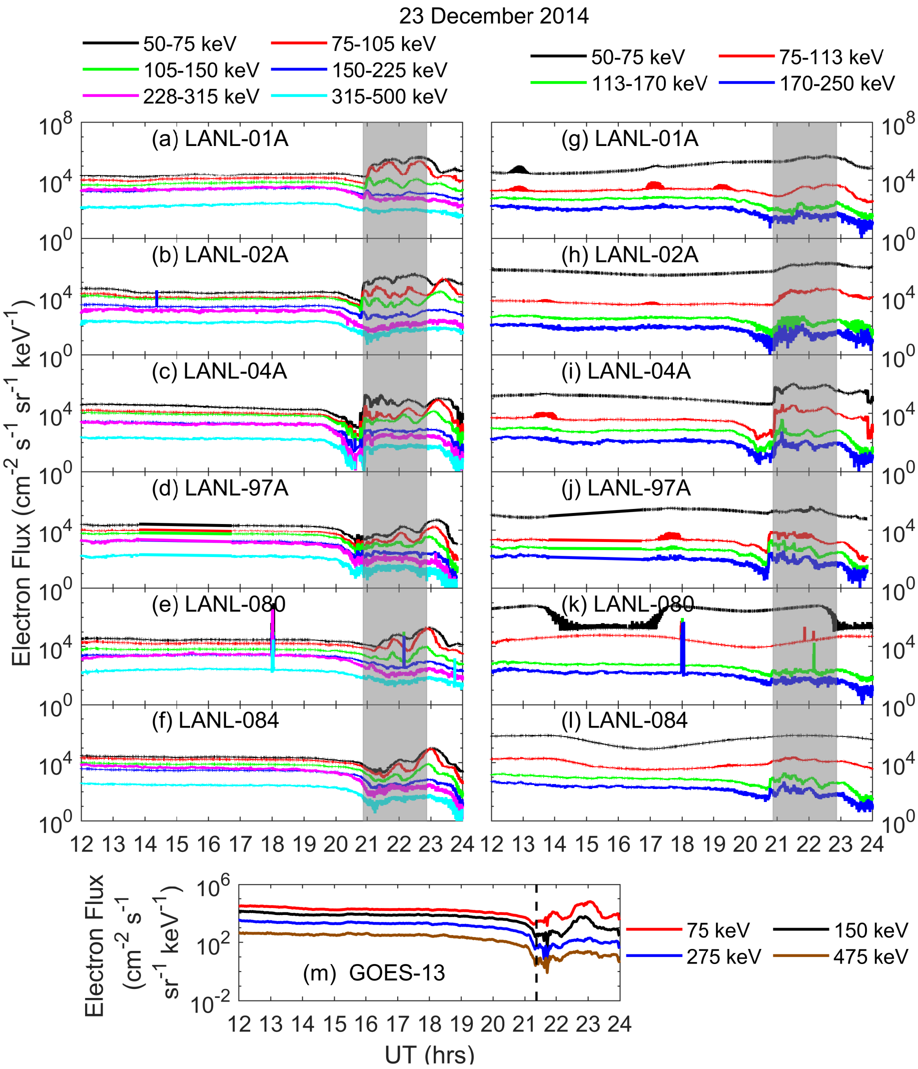

Figure 6.6: Same as Figure 6.3 but for 23 December 2014. Interval 2052-2252 UT is marked with brown color rectangular box in panels a-l where the dispersionless particle injection can be identified in both electrons and ions' fluxes. In panel m, a dashed vertical line is shown at 2122 UT where the dispersion particle injection is also noted.

6.4 On the evaluation of quiet time vertical drift reference

In Chapter-5, the vertical drift on 28 November 2014 is used as quiet reference for the dip equatorial vertical drift over Tirunelveli during post-sunset hours. In this chapter, we again use the post-midnight vertical drift variation on 28 November 2014 as a quiet time reference. Figure 6.7 shows a comparison of vertical drift on

28 November 2014 (in black) with the quiet time average vertical drift (in blue) over Tirunelveli and quiet time average ROCSAT vertical drift (in red) along 60°E longitude. Four quiet days (28 November 2014, 11, 17, and 27 December 2014) in this season and solar epoch are chosen to construct the average quiet vertical drift variation over Tirunelveli. It is to be noted that during post-midnight hours, maximum Ap values of all four days are 5, 4, 8, and 18, and the Sym-H and AL values are more than ~-13 nT and ~-200 nT, respectively. In this Figure, we note that regardless of the choice of quiet time vertical drift reference, the vertical drift is downward all the time during post-midnight hours during quiet time, whereas unambiguously upward vertical drifts ($\sim$ 50 ms^{-1} in event-I and $\sim$ 20 ms^{-1} in Event-II) are observed around $\sim$ 0300 LT in both the events. Therefore, similar to Chapter-5, it can be inferred that although the magnitudes of the perturbation electric fields may vary depending on the choice of the quiet time reference, the inference on the polarity of the perturbation electric fields remains unchanged. As stated in Chapter-5, we reiterate that we used a single day quiet time reference because this allowed us to compare the OI 630.0 nm airglow intensity variations during event day with the quiet time variations.

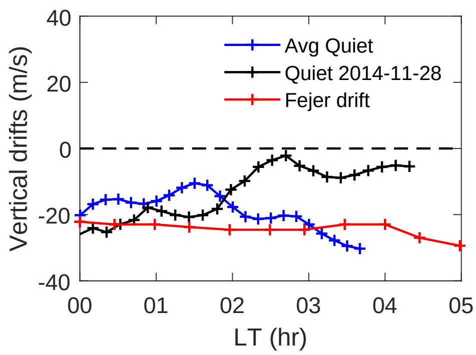

Figure 6.7: Local time variations of measured average vertical drift (in blue) and a typical quiet day (28 November 2014) vertical drift (in black) over Tirunelveli are shown. In addition, these variations also compares with the ROCSAT quiet time average vertical drift (in red) along 60°E longitude [Fejer et al., 2008a].

6.5 Discussion

The quiet time vertical drift is downward during the post-midnight hours [*Fejer et al.*, 2008a]. Therefore, it is clear that if the vertical drift becomes upward during post-midnight hours, space weather induced electric field perturbations are the prime suspects. At first look, since the overshielding events are found to be very prominent in the two cases, we compared the changes in vertical drift corresponding to these overshielding events. It is noted that the perturbations in vertical drift during post-midnight hours are not commensurate with the degree of the respective overshielding events marked by the net changes in IEFy from positive to negative direction within a short period of time. This suggests that there are contributions from other electric field drivers in these cases that cause these anomalous responses. In the previous chapter, we have discussed the influence of substorm and IMF By over the dip equatorial ionosphere during the post-sunset hours on 24 December 2014. It was shown that during post-sunset hours, substorm can generate westward electric field perturbations over the equatorial ionosphere. In this chapter, the role of a substorm-induced electric field perturbations is investigated during post-midnight hours on 23 December 2014. It is known that vertical drift becomes upward on many occasions during post-midnight hours in June solstice and in low solar activity period [e.g., *Pham Thi Thu et al.*, 2022; *Zhang et al.*, 2015; *Stoneback et al.*, 2011; *Yizengaw et al.*, 2009]. However, this is not the situation here, as these observations pertain to neither June solstice, nor solar minimum period. Moreover, significant upward drifts in the post-midnight hours are observed on 21 (Event-1) and 23 (Event-II) December 2014 over the Indian dip equator during minor geomagnetic storms. Therefore, these observations clearly suggest that the observed drift perturbations during Events-I and II are associated with space weather induced electric field perturbations and OS electric field perturbations are not the only driver in both cases. The peak in Vd_{TIR} during Events-I and II are observed at 2200 UT and 2225 UT with amplitudes of ~ 50 ms^{-1} and ~ 21 ms^{-1}, respectively (Figure 6.1a and 6.1d). These post-midnight amplitudes are not only higher than the quiet time reference drifts but also larger than the PRE-associated vertical drifts on the respective dates. However, unlike the post-sunset hours, these enhanced vertical drifts (or zonal electric fields) during post-midnight hours do not produce any perceptible changes in the plasma distribution over low latitudes (see Figure 6.1b-f). It is because of the presence of depleted plasma density in the F region over the equatorial and low latitudes, and as a consequence, even if the plasma fountain process gets reinvigorated by the enhanced electric field, the amount of plasma that gets transported at this hour is not significant. Therefore, in the ensuing paragraphs, we will try to understand the drivers of the space weather induced electric field perturbations rather than the impact over the low latitude ionosphere.

We first focus on Event-I and try to understand the nature of the space weather induced electric field perturbations based on Figures 6.2, 6.3, 6.4. In panel 6.2e, a gradual increase in vertical drift over Tirunelveli (Vd_{TIR}) is observed to start at ∼ 2000. On careful scrutiny, it can be seen that this increase occurs in two steps. Vd_{TIR} starts to increase after 1933 UT (2433 LT). At this time, a sudden jump in IMF By (Figure 6.2b) is observed, with IEFy continuing ∼ 3 mV/m. A positive value of IEFy is expected to cause downward drift (westward electric field perturbation) at this local time [*Fejer et al.*, 2008b]. We already mentioned in the results section that pressure-induced transient electric field perturbations are not seen on the dayside. Hence, we assume that it does not have any significant impact on the night side also. Therefore, despite westward electric field perturbations are expected during 1933 - 2130 UT, we see vertical drift starts increasing, indicating eastward electric field perturbations. It happens because of the sharp change in IMF By at 1933 UT. *Chakrabarty et al.* [2017] showed strong evidence of the role of IMF By during post-sunset hours in the equatorial ionosphere and showed that identical polarity of electric field perturbations at the antipodal locations (in the Indian and Jicamarca sectors) is one of the clear indications of the IMF By influence. They explained this from the curl-free nature of the ionospheric electric field. Further, *Hui and Vichare* [2021], based on TIE-GCM simulations, suggested that IMF By influence is more effective around the terminator. However, in the present case, we see a possible

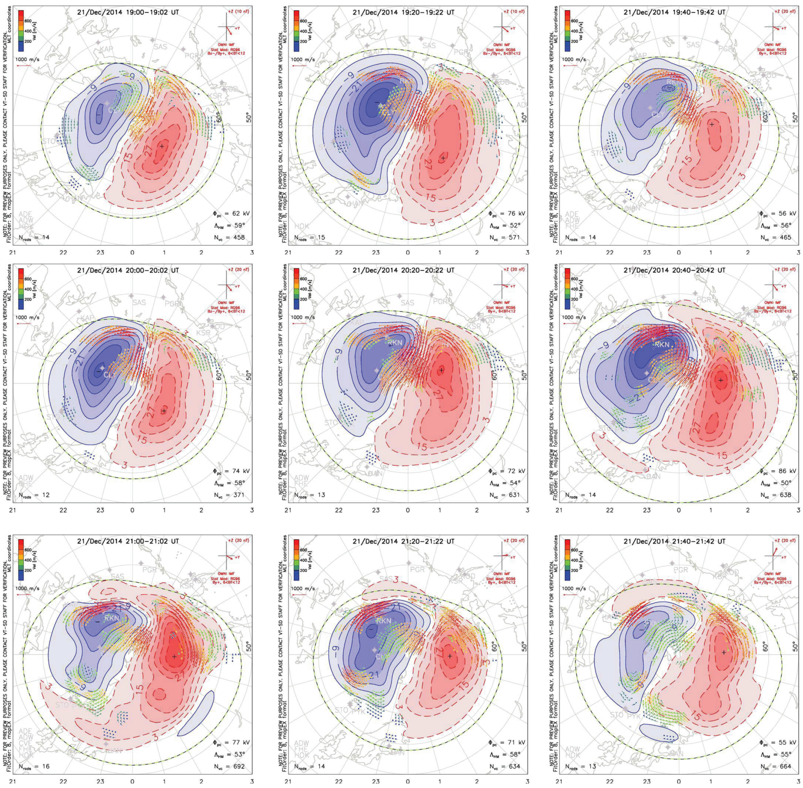

Figure 6.8: SuperDARN ionospheric convection maps on 21 December 2014 are presented in the top row (1900, 1920, and 1940 UT from the left to the right), middle row (2000, 2020, and 2040 UT) and bottom row (2100, 2120, 2140 UT). The orange and blue cells represent the dawn and dusk cells respectively. After sudden increase in IMF By at ~ 1933 UT under strongly positive IEFy condition, the size of dawn cell increases and it seems to gradually enter into the dusk cell. Note, Tirunelveli, being in the post-midnight sector, is located under the dawn cell (red) while Jicamarca, being in the afternoon sector, is located under the dusk cell initially. Here we assume that cell configurations and electrodynamic boundary between the two cells are similar even over the equatorial latitudes.

influence of IMF By in the equatorial ionosphere during post-midnight hours. This is also supported by SuperDARN observations. The ionospheric plasma convection maps from SuperDARN radar over high latitudes from 1900 UT to 2240 UT with 20 minutes cadence are shown in Figures 6.8 and 6.9. Orange and blue colored cells represent the dawn and dusk cells, respectively. These contour maps have been used to indicate the effects of IMF By over the dip equatorial ionosphere as well during post-sunset hours [*Chakrabarty et al.*, 2017]. We use

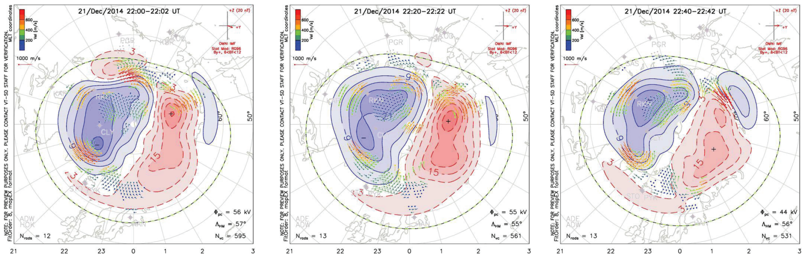

Figure 6.9: Similar to Figure 6.8 but for 2200, 2220 and 2240 UT (from left to right)

these maps to understand the possible role of IMF By during postmidnight hours over the dip equatorial ionosphere during Event-I. It is noted that during the sharp change in IMF By at 1933 UT, there was no change observed in both cells. However, at 2040 UT, the dawn cell enters the dusk cell from the morning side, and the size of the dawn cell increases. Owing to this, the dawnside polarity may become the same as that of the morning time polarity that is eastward. It is noted that the effects of IMF By are prominent before the occurrence of the overshielding effect at 2130 UT. After 1933 UT, due to OS electric field, the vertical drift becomes further upward and becomes maximum (50 ms^{-1}) at 2200 UT. Surprisingly, the change in IEFy is around 6 mV/m during the overshielding process. Considering a 10-15% penetration efficiency of OS electric field, an electric field perturbation of amplitude ∼0.6 mV/m is expected over the dip equator at this time. Considering the fact the quiet time vertical drift is expected to be downward at this local time, an externally imposed 0.6 mV/m cannot cause such a large vertical drift of +50 ms^{-1} unless one considers the previous eastward electric field perturbations (possibly due to the combined effects of IEFy and IMF By) that already enhanced the vertical drift to ∼-20 ms^{-1} to ∼+20 ms^{-1}. In fact, it is difficult to account for the difference between the peak drift (50 ms^{-1}) and 20 ms^{-1} (drift before the onset of the overshielding event) by taking even 1 mV/m OS electric field perturbations and 15% penetration efficiency. Therefore, it appears that some other factor may be additionally operational here. This motivates us to explore the contribution of DD electric field perturbations also at this time. It is noticed in Figure 6.4 that disturbance dynamo (DD) comes into action after the occurrence of the peak in vertical drift. In fact, from Figure 6.4, an indication of DD influence is seen at 23 UT. However, the effects of D_{dyn} over the dip equator are small in this case as the equatorial amplitude of D_{dyn} gets enhanced (but does not become positive). During DD, a large change in current is observed over the dip equator in general [*Zaka et al.*, 2009; *Amory-Mazaudier et al.*, 2017]. Therefore, for Event-I, it appears that IEFy, IMF By and disturbance dynamo have played their roles in enhancing the vertical drift over the equatorial ionosphere to touch +50 ms^{-1} during post-midnight hours. It is a challenging task though to quantify their contributions.

Let us now consider Event-II (23 December 2014). In this case, also the post-midnight peak in vertical drift is noticed with the amplitude of $\sim$ 21 ms^{-1} at 2230 UT (0330 LT). It is noticed that solar wind pressure is decreasing, and IMF By is negative. Therefore, the effects of solar wind dynamic pressure and IMF By are ruled out for this event. It is noticed that Vd_{TIR} increases with the enhancements in the AE index. Similar to Event-I, in this case also, we see that while IEFy is positive, Vd_{TIR} increases during post-midnight hours. As discussed earlier, we expect the westward polarity of the PP electric field during post-midnight hours [e.g., *Fejer et al.*, 2008b]. Therefore, the polarity of the PP electric field is anomalous in this case also. It is noticed that a substorm has occurred at 2100 UT, which is confirmed by the different electron channels of LANL as well as GOES-13 satellites at 2122 UT. At 2133 UT, IEFy turns negative (magnitude is $\sim$ -6 mV/m) from a positive (magnitude is $\sim$ 4 mV/m) value. The change is around 10 mV/m. Owing to this sharp change in IEFy, an OS electric field gets generated that generates eastward electric field perturbation (provides upward drift) over the dip equator. However, it is to be kept in mind that IEFy is $\sim$+6mV/m when the vertical drift starts increasing on this night. And most importantly, this occurs before the first and the larger overshielding event. At this local time, we expect westward electric field perturbations due to prompt penetration of IEFy [e.g., *Fejer et al.*, 2008b]. Despite that, the downward drifts start reducing. This suggests that substorm-induced eastward electric field perturbations might have played a role in over-compensating the westward penetration electric field perturbations due to IEFy. We feel that the overshielding electric field adds to this eastward electric field perturbation afterward. If we consider 10% penetration efficiency of the total change in IEFy during the overshielding event ($\sim$10 mV/m), the equatorial electric field perturbation amplitude should be 1 mV/m that, in turn, should generate a vertical drift of $\sim$25 ms^{-1}. However, considering the peak vertical drift at this time is $\sim$+21 ms^{-1} and the vertical drift changes from -10 ms^{-1} to +21 ms^{-1}, the total change in drift is 31 ms^{-1}. This cannot be explained by only 1 mV/m electric field perturbation due to the overshielding process. This also indirectly suggests that the substorm might have generated eastward electric field perturbations before the overshielding-induced eastward electric field perturbations. Therefore, the peak in vertical drift during the post-midnight hours in Event-II is caused by both substorm-induced and OS electric fields. Therefore, these investigations bring out the important role of drivers other than IEFy in generating anomalous impacts of penetration electric field on the dip equatorial ionosphere during post-midnight hours. Note, the DD related electric field in Event-II is not discussed as IEFy is negative. This is why D_{dyn} in case of Event-II is not derived.

6.6 Summary

The upward vertical drifts over the equatorial ionosphere during the post-midnight hours on 21 and 23 Dcember 2014 are investigated. It is found that a smaller overshielding event on 21 December, 2014 makes a larger impact on the equatorial vertical drift compared to the stronger overshielding event on 23 December, 2014. Investigations reveal the additional roles of IMF By, overshielding induced electric field and disturbance dynamo electric field that determines the response of vertical drift on 21 December, 2014. On the other hand, it is found that substorm and overshielding induced electric field can explain the response of the equatorial vertical drift during 23 December 2014. Therefore, this investigation reveals the important roles of drivers other than IEFy in generating the so-called anomalous responses in the equatorial ionosphere during post-midnight hours.

Chapter 7

Summary and Future direction

In the present thesis, the low latitude F region ionosphere is studied during quiet and disturbed space weather conditions in the pre-and post-sunset hours. In the course of this thesis, the post-sunset enhancements over the EIA crest region are investigated, and it is found that they, in general, can occur any time after 1930 LT. These enhancements are primarily driven by the pre-reversal enhancement (PRE) of the zonal electric field/vertical plasma drift over the dip equator through the equatorial plasma fountain process. The post-sunset enhancement over the EIA crest region shows the seasonal, solar cycle, and solar flux dependence as that of PRE. These enhancements over the EIA crest region are prominent during December solstice and Equinox in the high solar activity period only, and this is similar to the corresponding variations in PRE. It is also shown that one can expect plasma density enhancements over the EIA crest region when the solar flux levels exceed $\sim$ 110 sfu in December solstice and Equinox. Interestingly, results obtained from this thesis additionally suggest that PRE is a necessary condition for post-sunset enhancement over the EIA crest region, and it can not solely enhance the plasma density over this region. It is shown that the latitudinal plasma density gradient works in tandem with the PRE to decide the degree of enhancement of the plasma density over the EIA crest region. In general, plasma takes 3-4 hrs to reach the EIA crest region from the dip equator through the daytime equatorial plasma fountain. In contrast, the re-invigorated plasma fountain due to PRE supplies the plasma to the EIA crest region within 1.7 hrs.

This shorter response time during the evening hours of the EIA crest region is explained based on the transportation of F region plasma from $5° - 10°$ magnetic latitudes to the EIA crest region.

During the course of the present work, the electric field perturbations are studied during the pre-and post-midnight hours on a number of occasions in December 2014. Enhanced PRE during disturbed periods can help to sustain the enhanced post-sunset plasma density over the EIA crest region for a longer duration with respect to a quiet day. On the contrary, it is important to evaluate how enhanced electric field perturbations during post-midnight hours affect the low latitude ionosphere. In view of this, we investigated a few anomalous electric field perturbations during both post-sunset and post-midnight hours to evaluate their impact on low latitude ionosphere with respect to the quiet time patterns. In one case, it is noticed that when the prompt penetration (PP) electric field magnitude is expected to be higher, the change in vertical drift over the dip equator is less and vice-versa during the post-sunset hours. Investigations revealed that this unusual perturbation in the electric field over the dip equator occurred due to the additional modulating effects of the dawn-dusk component of interplanetary magnetic field (IMF By) and substorm-induced electric field perturbations. On other occasions, anomalous electric field perturbations are also noticed during the post-midnight hours, similar to PP electric field-related anomalous electric field perturbations over the dip equator during post-sunset hours mentioned earlier. It is observed that when the overshielding (OS) electric field perturbations is expected to be stronger, the change in the vertical drift over the dip equator is smaller and vice-versa during post-midnight hours. These unusual changes in vertical plasma drifts are also attributed to the modulating effects caused by the IMF By, substorm-induced electric field, and pressure-induced electric field. The work in this thesis suggests that the IEFy can not explain the electric field perturbations over the dip equator on many occasions. One has to verify the role of other drivers like solar wind pressure-induced transient electric field perturbation, effects of IMF By, substorm-induced electric field, and disturbance dynamo electric field perturbations. It is also noticed that if PRE-like enhancement occurs during the post-midnight hours, the change in plasma distribution over the EIA crest region is not significant. This indicates that if ionization is less or plasma density gradient is not significant over low latitudes, PRE-like electric field enhancement during post-midnight hours (due to space weather disturbance) cannot cause plasma density enhancements over the EIA crest region.

Future work: The present thesis addresses a few scientific problems of the low and equatorial F region ionosphere in pre-and post-midnight hours during the quiet and disturbed space weather conditions. During the course of this work, several interesting scientific issues are identified that require further critical attention. Understanding these issues will bring in a comprehensive understanding of the low latitude ionosphere under varying space weather conditions.

In Chapters- 3 and 4, enhancements in plasma density over the EIA crest regions is observed during the evening hours in the June solstice. In general, these enhancements occur during the PRE hours. Further, it is noticed that the amplitudes of these enhancements are not consistent with the solar flux levels similar to the post-sunset density enhancements in December solstice and Equinox. The exact cause(s) of evening hour enhancements over the EIA crest region during the June solstice are not very clear and this requires further attention.

The PRE-associated vertical drifts are higher during the December solstice [*Fejer et al.*, 2008a]. It is noticed in Chapter-4 that latitudinal plasma density gradients are also higher during the December solstice. Both parameters are relatively small in June solstice. These parameters are essential for understanding the plasma distribution over the low latitude ionosphere. It is important to address the cause of the higher latitudinal plasma density gradient during the post-sunset hours in December solstice. The simultaneous observations of ionospheric plasma density in altitude and latitude are unavailable. Therefore, a modeling investigation is needed to understand this aspect. Another problem comes out from Chapter-4 is that the vertical drifts are more negative (more downward) during the December solstice and Equinox. This can help to understand the process of reverse plasma fountain in a much better way [*Balan et al.*, 2018; *Yadav et al.*, 2020].

During the investigation of solar flux dependence of post-sunset enhancement in Chapter-4, it is found that during geomagnetically quiet periods, the integrated enhancements in VTEC over the EIA crest region get saturated at higher solar flux levels. It is similar to the behavior of PRE over the dip equator that was reported earlier [e.g., *Fejer et al.*, 1991; *Ramesh and Sastri*, 1995]. The cause(s) of the saturation of PRE and post-sunset enhancements over the EIA crest are not very clear. Continuous measurements of the vertical drifts over the dip equator and VTEC over the EIA crest region are required to solve this issue. For better understanding, models like TIE-GCM, SAMI-3, and GITM can also be used.

The post-sunset enhancement in VTEC over the EIA crest region over the Indian sector changes more rapidly with solar flux levels during Equinox than in the December solstice (See the slope in Figure 4.6). Interestingly, this feature is consistent with the variations in PRE over the Indian (Chapter-4) but not over the Jicamarca (Figures 4.11 and 4.12) sectors. It could possibly happen due to the enhanced sensitivity of conductivity and electric field to the solar flux levels over the Indian sector in Equinox than in December solstice. This proposition is speculative at present and requires detailed investigations.

The results in Chapters-5 and 6 show an apparent violation of the conventional paradigm of the electric field perturbations over the low latitudes ionosphere due to interplanetary electric field. It is shown that IMF By can change the polarity of the PP electric field over the dip equator. However, the exact role of IMF By and its amplitude over low latitudes is not very clear. To address this aspect, a modeling approach is required. Similar to IMF By, the perturbations in the equatorial ionosphere due to the substorm-induced electric field fluctuations require detailed investigations. The polarity of substorm-induced electric field is another topic that needs further attention.

As shown in Chapters-5 and 6, if several space weather perturbations occur at the same time, their exact role over low latitude electric perturbations can not be addressed separately very easily. This requires a modeling approach.

Bibliography

Abdu, M., Brum, C., Batista, I., Sobral, J., de Paula, E., and Souza, J. (2008), Solar flux effects on equatorial ionization anomaly and total electron content over brazil: Observational results versus iri representations, *Advances in Space Research*, *42*(4), 617–625, doi:https://doi.org/10.1016/j.asr.2007.09.043.

Abdu, M. A., De Souza, J. R., Sobral, J. H. A., and Batista, I. S. (2006), *Magnetic Storm Associated Disturbance Dynamo Effects in the Low and Equatorial Latitude Ionosphere*, pp. 283–304, American Geophysical Union (AGU), doi:https://doi.org/10.1029/167GM22.

Abdu, M. A., Nogueira, P. A. B., Santos, A. M., de Souza, J. R., Batista, I. S., and Sobral, J. H. A. (2018), Impact of disturbance electric fields in the evening on prereversal vertical drift and spread f developments in the equatorial ionosphere, *Annales Geophysicae*, *36*(2), 609–620, doi:10.5194/angeo-36-609-2018.

Akasofu, S., and Chapman, S. (1961), The ring current, geomagnetic disturbance, and the van allen radiation belts, *Journal of Geophysical Research (1896-1977)*, *66*(5), 1321–1350, doi:https://doi.org/10.1029/JZ066i005p01321.

Akasofu, S.-I. (2021), A review of studies of geomagnetic storms and auroral/magnetospheric substorms based on the electric current approach, *Frontiers in Astronomy and Space Sciences*, p. 100, doi:https://doi.org/10.3389/fspas.2020.604750.

Alken, P., Thébault, E., Beggan, C. D., Amit, H., Aubert, J., Baerenzung, J., Bondar, T., Brown, W., Califf, S., Chambodut, A., et al. (2021), International geomagnetic reference field: the thirteenth generation, *Earth, Planets and Space*, *73*(1), 1–25.

Amory-Mazaudier, C., and Venkateswaran, S. V. (1988), Delayed ionospheric effects of march 22, 1979 studied by the sixth coordinated data analysis workshop (cdaw-6), in *Annales Geophysicae*, vol. 8, pp. 1–8.

Amory-Mazaudier, C., Bolaji, O. S., and Doumbia, V. (2017), On the historical origins of the cej, dp2, and ddyn current systems and their roles in the predictions of ionospheric responses to geomagnetic storms at equatorial latitudes, *Journal of Geophysical Research: Space Physics*, *122*(7), 7827–7833, doi:https://doi.org/10.1002/2017JA024132.

Anderson, D. (1971), Daily Variation of the Ionosphere F2 Equatorial Anomaly in the American & Asian Sectors, Ph.D. thesis, University of Colorado and High Altitude Observatory, NCAR.

Anderson, D. (1973a), A theoretical study of the ionospheric F region equatorial anomaly-I. Theory, *Planetary and Space Science*, *21*(3), 409 – 419, doi:https://doi.org/10.1016/0032-0633(73)90040-8.

Anderson, D. (1973b), A theoretical study of the ionospheric F region equatorial anomaly-II. Results in the American and Asian sectors, *Planetary and Space Science*, *21*(3), 421 – 442, doi:https://doi.org/10.1016/0032-0633(73)90041-X.

Anderson, D., and Roble, R. (1981), Neutral wind effects on the equatorial f-region ionosphere, *Journal of Atmospheric and Terrestrial Physics*, *43*(8), 835–843, doi:https://doi.org/10.1016/0021-9169(81)90061-1.

Anderson, D., and Rusch, D. (1980), Composition of the nighttime ionospheric f 1 region near the magnetic equator, *Journal of Geophysical Research: Space Physics*, *85*(A2), 569–574, doi:https://doi.org/10.1029/JA085iA02p00569.

Andriyas, T., and Andriyas, S. (2015), Relevance vector machines as a tool for forecasting geomagnetic storms during years 1996–2007, *Journal of Atmospheric and Solar-Terrestrial Physics*, *125-126*, 10–20, doi:https://doi.org/10.1016/j.jastp.2015.02.005.

Angelopoulos, V., Coroniti, F. V., Kennel, C. F., Kivelson, M. G., Walker, R. J., Russell, C. T., McPherron, R. L., Sanchez, E., Meng, C.-I., Baumjohann, W., Reeves, G. D., Belian, R. D., Sato, N., Friis-Christensen, E., Sutcliffe, P. R., Yumoto, K., and Harris, T. (1996), Multipoint analysis of a bursty bulk flow event on april 11, 1985, *Journal of Geophysical Research: Space Physics*, *101*(A3), 4967–4989, doi:https://doi.org/10.1029/95JA02722.

Aol, S., Buchert, S., and Jurua, E. (2020), Ionospheric irregularities and scintillations: a direct comparison of in situ density observations with ground-based l-band receivers, *Earth, Planets and Space*, *72*(1), 1–15, doi:https://doi.org/10.1186/s40623-020-01294-z.

Appleton, E. V. (1946), Two anomalies in the ionosphere, *Nature*, *157*(3995), 691–691.

Araki, T., Allen, J. H., and Araki, Y. (1985), Extension of a polar ionospheric current to the nightside equator, *Planetary and Space Science*, *33*(1), 11–16, doi:https://doi.org/10.1016/0032-0633(85)90137-0.

Arikan, F., Nayir, H., Sezen, U., and Arikan, O. (2008), Estimation of single station interfrequency receiver bias using gps-tec, *Radio Science*, *43*(4), doi:https://doi.org/10.1029/2007RS003785.

Aswathy, R. P., Manju, G., and Sunda, S. (2018), The response time of equatorial ionization anomaly crest: A unique precursor to the time of equatorial spread f initiation, *Journal of Geophysical Research: Space Physics*, *123*(7), 5949–5959, doi:10.1029/2018JA025469.

Ayyagari, D., Chakraborty, S., Das, S., Shukla, A., Paul, A., and Datta, A. (2020), Performance of navic for studying the ionosphere at an eia region in india, *Advances in Space Research*, *65*(6), 1544–1558, doi:10.1016/j.asr.2019.12.019.

Baker, D. (1985), Statistical analyses in the study of solar wind-magnetosphere coupling.

Baker, D. N., Pulkkinen, T. I., Angelopoulos, V., Baumjohann, W., and McPherron, R. L. (1996), Neutral line model of substorms: Past results and present view, *Journal of Geophysical Research: Space Physics*, *101*(A6), 12,975–13,010, doi:https://doi.org/10.1029/95JA03753.

Baker, D. N., Pulkkinen, T. I., Hesse, M., and McPherron, R. L. (1997), A quantitative assessment of energy storage and release in the earth's magnetotail, *Journal of Geophysical Research: Space Physics*, *102*(A4), 7159–7168, doi:https://doi.org/10.1029/96JA03961.

Balan, N., and Rao, P. B. (1984), Relationship between nighttime total electron content enhancements and vhf scintillations at the equator, *Journal of Geophysical Research: Space Physics*, *89*(A10), 9009–9013, doi:https://doi.org/10.1029/JA089iA10p09009.

Balan, N., Bailey, G., Moffett, R., Su, Y., and Titheridge, J. (1995), Modelling studies of the conjugate-hemisphere differences in ionospheric ionization at equatorial anomaly latitudes, *Journal of Atmospheric and Terrestrial Physics*, *57*(3), 279–292, doi:https://doi.org/10.1016/0021-9169(94)E0019-J.

Balan, N., Bailey, G., Abdu, M., Oyama, K., Richards, P., MacDougall, J., and Batista, I. (1997), Equatorial plasma fountain and its effects over three locations: Evidence for an additional layer, the F 3 layer, *Journal of Geophysical Research: Space Physics*, *102*(A2), 2047–2056, doi:10.1029/95JA02639.

Balan, N., Shiokawa, K., Otsuka, Y., Watanabe, S., and Bailey, G. J. (2009), Super plasma fountain and equatorial ionization anomaly during penetration electric field, *Journal of Geophysical Research: Space Physics*, *114*(A3), doi:https://doi.org/10.1029/2008JA013768.

Balan, N., Liu, L., and Le, H. (2018), A brief review of equatorial ionization anomaly and ionospheric irregularities, *Earth and Planetary Physics*, *2*(4), 257–275, doi:10.26464/epp2018025.

Barbier, D. (1961), Les variations d'intensité de la raie 6300 å de la luminescence nocturne, in *Annales de Geophysique*, vol. 17, p. 3.

Bartels, J. (1949), The standardized index, ks, and the planetary index, kp, *IATME Bull*, *97*(12b), 0001.

Bartels, J. (1957), The geomagnetic measures for the time-variations of solar corpuscular radiation, described for use in correlation studies in other geophysical fields, *Ann. Intern. Geophys.*, *4*, 227–236.

Bartels, J., Heck, N. H., and Johnston, H. F. (1939), The three-hour-range index measuring geomagnetic activity, *Terrestrial Magnetism and Atmospheric Electricity*, *44*(4), 411–454, doi:https://doi.org/10.1029/TE044i004p00411.

Basu, S., MacKenzie, E., and Basu, S. (1988), Ionospheric constraints on vhf/uhf communications links during solar maximum and minimum periods, *Radio Science*, *23*(3), 363–378, doi:10.1029/RS023i003p00363.

Basu, S., Groves, K., Basu, S., and Sultan, P. (2002), Specification and forecasting of scintillations in communication/navigation links: current status and future plans, *Journal of Atmospheric and Solar-Terrestrial Physics*, *64*(16), 1745–1754, doi:https://doi.org/10.1016/S1364-6826(02)00124-4.

Bhattacharyya, A., Gurram, P., Kakad, B., Sripathi, S., and Sunda, S. (2019), Signal frequency dependence of ionospheric scintillations: An indicator of irregularity spectrum characteristics, *Journal of Geophysical Research: Space Physics*, *124*(10), 8081–8091, doi:https://doi.org/10.1029/2019JA026987.

Bilitza, D., Altadill, D., Truhlik, V., Shubin, V., Galkin, I., Reinisch, B., and Huang, X. (2017), International reference ionosphere 2016: From ionospheric climate to real-time weather predictions, *Space Weather*, *15*(2), 418–429, doi:10.1002/2016SW001593.

Bittencourt, J. A., and Abdu, M. A. (1981), A theoretical comparison between apparent and real vertical ionization drift velocities in the equatorial f region, *Journal of Geophysical Research: Space Physics*, *86*(A4), 2451–2454, doi:10.1029/JA086iA04p02451.

Bittencourt, J. A., Pillat, V. G., Fagundes, P. R., Sahai, Y., and Pimenta, A. A. (2007), Lion: A dynamic computer model for the low-latitude ionosphere, *Annales Geophysicae*, *25*(11), 2371–2392, doi:10.5194/angeo-25-2371-2007.

Blanc, M., and Richmond, A. (1980), The ionospheric disturbance dynamo, *Journal of Geophysical Research: Space Physics*, *85*(A4), 1669–1686, doi: https://doi.org/10.1029/JA085iA04p01669.

Cahill Jr., L. J., Greenwald, R. A., and Nielsen, E. (1978), Auroral radar and rocket double-probe observations of the electric field across the harang discontinuity, *Geophysical Research Letters*, *5*(8), 687–690, doi:https://doi.org/10.1029/GL005i008p00687.

Chakrabarty, D., Sekar, R., Narayanan, R., Devasia, C. V., and Pathan, B. M. (2005), Evidence for the interplanetary electric field effect on the oi 630.0 nm airglow over low latitude, *Journal of Geophysical Research: Space Physics*, *110*(A11), doi:https://doi.org/10.1029/2005JA011221.

Chakrabarty, D., Sekar, R., Narayanan, R., Patra, A. K., and Devasia, C. V. (2006), Effects of interplanetary electric field on the development of an equatorial spread f event, *Journal of Geophysical Research: Space Physics*, *111*(A12), doi:https://doi.org/10.1029/2006JA011884.

Chakrabarty, D., Sekar, R., Sastri, J. H., and Ravindran, S. (2008), Distinctive effects of interplanetary electric field and substorm on nighttime equatorial f layer: A case study, *Geophysical Research Letters*, *35*(19), doi: 10.1029/2008GL035415.

Chakrabarty, D., Sekar, R., Sastri, J. H., Pathan, B. M., Reeves, G. D., Yumoto, K., and Kikuchi, T. (2010), Evidence for oi 630.0 nm dayglow variations over low latitudes during onset of a substorm, *Journal of Geophysical Research: Space Physics*, *115*(A10), doi:https://doi.org/10.1029/2010JA015643.

Chakrabarty, D., Bagiya, M. S., and Thampi, S. V. (2012), Solar euv flux (0.1-50 nm), f10.7 cm flux, sunspot number and the total electron content in the crest region of equatorial ionization anomaly during the deep minimum between solar cycle 23 and 24, *Indian Journal of Radio and Space Physics*, *41*(2), 110–120.

Chakrabarty, D., Fejer, B., Gurubaran, S., Pant, T. K., Abdu, M., and Sekar, R. (2014), On the pre-midnight ascent of f-layer in the june solstice during the deep solar minimum in 2008 over the indian sector, *Journal of Atmospheric and Solar-Terrestrial Physics*, *121*, 177–187, doi:https://doi.org/10.1016/j.jastp.2014.01.002.

Chakrabarty, D., Rout, D., Sekar, R., Narayanan, R., Reeves, G. D., Pant, T. K., Veenadhari, B., and Shiokawa, K. (2015), Three different types of electric field disturbances affecting equatorial ionosphere during a long-duration prompt penetration event, *Journal of Geophysical Research: Space Physics*, *120*(6), 4993–5008, doi:10.1002/2014JA020759.

Chakrabarty, D., Hui, D., Rout, D., Sekar, R., Bhattacharyya, A., Reeves, G. D., and Ruohoniemi, J. M. (2017), Role of imf by in the prompt electric field disturbances over equatorial ionosphere during a space weather event, *Journal of Geophysical Research: Space Physics*, *122*(2), 2574–2588, doi:https://doi.org/10.1002/2016JA022781.

Chapman, S. (1951), The equatorial electrojet as detected from the abnormal electric current distribution above huancayo, peru, and elsewhere, *Archiv Fuer Meteorologie, Geophysik und Bioklimatologie, Serie A*, *4*(1),]368–390, doi:https://doi.org/10.1029/GL005i008p00687.

Chau, J. L., Goncharenko, L. P., Fejer, B. G., and Liu, H.-L. (2012), Equatorial and low latitude ionospheric effects during sudden stratospheric warming events, *Space Science Reviews*, *168*(1), 385–417, doi:https://doi.org/10.1007/s11214-011-9797-5.

Chen, C.-H., Lin, C., Chen, W.-H., and Matsuo, T. (2017), Modeling the ionospheric prereversal enhancement by using coupled thermosphere-ionosphere data assimilation, *Geophysical Research Letters*, *44*(4), 1652–1659, doi:10.1002/2016GL071812.

Chen, Y., Liu, L., Le, H., Wan, W., and Zhang, H. (2016), Equatorial ionization anomaly in the low-latitude topside ionosphere: Local time evolution and longitudinal difference, *Journal of Geophysical Research: Space Physics*, *121*(7), 7166–7182, doi:10.1002/2016JA022394.

Clauer, C. R., Banks, P. M., Smith, A. Q., Jorgensen, T. S., Friis-Christensen, E., Vennerstrom, S., Wickwar, V. B., Kelly, J. D., and Doupnik, J. (1984), Observation of interplanetary magnetic field and of ionospheric plasma convection in the vicinity of the dayside polar cleft, *Geophysical Research Letters*, *11*(9), 891–894, doi:https://doi.org/10.1029/GL011i009p00891.

Davis, T. N., and Sugiura, M. (1966), Auroral electrojet activity index ae and its universal time variations, *Journal of Geophysical Research (1896-1977)*, *71*(3), 785–801, doi:https://doi.org/10.1029/JZ071i003p00785.

Davis, T. N., Burrows, K., and Stolarik, J. D. (1967), A latitude survey of the equatorial electrojet with rocket-borne magnetometers, *Journal of Geophysical Research (1896-1977)*, *72*(7), 1845–1861, doi:https://doi.org/10.1029/JZ072i007p01845.

de la Beaujardière, O., Wickwar, V. B., Kelly, J. D., and King, J. H. (1985), Effect of the interplanetary magnetic field y component on the high-latitude nightside convection, *Geophysical Research Letters*, *12*(7), 461–464, doi:https://doi.org/10.1029/GL012i007p00461.

de Paula, E. R., Jonah, O. F., Moraes, A. O., Kherani, E. A., Fejer, B. G., Abdu, M. A., Muella, M. T. A. H., Batista, I. S., Dutra, S. L. G., and Paes, R. R. (2015), Low-latitude scintillation weakening during sudden stratospheric warming events, *Journal of Geophysical Research: Space Physics*, *120*(3), 2212–2221, doi:https://doi.org/10.1002/2014JA020731.

Dickinson, R. E., Ridley, E., and Roble, R. (1984), Thermospheric general circulation with coupled dynamics and composition, *Journal of Atmospheric Sciences*, *41*(2), 205–219.

Drob, D. P., Emmert, J. T., Crowley, G., Picone, J. M., Shepherd, G. G., Skinner, W., Hays, P., Niciejewski, R. J., Larsen, M., She, C. Y., Meriwether, J. W., Hernandez, G., Jarvis, M. J., Sipler, D. P., Tepley, C. A., O'Brien, M. S., Bowman, J. R., Wu, Q., Murayama, Y., Kawamura, S., Reid, I. M., and Vincent, R. A. (2008), An empirical model of the earth's horizontal wind fields: Hwm07, *Journal of Geophysical Research: Space Physics*, *113*(A12), doi:https://doi.org/10.1029/2008JA013668.

Drob, D. P., Emmert, J. T., Meriwether, J. W., Makela, J. J., Doornbos, E., Conde, M., Hernandez, G., Noto, J., Zawdie, K. A., McDonald, S. E., Huba, J. D., and Klenzing, J. H. (2015), An update to the horizontal wind model (hwm): The quiet time thermosphere, *Earth and Space Science*, *2*(7), 301–319, doi:10.1002/2014EA000089.

Dungey, J. W. (1961), Interplanetary magnetic field and the auroral zones, *Phys. Rev. Lett.*, *6*, 47–48, doi:10.1103/PhysRevLett.6.47.

Eccles, J. V. (1998), A simple model of low-latitude electric fields, *Journal of Geophysical Research: Space Physics*, *103*(A11), 26,699–26,708, doi:https://doi.org/10.1029/98JA02657.

Eccles, J. V., St. Maurice, J. P., and Schunk, R. W. (2015), Mechanisms underlying the prereversal enhancement of the vertical plasma drift in the low-latitude ionosphere, *Journal of Geophysical Research: Space Physics*, *120*(6), 4950–4970, doi:10.1002/2014JA020664.

Emmert, J. T., Drob, D. P., Picone, J. M., Siskind, D. E., Jones Jr., M., Mlynczak, M. G., Bernath, P. F., Chu, X., Doornbos, E., Funke, B., Goncharenko, L. P., Hervig, M. E., Schwartz, M. J., Sheese, P. E., Vargas, F., Williams, B. P., and Yuan, T. (2021), Nrlmsis 2.0: A whole-atmosphere empirical model of temperature and neutral species densities, *Earth and Space Science*, *8*(3), e2020EA001,321, doi:https://doi.org/10.1029/2020EA001321.

Farelo, A. F., Herraiz, M., and Mikhailov, A. V. (2002), Global morphology of night-time NmF2 enhancements, *Annales Geophysicae*, *20*(11), 1795–1806, doi:10.5194/angeo-20-1795-2002.

Farley, D. T. (1959), A theory of electrostatic fields in a horizontally stratified ionosphere subject to a vertical magnetic field, *Journal of Geophysical Research (1896-1977)*, *64*(9), 1225–1233, doi:https://doi.org/10.1029/JZ064i009p01225.

Farley, D. T., Bonelli, E., Fejer, B. G., and Larsen, M. F. (1986), The prereversal enhancement of the zonal electric field in the equatorial ionosphere, *Journal of Geophysical Research: Space Physics*, *91*(A12), 13,723–13,728, doi:https://doi.org/10.1029/JA091iA12p13723.

Fejer, B., Gonzales, C., Farley, D. T., Kelley, M., and Woodman, R. (1979a), Equatorial electric fields during magnetically disturbed conditions 1. the effect of the interplanetary magnetic field, *Journal of Geophysical Research: Space Physics*, *84*(A10), 5797–5802, doi:https://doi.org/10.1029/JA084iA10p05797.

Fejer, B., Farley, D., Woodman, R., and Calderon, C. (1979b), Dependence of equatorial f region vertical drifts on season and solar cycle, *Journal of Geophysical Research: Space Physics*, *84*(A10), 5792–5796, doi:https://doi.org/10.1029/JA084iA10p05792.

Fejer, B. G. (1981), The equatorial ionospheric electric fields. a review, *Journal of Atmospheric and Terrestrial Physics*, *43*(5), 377–386, doi:https://doi.org/10.1016/0021-9169(81)90101-X.

Fejer, B. G. (2011), Low latitude ionospheric electrodynamics, *Space Science Reviews*, *158*(1), 145–166, doi:https://doi.org/10.1007/s11214-010-9690-7.

Fejer, B. G., Kudeki, E., and Farley, D. T. (1985), Equatorial f region zonal plasma drifts, *Journal of Geophysical Research: Space Physics*, *90*(A12), 12,249–12,255, doi:https://doi.org/10.1029/JA090iA12p12249.

Fejer, B. G., de Paula, E. R., Batista, I. S., Bonelli, E., and Woodman, R. F. (1989), Equatorial f region vertical plasma drifts during solar maxima, *Journal of Geophysical Research: Space Physics*, *94*(A9), 12,049–12,054, doi:https://doi.org/10.1029/JA094iA09p12049.

Fejer, B. G., de Paula, E. R., González, S. A., and Woodman, R. F. (1991), Average vertical and zonal f region plasma drifts over jicamarca, *Journal of Geophysical Research: Space Physics*, *96*(A8), 13,901–13,906, doi:https://doi.org/10.1029/91JA01171.

Fejer, B. G., de Paula, E. R., Heelis, R. A., and Hanson, W. B. (1995), Global equatorial ionospheric vertical plasma drifts measured by the ae-e satellite, *Journal of Geophysical Research: Space Physics*, *100*(A4), 5769–5776, doi: https://doi.org/10.1029/94JA03240.

Fejer, B. G., Scherliess, L., and de Paula, E. R. (1999), Effects of the vertical plasma drift velocity on the generation and evolution of equatorial spread f, *Journal of Geophysical Research: Space Physics*, *104*(A9), 19,859–19,869, doi: https://doi.org/10.1029/1999JA900271.

Fejer, B. G., Jensen, J. W., and Su, S.-Y. (2008a), Quiet time equatorial F region vertical plasma drift model derived from ROCSAT-1 observations, *Journal of Geophysical Research: Space Physics*, *113*(A5), doi:10.1029/2007JA012801.

Fejer, B. G., Jensen, J. W., and Su, S.-Y. (2008b), Seasonal and longitudinal dependence of equatorial disturbance vertical plasma drifts, *Geophysical Research Letters*, *35*(20), doi:https://doi.org/10.1029/2008GL035584.

Fejer, B. G., Navarro, L. A., Sazykin, S., Newheart, A., Milla, M. A., and Condor, P. (2021), Prompt penetration and substorm effects over jicamarca during the september 2017 geomagnetic storm, *Journal of Geophysical Research: Space Physics*, *126*(8), e2021JA029,651, doi:https://doi.org/10.1029/2021JA029651.

Francey, R. J. (1970), Electron production in the ionospheric d region by cosmic x rays, *Journal of Geophysical Research (1896-1977)*, *75*(25), 4849–4862, doi: https://doi.org/10.1029/JA075i025p04849.

Ganushkina, N. Y., Liemohn, M. W., and Dubyagin, S. (2018), Current systems in the earth's magnetosphere, *Reviews of Geophysics*, *56*(2), 309–332, doi:https://doi.org/10.1002/2017RG000590.

Gjerloev, J. W., Waters, C. L., and Barnes, R. J. (2018), Deriving global convection maps from superdarn measurements, *Journal of Geophysical Research: Space Physics*, *123*(4), 2902–2915, doi:https://doi.org/10.1002/2017JA024543.

Goncharenko, L. P., Coster, A. J., Chau, J. L., and Valladares, C. E. (2010a), Impact of sudden stratospheric warmings on equatorial ionization anomaly, *Journal of Geophysical Research: Space Physics*, *115*(A10), doi:https://doi.org/10.1029/2010JA015400.

Goncharenko, L. P., Chau, J. L., Liu, H.-L., and Coster, A. J. (2010b), Unexpected connections between the stratosphere and ionosphere, *Geophysical Research Letters*, *37*(10), doi:https://doi.org/10.1029/2010GL043125.

Gonzales, C., Kelley, M., Fejer, B., Vickrey, J., and Woodman, R. (1979), Equatorial electric fields during magnetically disturbed conditions 2. implications of simultaneous auroral and equatorial measurements, *Journal of Geophysical Research: Space Physics*, *84*(A10), 5803–5812, doi:https://doi.org/10.1029/JA084iA10p05803.

Gonzalez, W. D., Tsurutani, B. T., Gonzalez, A. L. C., Smith, E. J., Tang, F., and Akasofu, S.-I. (1989), Solar wind-magnetosphere coupling during intense magnetic storms (1978-1979), *Journal of Geophysical Research: Space Physics*, *94*(A7), 8835–8851, doi:https://doi.org/10.1029/JA094iA07p08835.

Gonzalez, W. D., Joselyn, J. A., Kamide, Y., Kroehl, H. W., Rostoker, G., Tsurutani, B. T., and Vasyliunas, V. M. (1994), What is a geomagnetic storm?, *Journal of Geophysical Research: Space Physics*, *99*(A4), 5771–5792, doi:https://doi.org/10.1029/93JA02867.

Gosling, J. T., Thomsen, M. F., Bame, S. J., Elphic, R. C., and Russell, C. T. (1990), Plasma flow reversals at the dayside magnetopause and the origin of asymmetric polar cap convection, *Journal of Geophysical Research: Space Physics*, *95*(A6), 8073–8084, doi:https://doi.org/10.1029/JA095iA06p08073.

Greenwald, R. A., Weiss, W., Nielsen, E., and Thomson, N. R. (1978), Stare: A new radar auroral backscatter experiment in northern scandinavia, *Radio Science*, *13*(6), 1021–1039, doi:https://doi.org/10.1029/RS013i006p01021.

Haaland, S. E., Paschmann, G., Förster, M., Quinn, J. M., Torbert, R. B., McIlwain, C. E., Vaith, H., Puhl-Quinn, P. A., and Kletzing, C. A. (2007), High-latitude plasma convection from cluster edi measurements: method and imf-dependence, *Annales Geophysicae*, *25*(1), 239–253, doi:10.5194/angeo-25-239-2007.

Haerendel, G., and Eccles, J. V. (1992), The role of the equatorial electrojet in the evening ionosphere, *Journal of Geophysical Research: Space Physics*, *97*(A2), 1181–1192, doi:https://doi.org/10.1029/91JA02227.

Hanson, W. B., and Moffett, R. J. (1966), lonization transport effects in the equatorial f region, *Journal of Geophysical Research (1896-1977)*, *71*(23), 5559–5572, doi:https://doi.org/10.1029/JZ071i023p05559.

Hargreaves, J. K. (1992), *The solar-terrestrial environment: an introduction to geospace-the science of the terrestrial upper atmosphere, ionosphere, and magnetosphere*, Cambridge university press.

Hashimoto, K. K., Kikuchi, T., Tomizawa, I., and Nagatsuma, T. (2017), Substorm overshielding electric field at low latitude on the nightside as observed by the hf doppler sounder and magnetometers, *Journal of Geophysical Research: Space Physics*, *122*(10), 10,851–10,863, doi:https://doi.org/10.1002/2017JA024329.

Heelis, R. (1985), Interplanetary magnetic field effects on high latitude ionospheric convection, in *The Polar Cusp*, pp. 293–303, Springer, doi:https://doi.org/10.1007/978-94-009-5295-9_21.

Heelis, R. (2004), Electrodynamics in the low and middle latitude ionosphere: a tutorial, *Journal of Atmospheric and Solar-Terrestrial Physics*, *66*(10), 825–838, doi:https://doi.org/10.1016/j.jastp.2004.01.034.

Heelis, R., Kendall, P., Moffett, R., Windle, D., and Rishbeth, H. (1974), Electrical coupling of the e- and f-regions and its effect on f-region drifts and winds, *Planetary and Space Science*, *22*(5), 743–756, doi:https://doi.org/10.1016/0032-0633(74)90144-5.

Henderson, M. G., Reeves, G. D., Belian, R. D., and Murphree, J. S. (1996), Observations of magnetospheric substorms occurring with no apparent solar wind/imf trigger, *Journal of Geophysical Research: Space Physics*, *101*(A5), 10,773–10,791, doi:https://doi.org/10.1029/96JA00186.

Huang, C. M. (2013), Disturbance dynamo electric fields in response to geomagnetic storms occurring at different universal times, *Journal of Geophysical Research: Space Physics*, *118*(1), 496–501, doi:https://doi.org/10.1029/2012JA018118.

Huang, C. M., and Chen, M. Q. (), Formation of maximum electric potential at the geomagnetic equator by the disturbance dynamo, *Journal of Geophysical Research: Space Physics*, *113*(A3), doi:https://doi.org/10.1029/2007JA012843.

Huang, C.-S. (2009), Eastward electric field enhancement and geomagnetic positive bay in the dayside low-latitude ionosphere caused by magnetospheric substorms during sawtooth events, *Geophysical Research Letters*, *36*(18), doi:https://doi.org/10.1029/2009GL040287.

Huang, C.-S., Foster, J. C., Goncharenko, L. P., Reeves, G. D., Chau, J. L., Yumoto, K., and Kitamura, K. (2004), Variations of low-latitude geomagnetic fields and dst index caused by magnetospheric substorms, *Journal of Geophysical Research: Space Physics*, *109*(A5), doi:https://doi.org/10.1029/2003JA010334.

Huang, C.-S., Sazykin, S., Chau, J. L., Maruyama, N., and Kelley, M. C. (2007), Penetration electric fields: Efficiency and characteristic time scale, *Journal of Atmospheric and Solar-Terrestrial Physics*, *69*(10), 1135–1146, doi:https://doi.org/10.1016/j.jastp.2006.08.016.

Huang, C.-S., Yumoto, K., Abe, S., and Sofko, G. (2008), Low-latitude ionospheric electric and magnetic field disturbances in response to solar wind pressure enhancements, *Journal of Geophysical Research: Space Physics*, *113*(A8), doi:https://doi.org/10.1029/2007JA012940.

Huang, F., Lei, J., Zhang, R., Li, N., Gu, S., Yu, Y., Liu, L., Owolabi, C., Ning, B., Li, G., Zhong, J., Dang, T., Ren, D., Yi, W., Luan, X., Xue, X., Yu, T., Li, F., Dou, X., and Yoshikawa, A. (2020), Prominent daytime tec enhancements under the quiescent condition of january 2017, *Geophysical Research Letters*, *47*(14), e2020GL088,398, doi:https://doi.org/10.1029/2020GL088398.

Huang, Y.-N., and Cheng, K. (1995), Solar cycle variation of the total electron content around equatorial anomaly crest region in east asia, *Journal of Atmospheric and Terrestrial Physics*, *57*(12), 1503 – 1511, doi:https://doi.org/10.1016/0021-9169(94)00147-G.

Huang, Y.-N., Cheng, K., and Chen, S.-W. (1989), On the equatorial anomaly of the ionospheric total electron content near the northern anomaly crest region, *Journal of Geophysical Research: Space Physics*, *94*(A10), 13,515–13,525, doi:https://doi.org/10.1029/JA094iA10p13515.

Huba, J. D., and Joyce, G. (2007), Equatorial spread f modeling: Multiple bifurcated structures, secondary instabilities, large density 'bite-outs,' and supersonic flows, *Geophysical Research Letters*, *34*(7), doi:https://doi.org/10.1029/2006GL028519.

Huba, J. D., and Joyce, G. (2010), Global modeling of equatorial plasma bubbles, *Geophysical Research Letters*, *37*(17), doi:https://doi.org/10.1029/2010GL044281.

Huba, J. D., Lyon, J. G., and Hassam, A. B. (1987), Theory and simulation of the rayleigh-taylor instability in the limit of large larmor radius, *Phys. Rev. Lett.*, *59*, 2971–2974, doi:10.1103/PhysRevLett.59.2971.

Huba, J. D., Joyce, G., Sazykin, S., Wolf, R., and Spiro, R. (2005), Simulation study of penetration electric field effects on the low- to mid-latitude ionosphere, *Geophysical Research Letters*, *32*(23), doi:https://doi.org/10.1029/2005GL024162.

Huba, J. D., Joyce, G., and Krall, J. (2008), Three-dimensional equatorial spread f modeling, *Geophysical Research Letters*, *35*(10), doi:https://doi.org/10.1029/2008GL033509.

Hui, D., and Vichare, G. (2021), Influence of imf-by on the equatorial ionospheric plasma drifts: Tiegcm simulations, *Journal of Geophysical Research: Space Physics*, *126*(9), e2021JA029,270, doi:https://doi.org/10.1029/2021JA029270.

Hui, D., Chakrabarty, D., Sekar, R., Reeves, G. D., Yoshikawa, A., and Shiokawa, K. (2017), Contribution of storm time substorms to the prompt electric field disturbances in the equatorial ionosphere, *Journal of Geophysical Research: Space Physics*, *122*(5), 5568–5578, doi:https://doi.org/10.1002/2016JA023754.

Iijima, T., and Potemra, T. A. (1978), Large-scale characteristics of field-aligned currents associated with substorms, *Journal of Geophysical Research: Space Physics*, *83*(A2), 599–615, doi:https://doi.org/10.1029/JA083iA02p00599.

Inglis, D. R. (1981), Dynamo theory of the earth's varying magnetic field, *Reviews of Modern Physics*, *53*(3), 481.

Kelley, M. C. (2009), *The Earth's ionosphere: Plasma physics and electrodynamics*, Academic press.

Kelley, M. C., and Makela, J. J. (2002), By-dependent prompt penetrating electric fields at the magnetic equator, *Geophysical Research Letters*, *29*(7), 57–1–57–3, doi:https://doi.org/10.1029/2001GL014468.

Kelley, M. C., Fejer, B. G., and Gonzales, C. A. (1979), An explanation for anomalous equatorial ionospheric electric fields associated with a northward turning of the interplanetary magnetic field, *Geophysical Research Letters*, *6*(4), 301–304, doi:https://doi.org/10.1029/GL006i004p00301.

Kelley, M. C., Makela, J. J., Chau, J. L., and Nicolls, M. J. (2003), Penetration of the solar wind electric field into the magnetosphere/ionosphere system, *Geophysical Research Letters*, *30*(4), doi:https://doi.org/10.1029/2002GL016321.

Kepko, L., McPherron, R., Amm, O., Apatenkov, S., Baumjohann, W., Birn, J., Lester, M., Nakamura, R., Pulkkinen, T. I., and Sergeev, V. (2015), Substorm current wedge revisited, *Space Science Reviews*, *190*(1), 1–46, doi:https://doi.org/10.1007/s11214-014-0124-9.

Khazanov, G. V. (2016), *Space weather fundamentals*, CRC Press.

Kikuchi, T., and Araki, T. (1979), Horizontal transmission of the polar electric field to the equator, *Journal of Atmospheric and Terrestrial Physics*, *41*(9), 927–936, doi:https://doi.org/10.1016/0021-9169(79)90094-1.

Kikuchi, T., Ishimine, T., and Sugiuchi, H. (1985), Local time distribution of hf doppler frequency deviations associated with storm sudden commencements, *Journal of Geophysical Research: Space Physics*, *90*(A5), 4389–4393, doi:https://doi.org/10.1029/JA090iA05p04389.

Kikuchi, T., Lühr, H., Schlegel, K., Tachihara, H., Shinohara, M., and Kitamura, T.-I. (2000), Penetration of auroral electric fields to the equator during a substorm, *Journal of Geophysical Research: Space Physics*, *105*(A10), 23,251–23,261, doi:https://doi.org/10.1029/2000JA900016.

Kikuchi, T., Tsunomura, S., Hashimoto, K., and Nozaki, K. (2001), Field-aligned current effects on midlatitude geomagnetic sudden commencements, *Journal of Geophysical Research: Space Physics*, *106*(A8), 15,555–15,565, doi:https://doi.org/10.1029/2001JA900030.

Kikuchi, T., Hashimoto, K. K., Kitamura, T.-I., Tachihara, H., and Fejer, B. (2003), Equatorial counterelectrojets during substorms, *Journal of Geophysical Research: Space Physics*, *108*(A11), doi:https://doi.org/10.1029/2003JA009915.

Kikuchi, T., Hashimoto, K. K., and Nozaki, K. (2008), Penetration of magnetospheric electric fields to the equator during a geomagnetic storm, *Journal of Geophysical Research: Space Physics*, *113*(A6), doi:https://doi.org/10.1029/2007JA012628.

Kivelson, M., and Russell, C. (1995), Introduction to space physics, cambridge, univ.

Klimas, A. J., Valdivia, J. A., Vassiliadis, D., Baker, D. N., Hesse, M., and Takalo, J. (2000), Self-organized criticality in the substorm phenomenon and its relation to localized reconnection in the magnetospheric plasma sheet, *Journal of Geophysical Research: Space Physics*, *105*(A8), 18,765–18,780, doi:https://doi.org/10.1029/1999JA000319.

Krishna Murthy, B. (1990), Nighttime equatorial thermospheric meridional winds from ionospheric h'f data, *Journal of Geophysical Research: Space Physics*, *95*(A4), 4307–4310, doi:10.1029/JA095iA04p04307.

Kulkarni, P. V. (1969), Airglow studies in low latitudes, *Proc. Third Int. Symp. on Equatorial Aeronomy*, *2*(1), 412.

Kumar, A., Chakrabarty, D., Pandey, K., Fejer, B. G., Sunda, S., Seemala, G. K., Sripathi, S., and Yadav, A. K. (2021), Evidence for the significant differences in response times of equatorial ionization anomaly crest corresponding to plasma fountains during daytime and post-sunset hours, *Journal of Geophysical Research: Space Physics*, *126*(3), e2020JA028,628, doi: https://doi.org/10.1029/2020JA028628.

Kumar, A., Chakrabarty, D., Pandey, K., and Yadav, A. K. (2022), Solar flux dependence of post-sunset enhancement in vertical total electron content over the crest region of equatorial ionization anomaly, *Journal of Geophysical Research: Space Physics*, *127*(5), e2021JA030,156, doi:https://doi.org/10.1029/2021JA030156.

Larsen, M. F., and Meriwether, J. W. (2012), Vertical winds in the thermosphere, *Journal of Geophysical Research: Space Physics*, *117*(A9), doi:https://doi.org/10.1029/2012JA017843.

Le, G., Russell, C. T., Petrinec, S. M., and Ginskey, M. (1993), Effect of sudden solar wind dynamic pressure changes at subauroral latitudes: Change in magnetic field, *Journal of Geophysical Research: Space Physics*, *98*(A3), 3983–3990, doi:https://doi.org/10.1029/92JA02397.

Le, G., Slavin, J. A., and Strangeway, R. J. (2010), Space technology 5 observations of the imbalance of regions 1 and 2 field-aligned currents and its implication to the cross-polar cap pedersen currents, *Journal of Geophysical Research: Space Physics*, *115*(A7), doi:https://doi.org/10.1029/2009JA014979.

Liao, X. (2001), *Carrier phase based ionosphere recovery over a regional area GPS network*, University of Calgary.

Liu, H., Stolle, C., Förster, M., and Watanabe, S. (2007), Solar activity dependence of the electron density in the equatorial anomaly regions observed by champ, *Journal of Geophysical Research: Space Physics*, *112*(A11), doi: 10.1029/2007JA012616.

Liu, H., Yamamoto, M., Tulasi Ram, S., Tsugawa, T., Otsuka, Y., Stolle, C., Doornbos, E., Yumoto, K., and Nagatsuma, T. (2011a), Equatorial electrodynamics and neutral background in the asian sector during the 2009 stratospheric sudden warming, *Journal of Geophysical Research: Space Physics*, *116*(A8), doi:https://doi.org/10.1029/2011JA016607.

Liu, J., Burns, A. G., Wang, W., and Zhang, Y. (2020), Modeled imf by effects on the polar ionosphere and thermosphere coupling, *Journal of Geophysical Research: Space Physics*, *125*(3), e2019JA026,949, doi:https://doi.org/10.1029/2019JA026949.

Liu, J.-M., Zhang, B.-C., Kamide, Y., Wu, Z.-S., Hu, Z.-J., and Yang, H.-G. (2011b), Spontaneous and trigger-associated substorms compared: Electrodynamic parameters in the polar ionosphere, *Journal of Geophysical Research: Space Physics*, *116*(A1), doi:https://doi.org/10.1029/2010JA015773.

Liu, L., and Chen, Y. (2009), Statistical analysis of solar activity variations of total electron content derived at jet propulsion laboratory from gps observations, *Journal of Geophysical Research: Space Physics*, *114*(A10), doi: https://doi.org/10.1029/2009JA014533.

Liu, L., He, M., Yue, X., Ning, B., and Wan, W. (2010), Ionosphere around equinoxes during low solar activity, *Journal of Geophysical Research: Space Physics*, *115*(A9), doi:https://doi.org/10.1029/2010JA015318.

Liu, L., Chen, Y., Le, H., Ning, B., Wan, W., Liu, J., and Hu, L. (2013), A case study of postmidnight enhancement in f-layer electron density over sanya of china, *Journal of Geophysical Research: Space Physics*, *118*(7), 4640–4648, doi:https://doi.org/10.1002/jgra.50422.

Loewe, C. A., and Prölss, G. W. (1997), Classification and mean behavior of magnetic storms, *Journal of Geophysical Research: Space Physics*, *102*(A7), 14,209–14,213, doi:https://doi.org/10.1029/96JA04020.

Lu, G., Goncharenko, L., Nicolls, M. J., Maute, A., Coster, A., and Paxton, L. J. (2012), Ionospheric and thermospheric variations associated with prompt penetration electric fields, *Journal of Geophysical Research: Space Physics*, *117*(A8), doi:https://doi.org/10.1029/2012JA017769.

Lukianova, R., and Kozlovsky, A. (2011), Imf b_y effects in the plasma flow at the polar cap boundary, *Annales Geophysicae*, *29*(7), 1305–1315, doi:10.5194/angeo-29-1305-2011.

Lyons, L. R. (1995), A new theory for magnetospheric substorms, *Journal of Geophysical Research: Space Physics*, *100*(A10), 19,069–19,081, doi:https://doi.org/10.1029/95JA01344.

Lyons, L. R. (1996), Substorms: Fundamental observational features, distinction from other disturbances, and external triggering, *Journal of Geophysical Research: Space Physics*, *101*(A6), 13,011–13,025, doi:https://doi.org/10.1029/95JA01987.

Lyons, L. R., Blanchard, G. T., Samson, J. C., Lepping, R. P., Yamamoto, T., and Moretto, T. (1997), Coordinated observations demonstrating external substorm triggering, *Journal of Geophysical Research: Space Physics*, *102*(A12), 27,039–27,051, doi:https://doi.org/10.1029/97JA02639.

MacDougall, J., Grant, I., and Shen, X. (1995), The canadian advanced digital ionosonde: design and results, *URSI INAG Ionospheric Station Inf. Bulletin, UAG-104*.

Madhav Haridas, M. K., Manju, G., and Pant, T. K. (2015), On the solar activity variations of nocturnal f region vertical drifts covering two solar cycles in the indian longitude sector, *Journal of Geophysical Research: Space Physics*, *120*(2), 1445–1451.

Mannucci, A. J., Wilson, B. D., and Edwards, C. D. (1993), A new method for monitoring the earth's ionospheric total electron content using the gps global network, *ION GPS-93, Proc of Sixth International Technical Meeting of The Satellite Division of the Institute of Navigation, USA (Institute of Navigation, Salt Lake City, UT)*, pp. 1323–1332.

Mannucci, A. J., Tsurutani, B. T., Iijima, B. A., Komjathy, A., Saito, A., Gonzalez, W. D., Guarnieri, F. L., Kozyra, J. U., and Skoug, R. (2005), Dayside global ionospheric response to the major interplanetary events of october 29–30, 2003 "halloween storms", *Geophysical Research Letters*, *32*(12), doi: https://doi.org/10.1029/2004GL021467.

Matsushita, S. (1969), Dynamo currents, winds, and electric fields, *Radio Science*, *4*(9), 771–780, doi:https://doi.org/10.1029/RS004i009p00771.

Matzka, J., Stolle, C., Yamazaki, Y., Bronkalla, O., and Morschhauser, A. (2021), The geomagnetic kp index and derived indices of geomagnetic activity, *Space Weather*, *19*(5), e2020SW002,641, doi:https://doi.org/10.1029/2020SW002641.

McPherron, R. L. (1979), Magnetospheric substorms, *Reviews of Geophysics*, *17*(4), 657–681, doi:https://doi.org/10.1029/RG017i004p00657.

McPherron, R. L., Russell, C. T., and Aubry, M. P. (1973), Satellite studies of magnetospheric substorms on august 15, 1968: 9. phenomenological model for substorms, *Journal of Geophysical Research (1896-1977)*, *78*(16), 3131–3149, doi:https://doi.org/10.1029/JA078i016p03131.

Miles, D. M. (2017), Advances in fluxgate magnetometry for space physics, Ph.D. thesis, Department of Physics, University of Alberta, Edmonton, Alberta, Canada.

Mitra, S. (1946), Geomagnetic control of region f2 of the ionosphere, *Nature*, *158*(4019), 668–669.

Mo, X. H., Zhang, D. H., Liu, J., Hao, Y. Q., Ye, J. F., Qin, J. S., Wei, W. X., and Xiao, Z. (2018), Morphological characteristics of equatorial ionization anomaly crest over nanning region, *Radio Science*, *53*(1), 37–47, doi: 10.1002/2017RS006386.

Muralikrishna, P., Vieira, L., and Abdu, M. (2003), Electron density and electric field fluctuations associated with developing plasma bubbles, *Journal of Atmospheric and Solar-Terrestrial Physics*, *65*(14), 1315–1327, doi:https://doi.org/10.1016/j.jastp.2003.08.010, equatorial Electroject Studies from Ground and Space.

Nath, D., Chen, W., Zelin, C., Pogoreltsev, A. I., and Wei, K. (2016), Dynamics of 2013 sudden stratospheric warming event and its impact on cold weather over eurasia: Role of planetary wave reflection, *Scientific reports*, *6*(1), 1–12.

Nicolet, M., and Aikin, A. C. (1960), The formation of the d region of the ionosphere, *Journal of Geophysical Research (1896-1977)*, *65*(5), 1469–1483, doi: https://doi.org/10.1029/JZ065i005p01469.

Nishida, A. (1968), Geomagnetic dp 2 fluctuations and associated magnetospheric phenomena, *Journal of Geophysical Research (1896-1977)*, *73*(5), 1795–1803, doi:https://doi.org/10.1029/JA073i005p01795.

Nopper Jr., R. W., and Carovillano, R. L. (1978), Polar-equatorial coupling during magnetically active periods, *Geophysical Research Letters*, *5*(8), 699–702, doi:https://doi.org/10.1029/GL005i008p00699.

Olwendo, O. J., Yamazaki, Y., Cilliers, P. J., Baki, P., and Doherty, P. (2016), A study on the variability of ionospheric total electron content over the east african low-latitude region and storm time ionospheric variations, *Radio Science*, *51*(9), 1503–1518, doi:https://doi.org/10.1002/2015RS005785.

Oryema, B., Jurua, E., and Ssebiyonga, N. (2016), Variations of crest-to-trough tec ratio of the east african equatorial anomaly region, *International Journal of Astrophysics and Space Science*, *4*(1), 12–20.

Otsuka, Y. (2018), Review of the generation mechanisms of post-midnight irregularities in the equatorial and low-latitude ionosphere, *Progress in Earth and Planetary Science*, *5*(1), 1–13, doi:https://doi.org/10.1186/s40645-018-0212-7.

Pandey, K. (2018), Investigations on ionospheric electrodynamics over low latitudes in indian sector, Ph.D. thesis, Indian Institute of Technology, Gandhinagar, India.

Pandey, K., Sekar, R., Gupta, S., Chakrabarty, D., and Anandarao, B. (2017), Comparison of quiet time vertical plasma drifts with global empirical models over the Indian sector: Some insights, *Journal of Atmospheric and Solar-Terrestrial Physics*, *157-158*, 42–54, doi:https://doi.org/10.1016/j.jastp.2017.03.012.

Pandey, K., Sekar, R., Anandarao, B. G., Gupta, S. P., and Chakrabarty, D. (2018), On the occurrence of afternoon counter electrojet over indian longitudes during june solstice in solar minimum, *Journal of Geophysical Research: Space Physics*, *123*(3), 2204–2214, doi:https://doi.org/10.1002/2017JA024725.

Pedatella, N., Liu, H.-L., Sassi, F., Lei, J., Chau, J., and Zhang, X. (2014), Ionosphere variability during the 2009 ssw: Influence of the lunar semidiurnal tide and mechanisms producing electron density variability, *Journal of Geophysical Research: Space Physics*, *119*(5), 3828–3843, doi:https://doi.org/10.1002/2014JA019849.

Peymirat, C., Richmond, A. D., and Kobea, A. T. (2000), Electrodynamic coupling of high and low latitudes: Simulations of shielding/overshielding effects, *Journal of Geophysical Research: Space Physics*, *105*(A10), 22,991–23,003, doi:https://doi.org/10.1029/2000JA000057.

Pham Thi Thu, H., Amory Mazaudier, C., Le Huy, M., Saito, S., Hozumi, K., Nguyen Thanh, D., and Luong Thi, N. (2022), Nighttime morphology of vertical plasma drifts over vietnam during different seasons and phases of sunspot cycles, *Advances in Space Research*, doi:https://doi.org/10.1016/j.asr.2022.04.010.

Picone, J. M., Hedin, A. E., Drob, D. P., and Aikin, A. C. (2002), Nrlmsise-00 empirical model of the atmosphere: Statistical comparisons and scientific issues, *Journal of Geophysical Research: Space Physics*, *107*(A12), SIA 15–1–SIA 15–16, doi:10.1029/2002JA009430.

Potemra, T. A. (1985), Field-aligned (birkeland) currents, *Space Science Reviews*, *42*, 295–311, doi:https://doi.org/10.1007/BF00214990.

Pulkkinen, T., Palmroth, M., Tanskanen, E., Ganushkina, N., Shukhtina, M., and Dmitrieva, N. (2007), Solar wind—magnetosphere coupling: A review of recent results, *Journal of Atmospheric and Solar-Terrestrial Physics*, *69*(3), 256–264, doi:https://doi.org/10.1016/j.jastp.2006.05.029.

Raghavarao, R., Gupta, S., Sekar, R., Narayanan, R., Desai, J., Sridharan, R., Babu, V., and Sudhakar, V. (1987), In situ measurements of winds, electric fields and electron densities at the onset of equatorial spread-f, *Journal of Atmospheric and Terrestrial Physics*, *49*(5), 485–492, doi:https://doi.org/10.1016/0021-9169(87)90042-0.

Raghavarao, R., Hoegy, W. R., Spencer, N. W., and Wharton, L. E. (1993), Neutral temperature anomaly in the equatorial thermosphere-a source of vertical winds, *Geophysical Research Letters*, *20*(11), 1023–1026, doi:https://doi.org/10.1029/93GL01253.

Rajaram, G. (1977), Structure of the equatorial f-region, topside and bottomside—a review, *Journal of Atmospheric and Terrestrial Physics*, *39*(9), 1125–1144, doi:https://doi.org/10.1016/0021-9169(77)90021-6.

Rama Rao, P. V. S., Gopi Krishna, S., Niranjan, K., and Prasad, D. S. V. V. D. (2006), Temporal and spatial variations in TEC using simultaneous measurements from the Indian GPS network of receivers during the low solar activity period of 2004–2005, *Annales Geophysicae*, *24*(12), 3279–3292, doi:10.5194/angeo-24-3279-2006.

Ramesh, K., and Sastri, J. (1995), Solar cycle and seasonal variations in f-region vertical drifts over kodaikanal, india, in *Annales Geophysicae*, vol. 13, pp. 633–640, doi:https://doi.org/10.1007/s00585-995-0633-7.

Rao, V., and Kulkarni, P. (1973), 6300 Å night airglow enhancements in low latitudes, *Journal of Atmospheric and Terrestrial Physics*, *35*(2), 193–206, doi:https://doi.org/10.1016/0021-9169(73)90087-1.

Rastogi, R., and Klobuchar, J. (1990), Ionospheric electron content within the equatorial f 2 layer anomaly belt, *Journal of Geophysical Research: Space Physics*, *95*(A11), 19,045–19,052, doi:https://doi.org/10.1029/JA095iA11p19045.

Rastogi, R., and Patel, V. (1975), Effect of interplanetary magnetic field on ionosphere over the magnetic equator, in *Proceedings of the Indian Academy of Sciences-Section A*, vol. 82, pp. 121–141, doi:10.1007/BF03046722.

Reeves, G. D. (1998), New perspectives on substorm injections, *Tech. rep.*, Los Alamos National Lab.(LANL), Los Alamos, NM (United States).

Reeves, G. D., Fritz, T. A., Cayton, T. E., and Belian, R. D. (1990), Multi-satellite measurements of the substorm injection region, *Geophysical Research Letters*, *17*(11), 2015–2018, doi:https://doi.org/10.1029/GL017i011p02015.

Reeves, G. D., Belian, R. D., and Fritz, T. A. (1991), Numerical tracing of energetic particle drifts in a model magnetosphere, *Journal of Geophysical Research: Space Physics*, *96*(A8), 13,997–14,008, doi:https://doi.org/10.1029/91JA01161.

Reeves, G. D., McAdams, K. L., Friedel, R. H. W., and O'Brien, T. P. (2003), Acceleration and loss of relativistic electrons during geomagnetic storms, *Geophysical Research Letters*, *30*(10), doi:https://doi.org/10.1029/2002GL016513.

Richmond, A. D., Ridley, E. C., and Roble, R. G. (1992), A thermosphere/ionosphere general circulation model with coupled electrodynamics, *Geophysical Research Letters*, *19*(6), 601–604, doi:https://doi.org/10.1029/92GL00401.

Richmond, A. D., Fang, T.-W., and Maute, A. (2015), Electrodynamics of the equatorial evening ionosphere: 1. importance of winds in different regions, *Journal of Geophysical Research: Space Physics*, *120*(3), 2118–2132, doi:https://doi.org/10.1002/2014JA020934.

Rishbeth, H. (1971a), The f-layer dynamo, *Planetary and Space Science*, *19*(2), 263–267, doi:https://doi.org/10.1016/0032-0633(71)90205-4.

Rishbeth, H. (1971b), Polarization fields produced by winds in the equatorial f-region, *Planetary and Space Science*, *19*(3), 357–369, doi:https://doi.org/10.1016/0032-0633(71)90098-5.

Rishbeth, H. (1972), Thermospheric winds and the f-region: A review, *Journal of Atmospheric and Terrestrial Physics*, *34*(1), 1–47, doi:https://doi.org/10.1016/0021-9169(72)90003-7.

Rishbeth, H. (1977), Dynamics of the equatorial f-region, *Journal of Atmospheric and Terrestrial Physics*, *39*(9), 1159–1168, doi:https://doi.org/10.1016/0021-9169(77)90024-1.

Rishbeth, H. (1981), The f-region dynamo, *Journal of Atmospheric and Terrestrial Physics*, *43*(5), 387–392, doi:https://doi.org/10.1016/0021-9169(81)90102-1.

Rishbeth, H., and Garriott, O. K. (1969), Introduction to ionospheric physics, *Introduction to ionospheric physics*.

Roble, R. G., Ridley, E. C., Richmond, A. D., and Dickinson, R. E. (1988), A coupled thermosphere/ionosphere general circulation model, *Geophysical Research Letters*, *15*(12), 1325–1328, doi:https://doi.org/10.1029/GL015i012p01325.

Rodrigues, F. S., Nicolls, M. J., Milla, M. A., Smith, J. M., Varney, R. H., Strømme, A., Martinis, C., and Arratia, J. F. (2015), Amisr-14: Observations of equatorial spread f, *Geophysical Research Letters*, *42*(13), 5100–5108, doi: https://doi.org/10.1002/2015GL064574.

Rostoker, G., Akasofu, S.-I., Foster, J., Greenwald, R., Kamide, Y., Kawasaki, K., Lui, A., McPherron, R., and Russell, C. (1980), Magnetospheric substorms—definition and signatures, *Journal of Geophysical Research: Space Physics*, *85*(A4), 1663–1668, doi:https://doi.org/10.1029/JA085iA04p01663.

Rout, D., Chakrabarty, D., Sekar, R., Reeves, G. D., Ruohoniemi, J. M., Pant, T. K., Veenadhari, B., and Shiokawa, K. (2016), An evidence for prompt electric field disturbance driven by changes in the solar wind density under northward imf bz condition, *Journal of Geophysical Research: Space Physics*, *121*(5), 4800–4810, doi:https://doi.org/10.1002/2016JA022475.

Rout, D., Pandey, K., Chakrabarty, D., Sekar, R., and Lu, X. (2019), Significant electric field perturbations in low latitude ionosphere due to the passage of two consecutive icmes during 6–8 september 2017, *Journal of Geophysical Research: Space Physics*, *124*(11), 9494–9510, doi:10.1029/2019JA027133.

Ruohoniemi, J. M., and Baker, K. B. (1998), Large-scale imaging of high-latitude convection with super dual auroral radar network hf radar observations, *Journal of Geophysical Research: Space Physics*, *103*(A9), 20,797–20,811, doi:https://doi.org/10.1029/98JA01288.

Ruohoniemi, J. M., and Greenwald, R. A. (1996), Statistical patterns of high-latitude convection obtained from goose bay hf radar observations, *Journal of Geophysical Research: Space Physics*, *101*(A10), 21,743–21,763, doi:https://doi.org/10.1029/96JA01584.

Russell, C. T., and Ginskey, M. (1993), Sudden impulses at low latitudes: Transient response, *Geophysical Research Letters*, *20*(11), 1015–1018, doi: https://doi.org/10.1029/93GL01257.

Russell, C. T., and Ginskey, M. (1995), Sudden impulses at subauroral latitudes: Response for northward interplanetary magnetic field, *Journal of Geophysical Research: Space Physics*, *100*(A12), 23,695–23,702, doi:https://doi.org/10.1029/95JA02495.

Sampath, S., and Sastry, T. S. G. (1979), Ac electric fields associated with the plasma instabilities in the equatorial electrojet-iii, *Journal of geomagnetism and geoelectricity*, *31*(3), 391–400, doi:10.5636/jgg.31.391.

Sastri, J. H. (1990), Equatorial aniomaly in F-region - A Review, *Indian Journal of Radio and Space Physics*, *19*(4), 225–240.

Sastri, J. H., Rao, J. V. S. V., and Ramesh, K. B. (1993), Penetration of polar electric fields to the nightside dip equator at times of geomagnetic sudden commencements, *Journal of Geophysical Research: Space Physics*, *98*(A10), 17,517–17,523, doi:https://doi.org/10.1029/93JA00418.

Sastri, J. H., Luhr, H., Tachihara, H., Kitamura, T.-I., and Rao, J. V. S. V. (2000), Letter to the editor: Electric field fluctuations (25-35 min) in the midnight dip equatorial ionosphere, *Annales Geophysicae*, *18*(2), 252–256, doi:10.1007/s00585-000-0252-2.

Savitzky, A., and Golay, M. J. (1964), Smoothing and differentiation of data by simplified least squares procedures., *Analytical chemistry*, *36*(8), 1627–1639.

Scherliess, L., and Fejer, B. G. (1997), Storm time dependence of equatorial disturbance dynamo zonal electric fields, *Journal of Geophysical Research: Space Physics*, *102*(A11), 24,037–24,046, doi:https://doi.org/10.1029/97JA02165.

Scherliess, L., and Fejer, B. G. (1999), Radar and satellite global equatorial f region vertical drift model, *Journal of Geophysical Research: Space Physics*, *104*(A4), 6829–6842, doi:https://doi.org/10.1029/1999JA900025.

Schunk, R., and Nagy, A. (2009), *Ionospheres: physics, plasma physics, and chemistry*, Cambridge university press.

Sekar, R., and Chakrabarty, D. (2008), Role of overshielding electric field on the development of pre-midnight plume event: Simulation results, *Journal of Atmospheric and Solar-Terrestrial Physics*, *70*(17), 2212–2221, doi:https://doi.org/10.1016/j.jastp.2008.04.015.

Sekar, R., and Kelley, M. C. (1998), On the combined effects of vertical shear and zonal electric field patterns on nonlinear equatorial spread f evolution, *Journal of Geophysical Research: Space Physics*, *103*(A9), 20,735–20,747, doi: https://doi.org/10.1029/98JA01561.

Sekar, R., and Raghavarao, R. (1987), Role of vertical winds on the rayleigh-taylor mode instabilities of the night-time equatorial ionosphere, *Journal of Atmospheric and Terrestrial Physics*, *49*(10), 981–985, doi:https://doi.org/10.1016/0021-9169(87)90104-8.

Sekar, R., Chakrabarty, D., Narayanan, R., Sripathi, S., Patra, A. K., and Subbarao, K. S. V. (2004), Characterization of vhf radar observations associated with equatorial spread f by narrow-band optical measurements, *Annales Geophysicae*, *22*(9), 3129–3136, doi:10.5194/angeo-22-3129-2004.

Sekar, R., Chakrabarty, D., and Pallamraju, D. (2012), Optical signature of shear in the zonal plasma flow along with a tilted structure associated with equatorial spread f during a space weather event, *Journal of Atmospheric and Solar-Terrestrial Physics*, *75-76*, 57–63, doi:https://doi.org/10.1016/j.jastp.2011.05.009.

Senior, C., and Blanc, M. (1984), On the control of magnetospheric convection by the spatial distribution of ionospheric conductivities, *Journal of Geophysical Research: Space Physics*, *89*(A1), 261–284, doi:https://doi.org/10.1029/JA089iA01p00261.

Simi, K. G., Thampi, S. V., Chakrabarty, D., Pathan, B. M., Prabhakaran Nayar, S. R., and Kumar Pant, T. (2012), Extreme changes in the equatorial electrojet under the influence of interplanetary electric field and the associated modification in the low-latitude f region plasma distribution, *Journal of Geophysical Research: Space Physics*, *117*(A3), doi:https://doi.org/10.1029/2011JA017328.

Sivaraman, M., Suhasini, R., and Raghavarao, R. (1976), Role of ambipolar diffusion in the development of equatorial anomaly in solar maximum & minimum periods, *Indian Journal of Radio and Space Physics*, *05*(2), 136–140.

Smith, R. W. (1998), Vertical winds: a tutorial, *Journal of Atmospheric and Solar-Terrestrial Physics*, *60*(14), 1425–1434, doi:https://doi.org/10.1016/S1364-6826(98)00058-3.

Sori, T., Shinbori, A., Otsuka, Y., Tsugawa, T., Nishioka, M., and Yoshikawa, A. (2022), Generation mechanisms of plasma density irregularity in the equatorial ionosphere during a geomagnetic storm on 21–22 december 2014, *Journal of Geophysical Research: Space Physics*, *127*(5), e2021JA030,240, doi:https://doi.org/10.1029/2021JA030240.

Spiro, R., Wolf, R., and Fejer, B. (1988), Penetrating of high-latitude-electric-field effects to low latitudes during sundial 1984, in *Annales Geophysicae*, vol. 6, pp. 39–49.

Sridharan, R., Sekar, R., and Gurubaran, S. (1993), Two-dimensional high-resolution imaging of the equatorial plasma fountain, *Journal of Atmospheric and Terrestrial Physics*, *55*(13), 1661–1665, doi:https://doi.org/10.1016/0021-9169(93)90170-4.

Sripathi, S., Singh, R., Banola, S., Sreekumar, S., Emperumal, K., and Selvaraj, C. (2016), Characteristics of the equatorial plasma drifts as obtained by using canadian doppler ionosonde over southern tip of india, *Journal of Geophysical Research: Space Physics*, *121*(8), 8103–8120, doi:10.1002/2016JA023088.

Stoneback, R. A., Heelis, R. A., Burrell, A. G., Coley, W. R., Fejer, B. G., and Pacheco, E. (2011), Observations of quiet time vertical ion drift in the equatorial ionosphere during the solar minimum period of 2009, *Journal of Geophysical Research: Space Physics*, *116*(A12), doi:https://doi.org/10.1029/2011JA016712.

Su, Y., Bailey, G., and Balan, N. (1994), Night-time enhancements in TEC at equatorial anomaly latitudes, *Journal of Atmospheric and Terrestrial Physics*, *56*(12), 1619–1628, doi:https://doi.org/10.1016/0021-9169(94)90091-4.

Subbarao, K. S. V., and Krishna Murthy, B. (1994), Seasonal variations of equatorial spread-f, *Annales Geophysicae*, *12*(33-39), doi:https://doi.org/10.1007/s00585-994-0033-4.

Sunda, S., and Vyas, B. M. (2013), Local time, seasonal, and solar cycle dependency of longitudinal variations of TEC along the crest of EIA over India, *Journal of Geophysical Research: Space Physics*, *118*(10), 6777–6785, doi:10.1002/2013JA018918.

Sunda, S., Sridharan, R., Vyas, B. M., Khekale, P. V., Parikh, K. S., Ganeshan, A. S., Sudhir, C. R., Satish, S. V., and Bagiya, M. S. (2015), Satellite-based augmentation systems: A novel and cost-effective tool for ionospheric and space weather studies, *Space Weather*, *13*(1), 6–15, doi:10.1002/2014SW001103.

Themens, D. R., Jayachandran, P., Langley, R., MacDougall, J., and Nicolls, M. (2013), Determining receiver biases in gps-derived total electron content in the auroral oval and polar cap region using ionosonde measurements, *GPS solutions*, *17*(3), 357–369.

Titheridge, J. (1995), Winds in the ionosphere—a review, *Journal of Atmospheric and Terrestrial Physics*, *57*(14), 1681–1714, doi:https://doi.org/10.1016/0021-9169(95)00091-F.

Trattner, K., Petrinec, S., and Fuselier, S. (2021), The location of magnetic reconnection at earth's magnetopause, *Space Science Reviews*, *217*(3), 1–47, doi:https://doi.org/10.1007/s11214-021-00817-8.

Troshichev, O., Andrezen, V., Vennerstrøm, S., and Friis-Christensen, E. (1988), Magnetic activity in the polar cap—a new index, *Planetary and Space Science*, *36*(11), 1095–1102, doi:https://doi.org/10.1016/0032-0633(88)90063-3.

Troshichev, O. A., Lukianova, R. Y., Papitashvili, V. O., Rich, F. J., and Rasmussen, O. (2000), Polar cap index (pc) as a proxy for ionospheric electric field in the near-pole region, *Geophysical Research Letters*, *27*(23), 3809–3812, doi:https://doi.org/10.1029/2000GL003756.

Tsurutani, B. T., Gonzalez, W. D., Guarnieri, F., Kamide, Y., Zhou, X., and Arballo, J. K. (2004), Are high-intensity long-duration continuous ae activity (hildcaa) events substorm expansion events?, *Journal of Atmospheric and Solar-Terrestrial Physics*, *66*(2), 167–176, doi:https://doi.org/10.1016/j.jastp.2003.08.015, space Weather in the Declining Phase of the Solar Cycle.

Tsurutani, B. T., Verkhoglyadova, O. P., Mannucci, A. J., Saito, A., Araki, T., Yumoto, K., Tsuda, T., Abdu, M. A., Sobral, J. H. A., Gonzalez, W. D., McCreadie, H., Lakhina, G. S., and Vasyliūnas, V. M. (2008), Prompt penetration electric fields (ppefs) and their ionospheric effects during the great magnetic storm of 30–31 october 2003, *Journal of Geophysical Research: Space Physics*, *113*(A5), doi:https://doi.org/10.1029/2007JA012879.

Tsurutani, B. T., Lakhina, G. S., and Hajra, R. (2020), The physics of space weather/solar-terrestrial physics (stp): what we know now and what the current and future challenges are, *Nonlinear Processes in Geophysics*, *27*(1), 75–119, doi:https://npg.copernicus.org/articles/27/75/2020/.

Vasyliunas, V. M. (1970), Mathematical models of magnetospheric convection and its coupling to the ionosphere, in *Particles and Fields in the Magnetosphere*, pp. 60–71, Springer, doi:https://doi.org/10.1007/978-94-010-3284-1.

Vineeth, C., Kumar Pant, T., and Sridharan, R. (2009), Equatorial counter electrojets and polar stratospheric sudden warmings–a classical example of high latitude-low latitude coupling?, in *Annales Geophysicae*, vol. 27, pp. 3147–3153, doi:https://doi.org/10.5194/angeo-27-3147-2009.

Wan, X., Zhong, J., Xiong, C., Wang, H., Liu, Y., Li, Q., Kuai, J., and Cui, J. (2022), Seasonal and interhemispheric effects on the diurnal evolution of eia: Assessed by igs tec and iri-2016 over peruvian and indian sectors, *Remote Sensing*, *14*(1), doi:https://www.mdpi.com/2072-4292/14/1/107.

Wang, H., Lühr, H., Zheng, Z., and Zhang, K. (2019), Dependence of the equatorial electrojet on auroral activity and in situ solar insulation, *Journal of Geophysical Research: Space Physics*, *124*(12), 10,659–10,673, doi: https://doi.org/10.1029/2019JA027320.

Wang, W., Lei, J., Burns, A. G., Wiltberger, M., Richmond, A. D., Solomon, S. C., Killeen, T. L., Talaat, E. R., and Anderson, D. N. (2008), Ionospheric electric field variations during a geomagnetic storm simulated by a coupled magnetosphere ionosphere thermosphere (cmit) model, *Geophysical Research Letters*, *35*(18), doi:https://doi.org/10.1029/2008GL035155.

Wanliss, J. A., and Showalter, K. M. (2006), High-resolution global storm index: Dst versus sym-h, *Journal of Geophysical Research: Space Physics*, *111*(A2), doi:https://doi.org/10.1029/2005JA011034.

Whalen, J. A. (2004), Linear dependence of the postsunset equatorial anomaly electron density on solar flux and its relation to the maximum prereversal e × b drift velocity through its dependence on solar flux, *Journal of Geophysical Research: Space Physics*, *109*(A7), doi:https://doi.org/10.1029/2004JA010528.

Wolf, R., Spiro, R., Sazykin, S., and Toffoletto, F. (2007), How the earth's inner magnetosphere works: An evolving picture, *Journal of Atmospheric and Solar-Terrestrial Physics*, *69*(3), 288–302, doi:https://doi.org/10.1016/j.jastp.2006.07.026.

Wolf, R. A. (1970), Effects of ionospheric conductivity on convective flow of plasma in the magnetosphere, *Journal of Geophysical Research (1896-1977)*, *75*(25), 4677–4698, doi:https://doi.org/10.1029/JA075i025p04677.

Woodman, R. F. (1970), Vertical drift velocities and east-west electric fields at the magnetic equator, *Journal of Geophysical Research (1896-1977)*, *75*(31), 6249–6259, doi:https://doi.org/10.1029/JA075i031p06249.

Woodman, R. F., and La Hoz, C. (1976), Radar observations of f region equatorial irregularities, *Journal of Geophysical Research (1896-1977)*, *81*(31), 5447–5466, doi:https://doi.org/10.1029/JA081i031p05447.

Woodman, R. F., Chau, J. L., and Ilma, R. R. (2006), Comparison of ionosonde and incoherent scatter drift measurements at the magnetic equator, *Geophysical Research Letters*, *33*(1), doi:https://doi.org/10.1029/2005GL023692.

Woodman, R. F., Farley, D. T., Balsley, B. B., and Milla, M. A. (2019), The early history of the jicamarca radio observatory and the incoherent scatter technique, *History of Geo- and Space Sciences*, *10*(2), 245–266, doi:10.5194/hgss-10-245-2019.

Xiong, C., Zhou, Y.-L., Lühr, H., and Ma, S.-Y. (2016), Diurnal evolution of the F region electron density local time gradient at low and middle latitudes resolved by the Swarm constellation, *Journal of Geophysical Research: Space Physics*, *121*(9), 9075–9089, doi:10.1002/2016JA023034.

Yadav, S., Choudhary, R. K., Kumari, J., Sunda, S., Shreedevi, P. R., and Pant, T. K. (2020), Reverse Fountain and the Nighttime Enhancement in the Ionospheric Electron Density Over the Equatorial Region: A Case Study, *Journal of Geophysical Research: Space Physics*, *125*(5), doi:10.1029/2019JA027286.

Yamazaki, Y., and Maute, A. (2017), Sq and eej—a review on the daily variation of the geomagnetic field caused by ionospheric dynamo currents, *Space Science Reviews*, *206*(1), 299–405, doi:https://doi.org/10.1007/s11214-016-0282-z.

Yizengaw, E., Moldwin, M. B., Sahai, Y., and de Jesus, R. (2009), Strong postmidnight equatorial ionospheric anomaly observations during magnetically quiet periods, *Journal of Geophysical Research: Space Physics*, *114*(A12), doi:https://doi.org/10.1029/2009JA014603.

Yokoyama, T. (2017), A review on the numerical simulation of equatorial plasma bubbles toward scintillation evaluation and forecasting, *Progress in Earth and Planetary Science*, *4*(1), 1–13.

Young, D. M., Yuen, P., and Roelofs, T. (1970), Anomalous nighttime increases in total electron content, *Planetary and Space Science*, *18*(8), 1163–1179.

Zaka, K. Z., Kobea, A. T., Assamoi, P., Obrou, O. K., Doumbia, V., Boka, K., Adohi, B. J.-P., and Mene, N. M. (2009), Latitudinal profile of the ionospheric disturbance dynamo magnetic signature: comparison with the dp2 magnetic disturbance, *Annales Geophysicae*, *27*(9), 3523–3536, doi:10.5194/angeo-27-3523-2009.

Zhan, W., Rodrigues, F. S., and Milla, M. A. (2018), On the genesis of post-midnight equatorial spread f: Results for the american/peruvian sector, *Geophysical Research Letters*, *45*(15), 7354–7361, doi:https://doi.org/10.1029/2018GL078822.

Zhang, M.-L., Wan, W., Liu, L., and Ning, B. (2009), Variability study of the crest-to-trough tec ratio of the equatorial ionization anomaly around 120°e longitude, *Advances in Space Research*, *43*(11), 1762–1769, doi:https://doi.org/10.1016/j.asr.2008.09.031.

Zhang, R., Liu, L., Chen, Y., and Le, H. (2015), The dawn enhancement of the equatorial ionospheric vertical plasma drift, *Journal of Geophysical Research: Space Physics*, *120*(12), 10,688–10,697, doi:https://doi.org/10.1002/2015JA021972.

Zhao, B., Wan, W., Liu, L., and Ren, Z. (2009), Characteristics of the ionospheric total electron content of the equatorial ionization anomaly in the asian-australian region during 1996-2004, *Annales Geophysicae*, *27*(10), 3861–3873, doi:10.5194/angeo-27-3861-2009.

List of Publications

Publications included in the thesis

1. **Kumar, A.**, Chakrabarty, D., Pandey, K., Fejer, B. G., Sunda, S., Seemala, G. K., Yadav, A. K. (2021). Evidence for the significant differences in response times of equatorial ionization anomaly crest corresponding to plasma fountains during daytime and post-sunset hours. *Journal of Geophysical Research: Space Physics*, 126 (3), e2020JA028628. doi: https://doi.org/10.1029/2020JA028628

2. **Kumar, A.**, Chakrabarty, D., Pandey, K., and Yadav, A. K. (2022). Solar flux dependence of post-sunset enhancement in vertical total electron content over the crest region of equatorial ionization anomaly. *Journal of Geophysical Research: Space Physics*, 127 (5), e2021JA030156. doi: https://doi.org/10.1029/2021JA030156

3. **Kumar, A.**, Chakrabarty, D., Fejer, B.G., Reeves, G.D., Rout, D., Sripathi, S., et al. (2023). A case of anomalous electric field perturbations in the equatorial ionosphere during post-sunset hours: Insights. *Journal of Geophysical Research: Space Physics*, 128, e2022JA030826. doi: https://doi.org/10.1029/2022JA030826

4. **Kumar, A.**, Chakrabarty, D., Fejer, B. G., Reeves, G.D., Rout, D., Pandey, K, Sripathi, S., Sunda, S., Yadav, A. K. (2022). Unusual electric field perturbations over equatorial ionosphere during post-midnight hours: Case studies and insights (**To be submitted soon**).

Publications not included in the thesis

1. Pandey, K., Chakrabarty, D., **Kumar, A.**, Bhardwaj, A., Biswal, S., Hussey, M., Yadav, A. K. (2022). Characteristics of X-class flares of solar cycle 23 and 24 in X-ray and EUV bands. (**Accepted in Advances in Space Research**)

Presentations at International/National Conferences

1. **Kumar, A.**, Chakrabarty, D., Rout, D., Fejer, B. G., Reeves, G. D., Sripathi, S., Seemala, G. K., Sunda, S., Yadav, A. K., "A case study on anomalous electric field variations in the F region equatorial ionosphere during post-sunset hours: insights" presented in presented in *QUADRENNIAL SOLAR-TERRESTRIAL PHYSICS SYMPOSIUM (STP-15) held virtually at IIG, Mumbai during 21-25 February 2022* [**Oral presentation**].

2. **Kumar, A.**, Chakrabarty, D., Pandey, K., Fejer, B. G., Sunda, S., Seemala, G. K., Sripathi, S., Yadav, A., "Enhancements in plasma density over the EIA crest region during post-sunset hours in geomagnetically quiet periods" *presented in AGU Fall Meeting held virtually, during 1-17 December 2020* [**Poster presentation**].

3. **Kumar, A.**, Chakrabarty, D., Yadav, A., Seemala, G. K., "On the post-sunset responses of OI 630.0 nm nightglow intensity over the EIA crest region under various space weather conditions" *presented in 20th National Space Science Symposium (NSSS-2019) held at Savitribai Phule Pune University, India during 29-31 January 2019* [**Poster presentation**].

Attended Schools and Workshops

1. Attended "5th IAGA School." Hosted by CSIR-NGRI, Hyderabad, India on 16-20 August, 2021.
2. Attended "3rd ISEE symposium, PWING-ERG conference and school on the inner magnetosphere". Online conference held by ISEE Nagoya University, Japan during 8-12 March 2021.
3. Attended "IBERIAN SPACE SCIENCE SUMMER SCHOOL", virtually during 26-31 July 2021.
4. Attended "Workshop on NavIC/GNSS: Technique and Applications" held by National Atmospheric Research Laboratory, Gadanki, India during 3 - 5 August 2021.
5. Attended "Center for Geospace Storms (CGS) workshop" held virtually during 9-10 November 2020
6. Attended "STFC Introductory Solar System Plasmas Summer School" held virtually by Hosted by University of Birmingham during 24 – 27 August 2020.
7. Attended "CEDAR 2020 Virtual Workshop" during 22-26 June 2020.

Publications attached with thesis

1. **Kumar, A.**, Chakrabarty, D., Pandey, K., Fejer, B. G., Sunda, S., Seemala, G. K., Yadav, A. K. (2021). Evidence for the significant differences in response times of equatorial ionization anomaly crest corresponding to plasma fountains during daytime and post-sunset hours. *Journal of Geophysical Research: Space Physics*, 126 (3), e2020JA028628. doi: https://doi.org/10.1029/2020JA028628

2. **Kumar, A.**, Chakrabarty, D., Pandey, K., and Yadav, A. K. (2022). Solar flux dependence of post-sunset enhancement in vertical total electron content over the crest region of equatorial ionization anomaly. *Journal of Geophysical Research: Space Physics*, 127 (5), e2021JA030156. doi: https://doi.org/10.1029/2021JA030156

3. **Kumar, A.**, Chakrabarty, D., Fejer, B.G., Reeves, G.D., Rout, D., Sripathi, S., et al. (2023). A case of anomalous electric field perturbations in the equatorial ionosphere during post-sunset hours: Insights. *Journal of Geophysical Research: Space Physics*, 128, e2022JA030826. doi: https://doi.org/10.1029/2022JA030826

ADVANCING EARTH AND SPACE SCIENCE

JGR Space Physics

RESEARCH ARTICLE

10.1029/2020JA028628

Key Points:

- Post-sunset enhancement in plasma density over the equatorial ionization anomaly (EIA) crest region are found during December solstice and Equinox in high solar epoch
- Pre-reversal enhancement of the zonal electric field over the dip equator causes this enhancement in about 1.7 h
- Plasma transport from 5° to 10° magnetic latitude to the EIA crest region leads to shorter response time

Correspondence to:

A. Kumar,
ankitprl2017@gmail.com

Citation:

Kumar, A., Chakrabarty, D., Pandey, K., Fejer, B. G., Sunda, S., Seemala, G. K., et al. (2021). Evidence for the significant differences in response times of equatorial ionization anomaly crest corresponding to plasma fountains during daytime and post-sunset hours. *Journal of Geophysical Research: Space Physics*, *126*, e2020JA028628. https://doi.org/10.1029/2020JA028628

Received 24 AUG 2020
Accepted 5 FEB 2021

Evidence for the Significant Differences in Response Times of Equatorial Ionization Anomaly Crest Corresponding to Plasma Fountains During Daytime and Post-Sunset Hours

A. Kumar[1,2], D. Chakrabarty[1], K. Pandey[1,3], B. G. Fejer[4], S. Sunda[5], G. K. Seemala[6], S. Sripathi[6], and A. K. Yadav[1]

[1]Physical Research Laboratory, Ahmedabad, India, [2]Indian Institute of Technology, Gandhinagar, India, [3]Now at ISAS, Department of Physics and Engineering Physics, University of Saskatchewan, Saskatoon, Saskatchewan, Canada, [4]Utah State University, Logan, UT, USA, [5]Airport Authority of India, Ahmedabad, India, [6]Indian Institute of Geomagnetism, Navi Mumbai, India

Abstract Based on 10 years' (2010–2019) of vertical total electron content (VTEC) data from Ahmedabad (23.0°N, 72.6°E, dip angle 35.2°) and campaign based OI 630.0 nm airglow intensity measurements from Mt. Abu (24.6°N, 72.7°E, dip angle 38.0°), it is shown that plasma density over the equatorial ionization anomaly (EIA) crest region increases in varying degrees during post-sunset hours (2000–2100 LT) in magnetically quiet periods. The post-sunset peak in VTEC precedes the corresponding peak in airglow intensity. By comparing post-sunset VTEC enhancements with ionosonde observations from Tirunelveli (8.7°N, 77.7°E, dip angle 1.7°), it is shown that pre-reversal enhancement (PRE) of the zonal electric field causes these enhancements over the EIA crest region. These observations are supported by TEC measurements by GAGAN (GPS Aided Geo Augmented navigation), the Indian Satellite-based Augmentation System (SBAS). Comparison of average VTEC variations with global empirical model drifts reveals that the post-sunset enhancements in VTEC occurs ~1.7 h after the PRE and are significant only during December solstice and equinoctial months in high solar activity years similar to seasonal variations in PRE amplitudes. This time delay (response time of EIA crest) is almost half compared to the average response time (3–4 h) associated with the daytime fountain. Based on the latitudinal gradient in SBAS-TEC, it is proposed that the PRE drives plasma from 5°N to 10°N magnetic latitudes to the EIA crest region leading to shorter response time. These results show the important role of the PRE in conditioning the EIA crest region.

Plain Language Summary The equatorial ionization anomaly (EIA) crest region is one of the most important regions in the globe as far as the L-band scintillation during post-sunset hours is concerned. The plasma density variations over this region have important ramifications for the positional systems, navigation, and communication applications. Therefore, understanding the plasma density variations over this region during post-sunset hours is important. In this work, it is shown that the evening time electric field variations over the dip-equator changes the plasma density variations over the EIA crest region during post-sunset hours at a much faster time scale than what is expected based on daytime processes. The possible mechanism is discussed.

1. Introduction

The variability in the low latitude F region plasma distribution is greatly controlled by the equatorial F region plasma fountain process (Anderson, 1973a, 1973b). This process generates two ionization crests around ±15° geomagnetic latitudes and an ionization trough over the dip equator. This is known as equatorial ionization anomaly (EIA). Meridional winds cause asymmetry in the intensity and location of the EIA crest regions (e.g., Anderson, 1973a). The plasma distribution over the EIA crest regions shows day-to-day variability (e.g., Huang et al., 1989) as well as seasonal and solar activity dependences (e.g., Chakrabarty et al., 2012; Huang & Cheng, 1995; Mo et al., 2018). Understanding the plasma density variability over the EIA crest region is important as it is one of the most L-band scintillation affected regions in the globe (e.g., Basu et al., 1988). The L-band scintillation has ramifications for the positional systems, navigation, and communication applications.

It has been shown that the EIA crest region gets formed in the afternoon hours (e.g., Balan et al., 2018; Y. Chen et al., 2016; Mo et al., 2018; Sastri, 1990) during geomagnetically quiet periods. The time of occurrence of a well-developed EIA crest region during quiet period can, in general, be explained by adding a typical diffusion time of 3–4 h with the time of maximum eastward electric field over the dip equator around noon. Conventionally, the response time of the EIA crest region can be determined based on the time of occurrence of peak VTEC over the EIA crest region and the time of occurrence of peak vertical drift (present work) or EEJ strength (e.g., Rama Rao et al., 2006) or hmF2 (e.g., Aswathy et al., 2018). During the local evening hours, the eastward electric field in the equatorial F-region is greatly enhanced that is known as the pre-reversal enhancement (PRE) of the zonal electric field (e.g., Eccles et al., 2015; Fejer, 2011). As the amplitude of the PRE becomes comparable to the daytime maximum on occasions (e.g., Fejer et al., 2008), it is expected that the PRE should affect EIA crest region by re-invigorating the plasma fountain process. However, if one considers the duration of the PRE and 3–4 h of diffusion time (similar to daytime), the ionization over the EIA crest region is not expected to get affected by the PRE-driven fountain. This is because the equatorial zonal electric field changes to westward direction after the PRE and eventually reverse plasma fountain (e.g., Balan et al., 1995, 1997; C.-H. Chen et al., 2017; Sridharan et al., 1993; Yadav et al., 2020) sets in before the PRE-driven fountain can transport plasma from the dip equator to the crest region. Therefore, it is important to understand how much time the EIA crest region takes to respond to the PRE and how does it compare to the response time during daytime. Although several studies in the past reported (e.g., Bittencourt et al., 2007; Farelo et al., 2002; Rao & Kulkarni, 1973; Su et al., 1994; Xiong et al., 2016) conspicuous variations in the plasma density over the EIA crest region during post-sunset hours, the exact role of the PRE remains unclear. This important and unresolved scientific issue is addressed in the present work.

2. Data Set and Model

A narrow band and narrow field-of-view (bandwidth: 0.3 nm and field of view: 3°) airglow photometer was operated from Mt. Abu (24.6°N, 72.7°E, dip angle 38.0°), an EIA crest location, in campaign mode (operation during a specific period) in the winter months since 2013. The photometer was operated in moonless and cloudless nights to capture the variations in the OI 630.0 nm thermospheric airglow emission intensity. The details of this photometer are available in literature (e.g., Chakrabarty et al., 2008, 2015; Sekar & Chakrabarty, 2011). In the present work, airglow intensity data with 10 s cadence are used.

Vertical total electron content (VTEC) data from a dual frequency (L-band, 1575 and 1227 MHz) GPS receiver (GISTM GSV4004B) at Physical Research Laboratory (PRL), Ahmedabad (23.0°N, 72.6°E, dip angle 35.2°) during 2010–2019 are used in this work. The details of this receiver, the data analysis techniques are available in Manke and Chakarabarty (2016). Raypath elevation angles less than 30° are not considered in this work to minimize the multipath error and tropospheric scattering effects. Five minutes' average VTEC data are used for this study. Based on variations in F10.7 solar radio flux, the VTEC data during 2011–2015 are classified as belonging to high solar activity years and the rest of the data are categorized as falling in low solar activity years. Average F10.7 flux levels for high and low solar activity periods during 2010–2019 are ~130 sfu and ~80 sfu (sfu = solar flux unit, 1 sfu = $10^{-22}\,Wm^{-2}Hz^{-1}$) respectively. In both the solar epochs, the VTEC data are further categorized into three seasons namely December solstice (November, December, January, and February), Equinox (March and April, September and October), and June solstice (May, June, July, and August). This work pertains to geomagnetically quiet periods. Quiet periods are selected based on A_p index (based on $A_p \le 15$ on the chosen day and the previous day).

The TEC maps generated from the ionospheric delay broadcast by Indian Satellite-based Augmentation System (SBAS) are used in the present work. Indian SBAS is known as GAGAN (GPS Aided Geo Augmented Navigation). The SBAS-GAGAN network has 13 ground stations that constitute an ionospheric grid with 5° separation between grid points. At each ionospheric grid point (IGP), TEC has been derived with ~ 5 min cadence. The details of the GAGAN architecture are available in Sunda et al. (2015). GAGAN TEC maps are used to examine the latitudinal variation of F region plasma over the Indian sector.

Following the methodology of Rastogi and Patel (1975), systematic measurements of horizontal component (H) of geomagnetic field from a dip equatorial station Tirunelveli (TIR, 8.7°N, 77.7°E, dip angle 1.7°) and the off-equatorial station Alibag (ABG, 18.6°N, 72.9°E, dip angle 26.4°) over the Indian sector are used to calculate the strength of the equatorial electrojet (EEJ) given by $H_{\mathrm{EEJ}} = \Delta H_{\mathrm{TIR}} - \Delta H_{\mathrm{ABG}}$. Here, ΔH represents the daytime instantaneous H value corrected for the nighttime base value of H. The temporal cadence of EEJ data is 1 min. Integrated EEJ strength (in nT-h) is calculated between 0700 and 1700 LT.

The measurements of the bottomside F layer height ($h'F$, in km) by the Canadian Advanced Digital Ionosonde (CADI) over the dip equatorial station Tirunelveli are used in the present work. The details of the CADI system are discussed in MacDougall et al. (1995) and Sripathi et al. (2016). The temporal variation of $h'F$, $dh'F\ /\ dt = \left[(h'F)_{t_2} - (h'F)_{t_1}\right] / \left[t_2 - t_1\right]$, during post-sunset hours is used as a proxy for the equatorial F region vertical drift (in m/s). In order to derive $dh'F/dt$, the $h'F$ values are first subjected to Savitzky-Golay (SG) algorithm (e.g., Savitzky & Golay, 1964) with 15% smoothing window as the data are slightly noisy. The smoothed h'F data are then used to calculate the temporal derivative. The smoothing is done to suppress the fast fluctuations in $dh'F/dt$. The advantage of SG algorithm is its ability to smooth out fast fluctuations without causing significant distortion in the time series data. Further, since the derivation of electron density profiles from the CADI ionograms could not be done unambiguously, the correction for the chemical recombination is not incorporated in the derived drift. However, $h'F$ during PRE hours in high solar activity periods are mostly above 300 km. Hence the correction for the recombination effect is insignificant and can be neglected (e.g., Bittencourt & Abdu, 1981). On the other hand, $h'F$ during PRE hours in low solar activity periods can sometimes lie below 300 km. On those occasions, the real vertical drifts are smaller than calculated.

Since continuous vertical drift/electric field measurements are not available from Indian dip equatorial stations, the quiet time vertical drift outputs are generated using the global climatological model of Fejer et al. (2008). It has been shown earlier (e.g., Pandey et al., 2017) that the vertical drifts from this model represent the Indian sector well. The model outputs are generated for 75°E longitude corresponding to sfus of 130 and 80, respectively. It is also to be noted that the local time for all the data set used in this work is with respect to 75°E longitude (LT = UT + 5 h).

3. Results

Figures 1a and 1b depict the variations in 630.0 nm nightglow intensity (solid red line), VTEC (solid blue line), and EEJ strength (gray area) from 0600 LT to midnight on 29–30 November, 2013. Figures 1c–1f depict the same except for 03–04 December 2013 and 24–25 November 2014. In Figures 1a–1d, post-sunset enhancements in airglow intensity and VTEC are clearly seen during 1945–2045 LT. The daytime peak VTEC seems to vary in accordance with the integrated EEJ strength. However, the post-sunset enhancements in the airglow intensity and VTEC can be seen to be uncorrelated with the integrated EEJ strength (particularly, see Figures 1b and 1e). It is also clear from Figures 1a–1d and 1f that the airglow intensity enhancements over Mt. Abu start slightly earlier than the onset of increases in the VTEC over Ahmedabad during post-sunset hours (marked by orange vertical boxes). However, the peak in the airglow intensity occurs slightly later than the peak in VTEC. It is to be noted here that unlike the sharp airglow intensity peaks, VTEC variations are, in general, characterized by step-like increase followed by gradual decrease. The time corresponding to the peak VTEC is taken as the time corresponding to the end point of the step-like increase. In order to aid visual inspection, two vertical dashed lines are superimposed that mark the times corresponding to the onset of increase and peak of the airglow intensity. Further, it can be noticed in Figure 1e that although there is a peak in VTEC at ∼1920 LT, there is no corresponding enhancement in airglow intensity. In contrast to Figure 1e, strong intensity peak is observed in Figure 1f. It can also be noticed that the enhancement in VTEC occurs slightly earlier in Figure 1e (∼1920 LT) compared to Figure 1f (∼2000 LT). This difference in timing makes the peak in VTEC to coincide with the sharp fall in the airglow intensity associated with the F-region sunset in Figure 1e. This is in contrast to Figure 1f when the peak in VTEC coincides with the inflection point when airglow intensity starts increasing again after the sharp fall associated with F region sunset.

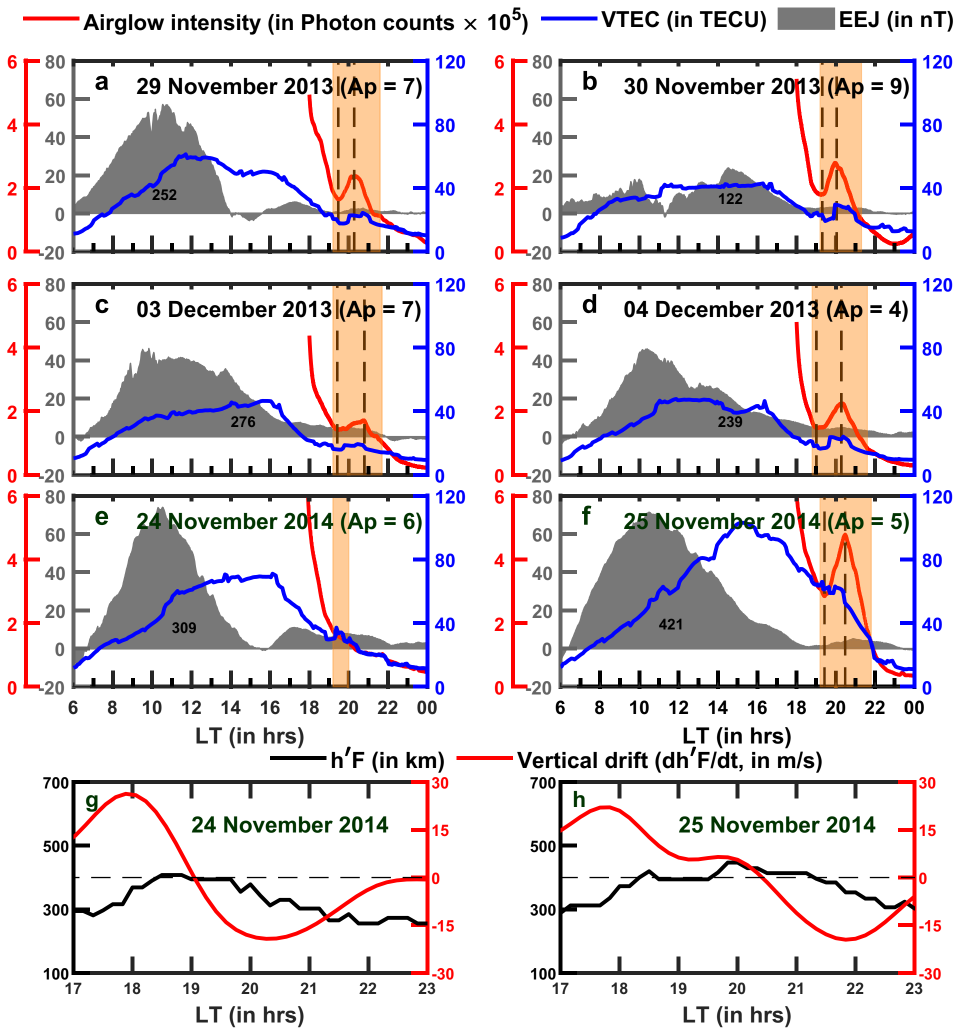

Figure 1. Variation of thermospheric OI 630.0 nm airglow intensity over Mt. Abu (red), VTEC over Ahmedabad (blue), and Equatorial electrojet (gray area) with local time on (a) 29 November 2013, (b) 30 November 2013, (c) 03 December 2013, (d) 04 December 2013, (e) 24 November 2014, and (f) 25 November 2014. Calculated integrated EEJ strength (numeric value) is written with black color over gray area. Virtual height-time-frequency plot from CADI measurement over Tirunelveli along with variation of bottomside F-layer height (black) and its derivative $dh'F/dt$ (red) with local time on (g) 24 November 2014, and (h) 25 November 2014.

Although airglow observations for a number of nights are available, two representative cases (24 and 25 November, 2014) of contrasting post-sunset variations in airglow intensity are selected for further investigations. Note that while post-sunset VTEC peaks are observed on both the days, the airglow intensity peak is significant on 25 November and almost absent on 24 November. In order to investigate the location of the base of F-layer and its vertical movement on 24 and 25 November 2014, the variations in $h'F$ and smoothed vertical drift ($dh'F/dt$) during 1700–2300 LT are shown with black and red lines respectively in Figures 1g and 1h. It can be noted that on 25 November, the PRE associated vertical drifts are upward for much longer duration compared to 24 November. The PRE sustains till ~1900 LT and ~2015 LT on 24 and 25 November, respectively. Impact of these differences in vertical drift on the VTEC and airglow enhancements over EIA crest region during post-sunset hours is provided in discussion section.

In order to explore the causal connection between the PRE and the post-sunset enhancement over the EIA crest region, Figure 2 is presented. In Figures 2a and 2b, two contrasting vertical drift scenarios during

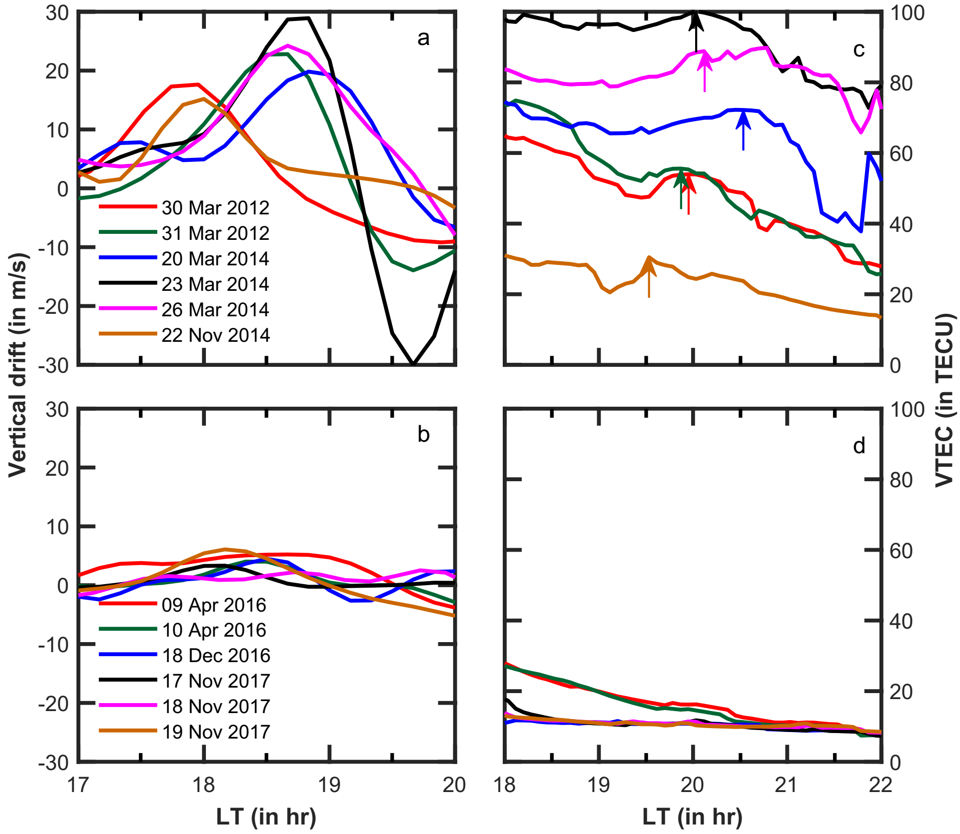

Figure 2. Variation of $dh'F/dt$ and VTEC is shown for the 30 March 2012 (red), 31 March 2012 (green), 20 March 2014 (blue), 23 March 2014 (black), 26 March 2014 (magenta), and 22 November 2014 (dark orange) in panels (a and c) respectively. The colored arrows indicate the time of occurrence of the peak VTEC. Similar variations on 09 April 2016 (red), 10 April 2016 (green), 18 December 2016 (blue), 17 November 2017 (black), 18 November 2017 (magenta), and 19 November 2017 (dark orange) are shown in panels (b and d).

1700–2000 LT are shown for six representative days. While Figure 2a shows the vertical drift variations with strong PRE features, Figure 2b reveals the variations when the PRE features are absent/subdued. Figures 2c and 2d represent the VTEC variations during 1800–2200 LT corresponding to Figures 2a and 2b, respectively. Interestingly, conspicuous enhancements in VTEC (peaks marked by colored arrows) can be noted in Figure 2c. On the other hand, Figure 2d is characterized by absence of any clear enhancement in VTEC. Therefore, the post-sunset enhancements in VTEC over the EIA crest region are observed whenever the PRE is strong over the dip equator. It is also important to note that the time delay between the peak vertical drift and post-sunset VTEC peak ranges from ~1.4 h (31 March 2012) to ~2 h (30 March 2012).

Figure 1 provides samples of day-to-day variability in the post-sunset enhancements in VTEC and airglow intensity over the EIA crest region. Figure 2 shows the connection between the PRE and the post-sunset enhancements in VTEC for a few representative cases. In Figure 3, the large database of VTEC are used in conjunction with model drifts to understand the seasonal and solar activity dependence of the post-sunset enhancement in VTEC over the EIA crest region (Ahmedabad). In Figures 3a–3f, VTEC variations for all the quiet days in three seasons during high (left column) and low (right column) solar activity years are shown (gray curves). The average variations in VTEC (black line) are overlaid on all these subplots. The average curves in Figures 3a–3f comprise of 428, 362, 450, 456, 327 and 317 days' of data. In addition, the vertical drift outputs from the Fejer et al. (2008) model (blue line) as well as smoothed d(VTEC)/dt (red line) are superimposed on each subplot. The smoothed d(VTEC)/dt is derived in the same way as has been adopted for vertical drift described earlier in Figures 1g and 1h. The peak VTEC values during noon (primary maximum) and post-sunset hours (secondary maximum) are identified by P' and S' respectively in the d(VTEC)/

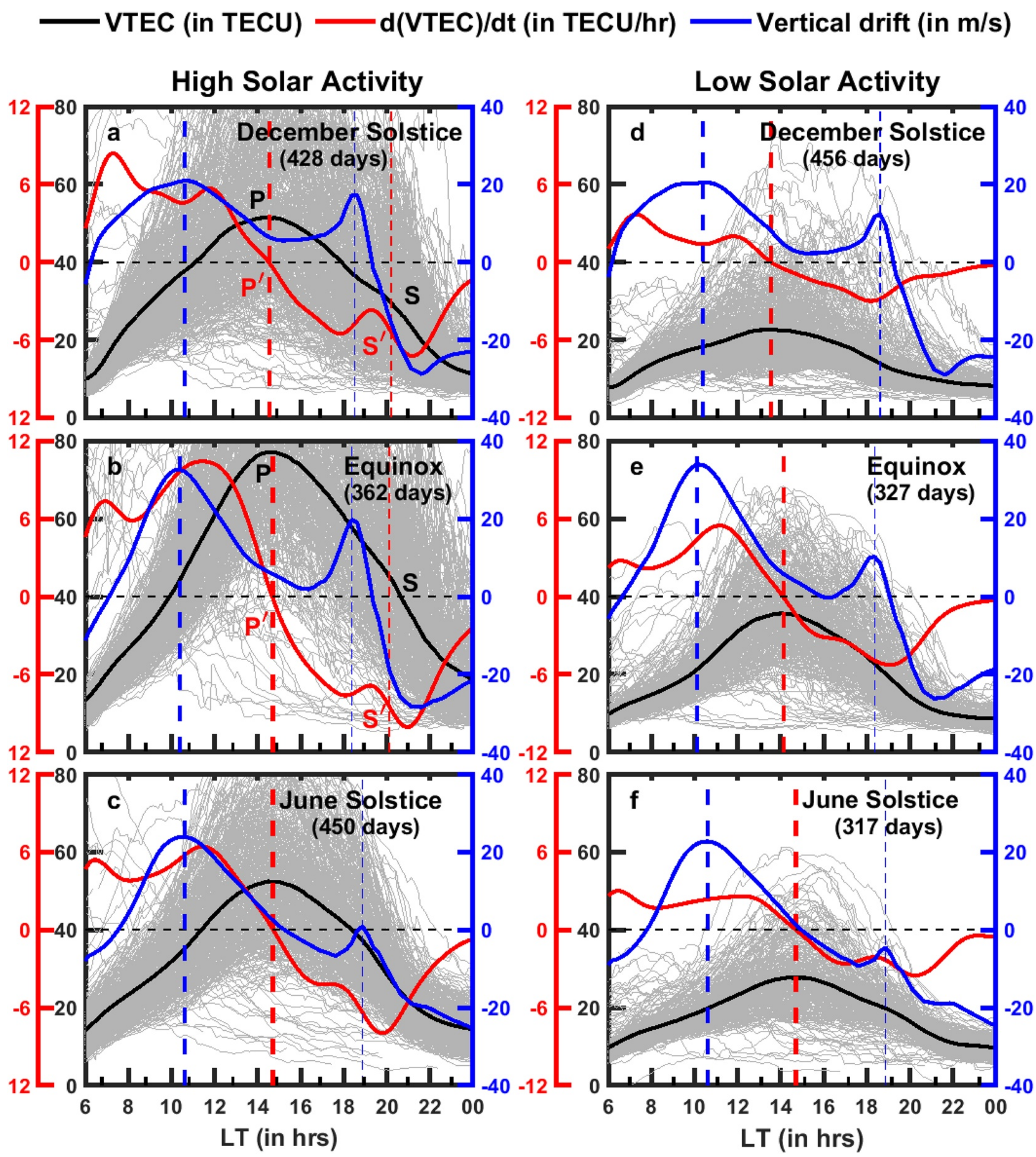

Figure 3. Variation of individual days' VTEC over Ahmedabad (gray), average of seasonal VTEC (black), temporal derivative of seasonal VTEC (red), and vertical drift (blue) in December solstice (top), Equinox (middle), and June solstice (bottom) under high (left panel) and low (right panel) solar activity years. The number of days used to calculate the seasonally averaged VTEC curve is also mentioned in each subplot. The points P and S represent primary (afternoon) and secondary (post-sunset) maxima of VTEC. P and S are determined based on P′ and S′ that are overall and local zero crossing points of *d*VTEC/*dt*. The intervals between the thick and thin vertical dashed lines (blue and red) are the response times of the EIA crest region during noon and post-sunset hours respectively.

dt curves shown in Figures 3a and 3b. *P*′ is the point when *d*(VTEC)/*dt* is zero indicating this is the time when primary maximum (daytime/overall maximum in VTEC) in VTEC is encountered. The trickier part is the *S*′ point based on which the secondary maximum (post-sunset peak) in VTEC is identified. Note that *S*′ is midway (local zero-crossing point) between the point when *d*(VTEC)/*dt* starts increasing and the point when it returns back to the original variation. The *P*′ and *S*′ points help to identify the points P and S that are the maxima during noon and post-sunset hours. As the post-sunset increase in VTEC is embedded in the large amplitude diurnal variation, it is not immediately identifiable and hence, *d*(VTEC)/*dt* helps to identify the VTEC peaks particularly the post-sunset one conspicuously. It is evident from Figure 3 that peak VTEC values are larger during high solar activity period. Interestingly, the enhancements in VTEC during post-sunset hours (after the occurrence of the PRE) occur only in December solstice (Figure 3a) and Equinox (Figure 3b). The times of occurrence of daytime peaks in vertical drifts and VTEC are marked by thick vertical dashed lines in blue and red respectively. On the other hand, the PRE peak and peak of the post-sunset enhancement in VTEC are identified by thin vertical dashed line in blue and red respectively. It can be noted that while the daytime peaks in the VTEC occur during 1330–1500 LT for all seasons and solar epochs, the post-sunset peaks in VTEC occur at ~2000 LT in December solstice and Equinox during the high solar activity period only. Interestingly, the peak drifts during December solstice and Equinox occur at ~1830 LT. At this juncture, the response time of the EIA crest region can be defined as the interval between the time of occurrence of the peak drift (the daytime peak and the PRE-associated peak) and the peak VTEC (the points P and S). Going by this definition, it can be noted that the response time during afternoon hours is more than three hours. However, the response time during post-sunset hours are found to be applicable only during December solstice and Equinox in high solar activity epoch as post-sunset enhancements in VTEC are conspicuously observed after the PRE only for these two cases. The response times in these two cases is found out to be ~1.7 h. It is also to be noted that an evening peak in VTEC is also observed during June solstice in high solar epoch (Figure 3c). However, this peak occurs slightly before the PRE and it can be safely inferred that this peak is not causally related to the PRE. The physical mechanism for the generation of this VTEC peak is a subject matter of a separate investigation and will be taken up in future. Therefore, the response time of the EIA crest region during post-sunset hours is almost half compared to the response time during day.

Figure 4 depicts the SBAS-TEC maps around noon (first and third columns) and post-sunset hours (second and fourth columns) for 24 and 25 November 2014 respectively. Locations of Ahmedabad and Mt. Abu are marked by black (filled) circles in all the subplots. Local times are also shown in each subplot. Different color scales are chosen for all the four columns to bring out the large-scale plasma features conspicuously. It is striking to note that as time progresses in the afternoon hours, TEC gradually decreases over Mt. Abu/Ahmedabad on 24 November (Figures 4a–4d), whereas it gradually increases (Figures 4i–4l) on 25 November. Interestingly, during post-sunset hours on 24 November, TEC sharply decreases over the EIA crest region (Figures 4e–4h). However, on 25 November, the TEC values are comparatively larger over Ahmedabad and Mt. Abu till ~2100 LT (Figures 4m–4o). In fact, a very important feature that comes out after evaluating SBAS-TEC maps on many days during high solar activity period (not shown here) is that the daytime EIA crest becomes stronger (more TEC) over the Mt. Abu/Ahmedabad region during afternoon hours followed by a weakening (less TEC) in the evening hours. However, during post-sunset hours, TEC again increases (albeit in smaller degree) over this region followed by monotonic decrease during the nighttime. It is also to be noted that the post-sunset observations of TEC around Ahmedabad/Mt. Abu are mostly consistent with the post-sunset peak observed in airglow intensity on 24–25 November (Figures 1e and 1f).

Figure 5 is planned to bring out the latitudinal gradient in TEC during the intervals addressed in Figure 4. Figures 5a and 5c depict the latitudinal variations in SBAS-TEC along the 75°E longitude at multiple noon/afternoon (dashed lines) and post-sunset/pre-midnight (solid lines) local times on 24 and 25 November 2014 whereas Figures 5b and 5d show the same plots in normalized scales. TEC variations for each time is normalized with respect to the maximum TEC observed at that local time across all latitudes considered here. This is done to facilitate easy comparison of the latitudinal gradients in the TEC variation at different local times. The latitudes of Ahmedabad and Mt. Abu are shown with vertical thin and thick brown arrows respectively at the *X*-axes of each panel. TEC variations around noon (1105, 1202, 1300, and 1422 h) and sunset hours (1802, 1900, 2002, 2100, and 2202 h) are represented by dashed and solid lines (in different colors) respectively. From Figures 5b and 5d, the locations of the EIA crest region can be clearly identified at different local times. It can be noted from Figure 5, that the daytime latitudinal TEC gradients on the equatorial side of the EIA crests are much smaller than the post-sunset gradients on 25 November. It is also clear that TEC maximizes closer to the location of Ahmedabad/Mt. Abu (between 10° and 15°) on both 24 and 25 November during daytime. However, the nighttime EIA crest is located much closer to the dip-equator during the post-sunset hours on 24 November. In contrast, the crest location in post-sunset hours on 25 November is closer to the daytime crest location and moves toward the dip-equator around 2200 h (green solid line in Figure 5d). This is a classic example of the reverse fountain and this happens between 2100 and 2200 h. Most strikingly, the latitudinal gradient in TEC gradually becomes maximum during 2000–2100 h

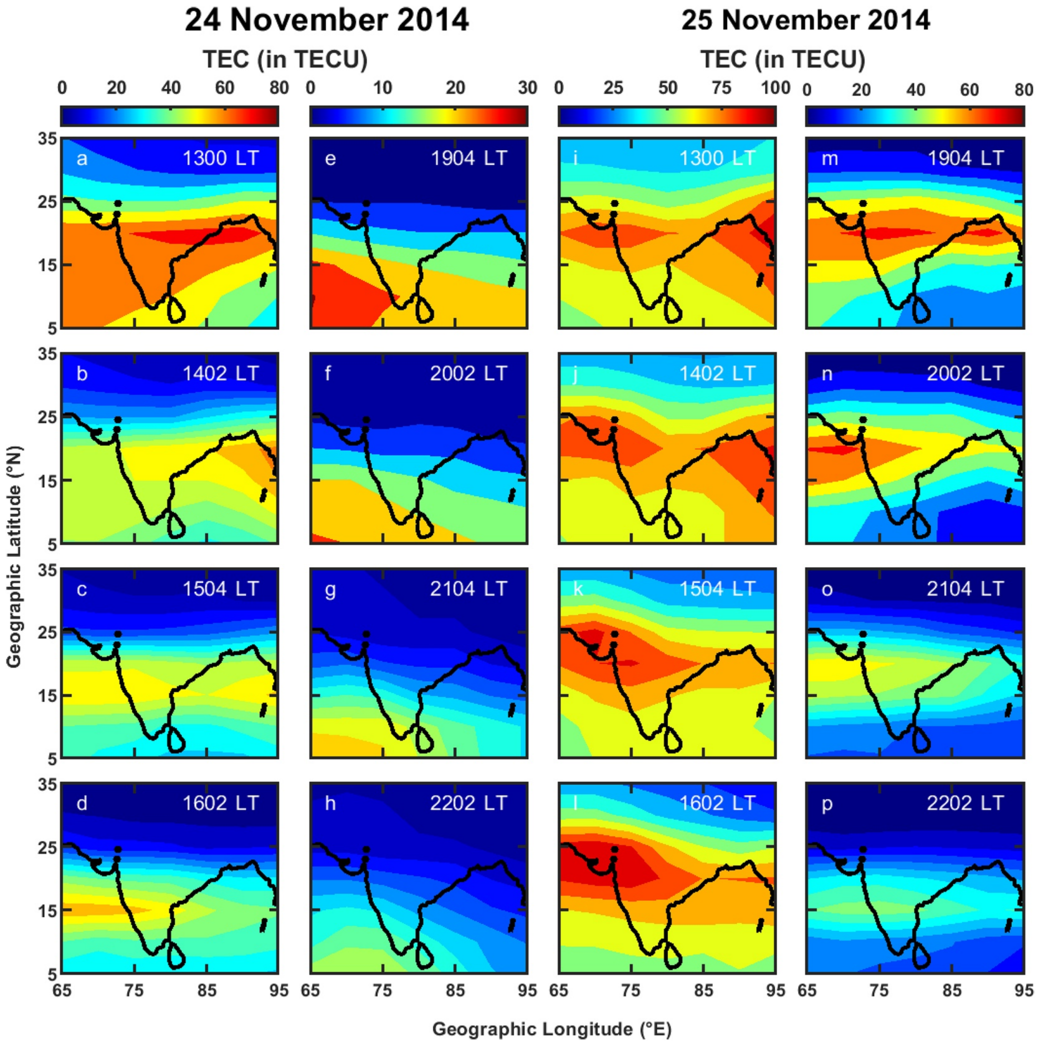

Figure 4. SBAS-TEC maps are shown for 24 November 2014 (a–h) and 25 November 2014 (i–p). Different color scales are adopted for all the four columns to make the large-scale plasma features conspicuous.

just before the reverse fountain process starts. The implications of these observations will be discussed in the ensuing section.

4. Discussion

Earlier observations (e.g., Bittencourt et al., 2007; Farelo et al., 2002; Kulkarni, 1969; Rao & Kulkarni, 1973; Su et al., 1994; Xiong et al., 2016) over the years reported post-sunset enhancements in the plasma density over the EIA crest region. However, the processes that drive and generate this enhancement remain unaddressed. It is obvious from Figures 1 and 4 that the post-sunset enhancement in airglow intensity and VTEC are not directly related to the daytime plasma fountain. Interestingly, the airglow intensity enhancements over Mt. Abu start slightly earlier than the onset of increases in the VTEC over Ahmedabad. This is probably due to the reversal of the vertical drift from upward to downward direction associated with the reversal in the zonal electric field. On careful scrutiny, one can note that the onset of increase in airglow intensity starts sometime during ~1900–1930 LT. This approximately coincides with the time of polarity reversal in the model vertical drift over the Indian dip equatorial station (indicated by Figures 3a and 3b). A downward drift supplies more plasma to the airglow emitting layer resulting in the onset of increase of airglow intensity at this time. As the downward drift does not change the total columnar content of electrons, the VTEC

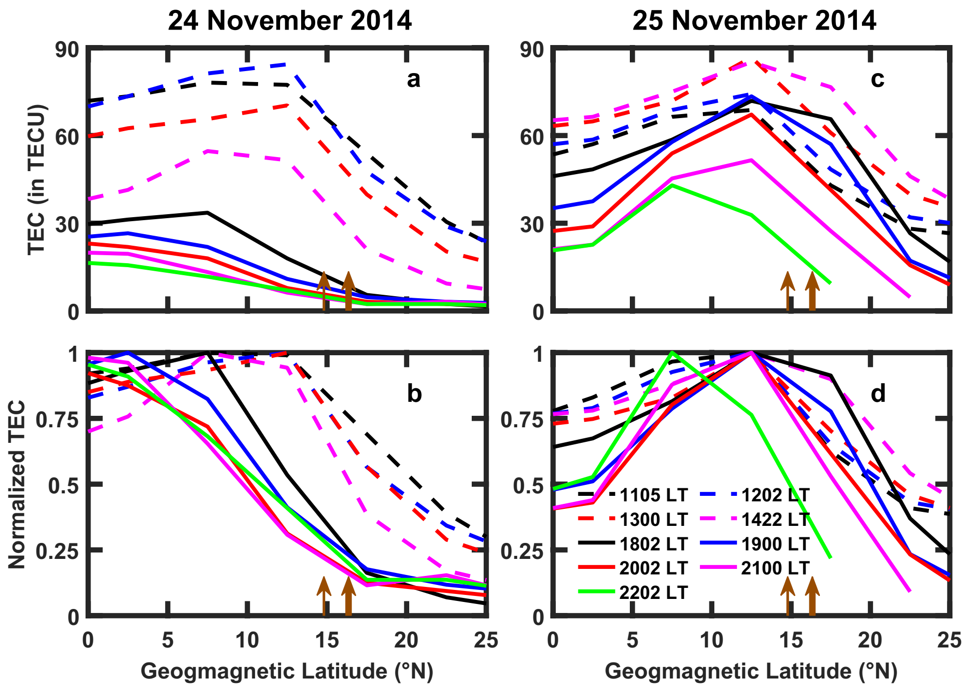

Figure 5. Panels (a) and (c) show the latitudinal variation of SBAS-TEC on 24 and 25 November 2014, respectively along 75°E geographic longitude (148°E geomagnetic longitude). Panels (b) and (d) represent the latitudinal variation of normalized SBAS-TEC corresponding to panels (a) and (b) respectively. Dashed and solid lines are used to show the variations during daytime (1105, 1202, 1300, and 1422 LT) and post-sunset hours (1802, 1900, 2002, 2100, and 2202 LT). Thin and thick brown arrows denote the latitudes of Ahmedabad and Mt. Abu, respectively.

remains unaffected. In fact, VTEC during post-sunset hours changes if there is a meridional transport of plasma. Therefore, the onset of the increase in VTEC marks the onset of arrival of additional plasma from meridional direction. In the intervening period between the onset of increase and the peak intensity, the airglow intensity variations are expected to be governed by both downward vertical drift and the meridional plasma transport. In addition, meridional wind and recombination chemistry can mask the enhancements in airglow intensity to a certain degree by contributing to vertical drift. Nevertheless, the peak in the airglow enhancement over Mt. Abu occurs at a slightly later time than the peak VTEC during post-sunset hours over Ahmedabad. During this time (2000–2030 LT), the changes in the downward drift are not significant as suggested by the model drifts in Figures 3a and 3b. Therefore, it is believed that both VTEC and airglow intensity enhancements at this time are governed by poleward plasma transport. This also rules out the role of reverse plasma fountain (e.g., Balan et al., 1997; Sridharan et al., 1993) that moves equatorward. Further, the reverse fountain over the EIA crest region reported by the earlier works suggests it's arrival at a later time compared to that of the post-sunset peak. This is supported by Figure 5d wherein the reverse fountain is detected sometime between 2100 and 2200 LT.

In order to explore the possible role of meridional wind, the outputs from the Horizontal Wind Model-14 (HWM-14, Drob et al., 2015) are evaluated (not shown here). These outputs as well as previous results (e.g., Balan et al., 1997; Drob et al., 2015) reveal that the poleward wind over the EIA crest region monotonically decreases during the time of occurrence of post-sunset enhancement in airglow intensity reported in this work. Under this condition, the poleward wind will be less efficient in pushing the plasma to the airglow emission altitude band centered at ~250 km. Therefore, the airglow intensity is expected to reduce monotonically during post-sunset hours. This is in contrast to the observations reported in the present work. Therefore, the role of poleward wind does not appear to be significant in this case. Nevertheless, the contribution of meridional wind along with others parameters is included in the subsequent paragraph to derive the parallel component of plasma diffusion velocity. It is also noteworthy that significant reduction in the amplitudes of the post-sunset VTEC peaks are seen during equinox in low solar activity years despite similar magnitudes in the daytime peak eastward electric field (Figures 3b and 3e). Therefore, the direct role of daytime plasma fountain in causing the post-sunset VTEC enhancement over the EIA crest region can be ruled out.

Figure 2 firmly establishes the causal connection between the PRE and the post-sunset enhancements in VTEC over the EIA crest region. The representative cases shown in Figure 2 bring out the time delays between the peak vertical drift associated with the PRE and the peak VTEC that range from 1.4 to 2 h. These time delays are consistent with the average time delay between the PRE and post-sunset enhancement in VTEC over the EIA crest region shown in Figure 3. Interestingly, the post-sunset peaks appear only during December solstice and equinoctial months in high solar activity years and an enhanced PRE is a hallmark feature for these two seasons in high solar activity years (Fejer et al., 2008) as seen in Figure 3. This result is also consistent with the statistical work of Farelo et al. (2002) who showed that the amplitudes of the pre-midnight peak in NmF2 over low latitudes are most pronounced during winter solstice and Equinox in high solar activity years. It is to be noted that the PRE is subdued on other occasions and the significant post-sunset peaks in VTEC are also absent (Figure 3). Therefore, it follows that the PRE strengthens the plasma fountain in the post-sunset hours and this causes enhancements in VTEC and OI 630.0 nm airglow intensity over the EIA crest region with an average delay of ~1.7 h.

The above understanding poses a conundrum. The post-sunset VTEC peak over the EIA crest region appears ~1.7 h later than the time of occurrence of the PRE as opposed to the daytime peak VTEC that occurs 3–4 h after the daytime peak in equatorial vertical drift. It is to be noted in this context that not only the plasma response time (dip equator to crest) during day is consistent with the earlier works (e.g., Rama Rao et al., 2006) but the occurrence of minimum delay during December solstice in low solar activity years is also consistent with the observations made by Aswathy et al. (2018). Further, it may be noted here that observations from the Indian sector suggest that the PRE occurs about half an hour later in Equinox compared to December solstice (e.g., Madhav Haridas et al., 2015; Sripathi et al., 2016). This may reduce the response time of the EIA crest region during Equinox if one uses vertical drift observations from the dip equatorial station. Considering the objective of the present work is to show the reduced response time of the EIA crest region corresponding to the PRE, the conclusion drawn in this work regarding the reduced response time remains unaffected. In order to understand the significantly less response time of the EIA crest region during post-sunset hours, the parallel component ($V_{\parallel}$) of plasma diffusion velocity in the meridional direction is estimated assuming the perpendicular component ($V_{\perp}$) to be negligible over low latitudes. This is reasonable as, over low latitudes, contribution of $V_{\perp}$ to the crest-ward movement of plasma is expected to decrease as dip angle increases. $V_{\parallel}$ is calculated at 350 km height for three representative magnetic latitudes (5°N, 10°N, and 15°N) in December Solstice and Equinox based on the following equation (Anderson, 1971):

$$NV_{\parallel} = -D_a\left[\frac{NsinI}{\epsilon H} + \frac{1}{\epsilon T_i}\left(sinI\frac{\partial(\epsilon NT_i)}{\partial N} + \frac{cosI}{r}\frac{\partial(\epsilon NT_i)}{\partial\theta}\right)\right] + NU_{\theta}cosI \tag{1}$$

In Equation 1, N, I, and U_{θ} represent the electron density, magnetic dip-angle, and meridional wind respectively. T_e and T_i denote electron and ion temperatures and $\epsilon = (T_e + T_i)/T_i$. H and D_a represent atomic Oxygen ion scale height and ambipolar diffusion coefficient respectively. The relevant plasma, neutral, geomagnetic field and meridional wind parameters used as inputs in Equation 1 are taken from IRI-16 (Bilitza et al., 2017), NRLMSISE-00 (Picone et al., 2002), IGRF-13 (Alken et al., 2021), and HWM-14 (Drob et al., 2015) models respectively. Interestingly, calculations based on Equation 1 reveals that $V_{\parallel}$ is smaller in post-sunset hours (~45–55 m/s) compared to noon time (~70–80 m/s) in December solstice. On the other hand, the $V_{\parallel}$ values during post-sunset and noon hours are ~20 m/s in Equinox. This is primarily due to the weaker meridional wind during Equinox. This has been verified by HWM-14 model outputs (figure not shown here). Although $V_{\parallel}$ values are smaller in Equinox than December solstice during post-sunset hours, the enhancements in VTEC over EIA crest region occur around the same local time in these two seasons (Figures 3a and 3b). It is because the PRE occurs later in Equinox than December solstice (e.g., Madhav Haridas et al., 2015; Sripathi et al., 2016). These results suggest that the F-region background conditions over low latitude do not support the reduced response time of the EIA crest region during post-sunset hours.

The present work shows that not only the plasma concentration increases over the EIA crest region (Figure 4) but the latitudinal gradient also becomes much steeper during the post-sunset hours (Figure 5). It

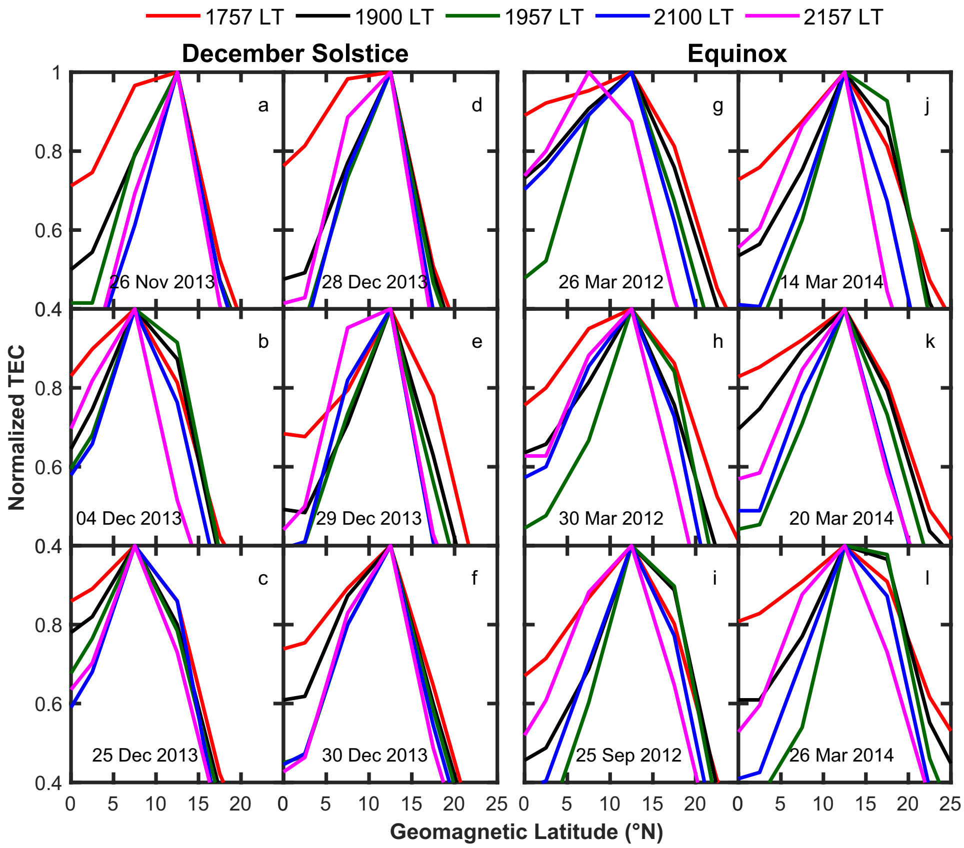

Figure 6. Variations of normalized SBAS-TEC with magnetic latitude (similar to Figures 5b and 5d) at 1757, 1900, 1957, 2100, and 2157 LT for six representative days during December solstice (a–f) and Equinox (g–l) are shown. It can be seen that the latitudinal gradient from 5°N to 10°N to the EIA crest region maximizes and then decays during the post-sunset hours.

is also verified that these results are consistent (not shown here) with the global GPS TEC maps (https://cdaweb.gsfc.nasa.gov/). Such an enhancement in TEC over EIA crest and depletion in the trough region during post-sunset hours can also be noticed in the earlier works corresponding to geomagnetically quiet (e.g., Figure 1 of C.-H. Chen et al., 2017) and disturbed periods (e.g., Figure 6 of Rout et al., 2019). A few earlier studies (e.g., Liu et al., 2007; Sunda & Vyas, 2013) have reported the crest to trough ratio to be larger during the post-sunset hours. Based on Sheffield University Plasmasphere Ionosphere Model (SUPIM), Balan et al. (1997) studied the equatorial plasma fountain under magnetically quiet equinoctial conditions in high solar activity period. Figure 4 of Balan et al. (1997) reveals that at the time of the PRE (1900 LT), the F region plasma gets transported to the EIA crest region from 5° to 10°N magnetic latitude. As the plasma transport from the dip equatorial region to EIA crest is expected to take 3–4 h, the post-sunset enhancement over EIA crest region is unlikely to have plasma contribution from latitudes closer to the dip equator. Owing to significant magnitude of $V_\perp$ till ~7.5° dip latitude (Fejer et al., 1995) plasma would primarily have vertical motions closer to the dip equator and would not get sufficient time to reach EIA crest region before electric field reversal. Therefore, it is evident that relative dominance ($V_\parallel$ becomes increasingly significant) of horizontal plasma transport from 5°N to 10°N causes the enhancement of VTEC and airglow intensity at the EIA crest region during post-sunset hours. As the latitudinal coverage is almost half, the time taken for the PRE-driven plasma to reach EIA crest region is also reduced almost by half. In order to confirm this proposition, the latitudinal TEC variations (normalized as in Figures 5b and 5d) on a large number of days have been investigated. Figure 6 shows the latitudinal TEC variations at five different local times (1757, 1900, 1957, 2100, and 2157 LT) separated by about an hour for six representative days during December solstice (Figures 6a–6f) and Equinox (Figures 6g–6l). It can be noted that the latitudinal gradient from 5°N to 10°N to the EIA crest region keeps increasing in the post-sunset hours, maximizes sometime during 2000–2100 LT and decreases afterward. This strongly suggests plasma transport from low latitude to the EIA crest region during 2000–2100 LT resulting in steep latitudinal gradient in TEC. The fact that the latitudinal gradient decreases from 5°N to 10°N to the EIA crest region at ∼2200 LT suggests that the PRE-driven transport of plasma gets over by this time. It is intuitively obvious that had the plasma traveled from the dip equator to the EIA crest region, it would have taken similar time as it takes during day. The PRE driven plasma closer to the dip equator does not get that time as the reverse fountain starts around 2100 LT (Balan et al., 1997). Once the reverse fountain starts, the post-sunset enhancement in VTEC and airglow intensity starts weakening.

As a concluding remark, it can be said that if the plasma transport from 5°N to 10°N to the EIA crest region occurs during the sharp fall in airglow intensity in the evening hours associated with the F region sunset, the signature of the PRE driven fountain may not be conspicuous in airglow. This is because the rate of reduction in airglow intensity due to the F region sunset is drastic and it will obscure the enhancements due to the PRE (Figure 1e).

5. Summary

It is shown that the PRE of the equatorial zonal electric field causes the enhancement in the plasma density over the EIA crest region during post-sunset hours before the reverse fountain process comes into play. This effect is seen only during December solstice and equinoctial months in high solar activity years. It is proposed that plasma is transported from 5° to 10°N magnetic latitude to the EIA crest region. The response time of the EIA crest region corresponding to the PRE driven fountain is found to be almost half compared to that associated with daytime plasma fountain.

Data Availability Statement

A_p index data is taken from the World Data Center for Geomagnetism, Kyoto (http://wdc.kugi.kyoto-u.ac.jp/). F10.7 solar flux values are obtained from NASA GSFC CDAWeb (http://cdaweb.gsfc.nasa.gov/). The remaining data can be obtained from https://osf.io/mkg6b.

Acknowledgments
The work of B. G. Fejer is supported by the NASA H-LWS program through grant 80SSC17K01. This work is supported by the Department of Space, Government of India.

References

Alken, P., Thebault, E., Beggan, C., Amit, H., Aubert, J., Baerenzung, J., et al. (2021). International geomagnetic reference field: The thirteenth generation. *Earth, Planets and Space*, *73*, 50.

Anderson, D. (1971). *Daily variation of the ionosphere F2 equatorial anomaly in the American & Asian sectors* (Unpublished doctoral dissertation). NCAR: University of Colorado and High Altitude Observatory.

Anderson, D. (1973a). A theoretical study of the ionospheric *F* region equatorial anomaly – I. Theory. *Planetary and Space Science*, *21*(3), 409–419. https://doi.org/10.1016/0032-0633(73)90040-8

Anderson, D. (1973b). A theoretical study of the ionospheric *F* region equatorial anomaly – II. Results in the American and Asian sectors. *Planetary and Space Science*, *21*(3), 421–442. https://doi.org/10.1016/0032-0633(73)90041-X

Aswathy, R. P., Manju, G., & Sunda, S. (2018). The response time of equatorial ionization anomaly crest: A unique precursor to the time of equatorial spread *F* initiation. *Journal of Geophysical Research: Space Physics*, *123*(7), 5949–5959. https://doi.org/10.1029/2018JA025469

Balan, N., Bailey, G., Abdu, M., Oyama, K., Richards, P., MacDougall, J., & Batista, I. (1997). Equatorial plasma fountain and its effects over three locations: Evidence for an additional layer, the F_3 layer. *Journal of Geophysical Research*, *102*(A2), 2047–2056. https://doi.org/10.1029/95JA02639

Balan, N., Bailey, G., Moffett, R., Su, Y., & Titheridge, J. (1995). Modeling studies of the conjugate-hemisphere differences in ionospheric ionization at equatorial anomaly latitudes. *Journal of Atmospheric and Terrestrial Physics*, *57*(3), 279–292. https://doi.org/10.1016/0021-9169(94)E0019-J

Balan, N., Liu, L., & Le, H. (2018). A brief review of equatorial ionization anomaly and ionospheric irregularities. *Earth and Planetary Physics*, *2*(4), 257–275. https://doi.org/10.26464/epp2018025

Basu, S., MacKenzie, E., & Basu, S. (1988). Ionospheric constraints on VHF/UHF communications links during solar maximum and minimum periods. *Radio Science*, *23*(3), 363–378. https://doi.org/10.1029/RS023i003p00363

Bilitza, D., Altadill, D., Truhlik, V., Shubin, V., Galkin, I., Reinisch, B., & Huang, X. (2017). International reference ionosphere 2016: From ionospheric climate to real-time weather predictions. *Space Weather*, *15*(2), 418–429. https://doi.org/10.1002/2016SW001593

Bittencourt, J. A., & Abdu, M. A. (1981). A theoretical comparison between apparent and real vertical ionization drift velocities in the equatorial *F* region. *Journal of Geophysical Research*, *86*(A4), 2451–2454. https://doi.org/10.1029/JA086iA04p02451

Bittencourt, J. A., Pillat, V. G., Fagundes, P. R., Sahai, Y., & Pimenta, A. A. (2007). LION: A dynamic computer model for the low-latitude ionosphere. *Annales Geophysicae*, *25*(11), 2371–2392. https://doi.org/10.5194/angeo-25-2371-2007

Chakrabarty, D., Bagiya, M. S., & Thampi, S. V. (2012). Solar EUV flux (0.1-50 nm), F10.7 cm flux, sunspot number and the total electron content in the crest region of equatorial ionization anomaly during the deep minimum between solar cycle 23 and 24. *Indian Journal of Radio and Space Physics*, *41*(2), 110–120.

Chakrabarty, D., Rout, D., Sekar, R., Narayanan, R., Reeves, G. D., Pant, T. K., et al. (2015). Three different types of electric field disturbances affecting equatorial ionosphere during a long-duration prompt penetration event. *Journal of Geophysical Research: Space Physics*, *120*(6), 4993–5008. https://doi.org/10.1002/2014JA020759

Chakrabarty, D., Sekar, R., Sastri, J. H., & Ravindran, S. (2008). Distinctive effects of interplanetary electric field and substorm on nighttime equatorial *F* layer: A case study. *Geophysical Research Letters*, *35*, L19108. https://doi.org/10.1029/2008GL035415

Chen, C.-H., Lin, C., Chen, W.-H., & Matsuo, T. (2017). Modeling the ionospheric prereversal enhancement by using coupled thermosphere-ionosphere data assimilation. *Geophysical Research Letters*, *44*(4), 1652–1659. https://doi.org/10.1002/2016GL071812

Chen, Y., Liu, L., Le, H., Wan, W., & Zhang, H. (2016). Equatorial ionization anomaly in the low-latitude topside ionosphere: Local time evolution and longitudinal difference. *Journal of Geophysical Research: Space Physics*, *121*(7), 7166–7182. https://doi.org/10.1002/2016JA022394

Drob, D. P., Emmert, J. T., Meriwether, J. W., Makela, J. J., Doornbos, E., Conde, M., et al. (2015). An update to the Horizontal Wind Model (HWM): The quiet time thermosphere. *Earth and Space Science*, *2*(7), 301–319. https://doi.org/10.1002/2014EA000089

Eccles, J. V., St Maurice, J. P., & Schunk, R. W. (2015). Mechanisms underlying the prereversal enhancement of the vertical plasma drift in the low-latitude ionosphere. *Journal of Geophysical Research: Space Physics*, *120*(6), 4950–4970. https://doi.org/10.1002/2014JA020664

Farelo, A. F., Herraiz, M., & Mikhailov, A. V. (2002). Global morphology of night-time NmF2 enhancements. *Annales Geophysicae*, *20*(11), 1795–1806. https://doi.org/10.5194/angeo-20-1795-2002

Fejer, B. G. (2011). Low latitude ionospheric electrodynamics. *Space Science Reviews*, *158*(1), 145–166.

Fejer, B. G., de Paula, E. R., Heelis, R. A., & Hanson, W. B. (1995). Global equatorial ionospheric vertical plasma drifts measured by the AE-E satellite. *Journal of Geophysical Research*, *100*(A4), 5769–5776. https://doi.org/10.1029/94JA03240

Fejer, B. G., Jensen, J. W., & Su, S.-Y. (2008). Quiet time equatorial *F* region vertical plasma drift model derived from ROCSAT-1 observations. *Journal of Geophysical Research*, *113*, A05304. https://doi.org/10.1029/2007JA012801

Huang, Y.-N., & Cheng, K. (1995). Solar cycle variation of the total electron content around equatorial anomaly crest region in East Asia. *Journal of Atmospheric and Terrestrial Physics*, *57*(12), 1503–1511. https://doi.org/10.1016/0021-9169(94)00147-G

Huang, Y.-N., Cheng, K., & Chen, S. W. (1989). On the equatorial anomaly of the ionospheric total electron content near the northern anomaly crest region. *Journal of Geophysical Research*, *94*(A10), 13515–13525. https://doi.org/10.1029/JA094iA10p13515

Kulkarni, P. V. (1969). Airglow studies in low latitudes. *Presented at Third International Symposium on Equatorial Aeronomy*, *2*(1), 412.

Liu, H., Stolle, C., Frster, M., & Watanabe, S. (2007). Solar activity dependence of the electron density in the equatorial anomaly regions observed by champ. *Journal of Geophysical Research*, *112*, A11311. https://doi.org/10.1029/2007JA012616

MacDougall, J., Grant, I., & Shen, X. (1995). The Canadian advanced digital ionosonde: Design and results. *URSI INAG Ionospheric Station Inf. Bulletin, UAG-104*.

Madhav Haridas, M. K., Manju, G., & Pant, T. K. (2015). On the solar activity variations of nocturnal *F* region vertical drifts covering two solar cycles in the Indian longitude sector. *Journal of Geophysical Research: Space Physics*, *120*(2), 1445–1451. https://doi.org/10.1002/2014JA020561

Manke, A. A., & Chakarabarty, D. (2016). An integrated software platform for GPS/GNSS ionospheric data analysis. *International Journal of Science, Engineering and Technology*, *4*(5), 796–804. https://doi.org/10.2348/ijset09160796

Mo, X. H., Zhang, D. H., Liu, J., Hao, Y. Q., Ye, J. F., Qin, J. S., et al. (2018). Morphological characteristics of equatorial ionization anomaly crest over nanning region. *Radio Science*, *53*(1), 37–47. https://doi.org/10.1002/2017RS006386

Pandey, K., Sekar, R., Gupta, S., Chakrabarty, D., & Anandarao, B. (2017). Comparison of quiet time vertical plasma drifts with global empirical models over the Indian sector: Some insights. *Journal of Atmospheric and Solar-Terrestrial Physics*, *157–158*, 42–54. https://doi.org/10.1016/j.jastp.2017.03.012

Picone, J. M., Hedin, A. E., Drob, D. P., & Aikin, A. C. (2002). NRLMSISE-00 empirical model of the atmosphere: Statistical comparisons and scientific issues. *Journal of Geophysical Research*, *107*, 1468. https://doi.org/10.1029/2002JA009430

Rama Rao, P. V. S., Gopi Krishna, S., Niranjan, K., & Prasad, D. S. V. V. D. (2006). Temporal and spatial variations in TEC using simultaneous measurements from the Indian GPS network of receivers during the low solar activity period of 2004–2005. *Annales Geophysicae*, *24*(12), 3279–3292. https://doi.org/10.5194/angeo-24-3279-2006

Rao, V., & Kulkarni, P. (1973). 6300 Å night airglow enhancements in low latitudes. *Journal of Atmospheric and Terrestrial Physics*, *35*(2), 193–206. https://doi.org/10.1016/0021-9169(73)90087-1

Rastogi, R., & Patel, V. (1975). Effect of interplanetary magnetic field on ionosphere over the magnetic equator. *Proceedings of the Indian Academy of Sciences-Section A*, *82*, 121–141. https://doi.org/10.1007/BF03046722

Rout, D., Pandey, K., Chakrabarty, D., Sekar, R., & Lu, X. (2019). Significant electric field perturbations in low latitude ionosphere due to the passage of two consecutive ICMEs during 6–8 September 2017. *Journal of Geophysical Research: Space Physics*, *124*(11), 9494–9510. https://doi.org/10.1029/2019JA027133

Sastri, J. H. (1990). Equatorial anomaly in *F*-region – A review. *Indian Journal of Radio and Space Physics*, *19*(4), 225–240.

Savitzky, A., & Golay, M. J. (1964). Smoothing and differentiation of data by simplified least squares procedures. *Analytical Chemistry*, *36*(8), 1627–1639.

Sekar, R., & Chakrabarty, D. (2011). A review of the recent advances in the investigation of equatorial spread F and space weather effects over Indian sector using optical and other techniques. In M. A. Abdu, & D. Pancheva (Eds.), *Aeronomy of the Earth's Atmosphere and Ionosphere* (pp. 251–268). Springer.

Sridharan, R., Sekar, R., & Gurubaran, S. (1993). Two-dimensional high-resolution imaging of the equatorial plasma fountain. *Journal of Atmospheric and Terrestrial Physics*, *55*(13), 1661–1665. https://doi.org/10.1016/0021-9169(93)90170-4

Sripathi, S., Singh, R., Banola, S., Sreekumar, S., Emperumal, K., & Selvaraj, C. (2016). Characteristics of the equatorial plasma drifts as obtained by using Canadian Doppler ionosonde over southern tip of India. *Journal of Geophysical Research: Space Physics*, *121*(8), 8103–8120. https://doi.org/10.1002/2016JA023088

Su, Y., Bailey, G., & Balan, N. (1994). Night-time enhancements in TEC at equatorial anomaly latitudes. *Journal of Atmospheric and Terrestrial Physics*, *56*(12), 1619–1628. https://doi.org/10.1016/0021-9169(94)90091-4

Sunda, S., Sridharan, R., Vyas, B. M., Khekale, P. V., Parikh, K. S., Ganeshan, A. S., & Bagiya, M. S. (2015). Satellite-based augmentation systems: A novel and cost-effective tool for ionospheric and space weather studies. *Space Weather*, *13*(1), 6–15. https://doi.org/10.1002/2014SW001103

Sunda, S., & Vyas, B. M. (2013). Local time, seasonal, and solar cycle dependency of longitudinal variations of TEC along the crest of EIA over India. *Journal of Geophysical Research: Space Physics*, *118*(10), 6777–6785. https://doi.org/10.1002/2013JA018918

Xiong, C., Zhou, Y.-L., Lhr, H., & Ma, S.-Y. (2016). Diurnal evolution of the *F* region electron density local time gradient at low and middle latitudes resolved by the Swarm constellation. *Journal of Geophysical Research: Space Physics*, *121*(9), 9075–9089. https://doi.org/10.1002/2016JA023034

Yadav, S., Choudhary, R. K., Kumari, J., Sunda, S., Shreedevi, P. R., & Pant, T. K. (2020). Reverse fountain and the nighttime enhancement in the ionospheric electron density over the equatorial region: A case study. *Journal of Geophysical Research: Space Physics*, *125*, e2019JA027286. https://doi.org/10.1029/2019JA027286

ADVANCING EARTH AND SPACE SCIENCE

JGR Space Physics

RESEARCH ARTICLE

10.1029/2021JA030156

Key Points:

- Post-sunset enhancements in vertical total electron content (VTEC) over the equatorial ionization anomaly crest region are significant only above 110 solar flux unit level during December solstice and Equinox
- Pre-reversal enhancement (PRE) of equatorial zonal electric field is shown to primarily drive the post-sunset enhancements in VTEC
- Thermosphere Ionosphere Electrodynamics-General circulation model simulations reveal the additional importance of latitudinal plasma density gradients over low latitudes

Supporting Information:

Supporting Information may be found in the online version of this article.

Correspondence to:

A. Kumar,
ankitprl2017@gmail.com

Citation:

Kumar, A., Chakrabarty, D., Pandey, K., & Yadav, A. K. (2022). Solar flux dependence of post-sunset enhancement in vertical total electron content over the crest region of equatorial ionization anomaly. *Journal of Geophysical Research: Space Physics*, *127*, e2021JA030156. https://doi.org/10.1029/2021JA030156

Received 16 DEC 2021
Accepted 9 APR 2022

Solar Flux Dependence of Post-Sunset Enhancement in Vertical Total Electron Content Over the Crest Region of Equatorial Ionization Anomaly

A. Kumar[1,2], D. Chakrabarty[1], K. Pandey[1,3], and A. K. Yadav[1]

[1]Physical Research Laboratory, Ahmedabad, India, [2]Indian Institute of Technology, Gandhinagar, India, [3]ISAS, Department of Physics and Engineering Physics, University of Saskatchewan, Saskatoon, SK, Canada

Abstract Based on 10 years' of vertical total electron content (VTEC) data in solar cycle 24 from Ahmedabad (23.0°N, 72.6°E, dip angle 35.2°), a station under the crest region of equatorial ionization anomaly (EIA), it is shown that both the integrated residual and total post-sunset enhancements in VTEC are conspicuous during Equinox and December solstice when solar flux level exceeds 110 solar flux unit (sfu) with the exception of the year 2012–2013. The post-sunset enhancements are absent in June solstice at this local time even if the solar flux level exceeds 110 sfu. The integrated residual and total VTEC enhancements during post-sunset hours are found to be linearly correlated with the solar flux level in Equinox and December solstice. It is noted that a parabolic fit works better for the integrated total VTEC enhancement during December solstice suggesting a possible saturation of VTEC enhancements at high solar flux levels. Based on these observations and Thermosphere Ionosphere Electrodynamics-General circulation model (TIE-GCM) outputs, it is argued that the pre-reversal enhancement (PRE) in the equatorial F region zonal electric field works in tandem with latitudinal gradient in the F region plasma density to determine the degree of VTEC enhancement over the EIA crest region during post-sunset hours. These results highlight the solar flux dependence of the post-sunset enhancement of VTEC over the crest region and show that sudden stratospheric warming events in 2012–2013 suppressed these enhancements in December solstice even if solar flux levels exceeded 110 sfu.

Plain Language Summary The low latitude region is one of the most L-band scintillation affected region in the whole globe. In addition, owing to the equatorial plasma fountain process, the low latitude F region ionosphere is also marked by steep latitudinal plasma density gradient during post-sunset hours. It is shown that the evening plasma fountain driven by pre-reversal enhancement of the zonal electric field controls the post-sunset enhancement of the F region plasma density over the crest region of equatorial ionization anomaly (EIA) region with the assistance from the latitudinal plasma density gradient. This result is important to forecast the ionospheric condition over the EIA crest region during post-sunset hours.

1. Introduction

The low latitude ionosphere has the distinction of causing the maximum L-band scintillation during post-sunset hours in the whole globe. In fact, the scintillations over the crest region of the Equatorial Ionization Anomaly (henceforth, EIA crest) are the most pronounced during the high solar activity period (e.g., Basu et al., 1988). Therefore, the equatorial ionization anomaly (EIA) crest region is particularly important in the context of global communication and navigational applications. Even in the absence of plasma irregularities that cause L-band scintillation, the F region ionosphere over the low latitudes is known (e.g., Bittencourt et al., 2007; Farelo et al., 2002; Kulkarni, 1969; Rao & Kulkarni, 1973; Su et al., 1994; Xiong et al., 2016) to show enhancements in plasma density after the sunset. Morphologically, these enhancements start anytime after 1900 LT and peak around 2000 LT. These post-sunset enhancements in plasma density leave their footprints in the measured total electron content (TEC), thermospheric airglow intensities (e.g., Kumar et al., 2021) and can play an important role in conditioning the equatorial ionization anomaly (EIA) crest region.

In order to understand the genesis of these post-sunset enhancements, it is important to understand the F region equatorial plasma fountain (EPF) process (e.g., Anderson, 1973a; Anderson, 1973b) comprehensively as this process distributes the equatorial F region plasma over low latitudes. equatorial plasma fountain (EPF) is the resultant effect of the vertical $E \times B$ drift (as a consequence of eastward electric field and northward magnetic field configuration over the dip equator) followed by the ambipolar diffusion of the F region plasma in the meridional direction assisted by pressure gradient force and gravity. The equatorial plasma fountain (EPF) generates two higher plasma density regions around ±15° magnetic latitudes. Thus, EPF generates an anomalous distribution of F region plasma over the low latitudes that cannot be explained by the production and loss processes. Hence, this low latitude F region plasma density distribution has come to be known as the equatorial ionization anomaly (EIA). The enhanced plasma density regions over the low latitudes are termed as the EIA crests and the plasma depleted region over the dip equator is known as the EIA trough. It is known that the EIA crests become asymmetric due to the effects of the meridional wind (e.g., Anderson, 1973a). In fact, the variabilities in the ionospheric electric field and meridional wind cause variability in the F region plasma distribution over low latitudes that show not only day-to-day (e.g., Y.-N. Huang et al., 1989) but seasonal and solar flux dependence (e.g., Chakrabarty et al., 2012; Y.-N. Huang & Cheng, 1995; Mo et al., 2018) as well.

The daytime equatorial F region zonal electric field polarity is eastward and it flips to westward direction during nighttime. However, this transition is not monotonic and punctuated by enhancement of the F region electric field due to the competition between E and F region dynamo mechanisms at the local sunset terminator. This enhancement in the zonal electric field (or vertical drift) is known as pre-reversal enhancement (PRE) (e.g., Eccles et al., 2015; Fejer, 2011). Interestingly, Pre-reversal enhancement (PRE) shows day-to-day, seasonal, and solar flux variability (e.g., Fejer et al., 2008; Liu et al., 2020; Whalen, 2004). As the zonal electric field gets enhanced during Pre-reversal enhancement (PRE) hours, it is expected that the plasma fountain process should get reinvigorated at this time and the low latitude plasma distribution should bear its signature. This is what is shown recently by Kumar et al. (2021). In this work, it is shown that the PRE rejuvenates the EPF that, in turn, enhances the plasma density over the EIA crest during 20–21 LT. It has also been shown (e.g., Kumar et al., 2021) that PRE-driven fountain reaches the EIA crest region earlier than the daytime fountain as the F region plasma primarily gets transported from the low latitudes to the EIA crest region.

Kumar et al. (2021) also suggested that the post-sunset F region plasma density enhancements over the EIA crest region are pronounced during Equinox and December solstice in the high solar activity period. These seasonal and solar activity dependences of the post-sunset enhancements seem to be in-sync to what had been observed in case of PRE (e.g., Fejer et al., 2008; Scherliess & Fejer, 1999). Kumar et al. (2021) showed that the day-to-day and seasonal dependences of the post-sunset plasma density enhancements near the EIA crest region are consistent with the day-to-day and seasonal variabilities of PRE. However, it remains to be seen whether the solar flux dependence of PRE (stronger PRE during high solar flux conditions) gets reflected in the similar solar flux dependence of the post-sunset enhancement of plasma density near the EIA crest region. This is an important missing link as evidence in this regard has the potential to put the causal connection between the PRE and the post-sunset enhancement on a firm footing.

There have been indications of the solar flux dependence on the connection between PRE and low latitude plasma distribution in post-sunset hours in the earlier works. Whalen (2004) showed that both post-sunset EIA and PRE vary linearly with solar flux. Abdu et al. (2008) suggested that the EPF driven by PRE in the evening hours changes the total electron content (TEC), foF2 and the intensity of EIA and these changes have solar flux dependence. However, it was not clear whether enhancements in total electron content (TEC) or foF2 would occur at any solar flux level and whether PRE is a necessary as well as sufficient condition for these enhancements. Chen et al. (2017) modeled the PRE by coupled ionosphere-thermosphere data assimilation and showed that a stronger PRE generates a stronger EPF during evening hours deepening the equatorial trough. This result is consistent with the observations (e.g., H. Liu et al., 2007; Zhang et al., 2009) in which it is shown that the latitudinal plasma gradient from trough to crest becomes higher during post-sunset hours and crest to trough ratio (CTR) also becomes maximum. Interestingly, in these works, crest to trough ratio (CTR) has been shown to have stronger solar flux dependence during post-sunset hours than noon time. Further, the local time (e.g., Oryema et al., 2016; Zhang et al., 2009), seasonal (e.g., Olwendo et al., 2016), solar flux (e.g., H. Liu et al., 2007; Zhang et al., 2009), longitudinal (e.g., Sunda & Vyas, 2013) and solar activity dependence (e.g., Zhao et al., 2009) of crest to trough ratio (CTR) have been brought out. Oryema et al. (2016) showed that CTR is maximum during the period 21–23 LT. Liu et al. (2007) also found 2–3 times higher CTR during post-sunset hours than noon-hours with increasing solar activity. These results suggest that it is important to understand the solar flux dependence of the post-sunset enhancements of the plasma density over the EIA crest region in greater detail to address its' causal connection with PRE. This is an important question as it is not clear whether an enhanced PRE guarantees enhancements in plasma density over the EIA crest region or there are other additional factors that contribute to these enhancements. The answer to this question will determine whether PRE is a necessary as well as sufficient condition for the post-sunset enhancements reported by Kumar et al. (2021).

2. Datasets and TIE-GCM Outputs

The vertical total electron content (VTEC) data used in this work is derived based on the measurements using the dual-frequency (L-band, 1,575 and 1,227 MHz) Global Positioning System (GPS)-receiver (GISTM GSV4004 B) at the Physical Research Laboratory, Ahmedabad (23.0°N, 72.6°E, dip angle 35.2°) for more than a decade (November 2009–December 2019). Manke and Chakarabarty (2016) described this instrument and the data analysis technique to derive vertical total electron content (VTEC). In this work, the quiet period data are selected based on the Ap index. Daily mean Ap ≤15 on the chosen day and the previous day qualify the chosen day as a "quiet day". It is to be noted that slant TEC (STEC) values are first derived based on the GPS observations. These slant TEC (STEC) values are converted to vertical TEC values (VTEC) using an obliquity factor or mapping function (Mannucci et al., 1993), which is a function of the elevation angle of the respective GPS satellite. In the present investigation, an elevation mask of 30° is used to minimize the multipath and troposphere scattering effects (e.g., Chakrabarty et al., 2012) as these effects are more prominent at lower elevation angles. It is also to be noted here that the ionospheric pierce points (IPPs) change with movements of the GPS satellites (e.g., Huang et al., 2020). This may result in slight changes in the averaged GPS-VTEC. However, for geostationary (GEO) satellites, the ionospheric pierce points (IPPs) are nearly stationary. Therefore, before using GPS-VTEC data in the present work, we compared GPS-TEC variations with the geostationary vertical total electron content (GEO-VTEC) variations from the same location (Ahmedabad). The GEO-VTEC data used in the present work comes from the Indian Regional Navigation Satellite System known as Navigation with Indian Constellation (NavIC). It has been shown (e.g., Ayyagari et al., 2020) that the NavIC-VTEC and GPS-VTEC are remarkably consistent over the Indian sub-continent in general and the northern EIA crest region in particular. The Figure S1 in Supporting Information S1 captures independent comparisons of GPS-VTEC with NavIC-VTEC derived from one of the GEO satellites (PRN I03 at 83°E) for four geomagnetically quiet days. It is found that the variations in GPS-VTEC and NavIC-VTEC closely follow each other. The GPS-VTEC values are well within 15% of the NavIC-VTEC values regardless of the local time.

The GPS-VTEC data are grouped into three seasons for 10 consecutive years (November 2009–October 2019) and compared. To provide an example, the data for the year 2009–2010 comprise of the VTEC data from November 2009 to October 2010, 2010–2011 consists of the VTEC data from November 2010 to October 2011 and so on. Further, each year is divided into three seasons - December solstice (November, December, January, and February), Equinox (March and April, September and October), and June solstice (May, June, July, and August). Daily average F10.7 cm solar radio flux is also grouped in the same manner for comparison. In addition, to quantify the relationship between the post-sunset enhancements in VTEC (ΔVTEC) and the solar flux, the ΔVTEC data are also grouped according to the solar flux values ranging from 80 to 180 sfu (sfu = solar flux unit, 1 sfu = 10^{-22}Wm^{-2} Hz^{-1}) in bin size of 5 sfu. It is to be noted here that the bins with less than 10 days' of VTEC data are not considered in the present investigation. The VTEC data used in the present work are averaged for 5 min.

In order to identify the post-sunset enhancements in VTEC, two representative classes are chosen and shown in Figure 1. Figures 1a and 1c show the local time variations of individual VTEC variations (gray lines) during 06–24 LT in December solstice in the year 2014–2015 and 2017–2018. In the first class (2014–2015), the post-sunset enhancement in VTEC is observed and in the second class (2017–2018), it is not. This is diagnosed by the average curve (black, bold line) superimposed on the gray curves and this average curve is constructed based on the mean of VTEC variations for all the individual days shown in gray lines. The average solar flux levels and the number of days used to construct the average curve are also mentioned in the figures. Even without the aid of any analysis, it can be noted that the post-sunset enhancement in VTEC in the average curve at ~20 LT is conspicuously identifiable for the first class and not for the second class. In order to clearly identify the enhancements, the VTEC variations during 17–23 LT are expanded and shown in Figures 1b and 1d. In these figures, the linear fitting technique is applied to join the points that mark the start and end of the enhancements as in Figure 1b (or negative enhancements/decrease as in Figure 1d). The start and end of the linear fits are marked by the vertical dashed lines. The linear fits are shown in dashed blue lines. The residuals obtained by subtracting

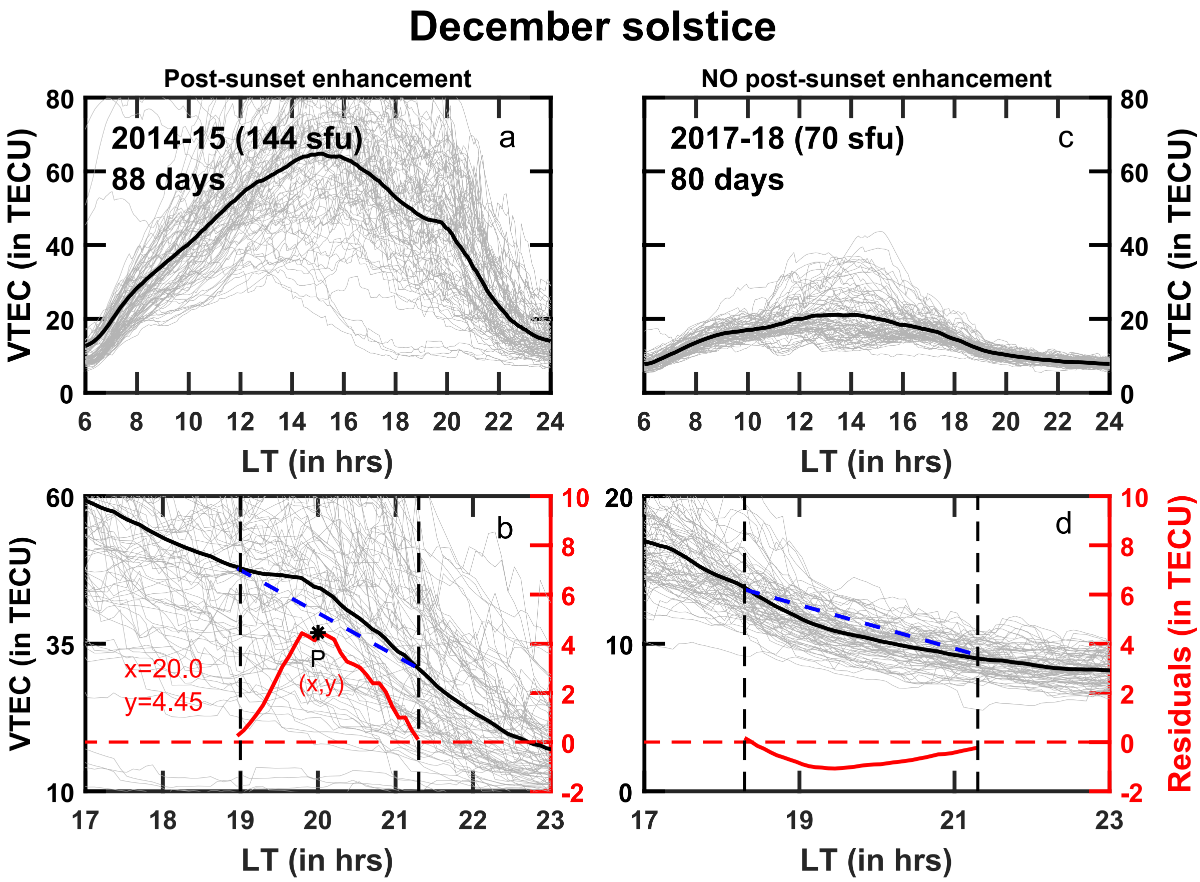

Figure 1. Two representative classes of diurnal vertical total electron content (VTEC) variations (a) with post-sunset enhancement (December solstice, 2014–2015) and (c) without post-sunset enhancement (December solstice, 2017–2018) are shown. The gray curves in a-d are the variations on individual days and the bold black curves represent the average variations. The solar flux levels and the number of days' data used to construct the average curve are also provided in each Figure. VTEC variations during 17–23 LT are blown-up in Figures b and d to show the presence and absence of post-sunset enhancement in VTEC in the average variations. Linear fitting (blue dashed lines) is carried out to extract the residuals (red lines) that reveal the post-sunset enhancement in (b) and post-sunset reduction (d) in VTEC in the average variations. The coordinates of the point P(x,y) in (b) shows the peak VTEC level during the post-sunset enhancement period and the corresponding local time.

the blue lines from the black lines are shown by the red curves and the corresponding Y-axis scales are also shown on the RHS of Figures 1b and 1d. Positive residuals suggest presence of enhancements in VTEC and negative residuals suggest absence of any enhancement. It can be seen that in case of the first class (Figure 1b), the residuals are positive whereas in case of the second class (Figure 1d), the residuals are negative. The peak value of the positive residual (enhancement) is marked by a black star and denoted by P(x, y) where x, y denote the coordinates of the abscissa and the ordinates. For example, in case of Figure 1b, the peak in the post sunset enhancement is found to occur at 20 LT with the magnitude of enhancement of 4.45 total electron content unit (TECU), 1 TECU = $10^{16} electrons/m^2$). In Figure 1 and subsequently in Figures 2–4, the coordinate values (x, y) of the peak positive residual are mentioned wherever enhancements are seen. It is to be noted here that in some of the earlier works (e.g., Young et al., 1970; Balan & Rao, 1984; Liu et al., 2013) related to post-sunset enhancements, exponentially fitted curves are used to extract the post-sunset enhancements in foF2 and VTEC. While the linear fitting may under/over-estimate the post-sunset enhancements to some extent on occasions, the exponential fitting is sensitive to the choice of the initial point from where the fitting starts. This too may lead to under/over-estimations of residuals. Nevertheless, it has been verified that the residuals obtained by both the fitting procedures closely match with each other if done carefully. In order to minimize the fitting subjectivity from one curve to another, linear fitting procedure is adopted in the present work to extract the residuals and to identify the post-sunset enhancements in VTEC.

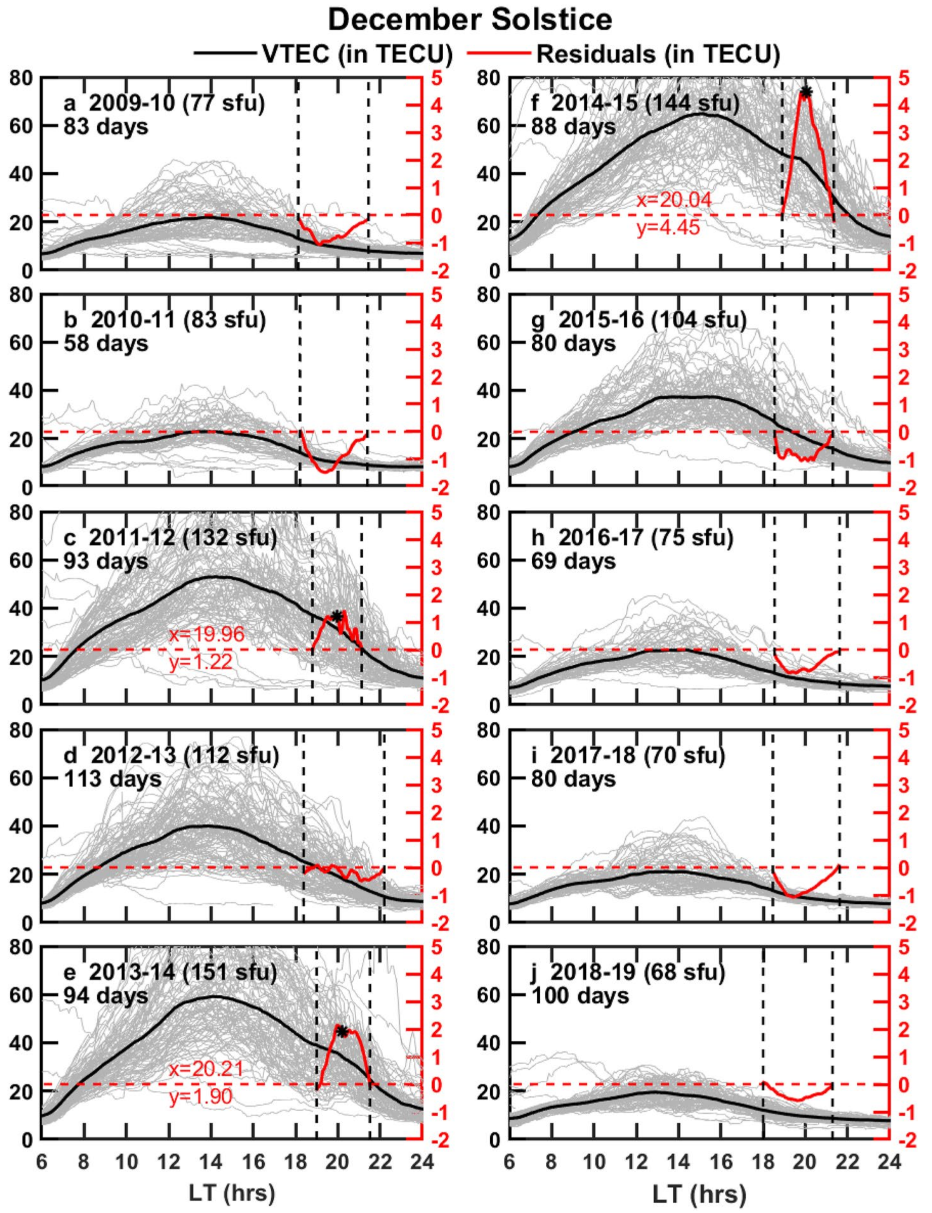

Figure 2. Vertical total electron content (VTEC) variations on individual days (gray), (a) average variation of VTEC (black) and residuals of average VTEC (red) in December solstice during 2009–2010, (b) 2010–2011, (c) 2011–2012, (d) 2012–2013, (e) 2013–2014, (f) 2014–2015, (g) 2015–2016, (h) 2016–2017, (i) 2017–2018, and (j) 2018–2019. The start/end times of the residuals are marked with the vertical dashed lines. The number of days that goes into the calculation of the average VTEC variations and corresponding average solar flux levels are also mentioned for each year. Unambiguous post-sunset enhancements are seen during 2011–2012, 2013–2014 and 2014–2015. In 2012–2013, the residuals start becoming positive.

2.1. TIE-GCM Outputs

Thermosphere Ionosphere Electrodynamics-General circulation model (TIE-GCM) outputs Thermosphere-Ionosphere-Electrodynamics General Circulation Model (TIE-GCM) is used to understand the altitudinal and latitudinal variation of the plasma density and vertical drift over low latitude ionosphere at different solar flux levels. TIE-GCM is a self-consistent, first principle, and physics-based model that is developed at the High Altitude Observatory, National Center for Atmospheric Research. The earlier version of Thermosphere Ionosphere Electrodynamics-General circulation model (TIE-GCM) was the Thermospheric General Circulation Model (TGCM) (Dickinson et al., 1984) that calculated upper atmospheric parameters like temperature, neutral density, etc. Roble

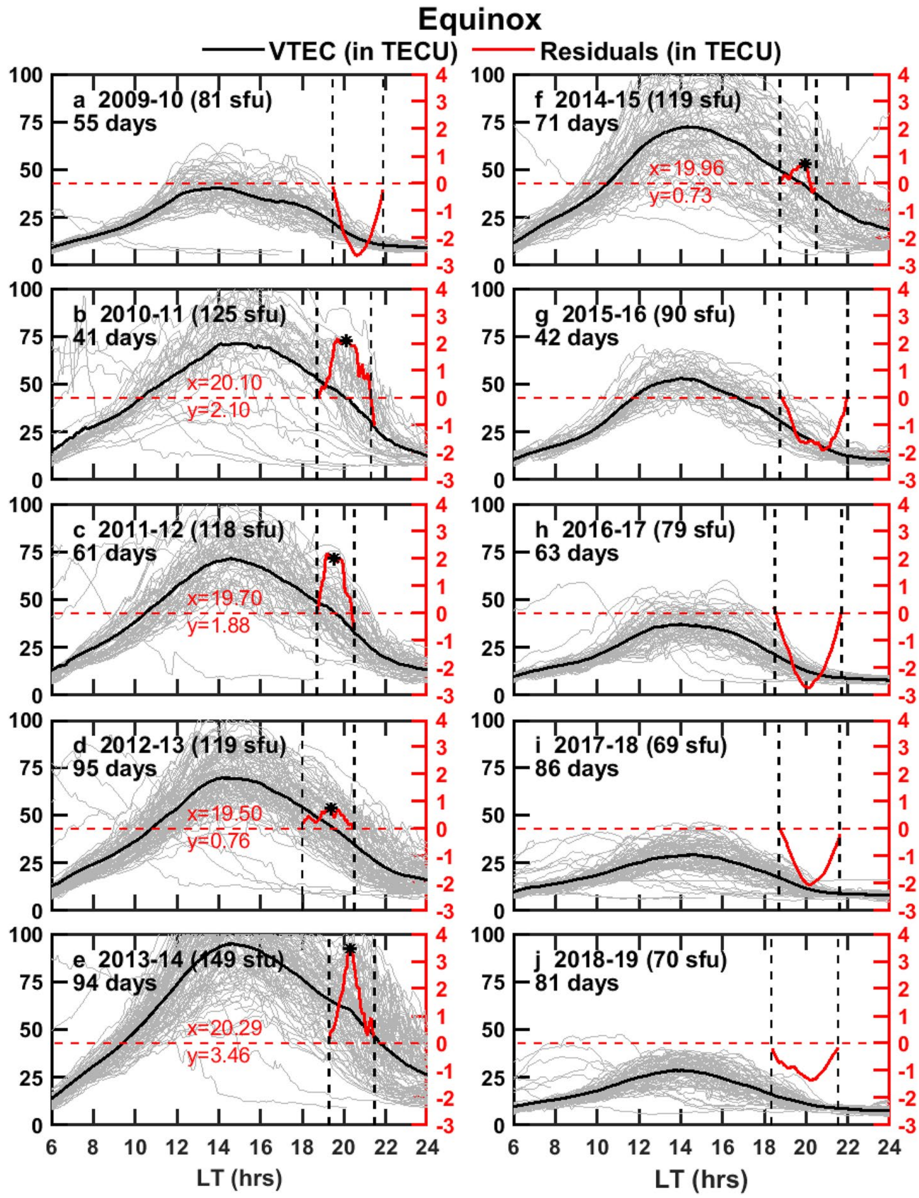

Figure 3. Same as Figure 2 but for equinox.

et al. (1988) and Richmond et al. (1992) included the self-consistent ionosphere and the electrodynamics part, respectively in the TGCM to make it TIE-GCM. TIE-GCM is capable of simulating the thermospheric neutral wind and ionospheric electric field, conductivity, and current self-consistently. The electron density and vertical drift outputs (https://ccmc.gsfc.nasa.gov/models/modelinfo.php?model=TIE-GCM) in the present work are generated for the height range of 100–700 km and in the latitudinal domain of ±30° magnetic latitude. For model run, the input solar wind magnetic field, velocity and plasma density are taken as 0 nT, 400 ms^{-1} and 4 cm^{-3} respectively. TIE-GCM outputs are obtained for three seasons - December solstice, Equinox, and June Solstice and at three solar flux levels (100, 130, and 160 sfu). The dates for the model runs are chosen accordingly during 2009–2019.

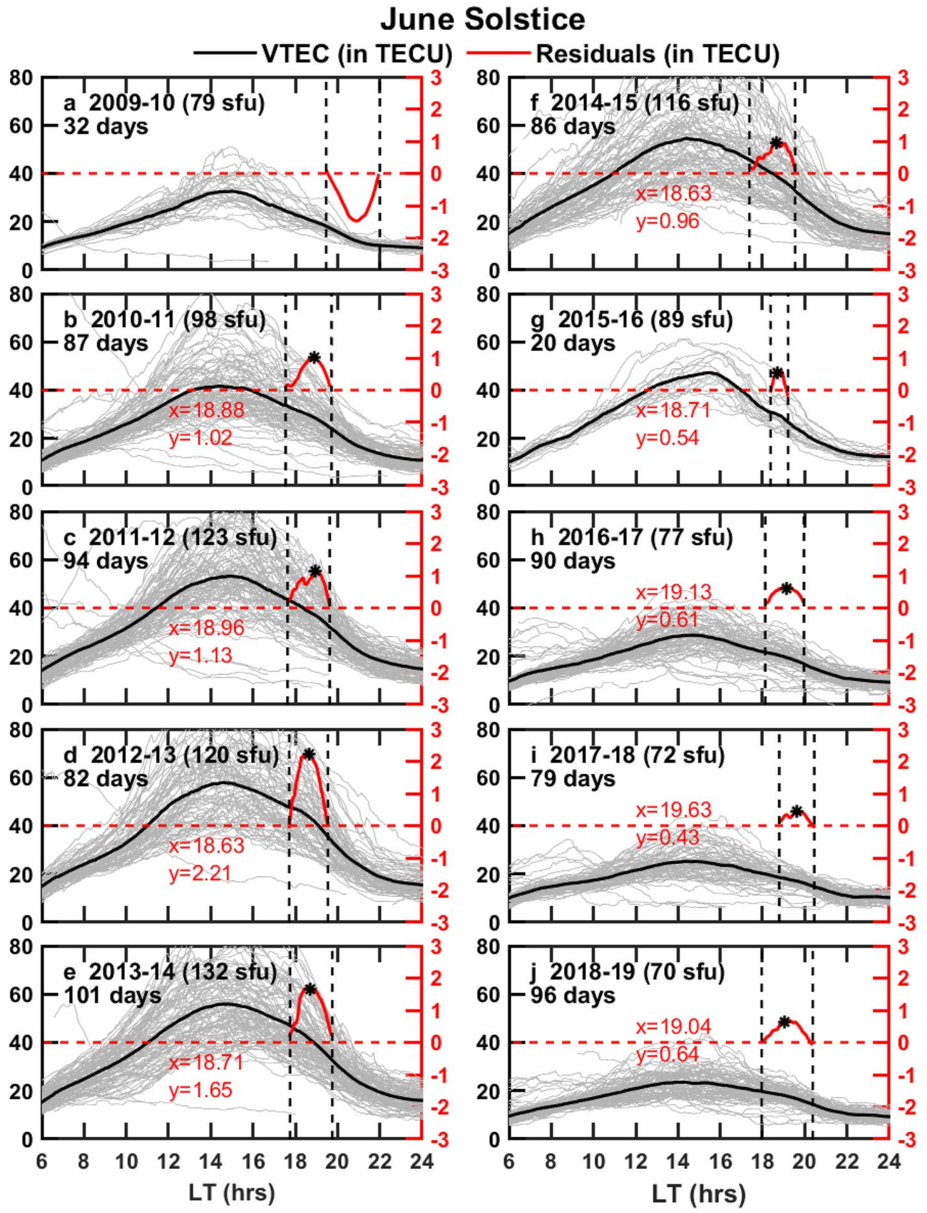

Figure 4. Same as Figures 2 and 3 but for June solstice.

3. Results

Figures 2a–2j depict the daily variations in VTEC (gray lines), mean variation in VTEC (black bold line) and the residuals (red line) respectively for consecutive 10 years (2009–2019) during the December solstice in solar cycle 24. Two vertical dashed lines in black color mark the intervals for which the residuals are calculated based on the linear fitting technique as described in Figure 1. The number of days to calculate the average VTEC as well as the average solar flux level of those days are provided in each subplot. By following the dashed black vertical lines, one can figure out the occurrence of post-sunset enhancements in VTEC in varying degrees identified by the residuals. It is interesting to note that the residuals have positive values in Figure 2c (2011–2012, 132 sfu), Figure 2e (2013–2014, 151 sfu), and Figure 2f (2014–2015, 144 sfu) only. In these 3 years, the peak residuals occur at ~2000 LT (with amplitude of 1.22 TECU), ~2010 LT (with amplitude of 1.90 TECU) and ~2000 LT (with amplitude of 4.45 TECU) respectively. On other occasions, either residuals are close to zero/slightly positive (as in 2012–2013) or unambiguously negative (rest of the cases). It is noted that the amplitude of the post-sunset peak in VTEC starts increasing as the solar activity starts increasing in cycle 24 with the exception of 2012–2013. The amplitude seems to become maximum in 2014–2015 and decreases thereafter. Interestingly, it appears from Figure 2 that the amplitude of the post-sunset enhancement in VTEC during December solstice starts to become positive if the solar flux value exceeds at least 112 sfu (as in 2012–2013). It is also important to note here that the year 2012–2013 and particularly the December solstice of 2012–2013 is associated with a number of sudden stratospheric warmings (SSWs) events (e.g., Nath et al., 2016). Obviously, Figure 2d suggests that the amplitudes of VTEC residuals are less during SSWs events. Therefore, for the sake of simplicity, this lower limit of the solar flux level at which the residuals start turning positive is taken approximately at 110 sfu. In absence of sudden stratospheric warming (SSW), this solar flux level may lie below 110 sfu but we will neglect this consideration here. It can be found in the ensuing paragraph that the choice of 110 sfu as a lower cut-off is consistent with Equinox also.

While Figure 2 shows the variations in December solstice, Figure 3 depicts similar variations during Equinox. During this season, the positive values of residuals or the post-sunset enhancements in VTEC are observed in Figure 3b (2010–2011, 125 sfu), Figure 3c (2011–2012, 118 sfu), Figure 3d (2012–2013, 119 sfu), Figure 3e (2013–2014, 149 sfu), and Figure 3f (2014–2015, 119 sfu). The peak residuals occur at ∼2006 LT (with amplitude of 2.10 TECU), ∼1940 LT (with amplitude of 1.88 TECU), ∼1930 LT (with amplitude of 0.70 TECU), ∼2020 LT (with amplitude of 3.46 TECU) and ∼2000 LT (with amplitude of 0.73 TECU) respectively. On other occasions, the residuals are unambiguously negative. The highest solar flux year during Equinox is noted in 2013–2014 (Figure 3e) and the magnitude of peak residual is also found to be the highest (3.46 TECU) in this year. It is also interesting to note that corresponding to same solar flux levels noticed in 2012–2013 (Figures 3d) and 2014–2015 (Figure 3f), the magnitudes of the peak residuals are also nearly equal. Unlike December solstice, the post-sunset enhancement in VTEC is present in the year 2012–2013. Since the residual is unambiguously positive corresponding to the solar flux level of 119 sfu (2014–2015), and it is negative for the solar flux level of 90 sfu (2015–2016), we assume that the residuals start becoming positive midway between 119 and 90 sfu. This mid solar flux level is ∼105 sfu. Therefore, for simplicity, it is assumed in this case also that if the solar flux level exceeds 110 sfu (lower cut-off), the residuals will be positive.

Similar to Figures 2 and 3, Figure 4 also depicts the daily variations in VTEC, mean variation in VTEC and residuals but for June Solstice. In contrast to Figures 2 and 3, positive residuals are observed on all the years in June solstice except in 2009–2010. However, most importantly, the peaks in positive residuals occur mostly around 1900 hr or before except mainly during 2017–2018 when it occurs considerably later than 1900 LT. This is in sharp contrast with the December solstice and equinox wherein the peaks in the positive residuals occur mostly ∼2000 LT. In fact, negative residuals (not shown here) are obtained during 2000–2100 LT for almost all the years in June solstice. Another noticeable feature is the apparent disconnect of the amplitude of the positive residual with the solar flux levels. For example, in 2012–2013 when the solar flux level is 120 sfu, the amplitude of the positive residual is 2.21 TECU whereas in 2013–2014, when the solar flux level is 132 sfu, the amplitude of positive residual is 1.65 TECU. Therefore, it appears that the VTEC residuals have little connection with the solar flux levels in June solstice. This aspect is addressed in detail again in Figure 5.

Figures 2–4 bring out the variations in the VTEC residuals with solar activity for three seasons in solar cycle 24 over Ahmedabad. However, since post-sunset enhancements take place for a finite interval, it is necessary to consider the integrated VTEC under the residual curves to quantitatively explore the relationship between the post-sunset enhancement in VTEC and solar flux levels. In other words, the area under the curve of the residual VTEC curve (ΔVTEC) is more important than the peak amplitude of residual VTEC. This is done in Figure 5 for December solstice, Equinox and June solstice. Figures 5a and 5b depict the representative local time variation of VTEC for individual days (in gray) as well as average VTEC (black line) with the standard deviations ($\pm 1\sigma$) during equinox wherein the solar flux levels vary between 146 and 150 sfu. For the sake of clear representation, $\pm 1\sigma$ variations are shown only at a few points. The upper and lower envelopes of the $\pm 1\sigma$ variations are marked by solid and dashed blue lines. The calculation of integrated VTEC is carried out in two ways and demonstrated in Case-1 (Figure 5a) and Case-2 (Figure 5b). In Case-1, only the residual area under the curve is considered (marked by the red shaded area) and in Case-2, the total area under the curve (red + green shaded area) is considered. Therefore, while in Case-1, only the integrated residual enhancement in VTEC is calculated, the integrated total VTEC enhancement is calculated in Case-2. We term these as integrated residual VTEC (Case-1) and integrated total VTEC (Case-2). It is obvious that Case-2 additionally integrates the background VTEC level over

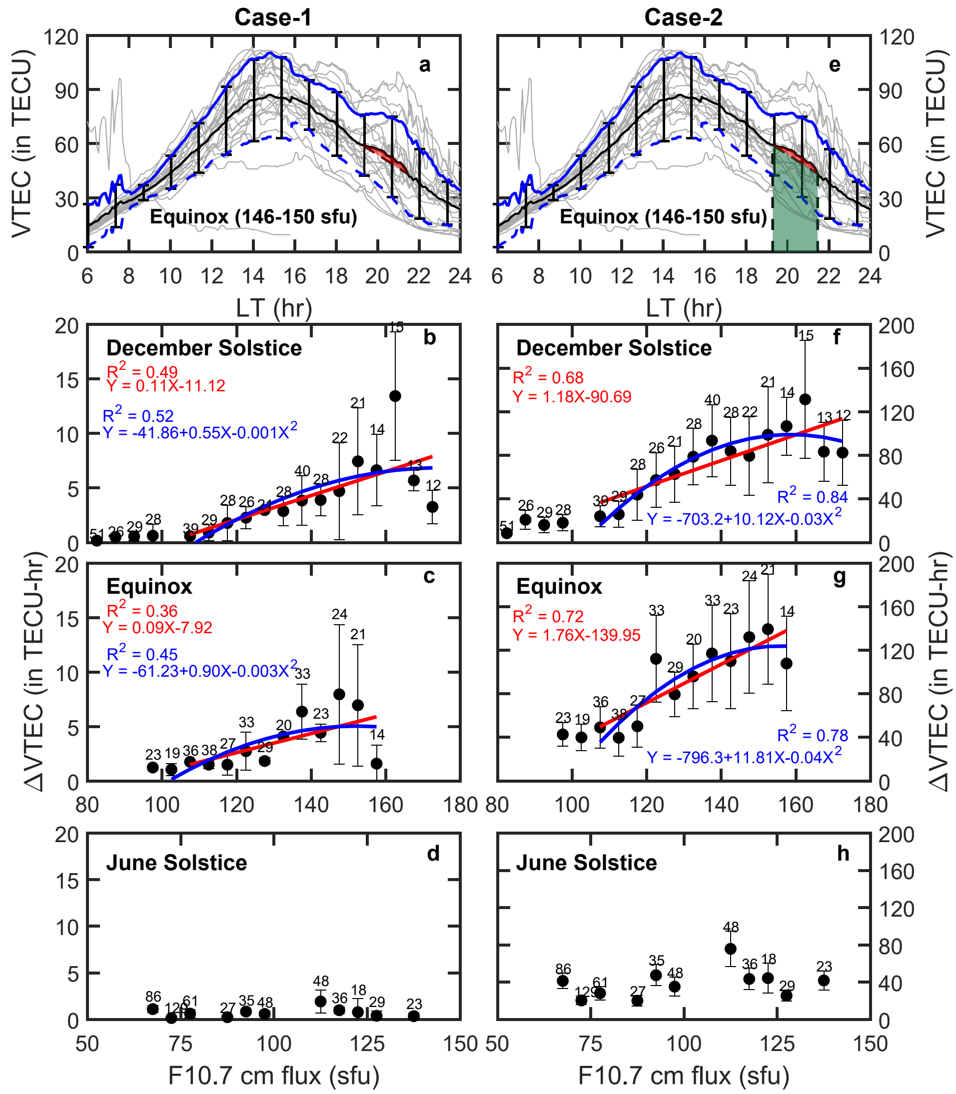

Figure 5. Local time variations in vertical total electron content (VTEC) over Ahmedabad, two methods of calculating integrated VTEC and as well as the solar flux dependences of post -sunset enhancements in VTEC are shown. Figure (a and e): The variations during equinox (gray lines) along with the average VTEC (black line) variation and standard deviations (a few $\pm 1\sigma$ lines are only shown to avoid cluttering) are shown. Integrated VTEC (ΔVTEC) calculated in two different ways during the post-sunset enhancement period. During this period, the solar flux levels vary between 146 and 150 sfu. The solid and dashed blue lines in Case-1 and Case-2 are the upper and lower envelopes of $\pm 1\sigma$ variations respectively. While in Case-1, only the area under the curve of residual enhancement (shaded by red) is calculated, the total area under the curve of residual enhancement (shaded by red + green in Figure 5b) is calculated for Case-2. Figure (b–d and f–h) show the variations of ΔVTEC (along with the $\pm 1\sigma$ calculated based on the solid and dashed blue curves in Figures 5a and 5e) with respect to the binned (in steps of 5) F10.7 cm solar flux levels for three seasons but for Case-1 and Case-2 respectively. Note the X-axis scales for December solstice and equinox are different from that of June solstice. For both Case-1 and Case-2, the linear fits (red line), parabolic fits (blue lines) as well as the corresponding correlation coefficients (R^2) are shown along with the fitting equations for December solstice and Equinox. Fitting starts from 110 sfu. The ΔVTEC and F10.7 cm solar flux seem to be unrelated for June solstice unlike December solstice and equinox.

Ahmedabad on which the post-sunset enhancement can be thought to be superimposed. In similar fashion, the area under the curves is also calculated for the $\pm 1\sigma$ curves marked in red and blue lines in Figures 5a and 5e. The number of days that goes into the calculation of each point in a particular solar flux bin is mentioned and the $\pm 1\sigma$ values are shown in Figures 5b–5d and 5f–5h. The unit of ΔVTEC in both the cases is TECU-hr.

In Figures 5b–5d, ΔVTEC changes as per Case-1 are averaged over 5 sfu bin for December solstice, Equinox and June solstice respectively and are plotted against the binned solar flux levels. On the other hand, in Figures 5f–5h the same is done for Case-2. In Figures 5b and 5c and Figures 5f and 5g, the linear and parabolic fits are shown with red and blue lines along with the fitted equations and corresponding R^2 values. Both the linear and parabolic fits start from 110 sfu as the residuals start becoming positive from this solar flux level (stated while describing Figures 2 and 3). A few important observations can be made based on Figure 5b, 5c, 5f and 5g that are listed below.

1. The R^2 values are not significantly different for December solstice and equinox for both Case-1 and Case-2 and fits (compare Figures 5b and 5c & Figure 5f and 5g).
2. Most importantly, the R^2 values in Case-2 are significantly higher than those in Case-1 during both December solstice and equinox for both linear and parabolic fits (compare 5b–5f and 5c–5 g). Therefore, it appears that the background VTEC level, on which the post-sunset enhancement is superposed, is an important factor if one wants to evaluate the correlation between solar flux and post-sunset enhancement (ΔVTEC).
3. Based on R^2 values, it can also be inferred that parabolic fits approximate the relationship between ΔVTEC and F10.7 cm solar flux in a slightly better way than the linear fits particularly during December solstice for Case-2 (Figure 5f).
4. The better applicability of parabolic fit during December solstice for the total integrated VTEC (Figure 5f) seems to suggest a possible saturation effect at higher solar flux levels.
5. In sharp contrast to December solstice and equinox, no systematic relationship could be established between ΔVTEC and solar flux levels during June solstice in both the cases as seen in Figures 5d and 5h.
6. The degree of scatter seems to increase as one goes to higher solar flux levels during December solstice and equinox.
7. Finally, the slope of the linear fit is more for equinox (slope = 1.76, see Figure 5g) than for December solstice (Slope = 1.18, for Figure 5f).

In order to understand the results obtained in Figure 5 from a bigger perspective, TIE-GCM outputs are obtained. These results are shown in Figure 6. In this figure, the TIE-GCM outputs are shown for the three seasons (December solstice, Equinox and June solstice), for three different solar flux conditions (100, 130 and 160 sfu) and at five local times (1800, 1900, 2000, 2100 and 2200 hr). This figure is labeled as a matrix consisting of 5 × 3 subplots wherein the December solstice, Equinox and June solstice are represented by a, b and c respectively. The subplots in the first ($a_{11} - a_{51}$), second ($a_{12} - a_{52}$) and third ($a_{13} - a_{53}$) columns of a particular season represent the temporal evolution of F region plasma density in the geomagnetic latitude (from −30° to +30°N) and altitude plane during post-sunset hours. One can note from Figure 6 that not only the location of the crest region (identified by the maximum plasma density over latitudes) but also the density over the EIA crest region varies with solar flux, seasons, and local time. In order to calculate the latitudinal plasma density gradient, the altitude corresponding to the maximum F region plasma density $\left(N_{crest}^{\max}\right)$ over the EIA crest region is identified. The F region plasma density over the EIA trough region corresponding to the same altitude is taken as $N_{trough}^{\min}$. For the present work, the latitudinal plasma density gradient in the northern hemisphere is considered as the Ahmedabad-TEC measurements are from northern hemisphere. The latitudinal plasma density gradient is defined here as $\left(N_{crest}^{\max} - N_{trough}^{\min}\right) / (Lat_{crest} - Lat_{trough})$ in the unit of cm^{-3} deg^{-1}. Table 1 lists the values of the latitudinal plasma density gradients for five local times, three solar flux levels and three seasons derived from the TIE-GCM outputs. Figure 6 reveals that the plasma density over the EIA crest region is lower at 100 sfu and as the solar flux level increases, the plasma density over the crest region increases conspicuously. The density at the trough does not seem to change so significantly with solar flux levels. This leads to higher CTR and latitudinal plasma density gradient at higher solar flux levels as confirmed by the values shown in Table 1. The latitudinal density gradient is, therefore, highest at 160 sfu. Interestingly, the latitudinal density gradient during December solstice (Figures $a_{13} - a_{53}$) and Equinox (Figures $b_{13} - b_{53}$) are larger than that during June solstice (Figures $c_{13} - c_{53}$). It can also be noted that the plasma densities over the EIA crest region during December solstice and Equinox are either comparable or slightly higher during Equinox. However, the latitudinal density gradients are found to be higher during the December solstice as can be noted from Table 1.

Based on TIE-GCM outputs, we have also found out the variations in vertical drift with magnetic latitude at the above-mentioned five local times during December solstice, Equinox and June solstice for the solar flux levels of 100, 130, and 160 sfu. Table 1 captures the equatorial vertical drifts at five local times and three solar flux levels

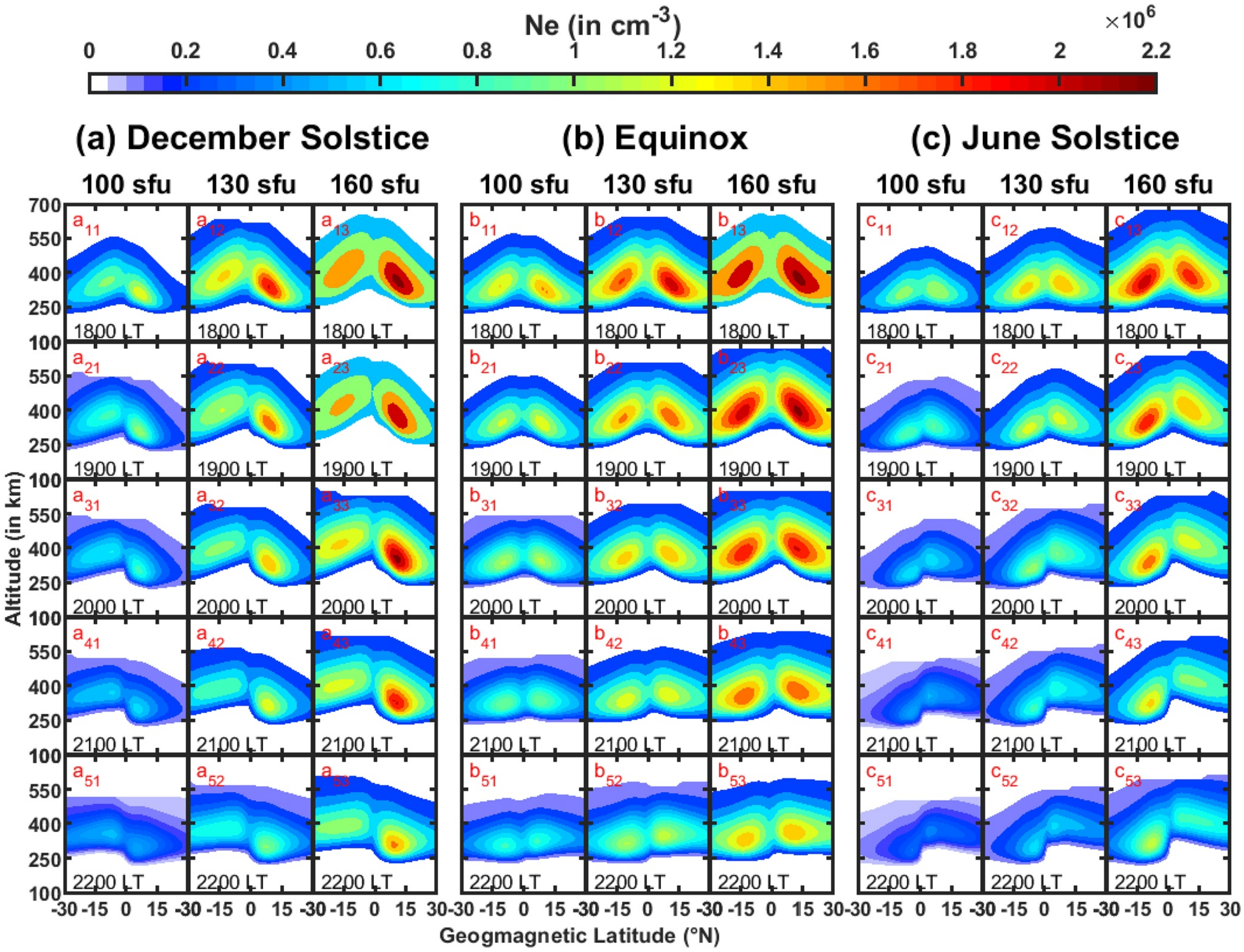

Figure 6. (a) Left to right: Electron density variations in the magnetic latitude (from −30° to +30°) versus altitude (from 100 to 700 km) plane along 75° E longitude in December solstice corresponding to solar flux levels of 100, 130, and 160 sfu. Panels b and c are same as a but for Equinox and June solstice respectively. From top to bottom, the local time increases from 1800 to 2200 LT. A common color scale is used throughout the figure. This figure is generated based on Thermosphere Ionosphere Electrodynamics-General circulation model model outputs.

for the three seasons as well. In addition, the results corresponding to these three solar flux levels are provided as Figures S2, S3 and S4 in Supporting Information S1 respectively. It is noted from Table 1 that the maximum (positive) vertical drift associated with PRE occurs at 1900 LT for all the three seasons. This is slightly delayed as one compares this with the observations over the Indian sector (e.g., Madhav Haridas et al., 2015; Pandey et al., 2017) and also with the global empirical model outputs (Fejer et al., 2008). Further, for a given solar flux level, the equatorial vertical drift at 1900 LT during Equinox is more than the corresponding drift during December solstice. This is in contrast with the outputs obtained for latitudinal plasma density gradients for these two seasons. Interestingly, both the latitudinal plasma density gradient and equatorial vertical drift are minimum during June solstice. The implications of these results are discussed in the ensuing section.

4. Discussion

The post-sunset enhancements in the F region plasma density over low latitudes have been previously reported (e.g., Bittencourt et al., 2007; Farelo et al., 2002; Kulkarni, 1969; Su et al., 1994; Xiong et al., 2016) but its causative mechanism is not comprehensively investigated. The work of Kumar et al. (2021) revealed that these enhancements during December solstice and Equinox are driven by the reinvigorated plasma fountain driven

Table 1

Latitudinal Plasma Gradients in Black (in 10^5 cm^{-3} deg^{-1}) and Vertical Drifts (in ms^{-1}) Over the Dip Equator in Blue at 1800, 1900, 2000, 2100 and 2200 LT (Top to Bottom) in December Solstice Corresponding to 100, 130 and 160 sfu Levels (Left to Right), as Derived From the TIEGCM Outputs, Are Tabulated in the Left Block

	December solstice			Equinox			June solstice		
Local time	100 sfu	130 sfu	160 sfu	100 sfu	130 sfu	160 sfu	100 sfu	130 sfu	160 sfu
	Latitudinal density gradients are in the unit of 10^5 cm^{-3} deg^{-1} and equatorial vertical drifts are in the unit of ms^{-1}								
1800	1.0 2.9	1.3 10.0	1.6 15.6	0.8 5.8	1.1 9.3	1.4 15.0	0.4 –5.7	0.7 –2.6	0.8 3.7
1900	0.8 5.7	1.5 12.4	1.8 16.8	0.8 10.0	1.0 14.5	1.2 20.5	0.4 –3.3	0.6 1.2	0.7 10.5
2000	0.8 –3.3	1.4 –2.7	1.7 –3.7	0.6 –2.5	0.7 –3.7	1.2 –3.5	0.2 –5.4	0.4 –4.8	0.5 –0.8
2100	0.4 –10.5	1.0 –12.5	1.5 –14.7	0.6 –11.0	0.7 –13.0	1.0 –14.6	0.3 –8.0	0.3 –8.8	0.3 –8.0
2200	0.3 –14.5	0.9 –17.8	1.3 –19.9	0.4 –14.8	0.7 –16.7	0.7 –18.7	0.3 –8.4	0.5 –10.0	0.5 –11.3

Note. Similar data derived for equinox and june solstice are provided in middle and right blocks respectively.

by PRE in the post-sunset hours. The present investigation takes it a step forward by analyzing the year-wise progression of the post-sunset enhancements in solar cycle 24 (2009–2019) and elicits that these enhancements are significant only if the solar flux level exceeds 110 sfu during December solstice and Equinox. Since the post-sunset enhancements are primarily driven by PRE and the amplitude of the PRE depends on solar flux level (e.g., Fejer et al., 1989; Fejer et al., 2008, 1991; Ramesh & Sastri, 1995), it can be expected that for a detectable post-sunset enhancement over the EIA crest region, one requires a minimum PRE amplitude or vertical drift over the dip equator. In fact, the work of Scherliess and Fejer (1999) suggests that the amplitude of PRE is close to zero during June solstice as well as in December solstice and significantly less than the daytime maximum of the zonal electric field at 90 sfu. Therefore, it is understandable that the solar flux needs to exceed a threshold level to make the PRE amplitude large enough to cause post-sunset enhancement over the EIA crest region. Ramesh and Sastri (1995) explored the association of solar flux level and equatorial vertical drift over the Indian sector and it can be found from their work (see Figure 4 of Ramesh & Sastri, 1995) that the magnitude of vertical drift is ∼16ms^{-1} during December solstice and Equinox at 110 sfu whereas it is ∼10 ms^{-1} for the same solar flux level at the June solstice. Therefore, it implies that the equatorial vertical drift associated with PRE should be at least ∼16 ms^{-1} over the Indian sector for detectable post-sunset enhancement of VTEC over the EIA crest region. This explains why even during high solar flux conditions, the post-sunset enhancement in VTEC is not observed over the EIA crest region during June solstice. This is because PRE amplitude during June solstice does not exceed this threshold level on most of the occasions over the Indian sector even during high solar flux condition.

One more point deserves attention at this stage. This is the better applicability of the parabolic fit while constructing the empirical relationship between the F10.7 cm flux and post-sunset enhancement of VTEC over the EIA crest region during the December solstice. As the VTEC enhancements are caused by the PRE as shown by Kumar et al. (2021), it is important to evaluate the variation of PRE with the solar flux levels at different seasons for different levels of solar flux. Using Jicamarca observations, Fejer et al. (1989) first indicated that average vertical drifts during winter (May-August for the Southern hemisphere) remains nearly constant after a certain solar flux level. This solar flux level can change with the magnetic activity. The indication obtained in this work was consolidated and quantified further in a follow-up work (Fejer et al., 1991) wherein the evening PRE of vertical drifts was shown to increase linearly with the solar flux during equinox but saturate beyond a high solar solar flux level during winter. This inference was drawn based on the applicability of linear and parabolic fits (see Figure 3 of Fejer et al., 1991). Over the Indian sector, similar results were obtained by Ramesh and Sastri (1995). Interestingly, and for the first time, we do see such effects over the EIA crest region when the VTEC enhancements reveal similar seasonal and solar flux behavior (Figure 5). This puts the cause of these enhancements on a very firm footing and based on the work of Kumar et al. (2021) and this work, it is now abundantly clear that PRE of equatorial zonal electric field is responsible for the post-sunset VTEC enhancements over the EIA crest region. Therefore, as PRE vertical drift tends to saturate during December solstice at higher solar flux levels, VTEC enhancements also tend to saturate and parabolic fit works better than the linear fit. In this work, we do see saturation effect is kicking in beyond 150–160 sfu over the Indian sector. This solar flux level can change at different magnetic activity levels as suggested by Fejer et al. (1989); Fejer et al. (1991). However, since only the quiet time cases are considered here, we do expect that estimation of the higher cut-off of this solar flux level is relatively robust. Another interesting point is, similar to Fejer et al. (1991), we also observe relatively large degree of scatter at higher solar flux levels (particularly Figures 5b and 5c) during December solstice and equinox. As suggested by Fejer et al. (1991), this may be due to the large variability of PRE amplitudes at higher solar flux levels during these two seasons. In addition, the slope of the linear fit (1.76) in equinox (Figure 5g) is significantly higher than that (1.18) during December solstice in Figure 5f which is also consistent with the results of Ramesh and Sastri (1995) wherein they obtained (see Figure 4) higher slope (0.13) in equinox than December solstice (0.07) for the linear relationships between average peak PRE vertical drift and F10.7 flux for these seasons. These observations strengthen the arguments that PRE plays the primary role for the post-sunset enhancement of VTEC over the EIA crest region. However, the possible saturation effect of PRE of vertical drift during winter remains an unresolved problem till date and further modeling works (beyond the scope of the present work) are needed to understand this enigmatic aspect of PRE in future. The lack of sufficient VTEC data at higher solar flux levels (beyond 160 sfu) prevents us from observationally addressing this feature in detail. It is interesting to note that TIE-GCM outputs capture this saturation effects particularly during December solstice (Figure S5 in Supporting Information S1). It is possible that changes in thermospheric neutral composition, neutral wind, background ionospheric electric field and conductivity during higher solar activity interact with one another in such a way that VTEC gets saturated. Since PRE that drives post-sunset enhancements in VTEC gets saturated (e.g., Fejer et al., 1991) with increasing solar flux level, it is expected that VTEC also get saturated with the increasing solar flux levels. However, the exact processes that lead to PRE/VTEC saturation need to be understood comprehensively based on further investigation and importantly, through modeling studies.

The above discussion suggests that the amplitude of PRE is important and a necessary factor that determines the post-sunset enhancement in VTEC over the EIA crest region. However, the present investigation extends this argument critically by showing that amplitude of PRE may not be a sufficient condition and one needs to also factor in the F region background plasma distribution over the low latitude upon which the PRE-driven plasma fountain operates during post-sunset hours. This aspect comes out of Figure 5 wherein the correlation coefficients (for both linear or parabolic fits) are found to increase significantly when background VTEC levels are also considered (Figures 5f and 5g vis-à-vis Figures 5b and 5c). The background VTEC level over the EIA crest region during post-sunset hours depends on the daytime plasma fountain process. The PRE-driven post-sunset plasma fountain operates on the low latitude plasma distribution left behind by the daytime fountain. Figure 5 reveals that the correlation coefficients between the post-sunset enhancement (ΔVTEC) and solar flux for Case-2 (total integrated VTEC) are higher during both December solstice and Equinox when compared with the post-sunset enhancements (ΔVTEC) for Case-1 (residual integrated VTEC). It suggests that the elevated background plasma density around the EIA crest is more likely to produce the higher post-sunset enhancements in VTEC. The work of Fejer et al. (2008) reveals that the vertical drift remains upward throughout daytime in Equinox and December solstice over the Indian sector. However, around 1600 LT in June solstice, the polarity of vertical drift is reversed at low and moderate solar flux levels (e.g., Pandey et al., 2018) and remains close to zero even at higher solar flux levels (e.g., Fejer et al., 2008). Therefore, it is clear that, unlike June solstice, the daytime fountain process, during December solstice and Equinox, continues to supply plasma over the EIA crest region till the PRE occurs. On top of that, the amplitude of PRE is significantly more/more during Equinox/December solstice than the daytime maximum amplitude of the zonal electric field in high solar flux condition over the Indian sector. During June solstice, even during high solar flux condition, the amplitude of PRE does not exceed the maximum amplitude of the daytime zonal electric field. Therefore, during Equinox and December solstice, the PRE of zonal electric field during post-sunset hours operates on already present higher plasma density background over low latitudes generated by the daytime plasma fountain process that, in turn, is driven by the daytime zonal electric field over the dip equatorial region. Therefore, PRE, during these two seasons in high solar flux condition, can push more plasma toward the EIA crest region causing the post-sunset enhancement in VTEC. This explains the enhanced correlation coefficients between ΔVTEC and solar flux for during both Equinox and December solstice (Figure 5b vs. 5f and 5c vs. 5g). However, one aspect still remains enigmatic at this point. Why is the slope of the linear fit is more for equinox (slope = 1.76, see Figure 5g) than for December solstice (Slope = 1.18, for Figure 5f)? This indicates that the post-sunset enhancement in VTEC over the EIA crest region changes more rapidly with solar flux during equinox than in December solstice. Interestingly, this feature is consistent with the work of Ramesh and Sastri (1995) carried out for the Indian sector but not with the work of Fejer et al. (1991) that was carried out for the Jicamarca sector. This could be due to the enhanced sensitivity of the electric field amplitudes related to PRE to the changes in the solar flux (possibly through changes in ionospheric conductivity over northern and southern low latitudes) over the Indian sector in equinox than in December solstice. This proposition is speculative at present and needs further detailed investigation in future.

In order to verify whether post-sunset enhancements in VTEC are captured by the TIE-GCM outputs, TIE-GCM is also run for the three seasons. These results are provided as Figure S5 in Supporting Information S1. In Figure S5 of Supporting Information S1, TEC variations corresponding to 23°N and 23°S along the 75°E meridian are shown for different solar flux levels. While the outputs corresponding to three seasons are generated for 100, 130 and 160 sfu, additional runs are made for December solstice and Equinox for 170–200 sfu in steps of 10 sfu to check the saturation effect. A few interesting features are noted from these outputs.

1. The post-sunset enhancements in TEC are prominent in December solstice. This is consistent with observations.
2. Although present, the enhancements are not as conspicuous in Equinox as in December solstice. This is where the model outputs differ from observations.
3. The post-sunset enhancements are absent in June solstice in accordance with observations.
4. The saturation effect seems to be present in the TIE-GCM outputs and particularly visible during December solstice.
5. Interhemispheric asymmetry is seen in the post-sunset enhancements. This could not be verified with the observations as VTEC data from a conjugate station in the southern hemisphere at 75°E meridian (part of Indian ocean) is not available. In this context, the work of Wan et al. (2022) is relevant as it indicates the role of wind in generating interhemispheric effects on the diurnal evolution of TEC along 75°E meridian using International GNSS service-total electron content (IGS-TEC) and International reference ionosphere (IRI)-2016 model outputs. Detailed investigations in future are needed to understand various aspects of interhemispheric and longitudinal asymmetries of the post-sunset enhancements.

Figure 6 and Table 1 capture the salient TIE-GCM outputs related to the relative roles of latitudinal density gradient and equatorial vertical drift in the post-sunset plasma density enhancement over the EIA crest region at different seasons and solar flux levels. It is suggested by Kumar et al. (2021) that the plasma transport in the meridional direction during the post-sunset hours occurs from 5°−10° magnetic latitude to the EIA crest region under the influence of PRE of the equatorial zonal electric field. Table 1 suggests that PRE amplitudes at 1900 LT are larger in equinox than in December solstice. In fact, earlier works (e.g., Fejer et al., 2008; Scherliess & Fejer, 1999) reveal that the amplitude of PRE during Equinox is more than that in December solstice. Therefore, the TIE-GCM outputs are consistent with the earlier results in this regard. More importantly, Figure 6 and Table 1 (TIE-GCM outputs) also reveal that latitudinal plasma density gradient shows contrasting feature and it is more during December solstice than equinox over Northern hemisphere. Considering ionospheric plasma as an incompressible fluid and neglecting the production and loss processes, the continuity equation suggests that the rate of change of plasma density over low latitudes depends on the $\mathbf{V}.\nabla\mathbf{N}$ term where $\mathbf{V}$ is the velocity and $\nabla\mathbf{N}$ is the plasma density gradient. It is clear from this term that the rate of change of plasma density over low latitude depends not only on the amplitude of PRE (upward velocity) during post-sunset hours but also on the latitudinal plasma density gradient. Therefore, it appears that although PRE amplitude is important, it may not be a sufficient condition to determine the post-sunset VTEC enhancement over the EIA crest region. In fact, PRE amplitude and latitudinal plasma density gradient can be expected to work in tandem to determine the degree of post-sunset enhancement in VTEC over the EIA crest region. This proposition gets credence from the fact that both the amplitude of PRE in vertical drift and latitudinal plasma density gradient are much smaller in June solstice compared to equinox and December solstice and hence one does not observe post-sunset enhancement in VTEC over the EIA crest region during this season. It is also important to mention here that the latitudinal plasma density gradient during evening hours over low latitudes is primarily a consequence of daytime plasma fountain upon which PRE-driven fountain during post-sunset hours is superposed. Hence, the VTEC enhancement due to PRE over the EIA crest region is dependent not only on PRE amplitude but also on the latitudinal plasma density gradient left behind by the daytime plasma fountain process. Therefore, daytime fountain also plays an important role in determining the degree of post-sunset VTEC enhancement over the EIA crest region.

Interestingly, the present work brings into attention an anomalous feature that is not consistent with the rest of the observations. The post-sunset enhancements in VTEC are absent during December solstice in the year 2012–2013 (Figure 2d) even when the average solar flux level is slightly higher than 110 sfu. This feature is apparently surprising. However, it is to be noted that the winter months in the year 2012–2013 is characterized by intense and multiple sudden stratospheric warming (SSW) events (e.g., de Paula et al., 2015; Nath et al., 2016). It is now known that during sudden stratospheric warming (SSW) events, the semi-diurnal and lunar tides are modulated that, in turn, affect the E-region electric field (e.g., Chau et al., 2012; Goncharenko et al., 2010; Pedatella et al., 2014). As the low latitude E region electric field gets communicated to the dip-equatorial F region heights, the plasma distribution over the low latitude region gets affected owing to the modified plasma fountain. It has been shown that the F region plasma shows large variability at local noon as well as in evening hours (e.g., Chau et al., 2012; Goncharenko et al., 2010) during and after sudden stratospheric warming (SSW) events. de Paula et al. (2015) investigated three major SSW events in 2013 and found that the peak vertical drifts associated with PRE were consistently smaller than their counterparts in the pre-SSW days. Vineeth et al. (2009) also brought out occurrences of counter electrojet (CEJ) with a quasi 16-day periodicity over Trivandrum, an Indian dip-equatorial station during the polar SSW events. Once the electric field is reversed during counter electrojet (CEJ) events, the F region plasma fountain gets weakened and it does not reach near the vicinity of the EIA crest region like Ahmedabad. Under this condition, PRE of zonal electric field would be unable to transport additional plasma to the EIA crest region leading to the weakening of the post-sunset enhancement of VTEC. Therefore, SSW can affect both PRE as well as the latitudinal plasma density gradient that determine the post-sunset enhancement in VTEC over the EIA crest region. The absence of post-sunset enhancements in VTEC during December solstice is, therefore, attributed to the recurrent occurrence of SSW events during 2012–2013.

5. Conclusions

The present investigation brings out the following.

1. The post-sunset enhancement in VTEC over the EIA crest region depends critically on solar flux level as the amplitude of PRE of zonal electric field depends on solar flux level.
2. As the VTEC enhancements are consistent with the amplitude of PRE (of zonal electric field), significant VTEC enhancements are observed over the EIA crest region in equinox and December solstice and not during June solstice.
3. The post-sunset enhancements in VTEC are conspicuous in Equinox and December solstice when solar flux level exceeds ∼110 sfu. It is suggested that minimum equatorial vertical drift associated with PRE needs to reach at least 16 ms^{-1} so as to generate conspicuous post-sunset enhancement in VTEC over the EIA crest region.
4. VTEC over the EIA crest region seems to saturate at higher solar flux levels (>160 sfu).
5. TIE-GCM simulations confirm the presence of conspicuous post-sunset enhancement in TEC particularly during December solstice. Similar to observations, TIE-GCM outputs also confirm the absence of enhancement in TEC during June solstice. However, enhancements during equinox are not as conspicuous as in December solstice. Clear interhemispheric asymmetry in the post-sunset enhancement in TEC is also seen. Importantly, the saturation effect during December solstice is captured by TIE-GCM.
6. It is suggested that the amplitude of PRE is a necessary but not sufficient condition for the post-sunset enhancements in VTEC. This proposition is supported by TIE-GCM simulation outputs that reveals that latitudinal gradient in the F region plasma density over low latitude plays an additionally important role to determine the amplitude of post-sunset enhancement in VTEC over the EIA crest region. While the PRE amplitude is more at 1900 LT during equinox, the latitudinal plasma density gradient is enhanced at 1900 LT during December solstice. The reverse is true for amplitudes related to PRE in vertical drift. The combined effects of vertical drift and latitudinal plasma density gradient determine the degree of post-sunset enhancement during December solstice and Equinox. Both these parameters are significantly weaker during June solstice.
7. It is proposed that the daytime plasma fountain is suggested to play an important role in determining the latitudinal plasma density gradient during post-sunset hours over low latitudes. PRE-driven plasma fountain during post-sunset hours operates on this latitudinal plasma density gradient and determine the degree of VTEC enhancement over the EIA crest region.
8. Sudden stratospheric events seem to suppress the post-sunset enhancements in VTEC by reducing equatorial electric field.

Data Availability Statement

The Thermosphere Ionosphere Electrodynamics-General circulation model (TIE-GCM) simulation results are obtained from the CCMC at GSFC-NASA via their runs on request system (http://ccmc.gsfc.nasa.gov). The TIE-GCM model was developed by the R. G. Roble et al. at High Altitude Observatory, National Center for Atmospheric Research. Ap index data is taken from the World Data Center for Geomagnetism, Kyoto (http://wdc.kugi.kyoto-u.ac.jp/). F10.7 solar flux values are obtained from NASA GSFC CDAWeb (http://cdaweb.gsfc.nasa.gov/). The remaining data including the data for the Supporting Information S1 can be obtained from https://data.mendeley.com/datasets/4tv464h47w/draft?a=2525c7ad-f84f-4243-80da-15b20ef3a4c9.

Acknowledgments

We are grateful to the Space Application centre (SAC), Indian Space Research Organization (ISRO) for providing the IRNSS-NavIC receiver that is operational at the Physical Research Laboratory, Ahmedabad. K. Pandey acknowledges the support of the Canadian Space Agency (CSA) [16SUSTTPHF]. This work is supported by the Department of Space, Government of India.

References

Abdu, M., Brum, C., Batista, I., Sobral, J., de Paula, E., & Souza, J. (2008). Solar flux effects on equatorial ionization anomaly and total electron content over Brazil: Observational results versus IRI representations. *Advances in Space Research*, *42*(4), 617–625. https://doi.org/10.1016/j.asr.2007.09.043

Anderson, D. (1973a). A theoretical study of the ionospheric F region equatorial anomaly-I. Theory. *Planetary and Space Science*, *21*(3), 409–419. https://doi.org/10.1016/0032-0633(73)90040-8

Anderson, D. (1973b). A theoretical study of the ionospheric F region equatorial anomaly-II. Results in the American and Asian sectors. *Planetary and Space Science*, *21*(3), 421–442. https://doi.org/10.1016/0032-0633(73)90041-X

Ayyagari, D., Chakraborty, S., Das, S., Shukla, A., Paul, A., & Datta, A. (2020). Performance of navic for studying the ionosphere at an EIA region in India. *Advances in Space Research*, *65*(6), 1544–1558. https://doi.org/10.1016/j.asr.2019.12.019

Balan, N., & Rao, P. B. (1984). Relationship between nighttime total electron content enhancements and VHF scintillations at the equator. *Journal of Geophysical Research*, *89*(A10), 9009–9013. https://doi.org/10.1029/JA089iA10p09009

Basu, S., MacKenzie, E., & Basu, S. (1988). Ionospheric constraints on VHF/UHF communications links during solar maximum and minimum periods. *Radio Science*, *23*(3), 363–378. https://doi.org/10.1029/RS023i003p00363

Bittencourt, J. A., Pillat, V. G., Fagundes, P. R., Sahai, Y., & Pimenta, A. A. (2007). Lion: A dynamic computer model for the low-latitude ionosphere. *Annales Geophysicae*, *25*(11), 2371–2392. https://doi.org/10.5194/angeo-25-2371-2007

Chakrabarty, D., Bagiya, M. S., & Thampi, S. V. (2012). Solar EUV flux (0.1-50 nm), F10.7 cm flux, sunspot number and the total electron content in the crest region of equatorial ionization anomaly during the deep minimum between solar cycle 23 and 24. *Indian Journal of Radio and Space Physics*, *41*(2), 110–120.

Chau, J. L., Goncharenko, L. P., Fejer, B. G., & Liu, H.-L. (2012). Equatorial and low latitude ionospheric effects during sudden stratospheric warming events. *Space Science Reviews*, *168*(1), 385–417. https://doi.org/10.1007/s11214-011-9797-5

Chen, C.-H., Lin, C., Chen, W.-H., & Matsuo, T. (2017). Modeling the ionospheric prereversal enhancement by using coupled thermosphere-ionosphere data assimilation. *Geophysical Research Letters*, *44*(4), 1652–1659. https://doi.org/10.1002/2016GL071812

de Paula, E. R., Jonah, O. F., Moraes, A. O., Kherani, E. A., Fejer, B. G., Abdu, M. A., et al. (2015). Low-latitude scintillation weakening during sudden stratospheric warming events. *Journal of Geophysical Research: Space Physics*, *120*(3), 2212–2221. https://doi.org/10.1002/2014JA020731

Dickinson, R. E., Ridley, E., & Roble, R. (1984). Thermospheric general circulation with coupled dynamics and composition. *Journal of the Atmospheric Sciences*, *41*(2), 205–219. https://doi.org/10.1175/1520-0469(1984)041<0205:tgcwcd>2.0.co;2

Eccles, J. V., St Maurice, J. P., & Schunk, R. W. (2015). Mechanisms underlying the prereversal enhancement of the vertical plasma drift in the low-latitude ionosphere. *Journal of Geophysical Research: Space Physics*, *120*(6), 4950–4970. https://doi.org/10.1002/2014JA020664

Farelo, A. F., Herraiz, M., & Mikhailov, A. V. (2002). Global morphology of night-time NmF2 enhancements. *Annales Geophysicae*, *20*(11), 1795–1806. https://doi.org/10.5194/angeo-20-1795-2002

Fejer, B. G. (2011). Low latitude ionospheric electrodynamics. *Space Science Reviews*, *158*(1), 145–166. https://doi.org/10.1007/978-1-4614-1493-3_7

Fejer, B. G., de Paula, E. R., Batista, I. S., Bonelli, E., & Woodman, R. F. (1989). Equatorial F region vertical plasma drifts during solar maxima. *Journal of Geophysical Research*, *94*(A9), 12049–12054. https://doi.org/10.1029/JA094iA09p12049

Fejer, B. G., de Paula, E. R., González, S. A., & Woodman, R. F. (1991). Average vertical and zonal f region plasma drifts over Jicamarca. *Journal of Geophysical Research*, *96*(A8), 13901–13906. https://doi.org/10.1029/91JA01171

Fejer, B. G., Jensen, J. W., & Su, S.-Y. (2008). Quiet time equatorial F region vertical plasma drift model derived from ROCSAT-1 observations. *Journal of Geophysical Research*, *113*(A5), A05304. https://doi.org/10.1029/2007JA012801

Goncharenko, L. P., Coster, A. J., Chau, J. L., & Valladares, C. E. (2010). Impact of sudden stratospheric warmings on equatorial ionization anomaly. *Journal of Geophysical Research*, *115*(A10), A00G07. https://doi.org/10.1029/2010JA015400

Huang, F., Lei, J., Zhang, R., Li, N., Gu, S., Yu, Y., et al. (2020). Prominent daytime tec enhancements under the quiescent condition of January 2017. *Geophysical Research Letters*, *47*(14), e2020GL088398. https://doi.org/10.1029/2020GL088398

Huang, Y.-N., & Cheng, K. (1995). Solar cycle variation of the total electron content around equatorial anomaly crest region in East Asia. *Journal of Atmospheric and Terrestrial Physics*, *57*(12), 1503–1511. https://doi.org/10.1016/0021-9169(94)00147-G

Huang, Y.-N., Cheng, K., & Chen, S. W. (1989). On the equatorial anomaly of the ionospheric total electron content near the northern anomaly crest region. *Journal of Geophysical Research*, *94*(A10), 13515–13525. https://doi.org/10.1029/JA094iA10p13515

Kulkarni, P. V. (1969). Airglow studies in low latitudes. *Proceedings of Third international symposium on equatorial aeronomy*, *2*(1), 412.

Kumar, A., Chakrabarty, D., Pandey, K., Fejer, B. G., Sunda, S., Seemala, G. K., et al. (2021). Evidence for the significant differences in response times of equatorial ionization anomaly crest corresponding to plasma fountains during daytime and post-sunset hours. *Journal of Geophysical Research: Space Physics*, *126*(3), e2020JA028628. https://doi.org/10.1029/2020JA028628

Liu, H., Stolle, C., Förster, M., & Watanabe, S. (2007). Solar activity dependence of the electron density in the equatorial anomaly regions observed by champ. *Journal of Geophysical Research*, *112*(A11), A11311. https://doi.org/10.1029/2007JA012616

Liu, J., Zhang, D., Mo, X., Xiong, C., Hao, Y., & Xiao, Z. (2020). Morphological differences of the northern equatorial ionization anomaly between the eastern Asian and American sectors. *Journal of Geophysical Research: Space Physics*, *125*(3), e2019JA027506. https://doi.org/10.1029/2019JA027506

Liu, L., Chen, Y., Le, H., Ning, B., Wan, W., Liu, J., & Hu, L. (2013). A case study of postmidnight enhancement in F-layer electron density over sanya of China. *Journal of Geophysical Research: Space Physics*, *118*(7), 4640–4648. https://doi.org/10.1002/jgra.50422

Madhav Haridas, M. K., Manju, G., & Pant, T. K. (2015). On the solar activity variations of nocturnal f region vertical drifts covering two solar cycles in the Indian longitude sector. *Journal of Geophysical Research: Space Physics*, *120*(2), 1445–1451. https://doi.org/10.1002/2014ja020561

Manke, A. A., & Chakarabarty, D. (2016). An integrated software platform for GPS/GNSS ionospheric data analysis. *International Journal of Science, Engineering and Technology*, *4*(5). https://doi.org/10.2348/ijset09160796

Mannucci, A. J., Wilson, B. D., & Edwards, C. D. (1993). A new method for monitoring the earth's ionospheric total electron content using the GPS global network. ION GPS-93. In *Proc of sixth international technical meeting of the satellite division of the institute of navigation* (pp. 1323–1332). Institute of Navigation.

Mo, X. H., Zhang, D. H., Liu, J., Hao, Y. Q., Ye, J. F., Qin, J. S., et al. (2018). Morphological characteristics of equatorial ionization anomaly crest over Nanning region. *Radio Science*, *53*(1), 37–47. https://doi.org/10.1002/2017RS006386

Nath, D., Chen, W., Zelin, C., Pogoreltsev, A. I., & Wei, K. (2016). Dynamics of 2013 sudden stratospheric warming event and its impact on cold weather over Eurasia: Role of planetary wave reflection. *Scientific Reports*, *6*(1), 1–12. https://doi.org/10.1038/srep24174

Olwendo, O. J., Yamazaki, Y., Cilliers, P. J., Baki, P., & Doherty, P. (2016). A study on the variability of ionospheric total electron content over the east African low-latitude region and storm time ionospheric variations. *Radio Science*, *51*(9), 1503–1518. https://doi.org/10.1002/2015RS005785

Oryema, B., Jurua, E., & Ssebiyonga, N. (2016). Variations of crest-to-trough tec ratio of the east african equatorial anomaly region. *International Journal of Astrophysics and Space Science*, *4*(1), 12–20. https://doi.org/10.11648/j.ijass.20160401.12

Pandey, K., Sekar, R., Anandarao, B. G., Gupta, S. P., & Chakrabarty, D. (2018). On the occurrence of afternoon counter electrojet over indian longitudes during june solstice in solar minimum. *Journal of Geophysical Research: Space Physics*, *123*(3), 2204–2214. https://doi.org/10.1002/2017JA024725

Pandey, K., Sekar, R., Gupta, S., Chakrabarty, D., & Anandarao, B. (2017). Comparison of quiet time vertical plasma drifts with global empirical models over the Indian sector: Some insights. *Journal of Atmospheric and Solar-Terrestrial Physics*, *157–158*, 42–54. https://doi.org/10.1016/j.jastp.2017.03.012

Pedatella, N., Liu, H.-L., Sassi, F., Lei, J., Chau, J., & Zhang, X. (2014). Ionosphere variability during the 2009 SSW: Influence of the lunar semidiurnal tide and mechanisms producing electron density variability. *Journal of Geophysical Research: Space Physics*, *119*(5), 3828–3843. https://doi.org/10.1002/2014JA019849

Ramesh, K., & Sastri, J. (1995). Solar cycle and seasonal variations in f-region vertical drifts over kodaikanal, India *Annales geophysicae* (Vol. 13, pp. 633–640). https://doi.org/10.1007/s00585-995-0633-7

Rao, V., & Kulkarni, P. (1973). 6300 Å night airglow enhancements in low latitudes. *Journal of Atmospheric and Terrestrial Physics*, *35*(2), 193–206. https://doi.org/10.1016/0021-9169(73)90087-1

Richmond, A. D., Ridley, E. C., & Roble, R. G. (1992). A thermosphere/ionosphere general circulation model with coupled electrodynamics. *Geophysical Research Letters*, *19*(6), 601–604. https://doi.org/10.1029/92GL00401

Roble, R. G., Ridley, E. C., Richmond, A. D., & Dickinson, R. E. (1988). A coupled thermosphere/ionosphere general circulation model. *Geophysical Research Letters*, *15*(12), 1325–1328. https://doi.org/10.1029/GL015i012p01325

Scherliess, L., & Fejer, B. G. (1999). Radar and satellite global equatorial F region vertical drift model. *Journal of Geophysical Research*, *104*(A4), 6829–6842. https://doi.org/10.1029/1999JA900025

Su, Y., Bailey, G., & Balan, N. (1994). Night-time enhancements in TEC at equatorial anomaly latitudes. *Journal of Atmospheric and Terrestrial Physics*, *56*(12), 1619–1628. https://doi.org/10.1016/0021-9169(94)90091-4

Sunda, S., & Vyas, B. M. (2013). Local time, seasonal, and solar cycle dependency of longitudinal variations of TEC along the crest of EIA over India. *Journal of Geophysical Research: Space Physics*, *118*(10), 6777–6785. https://doi.org/10.1002/2013JA018918

Vineeth, C., Kumar Pant, T., & Sridharan, R. (2009). Equatorial counter electrojets and polar stratospheric sudden warmings–a classical example of high latitude-low latitude coupling? *Annales geophysicae* (Vol. 27, pp. 3147–3153). https://doi.org/10.5194/angeo-27-3147-2009

Wan, X., Zhong, J., Xiong, C., Wang, H., Liu, Y., Li, Q., et al. (2022). Seasonal and interhemispheric effects on the diurnal evolution of EIA: Assessed by IGS tec and iri-2016 over peruvian and indian sectors. *Remote Sensing*, *14*(1), 107. https://doi.org/10.3390/rs14010107

Whalen, J. A. (2004). Linear dependence of the postsunset equatorial anomaly electron density on solar flux and its relation to the maximum prereversal e × b drift velocity through its dependence on solar flux. *Journal of Geophysical Research*, *109*(A7), A07309. https://doi.org/10.1029/2004JA010528

Xiong, C., Zhou, Y.-L., Lühr, H., & Ma, S.-Y. (2016). Diurnal evolution of the F region electron density local time gradient at low and middle latitudes resolved by the Swarm constellation. *Journal of Geophysical Research: Space Physics*, *121*(9), 9075–9089. https://doi.org/10.1002/2016JA023034

Young, D. M., Yuen, P., & Roelofs, T. (1970). Anomalous nighttime increases in total electron content. *Planetary and Space Science*, *18*(8), 1163–1179. https://doi.org/10.1016/0032-0633(70)90210-2

Zhang, M.-L., Wan, W., Liu, L., & Ning, B. (2009). Variability study of the crest-to-trough tec ratio of the equatorial ionization anomaly around 120°e longitude. *Advances in Space Research*, *43*(11), 1762–1769. https://doi.org/10.1016/j.asr.2008.09.031

Zhao, B., Wan, W., Liu, L., & Ren, Z. (2009). Characteristics of the ionospheric total electron content of the equatorial ionization anomaly in the Asian–Australian region during 1996–2004. *Annales Geophysicae*, *27*(10), 3861–3873. https://doi.org/10.5194/angeo-27-3861-2009

AGU ADVANCING EARTH AND SPACE SCIENCE

JGR Space Physics

RESEARCH ARTICLE
10.1029/2022JA030826

A Case of Anomalous Electric Field Perturbations in the Equatorial Ionosphere During Postsunset Hours: Insights

A. Kumar[1,2], D. Chakrabarty[1], B. G. Fejer[3], G. D. Reeves[4], D. Rout[5], S. Sripathi[6], G. K. Seemala[6], S. Sunda[7], and A. K. Yadav[1]

[1]Physical Research Laboratory, Ahmedabad, India, [2]Indian Institute of Technology, Gandhinagar, India, [3]Utah State University, Logan, UT, USA, [4]Los Alamos National Laboratory, Space Science and Applications Group, Los Alamos, NM, USA, [5]GFZ German Research Centre for Geosciences, Potsdam, Germany, [6]Indian Institute of Geomagnetism, Navi Mumbai, India, [7]Airport Authority of India, Ahmedabad, India

Key Points:

- Under southward interplanetary magnetic field (IMF) Bz conditions, anomalous electric field perturbations are observed over the equatorial ionosphere
- The amplitude of electric field perturbations is more when the magnitude of IEFy is less and vice versa
- These anomalous electric field perturbations are explained based on the effects of IMF By and substorm

Correspondence to:

A. Kumar,
ankitprl2017@gmail.com

Citation:

Kumar, A., Chakrabarty, D., Fejer, B. G., Reeves, G. D., Rout, D., Sripathi, S., et al. (2023). A case of anomalous electric field perturbations in the equatorial ionosphere during postsunset hours: Insights. *Journal of Geophysical Research: Space Physics*, *128*, e2022JA030826. https://doi.org/10.1029/2022JA030826

Received 7 JUL 2022
Accepted 2 FEB 2023

Abstract During a weak geomagnetic storm (Ap = 15) on 24 December 2014, the penetration electric field perturbations over the Indian dip equatorial sector are found to be anomalous on a number of occasions during postsunset hours. The event is anomalous as the magnitude and polarity of penetration electric fields do not obey the existing paradigm. The penetration electric field perturbations are investigated using the vertical drifts derived from the CADI (Canadian Advanced Digital Ionosonde) measurements at Tirunelveli (8.7°N, 77.7°E, dip angle: 1.7°). During this event, we observed postsunset vertical drift of ~42 m s^{-1} not only at 18:10 LT but also ~36 m s^{-1} at ~21:00 LT which is anomalous. Interestingly, the dawn-dusk component of interplanetary electric field (IEFy) is relatively less (<2 mV/m) at ~21:00 LT compared to the interval 19:30–20:30 LT (IEFy ~3 mV/m). Despite that, the vertical drift observed over Tirunelveli is very close to zero or nominally upward during 19:30–20:30 LT. In addition, the downward drift just after 21:30 LT on this night is found to be exceptionally large (~−60 m s^{-1}). By combining vertical total electron content over the Indian sector with the OI 630.0 nm airglow intensity from Mt. Abu, chain of magnetometer and Los Alamos National Laboratory geosynchronous satellite particle measurements, it is suggested that the anomalous penetration electric field perturbations on this night arise from the effects of interplanetary magnetic field By and substorm.

Plain Language Summary Variation in the zonal electric field in the equatorial ionosphere during postsunset hours is important to understand the plasma distribution over low latitudes and also generation of plasma irregularities. The changes in the ionospheric conditions over low/equatorial latitudes have implications for communication and navigational applications. Therefore, if ionospheric electric field over equatorial ionosphere behaves anomalously during space weather events, it will be difficult to model the low latitude ionosphere for scientific understanding and practical applications. In this investigation, we show that the less studied *Y*-component of interplanetary magnetic field and substorm can significantly modulate the ionospheric electric field giving rise to anomalous response.

1. Introduction

The F region vertical drifts are upward in the daytime and downward in the night time during geomagnetically quiet periods (e.g., Fejer et al., 2008a). However, the equatorial F region vertical drifts can be enhanced or reduced under the influence of space weather related perturbation electric fields. It is known that the southward directed interplanetary magnetic field (IMF) Bz drives geomagnetic storm and during a storm, the *Y*-component (dawn-dusk direction) of solar wind/interplanetary motional electric field (IEFy) maps down to the polar ionosphere. This electric field drives a two-cell ionospheric plasma convection pattern or disturbance Polar type 2 or DP2 cells (e.g., Nishida, 1968). During this period, region 1 Field aligned current (R1 FAC) develops rapidly and region 2 field aligned current (R2 FAC) takes time to develop as it is sluggish in nature compared to R1 FAC. Owing to the different time constants of R1 and R2 FACs, the convection electric field perturbations penetrate to the low latitude ionosphere through the polar ionosphere. This is known as prompt penetration electric field (PPEF). In an equivalent description, this happens under undershielding condition when the shielding electric field in the inner magnetosphere is not fully developed in response to the convection electric field imposed at the outer magnetosphere. Earlier studies (e.g., Fejer et al., 2008b) reveal that PPEF generates eastward/westward electric field perturbations in the equatorial ionosphere during daytime/nighttime. On the contrary, when IMF Bz suddenly turns northward from southward condition, R1 FAC decays quickly compared to R2 FAC and the residual shielding electric field survives in the inner magnetosphere for some time. It is this residual electric field that has the opposite polarity of PPEF (e.g., Kikuchi et al., 2008). This is known as the overshielding effect and the electric field perturbations experienced in the inner magnetosphere/ionosphere during this time is commonly termed as overshielding electric field. The impact of PPEF over low and equatorial ionosphere has been reported observationally (e.g., Chakrabarty et al., 2005, 2008, 2015; Tsurutani et al., 2008) and studied through simulation (e.g., Lu et al., 2012; Wang et al., 2008). During PRE-hours, significant effects of PPEF over the dip equatorial ionosphere have been studied by several researchers (e.g., Abdu et al., 2018; Fejer et al., 2021; Rout et al., 2019; Tsurutani et al., 2008) in the past. The role of PPEF in generating ionospheric super fountain (e.g., Mannucci et al., 2005; Tsurutani et al., 2004) over the low latitude and latitudinal expansion of the equatorial ionization anomaly (EIA) crest toward higher latitudes (e.g., Rout et al., 2019), have also been shown. Rout et al. (2019) studied the largest PRE-associated vertical drift (~150 m^{-1}) over Jicamarca during a space weather event in September 2017. They also brought out latitudinal expansion of the EIA crest along the 75°W longitude. The modeling (e.g., Nopper & Carovillano, 1978) and observational (e.g., Fejer et al., 2008b) studies also suggest that the eastward perturbations of PPEF is expected till 22:00 LT. Further, it is also shown that 6–9% of IEFy penetrates to the equatorial/low latitude ionosphere (e.g., Huang et al., 2007; Kelley et al., 2003). Significantly large PPEF can change the plasma distribution over low latitudes during daytime and postsunset hours (e.g., Abdu et al., 2018; Balan et al., 2009, 2018; Rout et al., 2019; Tsurutani et al., 2008) substantially and can shift the location and strength of the EIA crest over low latitudes.

In addition to storm, magnetospheric substorms can also generate transient electric field disturbances (e.g., Chakrabarty et al., 2008, 2010, 2015; Huang, 2009; Huang et al., 2004; Kikuchi et al., 2000, 2003) over low latitude ionosphere. Substorms are magnetosphere's way of unloading excess energies stored during the reorganization of the magnetic flux in the magnetotail. Substorms can be directly triggered by the changes in the solar wind parameters like IMF Bz flipping from southward to northward suddenly, abrupt changes in the solar wind dynamic pressure, etc. (e.g., Lyons, 1995, 1996; Lyons et al., 1997; McPherron, 1979) or can be spontaneously triggered (e.g., Angelopoulos et al., 1996; Henderson et al., 1996) wherein clear solar wind triggering is not obvious. The spontaneously triggered substorms are believed to be triggered by internal magnetospheric processes or by the self-organized criticality (e.g., Baker et al., 1997; Klimas et al., 2000; Tsurutani et al., 2004) of the plasma sheet. Substorms are nightside, longitudinally confined phenomena. Although the substorm induced electric fields are experienced over low latitude ionosphere during nighttime (e.g., Chakrabarty et al., 2015), the dayside electric field perturbations in the low latitude ionosphere due to substorms are also not uncommon (e.g., Hashimoto et al., 2017; Huang, 2009; Kikuchi et al., 2003; Wang et al., 2019). Moreover, substorms can exert both eastward (e.g., Chakrabarty et al., 2010; Huang, 2009; Hui et al., 2017) and westward (e.g., Chakrabarty et al., 2015; Hashimoto et al., 2017; Hui et al., 2017; Kikuchi et al., 2003) electric field perturbations over low latitude ionosphere. Therefore, simultaneous presence of substorms can augment or annul the prompt electric field perturbations arising out of undershielding/overshielding effects as shown in a few earlier studies (e.g., Hui et al., 2017; Rout et al., 2019). In addition to the above processes, sudden changes in the solar wind dynamic pressure can also lead to changes in the Chapman Ferraro current and cause prompt electric field disturbances (e.g., Huang et al., 2008; Rout et al., 2016; Sastri et al., 1993) over equatorial ionosphere. In recent times, it is also unambiguously brought out that the effects of IMF By can also change the expected polarity of electric field perturbation (e.g., Chakrabarty et al., 2017) over equatorial ionosphere particularly during the postsunset hours.

Therefore, under disturbed space weather conditions, some of the prompt electric field disturbances can occur simultaneously and can reinforce or annul individual effects making the phenomenological understanding of the equatorial impact difficult (e.g., Chakrabarty et al., 2015; Hui et al., 2017; Rout et al., 2019). In addition, these prompt electric field perturbations can also compete with the delayed electric field perturbations owing to what is known as disturbance dynamo mechanism (e.g., Blanc & Richmond, 1980) associated with the altered circulations of thermospheric wind systems following storm and substorm. Therefore, understanding the origin of prompt electric field perturbations over low-equatorial ionosphere deserves further investigation. In this regard, those cases are particularly important wherein the magnitude and polarity of penetration electric field in the equatorial ionosphere do not follow the existing understanding. The present investigation is important as it brings out such a case and shows that the phenomenological origin of the PPEF perturbations over the low latitude ionosphere is more complex than what is believed.

2. Data Sets and Methodology

One-minute cadence data of the solar wind parameters like IMF, solar wind velocity, dynamic pressure, and density are obtained from space physics data facility (SPDF) of Goddard Space Flight Center (https://cdaweb.gsfc.nasa.gov/). It is to be noted that the solar wind data available at this site are already time-shifted to the nose of the bow shock. In order to evaluate the ionospheric impacts, the magnetosheath and Alfven transit times are calculated and added to the lag time, point by point, following the methodology reported in Chakrabarty et al. (2005). In addition, symmetric ring current (Sym-H) index, auroral electrojet (AE) index, and polar cap (PC) index are also taken from SPDF.

In the absence of incoherent scatter radar over the Indian sector, the nighttime F region vertical drift over the Indian dip equator is derived by taking the temporal derivative of the bottom-side F layer height (h′F). The h′F values are obtained from the CADI over Tirunelveli (8.7°N, 77.7°E, dip angle: 1.7°). The details of the CADI system are described by MacDougall et al. (1995) and Sripathi et al. (2016). As the CADI data are slightly noisy, the *h′F* is smoothed with the Savitzky-Golay (SG) algorithm (e.g., Savitzky & Golay, 1964) with 15% smoothing window. The advantage of SG algorithm lies in its ability to suppress the noise in the data without introducing any significant distortion. Subsequently, temporal derivative of h′F (dh′F/dt) is calculated. It is to be noted that below 300 km altitude, the recombination process can also introduce an apparent upward drift as pointed out by Bittencourt and Abdu (1981). Therefore, in order to obtain the actual electrodynamical vertical drift, the apparent upward drift due to chemical recombination needs to be corrected. βH values are subtracted from $dh'F/dt$ to get the corrected vertical drift where β and H are the attachment coefficient and the scale height of plasma, respectively. β is calculated by the following formula: $\beta = K_1[O_2] + K_2[N_2]$, where K_1, K_2 and $[O_2]$, $[N_2]$ are the reaction rate coefficients and molecular density of oxygen, nitrogen, respectively. H is calculated by the following formula: $\frac{1}{H} = \frac{1}{n}\frac{\partial n}{\partial h}$, where n and h are the plasma density and height from the earth's surface. The parameters K_1 and K_2 are taken from Anderson and Rusch (1980). The neutral parameters, for example, molecular densities and thermospheric temperature, are taken from the NRLMSIS 2.0 (Emmert et al., 2021). For the present investigation, the typical scale height is calculated corresponding to 21:00 LT on a quiet (28 November 2014) and the event day (24 December 2014) to calculate the recombination-corrected vertical drifts wherever applicable. Typical β is also calculated at 21:00 LT (from 100 to 600 km in steps of 5 km). The typical uncertainty in the drifts derived based on ionosonde measurements is of the order of 10% (e.g., Woodman et al., 2006).

In order to get an idea about the daytime ionospheric electric field behavior, the equatorial electrojet (EEJ) strength is derived over both the Indian and Peruvian sectors. Over the Indian sector (e.g., Rastogi & Patel, 1975), EEJ strength is calculated using the systematic measurements of horizontal component (H) of geomagnetic field from a dip equatorial station, Tirunelveli (TIR) and the off-equatorial station, Alibag (ABG, 18.6°N, 72.9°E, dip angle: 26.4°). EEJ is calculated using the following formula, $\mathrm{EEJ_{India}} = \Delta H_{\mathrm{TIR}} - \Delta H_{\mathrm{ABG}}$. Here, ΔH is the instantaneous value of H corrected for the nighttime (during 23:00–03:00 LT) average quiet base values of H. The temporal cadence of EEJ data is 1 min. The EEJ strength over the Peruvian sector is, in general, derived by taking magnetometer data over the equatorial station, for example, Jicamarca (JIC, 11.5°S, 76.5°W, dip angle: 1.0°), and off-equatorial station, Piura (PIU, 5.2°S, 80.6°W, dip angle: 12.5°) (e.g., Rastogi & Klobuchar, 1990). As the magnetometer data over Piura are not available during the event under consideration here, data from another off-equatorial station, Leticia (LET, 4.2°S, 70.0°W, dip angle: 12.6°) are used in place of Piura. The local time of Leticia is also appropriately corrected to take account for the longitudinal difference between Jicamarca and Leticia and the resultant EEJ strength corresponds to the local time of Jicamarca. One-minute cadence data of both magnetometer stations are used to derive EEJ strength over the Peruvian sector by the following formula: $\mathrm{EEJ_{Peru}} = \Delta H_{\mathrm{JIC}} - \Delta H_{\mathrm{LET}}$.

Magnetometer data from a set of nearly antipodal stations (nearly 12 hr difference in the local time of the given set of stations with nearly similar latitudes) along the Indian and Peruvian longitudes are also used in this work to understand the variations of DP2 currents over the two sectors. This is done following the methodology suggested in Chakrabarty et al. (2017). In this work, the important role of this approach in identifying the role of IMF By is pointed out. During the event under consideration, India is in the postsunset to premidnight sector while Peru is in the morning sector. The northward component of magnetic field, ΔX (ΔX is the instantaneous value corrected for the quiet nighttime base values), for stations is obtained from the SuperMAG worldwide network (https://supermag.jhuapl.edu/). For the present work, magnetometer stations along Indian (145°–177°E) and Jicamarca (3°–20°W) longitudes are Novosibirsk (NVS, 45.8°N, 159.9°E) and Ottawa (OTT, 54.9°N, 3.8°W); Irkutsk (IRT, 42.4°N, 177.4°E) and Fredericksburg (FRD, 47.8°N, 5.8°W); Alma Ata (AAA, 34.5°N, 153.1°E); and Bay St. Louis (BSL, 39.4°N, 18.9°W); Tirunelveli (TIR, 0.18°N, 150.7°E) and Huancayo (HUA, 2.2°S, 2.6°W) as well as Alibag (ABG, 10.4°N, 146.8°E). One-minute cadence data are used for all the stations.

In order to assess the effects of disturbance dynamo (DD) on 24 December 2014, we estimate magnetic disturbance in *H*-component (D_{dyn}) using an established methodology (e.g., Amory-Mazaudier et al., 2017; Pandey et al., 2018; Rout et al., 2019; Zaka et al., 2009).

$$D_{dyn} = \Delta H - S_R - SymH \times \cos(L) \tag{1}$$

In Equation 1, ΔH and S_R are the event day and quiet time average magnetic field variations above the crustal magnetic field values. *SymH* is the strength of the ring current. *L* is the magnetic latitude at that station where the magnetic disturbance (D_{dyn}) is calculated. As the *H* variation due to ionospheric current is unambiguous during daytime, the magnetometer data between the geographic longitudes 275°–300°E which is in day sector during the event under consideration, have been used to calculate D_{dyn} in this work. D_{dyn} is calculated over the stations, Vernadsky (AIA, 55.4°S, 6.1°E), Trelew (TRW, 33.4°S, 6.24°E), Pilar (PIL, 21.8°S, 7.9°E), Huancayo (HUA, 2.2°S, 2.7°S), San Juan (SJG, 27.7°N, 6.8°E), Ottawa (OTT, 54.9°N, 3.7°W), Iqaluit (IQA, 73.3°N, 6.2°E), and Thule (THL, 87.1°N, 14.2°E). These data are obtained from the INTERMAGNET network (https://www.intermagnet.org/index-eng.php).

The present investigation requires identification of the substorm induced electric field perturbations over the low latitude ionosphere. We identify substorms using observations of dispersionless injection of energetic particles (electrons and protons) at the geosynchronous orbit (e.g., Reeves et al., 2003). This is considered to be one of the telltale signatures of the onset of substorms (e.g., Reeves et al., 2003). The data from Los Alamos National Laboratory (LANL) −01, 02, 04, 97A, 080, and 084 geosynchronous satellites are used for the present study. The electron and proton flux data are taken from all these satellites for the event day from 12:00 to 19:00 UT (universal time).

To understand the low latitude plasma distribution over the Indian sector, and the approximate location of the EIA crest and its strength, the measurements of total electron content (TEC) by the Indian Satellite-based Augmentation System (SBAS) is used. Indian SBAS network is known as GAGAN (GPS Aided Geo Augmented Navigation). As part of GAGAN, 5 min cadence of SBAS-TEC data is available at 102 ionospheric grid points over the Indian sector. The data of these grid points are generated by using 13 ground stations. The details of GAGAN SBAS-system are described by Sunda et al. (2015).

OI 630.0 nm airglow intensity over Mt. Abu (24.6°N, 72.7°E, dip angle: 38.0°), a station typically under the crest of EIA, is used for the present study. Ten-seconds cadence airglow intensity data were captured by a narrow spectral band (bandwidth 0.3 nm) and narrow field-of-view (3°) airglow photometer in a campaign mode in cloudless and moonless conditions during December 2014. The details of this photometer are available in the literature (e.g., Chakrabarty et al., 2008, 2015; Sekar & Chakrabarty, 2011). Note, the instrumental parameters remain the same during the campaign and hence, despite absolute airglow intensity levels (in Rayleigh) are not being known during the nights under this campaign, gross comparison of the night-to-night changes in the peak intensity levels during the campaign can be made.

Slant total electron content (STEC) is measured over Ahmedabad (23.0°N, 72.6°E, dip angle: 35.2°) by a dual-frequency (L-band, 1,575 and 1,227 MHz) GPS receiver (GISTM GSV4004 B) at the Physical Research Laboratory (PRL). Vertical TEC (VTEC) is derived from STEC using a standard methodology described in Manke and Chakarabarty (2016). For the present work, raypath elevation angle of less than 30° is not considered to minimize the multipath error and tropospheric effects. five minutes cadence VTEC data are used in this case study. It is to be noted that, local time over Indian longitude is taken along 75°E longitudes (LT = UT + 5 hr) in present investigation.

3. Results

Figure 1 depicts the variations of a few interplanetary (Figures 1a–1d) and ground-based parameters (Figures 1e and 1f) from 21 to 25 December 2014. The Ap values for these days are 12, 19, 11, 15, and 11, respectively. In Figure 1 (from top to bottom), IMF Bx (in nT), IMF Bz (in nT), solar wind velocity (in km s^{-1}), IMF |*B*| (in

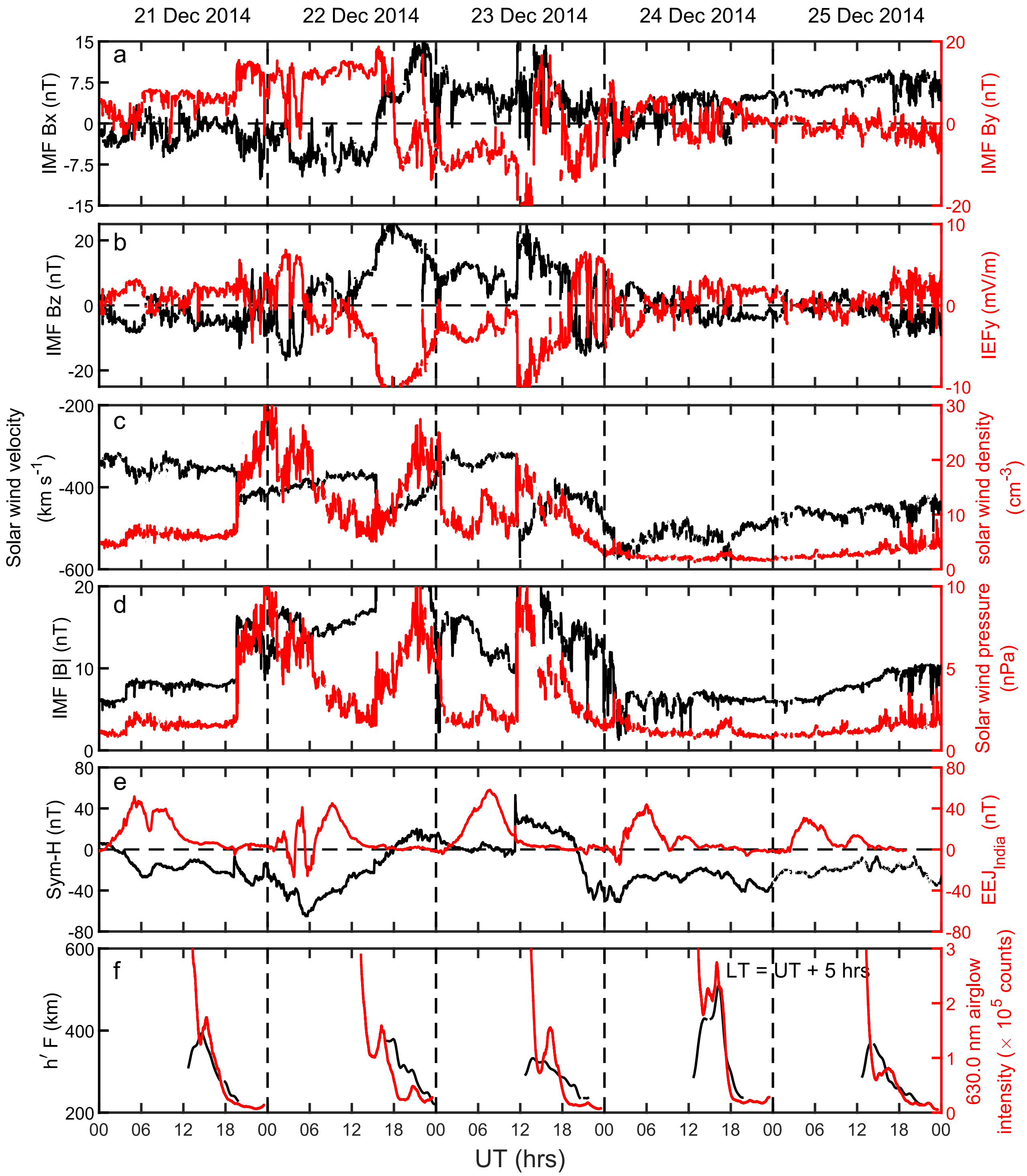

Figure 1. Variations in (a) interplanetary magnetic field (IMF) Bx (nT, black line) and IMF By (nT, red line), (b) IMF Bz (nT, black line) and IEFy (mV/m, red line), (c) solar wind velocity (km s^{-1}, black line) and density (cm^{-3}, red line), (d) IMF $|B|$ (nT, black) and pressure (nPa, red), (e) Sym-H index (nT, black) and equatorial electrojet strength (EEJ_{India}) over the Indian sector (nT, red), (f) $h'F$ (km, black) and OI 630.0 nm airglow intensity over Mt. Abu (in arbitrary units, red) from 21 December 2014 to 2025 December 2014.

nT), Sym-H (in nT) and $h'F$ (in km) are shown in black lines while IMF By (in nT), IEFy (in mV/m), solar wind density (cm^{-3}), solar wind pressure (nPa), EEJ_{India} (in nT) and OI 630.0 nm airglow intensity (in arbitrary units) are depicted in red lines. The Y axes corresponding to black and red lines are marked on the left and right side

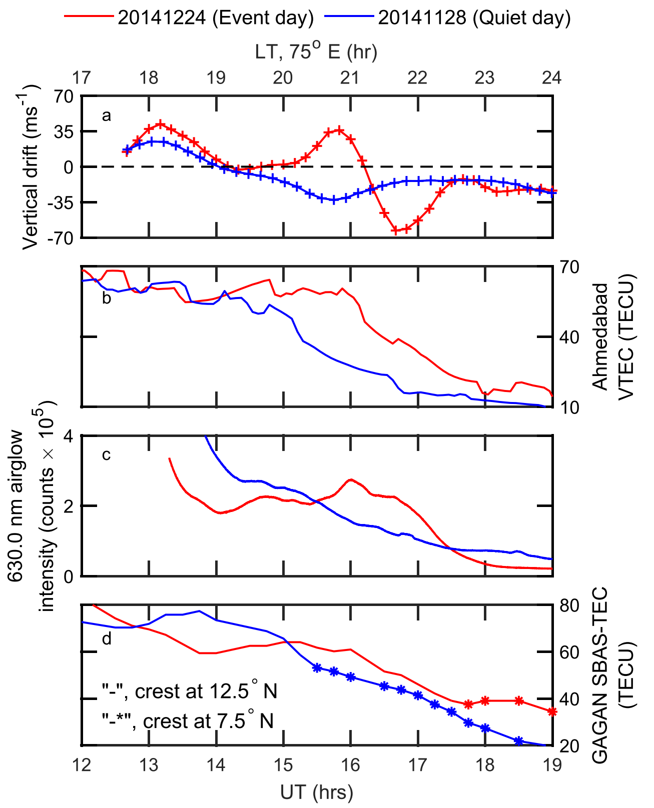

Figure 2. This figure illustrates the variations of a number of parameters on the event day (24 December 2014) and quiet day (28 November 2014) with red and blue colors, respectively. Subplots (a–d) represent vertical drifts (in m s^{-1}) over Tirunelveli, vertical total electron content (in TECU) over Ahmedabad, OI 630.0 nm airglow intensity (in arbitrary unit) over Mt. Abu, and SBAS-TEC (in TECU) variations over only the crest location, respectively. In subplot (d), solid and solid lines with stars are used to show the position of the crest at 12.5°N and 7.5°N magnetic latitudes.

of Figure 1. It can be clearly noticed from Figure 1 that the peak $h'F$ and 630.0 nm airglow intensity are higher in the local night of 24 December 2014 in comparison with the rest of the nights shown in Figure 1. This is despite IMF Bz being more southward for some time on 22 December (prenoon hours over the Indian sector) and 23 December (premidnight hours over the Indian sector) compared to the interval of interest on 24 December 2014. In fact, the characteristically different variation in OI 630.0 nm airglow intensity on this night motivated us to pursue this investigation.

Figure 2 shows observations on 24 December 2014 along with observations from a quiet day (28 November 2014) for comparison. Note, the daily mean Ap is three on 28 November 2014 and 2017 on the previous day. In all the panels, the quiet and disturbed variations are shown with blue and red colored lines, respectively. Figure 2a depicts the derived vertical drift variations over Tirunelveli (red) on the event day along with the vertical drift variations on the quiet day (blue). The vertical drift variation during postsunset hours is found to deviate from the variation on the quiet day. It can be seen that prereversal enhancement (PRE) of equatorial zonal electric field is enhanced on the event day (24 December 2014). The vertical drift corresponding to PRE occurs at ~13:10 UT (18:10 LT) on the event day with an amplitude of ~42 m s^{-1}, which is higher than PRE amplitude on a quiet day (~25 m s^{-1}). More importantly, although the vertical drift decreases after the PRE-hours, drift does not turn steadily downward on the event night compared to what happens on a quiet day. It can be noted that vertical drift turns downward during 14:00–14:30 UT (19:00–19:30 LT) on a quiet day. In sharp contrast to a quite day variation, the vertical drift again starts increasing from 15:00 UT (20:00 LT) on 24 December 2014 and another peak in vertical drift occurs at ~16:00 UT (21:00 LT) with an amplitude of ~36 m s^{-1} on the event night. Note that the vertical drift at this local time is expected to be significantly downward as indicated by the quiet time reference drift. Further, the vertical drift is found to be minimum (~−60 m s^{-1}) at ~16:40 UT (21:40 LT) which is significantly higher than the corresponding downward drift (~−15 m s^{-1}) during a quiet night at this local time. The vertical drift again starts decreasing just before 17:00 UT (22:00 LT) and becomes less downward at 17:30 UT (22:30 LT) to match with the corresponding quiet time drifts afterward.

Figure 2b shows vertical total electron content variation over Ahmedabad on 24 December 2014 (red) and 28 November 2014 (blue), respectively. The figure reveals that the postsunset enhancement in VTEC over Ahmedabad is higher and sustains for a longer period on the event day than on the quiet day. In Figure 2c, variations in OI 630.0 nm airglow intensity over Mt. Abu on the event day (red) shows different temporal pattern than what is noticed on the control day (blue). The intensity variation on the event night is characterized by three enhancements peaking at 14:45, 16:00, and 16:40 UT (19:45, 21:00, and 21:40 LT). In fact, the late enhancements at 16:00 UT and 16:40 UT are in sharp contrast with the monotonic decrease in intensity found on the control night at this local time.

Figure 2d is constructed with the help of SBAS-TEC data that shows the local time variations of TEC over the EIA crest location. The event and control days are marked by red and blue lines, respectively. On both days, the crest location is found either closer to 7.5°N (solid line with star) or 12.5° (solid line) magnetic latitudes during postsunset hours. One can notice in Figure 2d that the EIA crest is located at 12.5°N till 17:30 UT (22:30 LT) on event day, whereas on the quiet day, the EIA crest is observed at 12.5°N magnetic latitudes till 15:15 UT (20:15 LT). After this, the location of the EIA crest is found at 7.5°N.

Figure 3 is dedicated to identify the anomalous vertical drift variations on the event night (24 December 2014). Figure 3a is a replica of Figures 2a and 2is presented again for continuity. The variations in EEJ strength over Jicamarca for the event day (in red) and quiet day (in blue) are depicted in Figure 3b. In Figure 3c, the variations in ΔVd over Tirunelveli (red) and ΔEEJ over Jicamarca (black) are shown. The ΔVd and ΔEEJ are derived by

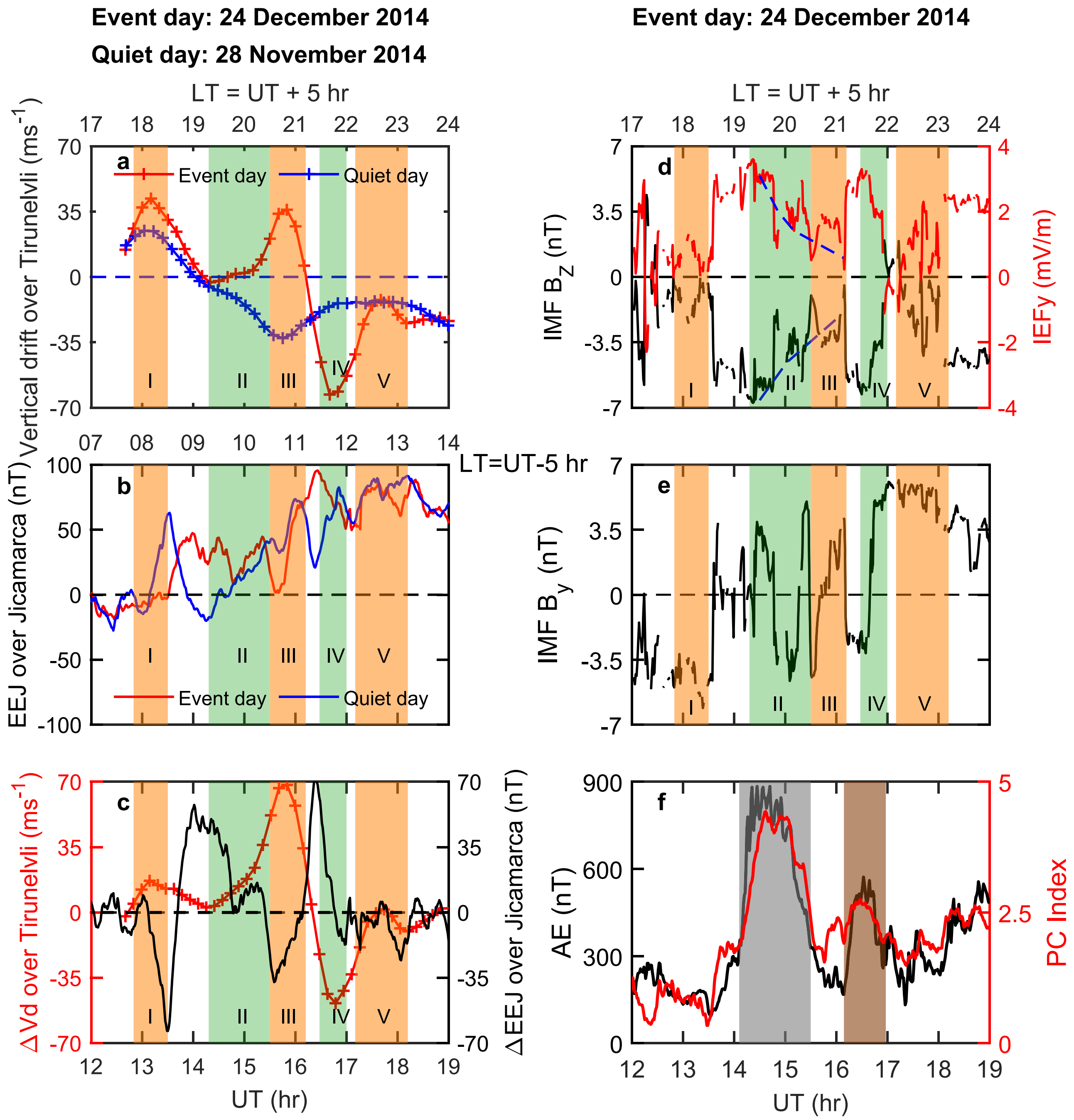

Figure 3. (a) The comparison of vertical drifts over Tirunelveli on the event day (24 December 2014, in red) with respect to a typical quiet day (28 November 2014, in blue) similar to what is shown in Figures 2a and 2b represents similar comparison in equatorial electrojet (EEJ) over Jicamarca, (c) shows the variations in the ΔVd over Tirunelveli (in red) and ΔEEJ over Jicamarca (in black) obtained by subtracting the quiet day variation from the event day variation, (d) depicts the variations in interplanetary magnetic field (IMF) Bz (in black) and IEFy (in red), (e) represents the variations in IMF By and, (f) depicts the variations in the AE (in black) and PC (in red) indices. Based on vertical drift variations on event day, intervals (I–V) are marked with orange and green colored rectangular boxes in the panels (a–e). In (e), two conspicuous peaks in the AE and PC indices are marked with gray and brown colored rectangular boxes.

subtracting the vertical drift and EEJ strength of the quiet day from their event day counterparts. Figures 3d–3f depict the variations of a few interplanetary parameters (IMF Bz, IEFy, and IMF By) and geomagnetic indices (AE and PC) on the event day only. Figure 3d represents the variations in IMF Bz (in black) and IEFy (in red). Variations in IMF By are shown in Figure 3e. Figure 3f depicts the variations in Auroral electrojet (AE) and polar cap (PC) indices. A few vertically shaded (in orange and green colors) intervals (marked by Roman numbers I–V) are overlaid at appropriate places in Figures 3a–3e to bring out the important features that emerge out of this set of observations. The criterion for the divisions of the intervals is based on the conspicuous differences of the vertical drift variations on the event night with reference to the quiet night. The interval-I shows that the vertical drift in event night is conspicuously more than the quiet night. On the other hand, interval-II highlights the onset of departures of the vertical drift polarity with respect to the quiet night. Interval-III captures significantly anomalous electric field perturbations with opposite polarity. Interval-IV captures much larger downward drift on the event night than what is expected during a quiet night at this local time. Lastly, during interval-V, the vertical drift on the event night recovers and catches up with the corresponding variations during the quiet night. In addition, two simultaneous peaks in AE and PC indices around 14:15 UT (19:15 LT) and 16:30 UT (21:30 LT) are shown by gray and brown shaded boxes. In Figure 3d, the dashed blue lines are used to guide the eye toward the net decrease in southward IMF Bz and IEFy, respectively, during the period ∼14:00–16:00 UT (19:00–21:00 LT). In the ensuing paragraphs, we highlight the important observational features of interval-I–interval-V.

Interval-I. During interval-I (∼12:50–13:30 UT, LT are shown at the top of the figure), IMF Bz is southward, and vertical drift is upward with an amplitude of −∼42 m s^{-1}. This drift is more than the quiet time drift (∼25 m s^{-1}) even if one considers 10% uncertainty in the vertical drift. Therefore, the enhanced PRE drift at this interval is due to the penetration of IEFy to equatorial ionosphere and this change is noticed ∼17 m s^{-1}.

Interval-II: In the course of interval-II (∼14:20–15:30 UT), southward IMF Bz decreases (from ∼−6 to −1 nT) leading to the decrease in IEFy. IEFy changes to +0.5 mv/m from +3 mV/m during this interval. However, equatorial vertical drifts remain close to zero for some period and then enhances with net decrease in the magnitude of IEFy. Note, IMF By oscillates with a sharp negative excursion sandwiched between two positive excursions during this interval. Further, strong enhancements in AE (reaches ∼900 nT) and PC indices are observed during this interval apparently suggesting occurrence of substorm. However, Figure 4 would subsequently confirm that the enhancement of AE and PC indices at this local time ∼19:15 LT (14:15 UT) are not due to substorm induced electric field perturbations but possibly due to enhancement in polar cap electric field at this time due to enhanced IEFy. Another important aspect emerges from Figure 3c shows the polarity of both ΔVd and ΔEEJ derived based on Figures 3a and 3b, respectively, is positive.

Interval-III: During interval-III (∼15:30–16:15 UT), IMF By changes polarity from negative to positive. Net IMF Bz (dashed line in blue) is less southward than interval-II. However, vertical drift keeps increasing with a maximum amplitude of ∼36 m s^{-1} at 15:50 UT (20:50 LT). Note, the maximum vertical drift during this interval is nearly comparable to PRE-associated vertical drift during postsunset hours. Although IMF By turns positive (similar to interval-II) during this interval, ΔVd and ΔEEJ are opposite unlike interval-II (Figure 3c).

Interval-IV. Interval-IV (∼16:30–17:00 UT) is characterized by highest downward drift amplitude (∼−62 m s^{-1}) at ∼16:40 UT (21:40 LT) on the event day. This is significantly different than the quiet day drift (∼−15 m s^{-1}) at this local time. During this interval, IMF Bz is southward and the amplitude is similar to interval-II. In addition, IMF By is initially negative and then sharply turns to positive direction. Considering 10% efficiency of the penetration electric field reaching to the dip equator, the difference in the observed and expected drifts ∼48 m s^{-1} (Figure 3c) cannot be explained even after considering a typical 10% uncertainty in the drift. In addition, enhancements in AE and PC indices are seen during this interval (peak ∼16:30 UT) although these enhancements are less compared to the enhancements in these indices seen around 14:15 UT. Based on Figure 4, it is confirmed subsequently that the enhancement of AE and PC indices at this local time (∼21:30 LT) are due to additional effects of substorm induced electric field perturbations. Further, similar to interval-III, the polarity of the electric field perturbations (vertical drift over Tirunelveli and ΔEEJ over Jicamarca) over the two antipodal locations is predominantly opposite during this interval (Figure 3c).

Interval-V. IMF Bz turns northward in the interval-V (∼17:10–18:10 UT) and vertical drift becomes less downward indicating a eastward electric field perturbation at this time. This appears to be under the influence of overshielding electric field. After the overshielding electric field perturbation, the vertical drift values reach the quiet time levels.

Figure 4 is used to identify the presence of substorm activity, if any, during 12:00–19:00 UT that encompasses the intervals (I–VI) under consideration (Figure 3) on 24 December 2014. In this plot, the variations in the electron and ion fluxes measured from geosynchronous orbit are presented in subplots a–f and subplots g–l, respectively. The LANL geosynchronous satellites are LANL-01A, LANL-02A, LANL-04A, LANL-97A, LANL-080, and

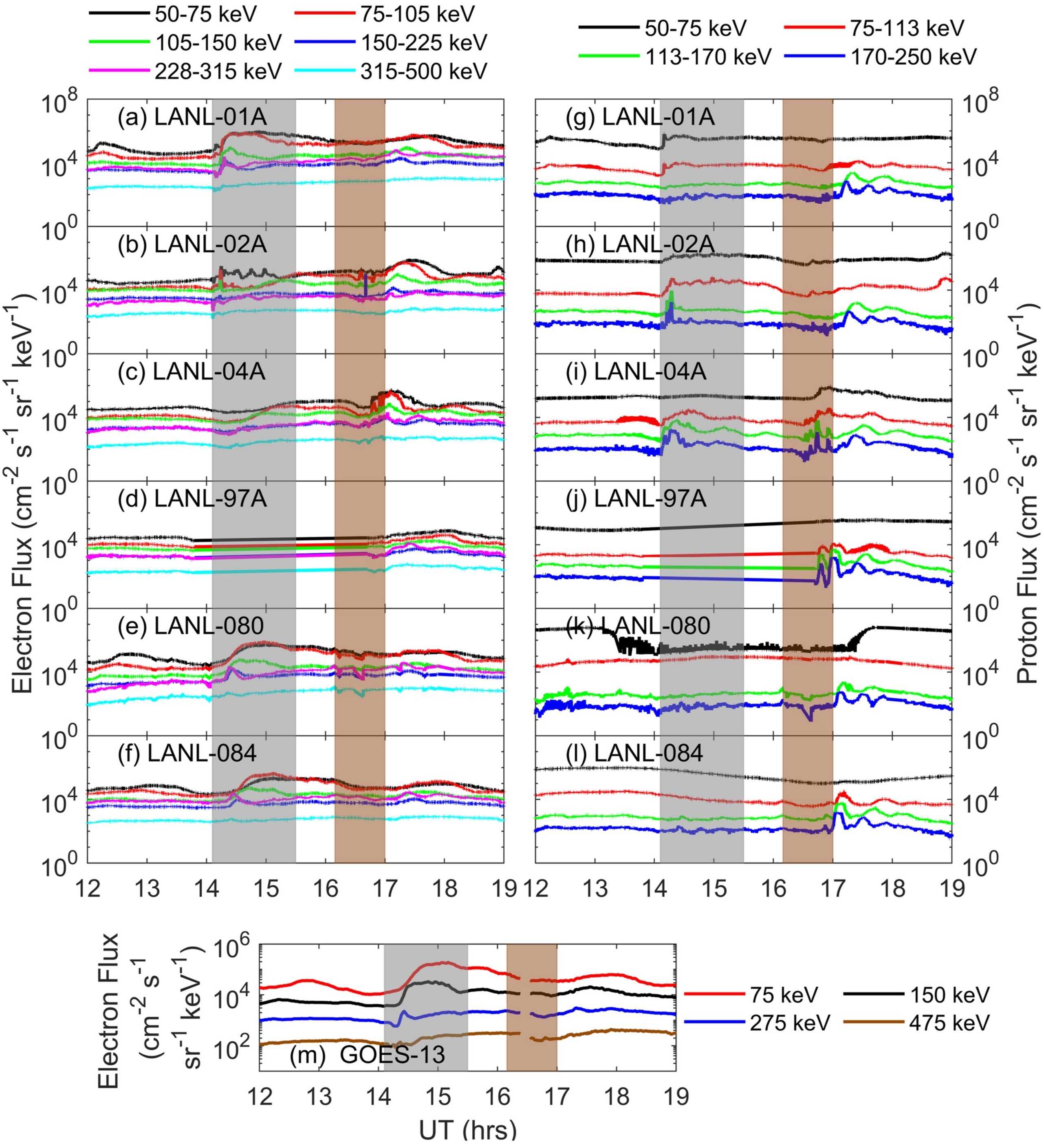

Figure 4. (a–f) and (g–l) The electron and proton flux variations measured by six LANL satellites (LANL-01A, LANL-02A, LANL-04A, LANL-97A, LANL-080, LANL-084) during 12:00–19:00 UT on 24 December 2014 for a number of energy channels mentioned at the top. (m) The electron flux variations at four energy channels (75, 150, 275, 475 kev) measured by GOES-13 for same interval and day depicted in (a–l). Two intervals are marked with gray (∼14:05–15:30 UT) and brown (∼16:10–17:00 UT) rectangular boxes in all subplots, similarly marked in Figure 3f.

LANL-084. Six energy bins for electrons and four energy bins for protons are used in this study. The electron energy bins are 50–75, 75–105, 105–150, 150–225, 228–315, and 315–500 keV whereas the ion energy bins are 0–75, 75–113, 113–170, and 170–250 keV. Differently colored lines are used to represent the different energy channels. In addition, the electron flux variations at four energy channels (75, 150, 275, and 475 keV) from

10.1029/2022JA030826

GOES-13 satellites are also shown in Figure 4m. Here also different colors correspond to different energy channels. Two intervals are marked with gray (∼14:06–15:30 UT) and brown (∼16:10–17:00 UT) rectangular boxes in all the subplots of Figure 4. These are the same intervals that are marked for AE and PC indices in Figure 4e. There are weak substorm injection activities noticed during intervals 14:10–15:30 UT (particularly in LANL-01A) and 16:10–17:00 UT (particularly in LANL-04A). The first substorm onset happens around 14:10 UT. At this time, LANL-01A detects identifiable ion injections. GOES-13 also sees dispersed electron injections ∼14:10 UT. It is to be noted that both satellites are far (LANL-01A at 165°W and GOES-13 at 75°W) from the Indian sector. On the other hand, injection activities (with dispersion) are noticed in the electron as well as ion channels starting at ∼16:30 UT which is particularly captured by LANL-04A (∼65°E). At this time, the injection activities are not captured by GOES- 13. This suggests energetic particle injection at the geosynchronous orbit closer to the location of LANL-04A. The other LANL satellites seem to be away from the proton injection front and as a consequence, the injection signatures are quite dispersed at the other satellite locations. Based on this figure, it appears that substorm is present during 16:10–17:00 UT closer to the Indian longitude. The implications of these results will be discussed in Section 4.

Figure 5 depicts the variations in the north-south (X) component of the magnetic field along the Indian and the Peruvian (antipodal location of Indian longitude) longitudes starting from the northern high latitudes to the equatorial regions. ΔX variations of Indian and Peruvian magnetometer stations are shown with red/green and blue colored lines, respectively, in Figures 5a–5d. Figure 5e shows the variations in IMF By and IMF Bz with blue and black colored lines, respectively (reproduced from Figure 1). The interval (∼14:20–15:30 UT, interval-II) is marked in this figure with green colored rectangular box. It can be noted that the ΔX variations are anticorrelated in Figures 5a and 5b (midlatitudes) and start becoming less anticorrelated and more correlated as one comes toward the low-equatorial latitudes (Figures 5c and 5d). As revealed by Figure 5e and also pointed out earlier, two positive peaks in IMF By with a negative excursion in between are observed in this interval. In addition, it is also shown in Figure 3c that ΔVd over Tirunelveli and ΔEEJ over Jicamarca are both positive during this time.

In order to evaluate the effects of disturbance dynamo during intervals I–V, Figure 6 is presented. Figures 6a–6f depict the latitudinal variations in D_{dyn} over the Jicamarca sector during 1:300–18:45 UT in steps of 15 min intervals. The values of D_{dyn} over the dip equatorial region is negative/nearly zero on all the times except during 15:30–15:45 UT (Figure 6c) and at 18:00 UT (Figure 6f). Therefore, Figures 6c and 6f suggest small contributions of D_{dyn} during interval-III and interval-V, respectively.

4. Discussion

The important role of PPEF in enhancing zonal electric field during local PRE-hours is evident on 24 December 2014 (see Figure 2a). This enhanced zonal electric field not only shifted the EIA crest but also caused enhancement in TEC over the crest region. Kumar et al. (2021, 2022) brought out the important role of PRE and solar flux dependence of the postsunset enhancement of OI 630.0 nm airglow intensity and VTEC over the EIA crest region. Therefore, it is not surprising that an enhanced PRE (interval-I in Figure 3d) would enhance the VTEC as well as OI 630.0 nm airglow intensity over the EIA crest region as brought out in Figures 2b and 2c. However, what is different here is the sustained (till 21:00 LT or 16:00 UT) enhancement of VTEC (Figure 2b) and airglow intensity (Figure 2c) over the crest region and also the longer sustenance of the EIA crest location at a higher latitude of 12.5° (Figure 2d) on the event day. It is also important to note that strength of EEJIndia on 24 December 2014 is, in fact, weaker compared to the other days. Despite that, we see an elevated OI 630.0 nm airglow intensity over the EIA crest region on this night. Therefore, it is apparent that the enhancements in VTEC and 630.0 nm airglow intensity on this night are not due to conditioning of the EIA crest region by the daytime F region plasma fountain process driven by daytime zonal electric field over the equatorial ionosphere. Elevated $h'F$ over Tirunelveli in the evening hours of 24 December 2014 provides the first clue that the impact on the EIA crest region on this night is because of what happened in the evening hours. It is noteworthy that the EIA crest is located at 12.5°N magnetic latitude till 20:15 LT on the quiet day as indicated in Figure 2d. The fact that the vertical drift does not really become downward on the event day during the postsunset hours (Figure 2a) and also get significantly upward at ∼16:00 UT (21:00 LT) have important connection with the behavior of EIA crest on the event night. This essentially means that the electric field is eastward at 21:00 LT on this night. This is in contrast with the results of Liu et al. (2013) and Le et al. (2014) who showed the primary role of westward electric field in the premidnight hours in the enhancements of ionospheric plasma density over low latitudes. It is to be noted

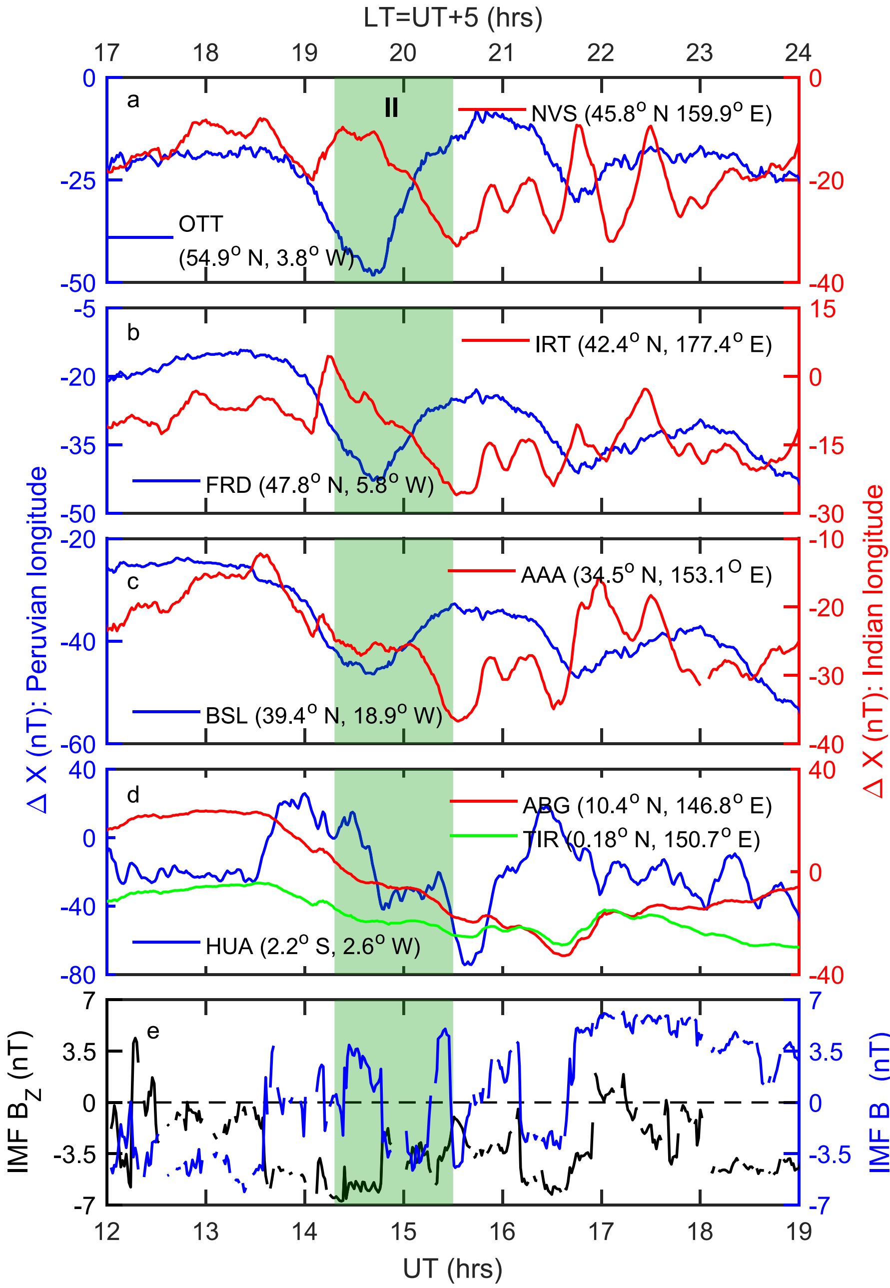

Figure 5. Variations of the northward component of magnetic field (ΔX) over Indian and Peruvian sectors from mid latitudes of the northern hemisphere to the equatorial region are shown in (a–d) with red/green and blue colors, respectively. (e) The interplanetary magnetic field (IMF) Bz and IMF By in black and blue colors, respectively. An interval is marked with green (~14:20–15:30 UT) colored rectangular box when ΔX variations are anticorrelated over mid latitudes and start becoming correlated as one comes toward the low-equatorial latitudes.

that under geomagnetically quiet conditions, westward electric field is expected during 21:00–22:00 LT and the mechanisms suggested by Liu et al. (2013) and Le et al. (2014) are important. However, as pointed out earlier, the plasma density enhancement in the present case is connected with the eastward electric field polarity over low latitudes. Therefore, the processes responsible for the unusual behavior of the vertical drift (proxy for the zonal electric field) on this night deserve critical attention. Once we understand the possible causative mechanisms for this eastward electric field perturbation, we will come back to the topic of plasma density enhancement at this local time.

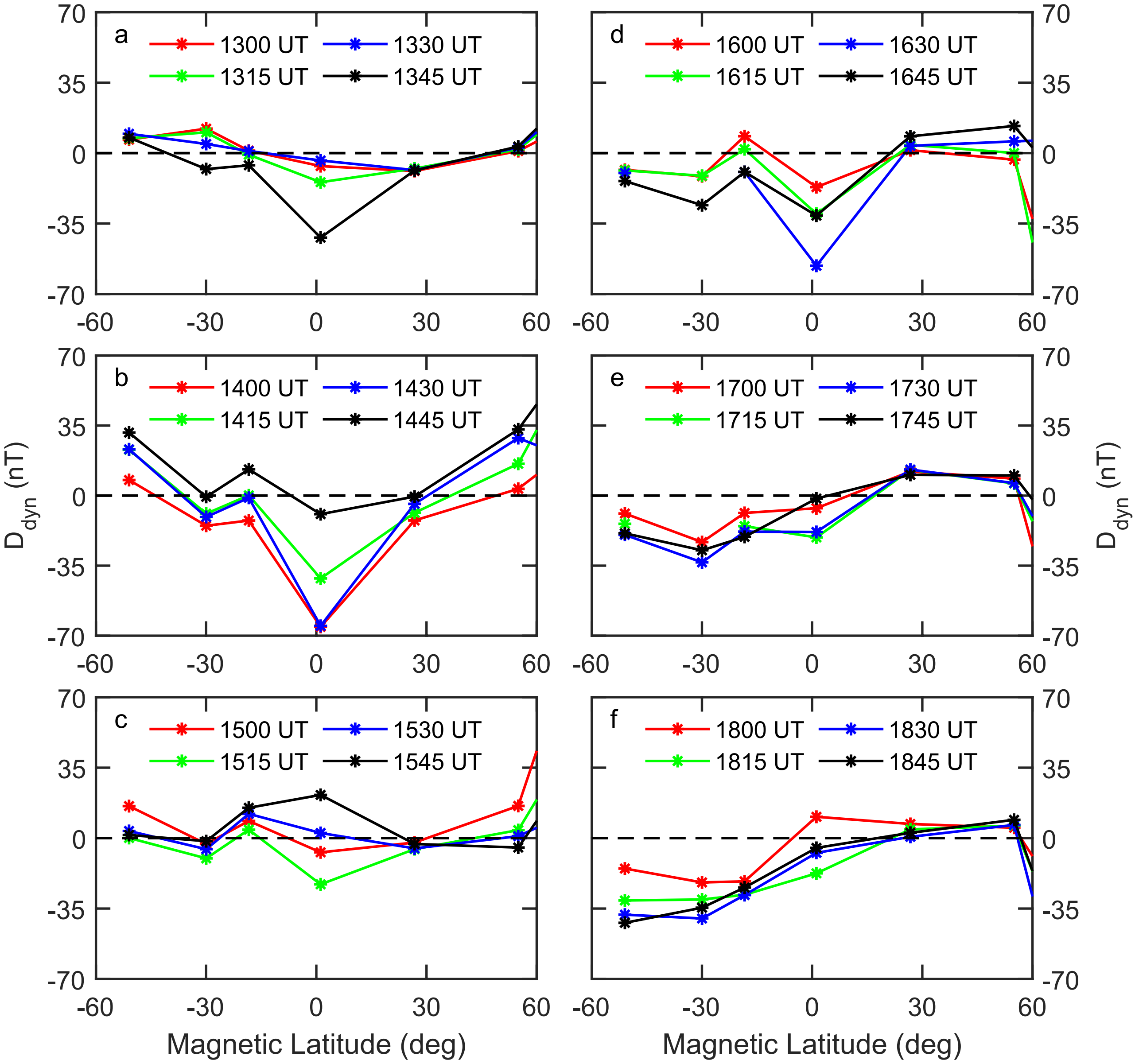

Figure 6. (a–f) The latitudinal variations in D_{dyn} during 13:00–18:45 UT in steps of 15 min intervals along Jicamarca longitudes on 24 December 2014. It can be seen that the positive deviations in D_{dyn} over equatorial latitudes are seen during 15:30–15:45 UT (in (c)) and 18:00 UT (in (f)) indicating influence of disturbance dynamo effects.

To understand the anomalous behavior of the zonal electric field on 24 December 2014, we now shift our attention to intervals II–IV in Figure 3. Note, IMF Bz is southward in these intervals. However, IMF Bz is more southward (IEFy is more positive) during intervals-II and interval-IV compared to interval-III. In view of this, we expect more changes in the equatorial vertical drift during intervals II and IV compared to interval-III. However, what we observe is contrary to this expectation and hence counter-intuitive. The perturbations in the electric field is nominally eastward (nominally upward drift or nearly zero drift) which is followed by an increase in eastward perturbation in the interval-II and significantly westward perturbation in the interval-IV. On the contrary, in the interval-III, the eastward electric field perturbations keep increasing. Another interesting feature is the observation that vertical drift keeps increasing through intervals II and III although IMF Bz becomes less southward in interval-III compared to interval-II. Therefore, even if eastward penetration electric field is operational during this period that resists the drifts to turn downward, one expects larger drifts when IMF Bz (or IEFy) is larger. This suggests contribution from other driver(s). Therefore, not only these observations cannot be explained by the eastward penetration electric field perturbations expected till 22:00 LT as per the existing understanding (e.g., Fejer et al., 2008b; Nopper & Carovillano, 1978) but the amplitude of perturbations also need attention here. Importantly, LANL geosynchronous particle fluxes (Figure 4) confirm that there is no significant substorm occurrence closer to Indian longitude during the interval of first enhancements of AE and PC indices that occur during interval-II. Further, the interval of the first and strong enhancements in AE and PC indices are also marked by relatively large magnitude of IEFy. This suggests strong influence of IEFy in the enhancements of AE and PC indices at this time. This leads us to envisage a strong IMF By role in the interval-II. From the work of Chakrabarty et al. (2017), we know that predominantly positive IMF By can rotate the DP2 convection cells (well-developed during southward IMF Bz condition) significantly so that the daytime eastward perturbation electric field encroach into the postsunset sector and affects the polarity of the perturbation electric field during postsunset hours. This gets credence from the present observations (Figure 3c) wherein the polarity of ΔEEJ and vertical drift over the Jicamarca and Indian sectors are identical during interval-II suggesting an eastward electric field perturbations over both the sectors (Jicamarca is the day sector whereas Tirunelveli is in the night sector). Note, this is the local time over the Indian sector when a westward electric field polarity (downward drift as per quiet day pattern) is expected. Considering the curl-free nature of the ionospheric electric field and maximum impact of the penetration electric field on the ionospheric zonal component, one may expect opposite polarities of perturbation electric field at the day and night side of the dip equatorial ionosphere. This is evident in earlier results also (e.g., see Figure 3 of Kelley & Makela, 2002). Therefore, it appears that the identical polarity of penetration electric field over both Indian and Jicamarca sectors during interval-II are possibly due to the effects of IMF By. Although based on these low cadence observations of drifts, it is difficult to evaluate the relative roles of magnitude and polarity reversal of IMF By, supporting evidences in the form of identical polarity of electric field perturbations over antipodal locations and specific pattern (discussed subsequently) of global ΔX variations reinforce the role of IMF By. The proposition of the rotation of the DP2 convection cells by the effects of IMF By (e.g., Chakrabarty et al., 2017) gets further credence from Figure 5 wherein one can see the anticorrelation of ΔX variations over mid latitudes but correlation over low latitudes. Kelley and Makela (2002) found the westward penetration of electric field over Jicamarca during the premidnight hours under the southward IMF Bz conditions and suspected the effect of IMF By. In the work of Chakrabarty et al. (2017) and this work, we see the IMF By effect during the postsunset hours. This is consistent with the work of Hui and Vichare (2021) who, using TIE-GCM simulations, showed that the effects of IMF By over low latitudes are most prominent at the terminator sector over low latitudes.

At this juncture, we note that ΔEEJ and ΔVd (Figure 3c) show anticorrelations during interval-III and interval-IV which is consistent with the curl-free nature of the ionospheric electric field as discussed in the previous paragraph. However, zonal electric field perturbations over the Indian sector are eastward and westward, respectively, during these intervals. Unlike interval-II, ΔX variations (Figure 5) during these intervals do not show any systematic changes in the behavior as one comes toward the low latitude (mentioned in the previous paragraph) and this is indicative of the absence of IMF By effect during interval-III and interval-IV. Therefore, although IMF By turns positive during interval-III, we rule out IMF By effect during this interval and it get credence form Figure 5 too. This also indicates that the changes in IMF By is a necessary but not sufficient condition for its effects to be detected in the electric field perturbations over the dip equator. This may be essentially due to the fact that the combined effects of IMF Bz and IMF By may not bring two antipodal stations under the same DP2 cell. We feel that the local time dependence of IMF By effects needs attention in the future.

Let us now investigate interval-III. In absence of any substorm onset activity during interval-III, the only way an enhanced eastward electric field perturbation can arise with a reduced (compared to interval-II) amplitude of southward IMF Bz condition is through the withdrawal of IMF By effect that was present before. In addition, during interval-III, some effects of eastward DD electric field perturbations cannot be ruled out as suggested by Figure 6c. However, it is not clear why DD effects that can last for a much longer duration (e.g., Fejer et al., 2017; Zhang et al., 2017, 2019) turns effective only for a short duration. Fejer et al. (2008b) shows that the polarity of DD electric field perturbation is eastward only after 21:00 LT and it is westward during 17:00–21:00 LT (as is the case here). This also suggests that any eastward electric field perturbation during 17:00–21:00 LT might not be affected by DD effects significantly. We, therefore, suggest that the usual eastward penetration electric field perturbations are experienced over the Indian sector during interval-II under the influence of southward IMF Bz (dawn-to-dusk IEFy) with no modification offered by IMF By and possibly some contribution of DD electric field. As a consequence, the eastward electric field perturbation seems to increase at this time. On the other hand,

10.1029/2022JA030826

during interval-IV, we notice westward penetration electric field that causes downward drift. There is no influence of disturbance dynamo observed during this interval (Figure 6). We propose that the penetration electric field is already westward during this time on this night which is, in general, expected at ~22:00 LT as some of the earlier works (e.g., Fejer et al., 2008b) suggested. However, the magnitude of the westward electric field perturbations during interval-IV cannot be explained by the IEFy magnitude during this time with even 10–15% penetration efficiency and 10% uncertainty in the drift magnitude. Although the AE and PC indices show minor enhancements during interval-IV, LANL-04A observations suggest the presence of substorm related particle injections at the geosynchronous orbit closer to the Indian longitude (Figure 4). On the other hand, IEFy starts decreasing during this interval. Therefore, we suggest that the combined effects of penetration electric fields due to IEFy and substorm cause the unusually large westward electric field perturbation during interval-IV. Earlier works by Hui et al. (2017) and Rout et al. (2019) show that substorm induced electric field can enhance the conventional penetration electric fields in a significant manner. However, it is to be kept in mind, that substorms have been shown earlier to cause both eastward (e.g., Chakrabarty et al., 2008; Chakrabarty et al., 2010; Huang, 2009; Hui et al., 2017; Rout et al., 2019) and westward (e.g., Chakrabarty et al., 2015; Hui et al., 2017; Kikuchi et al., 2000) electric field perturbations over the equatorial ionosphere.

During the interval-V (~22:10–23:10 LT, see Figure 3d), the IMF Bz turns northward from southward, and an overshielding electric field (e.g., Fejer et al., 1979; Gonzales et al., 1979; Kelley et al., 1979) is imposed over the equatorial ionosphere. This provides the eastward perturbations to the ionospheric electric field. In addition, a small effect of DD electric field may be presented at 23:00 LT (18:00 UT) as suggested by Figure 6f. Owing to this, vertical drift becomes less downward during the interval-V. It has been shown earlier (e.g., Chakrabarty et al., 2006; Rout et al., 2019; Sekar & Chakrabarty, 2008) that on many occasions, the nighttime eastward electric field perturbations due to overshielding effect can affect the equatorial F region vertical drifts significantly.

Last but not the least, two peaks are observed in VTEC (Figures 2b) and 630.0 nm airglow intensity (Figure 2c) during the postsunset hours on 24 December 2014. The peaks are more conspicuous in the airglow intensity variation. The first peak occurs at ~14:45 UT (19:45 LT) that is separated from the peak PRE drift (occurs at ~13 UT or 18 LT) by around 1.75 hr. This is consistent with the results of Kumar et al. (2021). The second peak that occurs just before 16:00 UT (or 21:00 LT) is probably a consequence of less quenching as the ionosphere goes up in altitude simultaneously over the entire low latitude due to the imposition of eastward penetration electric field.

5. Role of IMF by: Unresolved Issues

Identification of the role of IMF By on equatorial ionosphere is a complex problem as we feel that southward IMF Bz is precondition on which the effects of IMF By should operate. This inference is true for high latitude. For equatorial latitudes, there are two aspects that are not clear at the present moment. First, what are the optimal magnitudes of southward IMF Bz and IMF By under which the IMF By effects will be discernible? Although, some studies in this regard have been carried out for high latitudes (e.g., Ruohoniemi & Greenwald, 2005), this has not been studied over dip equatorial region. Second, whether IMF By magnitude is more important or polarity reversal in IMF By is more important? Based on the present study and the earlier work (Chakrabarty et al., 2017), we can speculate that both factors can be important and what matters is the combined effects of the resizing of DP2 cells by the southward IMF Bz, rotation of the cells by IMF By, the relative position of the station where IMF By effects are to be detected and finally, the local time at which it is to be detected. It is also clear that one needs high temporal resolution vertical drift data to capture the effects of the sharp changes in IMF By under southward IMF Bz condition. Note, over the Indian sector, there is no incoherent scatter radar and the vertical drifts during nighttime over the dip equatorial region can only be derived based on ionospheric height variations with temporal resolution of 10 min or 15 min under normal circumstances. This is why we abstain from evaluating the relative roles of magnitude and polarity reversal of IMF By based on the present drift data sets the cadence of which is 10 min.

In order to garner further evidence on the importance of high cadence data, we compare 1 minute cadence data of ΔX over Huancayo (in blue) with IMF By (in red) and IMF Bz (in magenta) separately in Figure 7. The intervals II (in green) and III (in orange) in Figure 7 are marked in the same way as that in Figure 3. It is to be noted that Huancayo is in day sector during intervals II and III. Therefore, if we consider that daytime ionospheric conductivity does not change significantly (which is a reasonable assumption) during intervals II and III (~2 hr), the changes in ΔX can be attributed to ionospheric electric field variations. It is interesting to note that

10.1029/2022JA030826

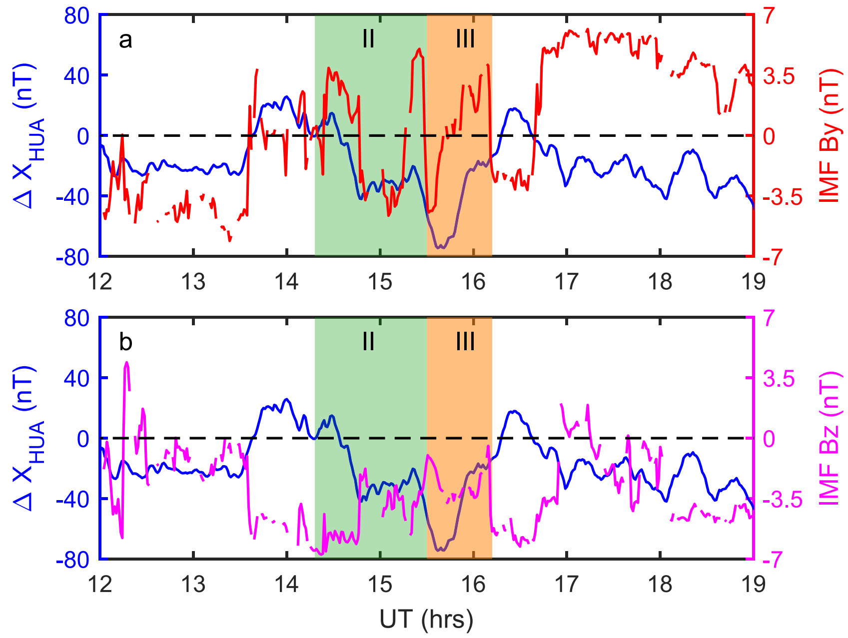

Figure 7. Variations in ΔX over Huancayo (HUA) on 24 December 2014 is shown with blue colored line in panels a and b similar to Figure 5d. Variation in interplanetary magnetic field (IMF) By (in red) and IMF Bz (in magenta) are superimposed on the variations Δ*X* in panels a and b, respectively. The intervals II and III are also marked similar to Figure 3.

the variations in Δ*X* over Huancayo and IMF By go hand in hand in interval-II and a phase offset starts coming up in interval-III. During interval-III, IMF Bz does not change much but IMF By changes significantly although with a phase delay. Therefore, it is possible that the influence of IMF By weakens during interval-III. Since the cadence of Δ*X* variations is 1 minute, this provides credence to the proposition of the influence of IMF By during interval-II. Eventually, the yardstick that we follow (and highlighted in Chakrabarty et al., 2017) for the detection of IMF By effect (under southward IMF Bz) is the identical polarity of electric field perturbations over antipodal stations (Figure 3c) and the systematic variations in Δ*X* from high to low latitudes as shown in Figure 5.

6. Conclusions

The space weather event on 24 December 2014 reported provides a number of critical insights on the nature of the penetration electric field. First, the equatorial/low latitude impact is anomalously enhanced during the postsunset hours of 24 December 2014 when the magnitude of IEFy is not very large but persists through local PRE/postPRE-hours. This suggest that as far as the low latitude ionospheric impacts are considered, the local time of the electric field disturbance is important. Penetration electric field perturbations occurring during PRE-hours when the zonal electric field is already enhanced can make the equatorial impact unusually stronger. Second, during one single event, we see occasion when a number of phenomenologically different penetration electric fields (like penetration electric fields due to IEFy, substorm, disturbance dynamo, etc.) acting simultaneously on the equatorial ionosphere. Therefore, the magnitude of electric field perturbations on some occasions cannot be determined based on the existing paradigm of penetration electric fields. Third and most importantly, due to the additional effects of IMF By for some time, the response of the equatorial electric field perturbations turns out to be anomalous both in terms of magnitude and polarity. These anomalous effects need more attention in future for a comprehensive phenomenological understanding of the nature of the penetration electric fields.

Data Availability Statement

Ap and Sym-H indices are taken from the World Data Center for Geomagnetism, Kyoto (http://wdc.kugi.kyoto-u.ac.jp/). Solar wind parameters are obtained from NASA GSFC CDAWeb (http://cdaweb.gsfc.nasa.gov/). The magnetometer data along the Jicamarca and Indian longitudes are obtained from SuperMag (https://supermag.jhuapl.edu/). One-minute corrected data over Jicamarca and Leticia are taken from the Low Latitude Ionospheric

Sensor Network (LISN) (http://lisn.igp.gob.pe/). The remaining data sets can be obtained from http://dx.doi.org/10.17632/xhm84smdvb.1.

Acknowledgments

We acknowledge the work of all the PIs and support staff for whom these data could be made available. D. Rout acknowledges the support from Humboldt Research Fellowship for Postdoctoral Researchers (Humboldt Foundation Grants PSP D-023-20-001). This work is supported by the Department of Space, Government of India.

References

Abdu, M. A., Nogueira, P. A. B., Santos, A. M., de Souza, J. R., Batista, I. S., & Sobral, J. H. A. (2018). Impact of disturbance electric fields in the evening on prereversal vertical drift and spread f developments in the equatorial ionosphere. *Annales Geophysicae*, *36*(2), 609–620. https://doi.org/10.5194/angeo-36-609-2018

Amory-Mazaudier, C., Bolaji, O. S., & Doumbia, V. (2017). On the historical origins of the CEJ, DP2, and Ddyn current systems and their roles in the predictions of ionospheric responses to geomagnetic storms at equatorial latitudes. *Journal of Geophysical Research: Space Physics*, *122*, 7827–7833. https://doi.org/10.1002/2017JA024132

Anderson, D., & Rusch, D. (1980). Composition of the nighttime ionospheric f 1 region near the magnetic equator. *Journal of Geophysical Research*, *85*(A2), 569–574. https://doi.org/10.1029/JA085iA02p00569

Angelopoulos, V., Coroniti, F. V., Kennel, C. F., Kivelson, M. G., Walker, R. J., Russell, C. T., et al. (1996). Multipoint analysis of a bursty bulk flow event on april 11, 1985. *Journal of Geophysical Research*, *101*(A3), 4967–4989. https://doi.org/10.1029/95JA02722

Baker, D. N., Pulkkinen, T. I., Hesse, M., & McPherron, R. L. (1997). A quantitative assessment of energy storage and release in the earth's magnetotail. *Journal of Geophysical Research*, *102*(A4), 7159–7168. https://doi.org/10.1029/96JA03961

Balan, N., Liu, L., & Le, H. (2018). A brief review of equatorial ionization anomaly and ionospheric irregularities. *Earth and Planetary Physics*, *2*(4), 257–275. https://doi.org/10.26464/epp2018025

Balan, N., Shiokawa, K., Otsuka, Y., Watanabe, S., & Bailey, G. J. (2009). Super plasma fountain and equatorial ionization anomaly during penetration electric field. *Journal of Geophysical Research*, *114*, A03310. https://doi.org/10.1029/2008JA013768

Bittencourt, J. A., & Abdu, M. A. (1981). A theoretical comparison between apparent and real vertical ionization drift velocities in the equatorial f region. *Journal of Geophysical Research*, *86*(A4), 2451–2454. https://doi.org/10.1029/JA086iA04p02451

Blanc, M., & Richmond, A. (1980). The ionospheric disturbance dynamo. *Journal of Geophysical Research*, *85*(A4), 1669–1686. https://doi.org/10.1029/JA085iA04p01669

Chakrabarty, D., Hui, D., Rout, D., Sekar, R., Bhattacharyya, A., Reeves, G. D., & Ruohoniemi, J. M. (2017). Role of IMF by in the prompt electric field disturbances over equatorial ionosphere during a space weather event. *Journal of Geophysical Research: Space Physics*, *122*, 2574–2588. https://doi.org/10.1002/2016JA022781

Chakrabarty, D., Rout, D., Sekar, R., Narayanan, R., Reeves, G. D., Pant, T. K., et al. (2015). Three different types of electric field disturbances affecting equatorial ionosphere during a long-duration prompt penetration event. *Journal of Geophysical Research: Space Physics*, *120*, 4993–5008. https://doi.org/10.1002/2014JA020759

Chakrabarty, D., Sekar, R., Narayanan, R., Devasia, C. V., & Pathan, B. M. (2005). Evidence for the interplanetary electric field effect on the oi 630.0 nm airglow over low latitude. *Journal of Geophysical Research*, *110*, A11301. https://doi.org/10.1029/2005JA011221

Chakrabarty, D., Sekar, R., Narayanan, R., Patra, A. K., & Devasia, C. V. (2006). Effects of interplanetary electric field on the development of an equatorial spread f event. *Journal of Geophysical Research*, *111*, A12316. https://doi.org/10.1029/2006JA011884

Chakrabarty, D., Sekar, R., Sastri, J. H., Pathan, B. M., Reeves, G. D., Yumoto, K., & Kikuchi, T. (2010). Evidence for oi 630.0 nm dayglow variations over low latitudes during onset of a substorm. *Journal of Geophysical Research*, *115*, A10316. https://doi.org/10.1029/2010JA015643

Chakrabarty, D., Sekar, R., Sastri, J. H., & Ravindran, S. (2008). Distinctive effects of interplanetary electric field and substorm on nighttime equatorial f layer: A case study. *Geophysical Research Letters*, *35*, L19108. https://doi.org/10.1029/2008GL035415

Emmert, J. T., Drob, D. P., Picone, J. M., Siskind, D. E., Jones, M., Jr., Mlynczak, M. G., et al. (2021). NRLMSIS 2.0: A whole-atmosphere empirical model of temperature and neutral species densities. *Earth and Space Science*, *8*, e2020EA001321. https://doi.org/10.1029/2020EA001321

Fejer, B. G., Blanc, M., & Richmond, A. D. (2017). Post-storm middle and low-latitude ionospheric electric fields effects. *Space Science Reviews*, *206*(1), 407–429. https://doi.org/10.1007/s11214-016-0320-x

Fejer, B. G., Gonzales, C., Farley, D., Kelley, M., & Woodman, R. (1979). Equatorial electric fields during magnetically disturbed conditions: 1. The effect of the interplanetary magnetic field. *Journal of Geophysical Research*, *84*(A10), 5797–5802. https://doi.org/10.1029/JA084iA10p05797

Fejer, B. G., Jensen, J. W., & Su, S.-Y. (2008a). Quiet time equatorial F region vertical plasma drift model derived from ROCSAT-1 observations. *Journal of Geophysical Research*, *113*, A05304. https://doi.org/10.1029/2007JA012801

Fejer, B. G., Jensen, J. W., & Su, S.-Y. (2008b). Seasonal and longitudinal dependence of equatorial disturbance vertical plasma drifts. *Geophysical Research Letters*, *35*, L20106. https://doi.org/10.1029/2008GL035584

Fejer, B. G., Navarro, L. A., Sazykin, S., Newheart, A., Milla, M. A., & Condor, P. (2021). Prompt penetration and substorm effects over Jicamarca during the September 2017 geomagnetic storm. *Journal of Geophysical Research: Space Physics*, *126*, e2021JA029651. https://doi.org/10.1029/2021JA029651

Gonzales, C., Kelley, M., Fejer, B., Vickrey, J., & Woodman, R. (1979). Equatorial electric fields during magnetically disturbed conditions: 2. Implications of simultaneous auroral and equatorial measurements. *Journal of Geophysical Research*, *84*(A10), 5803–5812. https://doi.org/10.1029/JA084iA10p05803

Hashimoto, K. K., Kikuchi, T., Tomizawa, I., & Nagatsuma, T. (2017). Substorm overshielding electric field at low latitude on the nightside as observed by the hf Doppler sounder and magnetometers. *Journal of Geophysical Research: Space Physics*, *122*, 10851–10863. https://doi.org/10.1002/2017JA024329

Henderson, M. G., Reeves, G. D., Belian, R. D., & Murphree, J. S. (1996). Observations of magnetospheric substorms occurring with no apparent solar wind/IMF trigger. *Journal of Geophysical Research*, *101*(A5), 10773–10791. https://doi.org/10.1029/96JA00186

Huang, C.-S. (2009). Eastward electric field enhancement and geomagnetic positive bay in the dayside low-latitude ionosphere caused by magnetospheric substorms during sawtooth events. *Geophysical Research Letters*, *36*, L18102. https://doi.org/10.1029/2009GL040287

Huang, C.-S., Foster, J. C., Goncharenko, L. P., Reeves, G. D., Chau, J. L., Yumoto, K., & Kitamura, K. (2004). Variations of low-latitude geomagnetic fields and Dst index caused by magnetospheric substorms. *Journal of Geophysical Research*, *109*, A05219. https://doi.org/10.1029/2003JA010334

Huang, C.-S., Sazykin, S., Chau, J. L., Maruyama, N., & Kelley, M. C. (2007). Penetration electric fields: Efficiency and characteristic time scale. *Journal of Atmospheric and Solar-Terrestrial Physics*, *69*(10), 1135–1146. https://doi.org/10.1016/j.jastp.2006.08.016

Huang, C.-S., Yumoto, K., Abe, S., & Sofko, G. (2008). Low-latitude ionospheric electric and magnetic field disturbances in response to solar wind pressure enhancements. *Journal of Geophysical Research*, *113*, A08314. https://doi.org/10.1029/2007JA012940

Hui, D., Chakrabarty, D., Sekar, R., Reeves, G. D., Yoshikawa, A., & Shiokawa, K. (2017). Contribution of storm time substorms to the prompt electric field disturbances in the equatorial ionosphere. *Journal of Geophysical Research: Space Physics*, *122*, 5568–5578. https://doi.org/10.1002/2016JA023754

Hui, D., & Vichare, G. (2021). Influence of IMF-by on the equatorial ionospheric plasma drifts: TIEGCM simulations. *Journal of Geophysical Research: Space Physics*, *126*, e2021JA029270. https://doi.org/10.1029/2021JA029270

Kelley, M. C., Fejer, B. G., & Gonzales, C. A. (1979). An explanation for anomalous equatorial ionospheric electric fields associated with a northward turning of the interplanetary magnetic field. *Geophysical Research Letters*, *6*(4), 301–304. https://doi.org/10.1029/GL006i004p00301

Kelley, M. C., & Makela, J. J. (2002). By-dependent prompt penetrating electric fields at the magnetic equator. *Geophysical Research Letters*, *29*(7), 571–573. https://doi.org/10.1029/2001GL014468

Kelley, M. C., Makela, J. J., Chau, J. L., & Nicolls, M. J. (2003). Penetration of the solar wind electric field into the magnetosphere/ionosphere system. *Geophysical Research Letters*, *30*(4), 1158. https://doi.org/10.1029/2002GL016321

Kikuchi, T., Hashimoto, K. K., Kitamura, T.-I., Tachihara, H., & Fejer, B. (2003). Equatorial counterelectrojets during substorms. *Journal of Geophysical Research*, *108*(A11), 1406. https://doi.org/10.1029/2003JA009915

Kikuchi, T., Hashimoto, K. K., & Nozaki, K. (2008). Penetration of magnetospheric electric fields to the equator during a geomagnetic storm. *Journal of Geophysical Research*, *113*, A06214. https://doi.org/10.1029/2007JA012628

Kikuchi, T., Lühr, H., Schlegel, K., Tachihara, H., Shinohara, M., & Kitamura, T.-I. (2000). Penetration of auroral electric fields to the equator during a substorm. *Journal of Geophysical Research*, *105*(A10), 23251–23261. https://doi.org/10.1029/2000JA900016

Klimas, A. J., Valdivia, J. A., Vassiliadis, D., Baker, D. N., Hesse, M., & Takalo, J. (2000). Self-organized criticality in the substorm phenomenon and its relation to localized reconnection in the magnetospheric plasma sheet. *Journal of Geophysical Research*, *105*(A8), 18765–18780. https://doi.org/10.1029/1999JA000319

Kumar, A., Chakrabarty, D., Pandey, K., Fejer, B. G., Sunda, S., Seemala, G. K., et al. (2021). Evidence for the significant differences in response times of equatorial ionization anomaly crest corresponding to plasma fountains during daytime and post-sunset hours. *Journal of Geophysical Research: Space Physics*, *126*, e2020JA028628. https://doi.org/10.1029/2020JA028628

Kumar, A., Chakrabarty, D., Pandey, K., & Yadav, A. K. (2022). Solar flux dependence of post-sunset enhancement in vertical total electron content over the crest region of equatorial ionization anomaly. *Journal of Geophysical Research: Space Physics*, *127*, e2021JA030156. https://doi.org/10.1029/2021JA030156

Le, H., Liu, L., Chen, Y., Zhang, H., & Wan, W. (2014). Modeling study of nighttime enhancements in f region electron density at low latitudes. *Journal of Geophysical Research: Space Physics*, *119*, 6648–6656. https://doi.org/10.1002/2013JA019295

Liu, L., Chen, Y., Le, H., Ning, B., Wan, W., Liu, J., & Hu, L. (2013). A case study of postmidnight enhancement in f-layer electron density over sanya of China. *Journal of Geophysical Research: Space Physics*, *118*, 4640–4648. https://doi.org/10.1002/jgra.50422

Lu, G., Goncharenko, L., Nicolls, M. J., Maute, A., Coster, A., & Paxton, L. J. (2012). Ionospheric and thermospheric variations associated with prompt penetration electric fields. *Journal of Geophysical Research*, *117*, A08312. https://doi.org/10.1029/2012JA017769

Lyons, L. R. (1995). A new theory for magnetospheric substorms. *Journal of Geophysical Research*, *100*(A10), 19069–19081. https://doi.org/10.1029/95JA01344

Lyons, L. R. (1996). Substorms: Fundamental observational features, distinction from other disturbances, and external triggering. *Journal of Geophysical Research*, *101*(A6), 13011–13025. https://doi.org/10.1029/95JA01987

Lyons, L. R., Blanchard, G. T., Samson, J. C., Lepping, R. P., Yamamoto, T., & Moretto, T. (1997). Coordinated observations demonstrating external substorm triggering. *Journal of Geophysical Research*, *102*(A12), 27039–27051. https://doi.org/10.1029/97JA02639

MacDougall, J., Grant, I., & Shen, X. (1995). *The Canadian advanced digital ionosonde: Design and results* (UAG-104). URSI INAG Ionospheric Station Inf. Bulletin.

Manke, A. A., & Chakarabarty, D. (2016). An integrated software platform for GPS/GNSS ionospheric data analysis. *International Journal of Science, Engineering and Technology*, *4*(5), 796–804. https://doi.org/10.2348/ijset09160796

Mannucci, A. J., Tsurutani, B. T., Iijima, B. A., Komjathy, A., Saito, A., Gonzalez, W. D., et al. (2005). Dayside global ionospheric response to the major interplanetary events of October 29–30, 2003 "Halloween storms". *Geophysical Research Letters*, *32*, L12S02. https://doi.org/10.1029/2004GL021467

McPherron, R. L. (1979). Magnetospheric substorms. *Reviews of Geophysics*, *17*(4), 657–681. https://doi.org/10.1029/RG017i004p00657

Nishida, A. (1968). Geomagnetic Dp 2 fluctuations and associated magnetospheric phenomena. *Journal of Geophysical Research*, *73*(5), 1795–1803. https://doi.org/10.1029/JA073i005p01795

Nopper, R. W., Jr., & Carovillano, R. L. (1978). Polar-equatorial coupling during magnetically active periods. *Geophysical Research Letters*, *5*(8), 699–702. https://doi.org/10.1029/GL005i008p00699

Pandey, K., Chakrabarty, D., & Sekar, R. (2018). Critical evaluation of the impact of disturbance dynamo on equatorial ionosphere during daytime. *Journal of Geophysical Research: Space Physics*, *123*, 9762–9774. https://doi.org/10.1029/2018JA025686

Rastogi, R., & Klobuchar, J. (1990). Ionospheric electron content within the equatorial f 2 layer anomaly belt. *Journal of Geophysical Research*, *95*(A11), 19045–19052. https://doi.org/10.1029/JA095iA11p19045

Rastogi, R., & Patel, V. (1975). Effect of interplanetary magnetic field on ionosphere over the magnetic equator. *Proceedings of the Indian Academy Of Sciences: Section A*, *82*(4), 121–141. https://doi.org/10.1007/BF03046722

Reeves, G. D., McAdams, K. L., Friedel, R. H. W., & O'Brien, T. P. (2003). Acceleration and loss of relativistic electrons during geomagnetic storms. *Geophysical Research Letters*, *30*(10), 1529. https://doi.org/10.1029/2002GL016513

Rout, D., Chakrabarty, D., Sekar, R., Reeves, G. D., Ruohoniemi, J. M., Pant, T. K., et al. (2016). An evidence for prompt electric field disturbance driven by changes in the solar wind density under northward IMF Bz condition. *Journal of Geophysical Research: Space Physics*, *121*, 4800–4810. https://doi.org/10.1002/2016JA022475

Rout, D., Pandey, K., Chakrabarty, D., Sekar, R., & Lu, X. (2019). Significant electric field perturbations in low latitude ionosphere due to the passage of two consecutive ICMES during 6–8 September 2017. *Journal of Geophysical Research: Space Physics*, *124*, 9494–9510. https://doi.org/10.1029/2019JA027133

Ruohoniemi, J. M., & Greenwald, R. A. (2005). Dependencies of high-latitude plasma convection: Consideration of interplanetary magnetic field, seasonal, and universal time factors in statistical patterns. *Journal of Geophysical Research*, *110*, A09204. https://doi.org/10.1029/2004JA010815

Sastri, J. H., Rao, J. V. S. V., & Ramesh, K. B. (1993). Penetration of polar electric fields to the nightside dip equator at times of geomagnetic sudden commencements. *Journal of Geophysical Research*, *98*(A10), 17517–17523. https://doi.org/10.1029/93JA00418

Savitzky, A., & Golay, M. J. (1964). Smoothing and differentiation of data by simplified least squares procedures. *Analytical Chemistry*, *36*(8), 1627–1639. https://doi.org/10.1021/ac60214a047

Sekar, R., & Chakrabarty, D. (2008). Role of overshielding electric field on the development of pre-midnight plume event: Simulation results. *Journal of Atmospheric and Solar-Terrestrial Physics*, *70*(17), 2212–2221. https://doi.org/10.1016/j.jastp.2008.04.015